

Optimization and Control of a Large-scale Solar Chimney Power Plant

by

Johannes Petrus Pretorius

*Dissertation presented for the degree of Doctor of Mechanical Engineering at
the University of Stellenbosch*

Department of Mechanical Engineering
University of Stellenbosch
Private Bag X1, 7602 Matieland, South Africa

Promoter: Prof D.G. Kröger

March 2007

Copyright © 2007 University of Stellenbosch
All rights reserved.

Declaration

I, the undersigned, hereby declare that the work contained in this dissertation is my own original work and that I have not previously in its entirety or in part submitted it at any university for a degree.

Signature:

J.P. Pretorius

Date:

Uittreksel

Optimering en Beheer van 'n Groot skaalse Sonskoorsteen-Kragstasie

(“Optimization and Control of a Large-scale Solar Chimney Power Plant”)

J.P. Pretorius

*Departement Meganiese Ingenieurswese
Universiteit van Stellenbosch
Privaatsak X1, 7602 Matieland, Suid-Afrika*

Proefskrif: PhD

Maart 2007

Die proefskrif bou op vorige navorsing (Pretorius, 2004) en ondersoek die optimering en beheer van 'n groot skaalse sonskoorsteen-kragstasie. Uitsetresultate word baseer op 'n verwysingsligging naby Sishen in Suid-Afrika en 'n sogenaamde verwysingskragstasie, met 'n kollektor deursnee van 5000 m en 'n 1000 m hoë, 210 m deursnee skoorsteen. Die numeriese rekenaarmodel is verbeter en gebruik vir die uitvoering van 'n sensitiwiteits-analise op die belangrikste bedryfs- en tegniese kragstasie spesifikasies. Termo-ekonomiese optimale aanlegkonfigurasies is bepaal volgens die uitsetresultate van die rekenaarmodel en benaderde aanleg-kosteberekeninge volgens 'n eenvoudige kostemodel. Die invloed van wind, atmosferiese temperatuur gradiënte en nagtelike temperatuur inversies op kragstasie uitset word beskou. Verskeie nuwe tegnologië word ondersoek met die doel om aanleg uitset te kan beheer volgens spesifieke elektrisiteit aanvraagspatrone. Die inkorporasie van plantegroei onder die kollektordak, en die invloed daarvan op kragstasie uitset, word ook beskou.

Bevindings dui aan dat, deur die wysiging van die kollektordak refleksie, kollektordak emissiwiteit, grondoppervlak absorptiwiteit of grondoppervlak emissiwiteit, groot verbeterings op aanleg uitset moontlik is. Die implementering van termiese isolasie of 'n dubbel-glaslaag vir die kollektordak veroorsaak ook 'n beduidende verheffing in kragstasie uitset. Simulasies voorspel 'n merkbare sensitiwiteit teenoor die grondoppervlak absorptiwiteits-waarde, terwyl veranderlike atmosferiese temperatuur daaltempos en winderige omgewings-toestande aanleg uitset beduidend mag belemmer. Verder is bevind dat Sand ongeskik is as aanleg grond tipe en dat termo-ekonomiese optimale sonskoorsteen-kragstasie dimensies in die algemeen groter is as die aanvaarde aanlegdimensies van vorige studies. Goeie dinamiese beheer van sonskoorsteen-kragstasie uitset is bevestig, wat suggereer dat die sonskoorsteen-kragstasie as 'n basis of pieklas elektrisiteitopwekkings-aanleg ingespan kan word. Ten laaste voorspel resultate dat plantegroei, mits dit voorsien word van genoegsame water, sal kan oorleef onder die kollektordak maar dat die inkorporasie van plantegroei die aanleg uitset beduidend sal benadeel.

Abstract

Optimization and Control of a Large-scale Solar Chimney Power Plant

J.P. Pretorius

*Department of Mechanical Engineering
University of Stellenbosch
Private Bag X1, 7602 Matieland, South Africa*

Dissertation: PhD

March 2007

The dissertation builds on previous research (Pretorius, 2004) and investigates the optimization and control of a large-scale solar chimney power plant. Performance results are based on a reference location near Sishen in South Africa and a so-called reference solar chimney power plant, with a 5000 m collector diameter and a 1000 m high, 210 m diameter chimney. The numerical simulation model is refined and used to perform a sensitivity analysis on the most prominent operating and technical plant specifications. Thermo-economically optimal plant configurations are established from simulation results and calculations according to an approximate plant cost model. The effects of ambient wind, temperature lapse rates and nocturnal temperature inversions on plant performance are examined. Various new technologies are investigated for the purpose of controlling plant output according to specific demand patterns. The incorporation of vegetation under the collector roof of the plant and the influence thereof on plant performance is also explored.

Results indicate that, through the modification of the collector roof reflectance, collector roof emissivity, ground surface absorptivity or ground surface emissivity, major improvements on plant performance are possible. Introducing thermal insulation or double glazing of the collector roof also facilitates substantial enhancements on plant yield. Simulations predict a notable sensitivity to the ground surface absorptivity value, while variable atmospheric temperature lapse rates and windy ambient conditions may impair plant performance significantly. Furthermore, Sand is found to be unsuitable as plant ground type and thermo-economically optimal solar chimney plant dimensions are determined to be generally larger than plant dimensions employed in previous studies. Good dynamic control of solar chimney power output is established, suggesting that a solar chimney power plant can be implemented as a base or peak load electricity generating facility. Lastly, results predict that vegetation, when provided with sufficient water, will be able to survive under the collector roof but the inclusion of vegetation will however cause major reductions in plant performance.

Acknowledgements

I would like to express my sincere gratitude to the following people who have contributed to making this work possible:

- Prof D.G. Kröger of the University of Stellenbosch as my promoter and mentor,
- Prof T.W. Von Backström, Mr T.P. Fluri and Mr C. Van Dyk of the University of Stellenbosch for their technical support,
- Mr D. Els of the University of Stellenbosch for his support regarding optimization and layout of this document,
- Mrs D. Westdyk of the University of Stellenbosch for her insights regarding vegetation,
- Dr C. Coetzee of the University of Stellenbosch for his advice on best practices,
- The National Research Foundation of South Africa for their financial support,
- Volkswagen Stiftung for their financial support.

I would also like to thank my family and friends for their steady love and support. Most of all, I thank the Lord in Heaven for His continual grace and guidance, without which this study would not have been possible.

Contents

Declaration	ii
Uittreksel	iii
Abstract	iv
Acknowledgements	v
Contents	vi
List of Figures	ix
List of Tables	xiv
Nomenclature	xvii
1 Introduction	1
1.1 Energy: consumption and availability	1
1.2 Global warming	2
1.3 The Kyoto Protocol	3
1.4 Renewable energy	4
1.5 Solar chimney power plants: concept and history	12
1.6 Why use solar chimney power plants?	13
1.7 Literature review	15
1.8 Objectives of current study	17
2 Plant Model Specification	18
2.1 Reference plant configuration	18
2.2 Governing conservation equations	19
2.3 Convective heat transfer equations	20
2.4 Momentum equations	24
2.5 Meteorological data of the reference location	26
2.6 Modelling ambient cross-winds	27
3 Critical Evaluation of Plant Performance	30
3.1 Convective heat transfer and momentum equations	30
3.2 Collector roof glass quality	32
3.3 Collector roof thickness	34
3.4 Collector roof reflectance	35
3.5 Collector roof emissivity	36
3.6 Collector roof insulation	38
3.7 Collector roof shape	39
3.8 Collector roof support diameter	40
3.9 Various ground types	42
3.10 Ground surface roughness	44

3.11	Ground absorptivity	46
3.12	Ground emissivity	47
3.13	Turbine inlet loss coefficient	48
3.14	Bracing wheel pressure loss coefficient	50
3.15	Ambient pressure	51
3.16	Ambient temperature lapse rate	53
4	Thermo-Economic Plant Optimization	55
4.1	Selecting dimensions for optimization	55
4.2	Approximate cost model	56
4.3	Simulation and results	56
5	Ambient Wind, Temperature Lapse Rate and Temperature Inversion Effects	68
5.1	Wind effects	68
5.2	Ambient temperature lapse rate effects	72
5.3	Nocturnal temperature inversion effects	76
6	Regulating Plant Power Output According to Demand	81
6.1	Base and peak load power stations	81
6.2	Including a double glazed main collector roof	82
6.3	Including a secondary collector roof	86
6.4	Including a double glazed secondary collector roof	92
6.5	Including a secondary and tertiary collector roof	95
6.6	Including plastic covered water tanks	101
6.7	Including a delta ground surface configuration	106
7	Vegetation Under the Collector Roof	111
7.1	Modification under collector roof	111
7.2	Determining the rate of evapotranspiration	111
7.3	Temperature lapse rates for moist air	114
7.4	Vegetation/Ground discretization scheme	115
7.5	Plant specifications	118
7.6	Assumptions	118
7.7	Simulations and results	119
7.8	Temperature lapse rates effects	123
8	Conclusion	129
8.1	Discussion and future work	132
	List of References	133
A	Including a Secondary Collector Roof	138
A.1	Definition of sections in the collector	139
A.2	Collector continuity equation	139
A.3	Collector momentum equation	142
A.4	Collector roof energy equation	149
A.5	Secondary roof energy equation	151
A.6	Ground energy equations	152
A.7	Air stream energy equation	154
B	Including a Double Glazed Main or Secondary Roof	159
B.1	Double glazed main collector roof	160
B.2	Double glazed secondary collector roof	162

C Including a Tertiary Collector Roof	164
C.1 Definition of sections in the collector	164
C.2 Collector continuity equation	165
C.3 Collector momentum equation	167
C.4 Collector roof energy equation	169
C.5 Secondary roof energy equation	169
C.6 Tertiary roof energy equation	170
C.7 Ground energy equations	171
C.8 Air stream energy equation	172
D Including Plastic Covered Water Tanks	174
D.1 Definition of sections in the collector	174
D.2 Ground section	175
D.3 Water tank section	175
E Including a Delta Ground Surface Configuration	177
E.1 Approximating the delta configuration numerically	177
E.2 Ground surface energy equation	178
E.3 Air stream energy equation	178
F Including Vegetation Under the Collector Roof	179
F.1 Definition of sections in the collector	179
F.2 Vegetation section	179
F.3 Ground section	188
G Solar Radiative Properties of the Solar Collector	189
G.1 The secondary collector roof	189
G.2 The double glazed main collector roof	193
G.3 The double glazed secondary collector roof	193
G.4 The secondary and tertiary collector roofs	195
G.5 The plastic covered water tanks	196
H Meteorological Data Tables	198

List of Figures

1.1	Global energy consumption by source (U.S. Energy Information Administration, 2001)	1
1.2	Energy sources: percentage contribution to global energy consumption (U.S. Energy Information Administration, 2001)	2
1.3	Commitments to the Kyoto Protocol	3
1.4	An example of a solid biofuel	4
1.5	Generating electricity using the earth's natural heat (co2balance.com, 2006)	5
1.6	A 240 MW tidal power facility on the Rance river, France (Bigelow laboratory for ocean sciences, 2006)	6
1.7	A computer generated image of a proposed offshore tidal turbine (Atkins Power, 2006)	6
1.8	A computer generated image of a proposed offshore tidal aerofoil-type generator	7
1.9	Schematic illustration of a tapered channel (TAPCHAN) wave energy device (UN atlas of the oceans, 2006)	7
1.10	Offshore horizontal axis wind turbines	8
1.11	A Darrieus-type vertical axis wind turbine	9
1.12	A Central Receiver solar power plant (US Department of Energy, 2006)	10
1.13	Photovoltaic solar panels	10
1.14	A parabolic trough solar collector (Solar-Auto-Controller, 2006)	11
1.15	A Solar dish-engine system with multiple reflectors (Innovative Power Systems, 2006)	11
1.16	Aerial view of a Solar Pond power plant (University of Texas El Paso, 2006)	12
1.17	A schematic illustration of a solar chimney power plant (single turbine configuration)	13
1.18	The pilot solar chimney power plant in Manzanares, Spain	13
1.19	Computer generated image of a proposed large-scale solar chimney power plant (Schlaich Bergermann und Partner, 2006)	14
1.20	Annual global solar radiation	15
2.1	A schematic illustration of a solar chimney power plant	19
3.1	Effect of the convective heat transfer and momentum equations on daily plant power output	31
3.2	Comparison between the new and original convective heat transfer coefficients	32
3.3	Effect of optical collector roof glass quality on the daily power output	33
3.4	Effect of collector roof (glass) thickness on daily plant power output	34
3.5	Effect of collector roof reflectance on daily plant power output	36
3.6	Effect of collector roof emissivity (top surface) on daily plant output	37
3.7	Effect of thermal collector roof insulation on daily plant output	38
3.8	Effect of collector roof shape on daily plant power output	40
3.9	Effect of collector roof support diameter on daily solar chimney power plant output	41
3.10	The influence of various ground types on the daily power output of a solar chimney power plant	43
3.11	Effect of ground surface roughness on daily plant power output	45

3.12	Effect of ground absorptivity on plant performance	46
3.13	Effect of ground emissivity on plant performance	48
3.14	Effect of turbine inlet loss coefficient on daily plant power output	49
3.15	Effect of bracing wheel pressure loss coefficient on plant performance	50
3.16	Effect of ambient pressure on plant performance	51
3.17	Effect of ambient lapse rate on solar chimney plant performance	53
4.1	Approximate annual power output for various solar chimney power plant configurations, for plants with a chimney height of $H_c = 500$ m	58
4.2	Approximate annual power output for various solar chimney power plant configurations, for plants with a chimney height of $H_c = 1000$ m	59
4.3	Approximate annual power output for various solar chimney power plant configurations, for plants with a chimney height of $H_c = 1500$ m	60
4.4	Approximate specific cost for various solar chimney power plant configurations, for plants with a chimney height of $H_c = 500$ m	61
4.5	Approximate specific cost for various solar chimney power plant configurations, for plants with a chimney height of $H_c = 1000$ m	62
4.6	Approximate specific cost for various solar chimney power plant configurations, for plants with a chimney height of $H_c = 1500$ m	63
5.1	The linear and power-law wind profiles for a 500 m high chimney ($v_w = 2$ m/s at 10 m above ground level)	69
5.2	The linear and power-law wind profiles for a 1000 m high chimney ($v_w = 2$ m/s at 10 m above ground level)	70
5.3	The linear and power-law wind profiles for a 1500 m high chimney ($v_w = 2$ m/s at 10 m above ground level)	70
5.4	Effect of ambient wind on plant power output	72
5.5	Graphical illustration of the modified ISA (Eq.(5.2)) and DALR (Eq.(5.4)) and their implementation into the numerical model	74
5.6	The specified DALR and actual atmospheric temperature distribution	74
5.7	The effect of two atmospheric lapse rate models on daily power output	76
5.8	Graphical illustration of the modified ISA (Eq. (5.2)), temperature inversion profile (Eq. (5.10)) and nocturnal DALR (Eq. (5.12)) and their implementation into the numerical model for modelling the night-time atmosphere	78
5.9	The effect of two atmospheric lapse rate models on daily power output	80
6.1	Typical electricity demand pattern for South Africa	82
6.2	Effect on plant performance of including a double glazed collector roof over the entire collector area; effect of spacing between double glazing sheets	84
6.3	Effect on plant performance of including a partially double glazed collector roof ($L = 0.01$ m, DG = Double glazed)	85
6.4	Controlling plant power output by regulating the collector air-flow	86
6.5	Schematic plan view of the solar chimney power plant collector, showing the proposed radial channels under the secondary collector roof	87
6.6	Daily solar chimney power plant performance as base load facility - controlled power output through the inclusion of a secondary collector roof (SR = Secondary roof)	89
6.7	Daily solar chimney power plant performance as peak load facility - controlled power output through the inclusion of a secondary collector roof (SR = Secondary roof)	91
6.8	Daily solar chimney power plant performance as base load facility - controlled power output through the inclusion of a double glazed secondary collector roof (DG = Double glazed; SR = Secondary roof)	93

6.9 Daily solar chimney power plant performance as peak load facility - controlled power output through the inclusion of a double glazed secondary collector roof (DG = Double glazed; SR = Secondary roof) 94

6.10 Daily solar chimney power plant performance as base load facility - controlled power output through the inclusion of a secondary and tertiary collector roof (STR = Secondary and tertiary roof) 97

6.11 Daily solar chimney power plant performance as peak load facility - controlled power output through the inclusion of a secondary and tertiary collector roof (STR = Secondary and tertiary roof) 99

6.12 Daily solar chimney power plant performance as base load facility - controlled power output through the inclusion of a secondary and tertiary collector roof (STR = Secondary and tertiary roof), while minimizing seasonal output variations100

6.13 Daily solar chimney power plant performance for a plant incorporating water tanks over various fractions of the collector ground surface area ($t_w = 0.2$ m) . . 103

6.14 Daily solar chimney power plant performance for a plant incorporating water tanks over the entire collector ground surface area; effect of varying water tank depths 105

6.15 Delta ground surface configuration 107

6.16 A section of the collector, showing the proposed idea of arranging the collector ground surface to have a delta configuration 107

6.17 Daily solar chimney power plant performance for a plant incorporating a delta ground surface configuration with varying angles of repose ($H_{2,D} = 1$ m) 109

6.18 Daily solar chimney power plant performance for a plant incorporating a delta ground surface configuration with varying perimeter heights ($\theta_D = 35^\circ$) 110

7.1 Collector finite difference grid for the ground/vegetation control volumes 116

7.2 Daily solar chimney power output profile, illustrating the influence of including vegetation under the collector roof, over a radial distance of 1978 m from the collector perimeter 120

7.3 The psychrometric chart, illustrating the heating and humidification and simple heating of the collector air at 09:00 and 14:00 on 21 June and 21 December, for $r_{ve} = 1978$ m 120

7.4 Vegetation or ground surface temperature and relative humidity of the collector air throughout the collector at 09:00 on 21 June and 21 December, for $r_{ve} = 1978$ m121

7.5 Vegetation or ground surface temperature and relative humidity of the collector air throughout the collector at 14:00 on 21 June and 21 December, for $r_{ve} = 1978$ m122

7.6 Mass-flow rate of water removed from the vegetation through evapotranspiration, throughout a typical day in June and December, for $r_{ve} = 1978$ m 123

7.7 Daily solar chimney power output profile, illustrating the influence of including vegetation under the collector roof, over a radial distance of 1012 m from the collector perimeter 124

7.8 The psychrometric chart, illustrating the heating and humidification and simple heating of the collector air at 09:00 and 14:00 on 21 June and 21 December, for $r_{ve} = 1012$ m 124

7.9 Vegetation or ground surface temperature and relative humidity of the collector air throughout the collector at 09:00 on 21 June and 21 December, for $r_{ve} = 1012$ m125

7.10 Vegetation or ground surface temperature and relative humidity of the collector air throughout the collector at 14:00 on 21 June and 21 December, for $r_{ve} = 1012$ m125

7.11 Mass-flow rate of water removed from the vegetation through evapotranspiration, throughout a typical day in June and December, for $r_{ve} = 1012$ m 126

7.12 Daily solar chimney power output for a plant employing vegetation under the collector roof over a radial distance of $r_{ve} = 1978$ m; effect of different temperature lapse rate models on plant performance 127

7.13	Daily solar chimney power output for a plant employing vegetation under the collector roof over a radial distance of $r_{ve} = 1012$ m; effect of different temperature lapse rate models on plant performance	128
A.1	Definition of sections created in the collector by the inclusion of a secondary collector roof	138
A.2	Conservation of mass applied to the air flowing through a defined top and bottom section collector control volume	140
A.3	Conservation of mass applied to the air flowing through a defined transitional collector control volume	141
A.4	Conservation of momentum applied to the air flowing through a defined top and bottom section collector control volume	143
A.5	Forces acting on the defined top and bottom air stream control volumes in the collector	144
A.6	Conservation of momentum applied to the air stream flowing through the defined transitional collector control volume	148
A.7	Conservation of energy applied to a radial control volume for the main collector roof	150
A.8	Conservation of energy applied to a radial control volume for the secondary collector roof	151
A.9	Conservation of energy applied to a radial control volume for the ground surface under the secondary collector roof	153
A.10	Conservation of energy applied to the air flowing through a defined top and bottom section collector control volume	155
A.11	Conservation of energy applied to the air stream flowing through the transitional control volume of the collector	157
B.1	Collector configuration incorporating double glazed main collector roof	159
B.2	Collector configuration incorporating a main and double glazed secondary collector roof	160
B.3	Conservation of energy applied to the top sheet of the double glazed main collector roof	160
B.4	Conservation of energy applied to the bottom sheet of the double glazed main collector roof	161
B.5	Conservation of energy applied to the top sheet of the double glazed secondary collector roof	162
B.6	Conservation of energy applied to the bottom sheet of the double glazed secondary collector roof	163
C.1	Definition of sections created in the collector by the inclusion of a secondary and tertiary collector roof	165
C.2	Conservation of energy applied to a radial control volume for the secondary collector roof	170
C.3	Conservation of energy applied to a radial control volume for the tertiary collector roof	171
D.1	Definition of sections created in the collector by the inclusion of plastic covered water tanks	174
D.2	Conservation of energy applied to a control volume for the water tank in the collector	176
E.1	Calculation of the F_D ratio	177
F.1	Definition of sections created in the collector by the inclusion of vegetation	180

F.2	Conservation of water vapor mass applied to a control volume in the vegetation section of the collector	180
F.3	Conservation of energy applied to a control volume for the vegetation surface in the collector	182
F.4	Conservation of energy applied to a control volume for the vegetation in the collector	183
F.5	Conservation of energy applied to a boundary control volume on the vegetation side of the interface between the vegetation and ground	184
F.6	Conservation of energy applied to a boundary control volume on the ground side of the interface between the vegetation and ground	185
F.7	Conservation of energy applied to a control volume for the air stream in the vegetation section of the collector	187
G.1	The path of incident solar radiation as it is reflected and transmitted through a double parallel sheet system, represented by the main and secondary collector roofs	190
G.2	Ray tracing through a system of multiple parallel semi-transparent sheets	191
G.3	The path of incident solar radiation as it is reflected and transmitted through a double parallel sheet system, represented by the top and bottom sheets of the double glazed main collector roof	193
G.4	The path of incident solar radiation as it is reflected and transmitted through a triple parallel sheet system, represented by the main and double glazed secondary collector roofs	194
G.5	The path of incident solar radiation as it is reflected and transmitted through a triple parallel sheet system, represented by the main, secondary and tertiary collector roofs	195
G.6	Single sheet and absorber configuration, represented by the main collector roof and water tank respectively	196
G.7	Reflectance and transmittance of a semi-transparent sheet (plastic film) surrounded by different media (air and water)	196

List of Tables

2.1	Reference solar chimney power plant configuration	18
2.2	Reference location co-ordinates and Standard Time Zone	26
3.1	Annual power output comparison, illustrating the effect of the convective heat transfer and corresponding momentum equations on plant performance	31
3.2	Annual power output comparison, illustrating the influence of optical collector roof glass quality on solar chimney power plant performance	33
3.3	Annual power output comparison, illustrating the influence of collector roof (glass) thickness on plant performance	35
3.4	Annual power output comparison, illustrating the effect of collector roof reflectance on the performance of the reference solar chimney power plant	36
3.5	Annual power output comparison, illustrating the effect of collector roof emissivity (top surface) on plant performance	37
3.6	Annual power output comparison, illustrating the effect of collector roof insulation on plant performance	39
3.7	Annual power output comparison, illustrating the influence of collector roof shape on plant performance	40
3.8	Annual power output comparison, illustrating the influence of collector roof support diameter on plant performance	41
3.9	Average properties of Granite, Limestone and Sandstone according to Holman (1992); Average properties of Sand and water (at 300 K) according to Incropera and DeWitt (2002); Average properties of wet soil according to Mills (1995)	42
3.10	Annual power output comparison for a solar chimney power plant employing various ground types	44
3.11	Extract of some natural surface roughness lengths by Kröger (2004)	45
3.12	Annual power output comparison, illustrating the effect of ground surface roughness on plant performance	45
3.13	Annual power output comparison, showing the influence of ground absorptivity on plant performance	47
3.14	Annual power output comparison, showing the influence of ground emissivity on plant performance	48
3.15	Annual power output comparison, showing the influence of the turbine inlet loss coefficient on plant performance	49
3.16	The influence of the bracing wheel pressure loss coefficient on annual solar chimney power plant output (values displayed based on one bracing wheel)	51
3.17	The influence of ambient pressure on annual solar chimney power plant output	52
3.18	Effect of the ambient lapse rate on the annual power output of the reference solar chimney power plant	54
4.1	Selected solar chimney plant dimensions for optimization	56
4.2	Varying cost parameters	57
4.3	Annual power output (in GWh) of various plant configurations for a chimney height of $H_c = 500$ m, with values in bold indicating which configurations experience cold inflow	64

4.4	Annual power output (in GWh) of various plant configurations for a chimney height of $H_c = 1000$ m, with values in bold indicating which configurations experience cold inflow	64
4.5	Annual power output (in GWh) of various plant configurations for a chimney height of $H_c = 1500$ m, with values in bold indicating which configurations experience cold inflow	65
4.6	Optimal solar chimney power plant configurations	66
4.7	Annual power output, total cost and specific cost for the optimal solar chimney power plant configurations of table 4.6	67
5.1	Annual solar chimney power plant performance for various wind profile approximations	71
5.2	Annual power output comparison, illustrating the effect of ambient winds on solar chimney power plant performance	72
5.3	Annual power output comparison, showing the influence of employing a DALR/ISA combination versus only a DALR to model the environment surrounding a solar chimney power plant	76
5.4	The influence on annual power output of employing a DALR/ISA/Inversion combination versus only a DALR to model the environment surrounding a solar chimney power plant	80
6.1	Full or partially double glazed collector roof specifications for each of the following simulations (DG = Double glazed)	83
6.2	Annual power output comparison, illustrating the effect of incorporating a double glazed collector roof over the full collector area and the effect of varying spacing between double glazing sheets	84
6.3	Annual power output comparison, illustrating the effect of incorporating a partially double glazed collector roof (with $L = 0.01$ m)	85
6.4	Secondary collector roof specifications	88
6.5	Annual power output comparison, illustrating the effect of incorporating a secondary collector roof for the purpose of base load electricity generation	90
6.6	Annual power output comparison, illustrating the effect of incorporating a secondary collector roof for the purpose of peak load electricity generation	92
6.7	Double glazed secondary collector roof specifications (DG = Double glazed)	92
6.8	Annual power output comparison, illustrating the effect of incorporating a double glazed secondary collector roof for the purpose of base load electricity generation (DG = Double glazed)	94
6.9	Annual power output comparison, illustrating the effect of incorporating a double glazed secondary collector roof for the purpose of peak load electricity generation (DG = Double glazed)	95
6.10	Secondary and tertiary collector roof specifications	96
6.11	Annual power output comparison, illustrating the effect of incorporating a secondary and tertiary collector roof for the purpose of base load electricity generation (DG = Double glazed)	97
6.12	Annual power output comparison, illustrating the effect of incorporating a secondary and tertiary collector roof for the purpose of peak load electricity generation (DG = Double glazed)	99
6.13	Annual power output comparison, illustrating the effect of employing a control strategy to minimize seasonal output variations; each plant model incorporates a secondary and tertiary collector roof and both models are subject to a base load control strategy	101
6.14	Water tanks specifications for each of the following simulations	102

6.15	Annual power output comparison, illustrating the effect of incorporating water tanks over various fractions of the collector ground surface area ($t_w = 0.2$ m) . . .	104
6.16	Annual power output comparison, illustrating the effect of varying water tank depths (total collector area covered by water tanks)	105
6.17	Delta ground configuration specifications	108
6.18	Annual power output comparison, illustrating the effect of incorporating a delta ground configuration under the collector roof and the effect of varying angles of repose ($H_{2,D} = 1$ m)	109
6.19	Annual power output comparison, illustrating the effect of incorporating a delta ground configuration under the collector roof and the effect of varying the delta perimeter height ($\theta_D = 35^\circ$)	110
7.1	Average properties of wet soil according to Mills (1995), emissivity of relatively short grass (0.1 m to 0.15 m) according to Dong <i>et al.</i> (1992) and absorptivity of grass (80 % to 90 % new, green grass) according to Hsu (1963)	118
7.2	Annual power output comparison, illustrating the effect of incorporating vegetation under the collector roof, over a radial distance of 1978 m from the collector perimeter	120
7.3	Annual power output comparison, illustrating the effect of incorporating vegetation under the collector roof, over a radial distance of 1012 m from the collector perimeter	124
7.4	Annual power output comparison for a plant incorporating vegetation under the collector roof over a radial distance of 1978 m; effect of different temperature lapse rate models on plant performance	127
7.5	Annual power output comparison for a plant incorporating vegetation under the collector roof over a radial distance of 1012 m; effect of different temperature lapse rate models on plant performance	128
H.1	Total (I_h) and diffuse (I_{hd}) solar radiation on a horizontal surface, W/m^2	198
H.2	Ambient air temperature, $^\circ\text{C}$	199
H.3	Ambient wind speed, in m/s , at 10 m above ground level	199
H.4	Ambient relative humidity, %	200

Nomenclature

Variables:

A	Area [m^2] or total absorptance
b	Exponent or coefficient
C	Coefficient or currency unit or cost
c	Specific heat capacity [$\text{J}/\text{kg}\cdot\text{K}$] or coefficient
d	Diameter [m]
F	Force [N] or radiation transfer factor or ratio
Fr	Froude number
f	Darcy friction factor
g	Gravitational acceleration [$9.8 \text{ m}/\text{s}^2$]
H	Height [m]
h	Convective heat transfer coefficient [$\text{W}/\text{m}^2\cdot\text{K}$] or enthalpy [J/kg]
I	Solar irradiation [W/m^2]
i	Latent heat of vaporization [J/kg]
K	Loss coefficient
k	Thermal conductivity [$\text{W}/\text{m}\cdot\text{K}$]
L	Spacing between double glazing sheets [m]
\dot{m}	Mass-flow rate [kg/s]
n	Number or refractive index or exponent
P	Pitch [m] or Power [W]
Pr	Prandtl number
p	Pressure [N/m^2]
pt	Percentage [%]
q	Heat flux [W/m^2]
R	Gas constant [$\text{J}/\text{kg}\cdot\text{K}$] or total reflectance
Re	Reynolds number
r	Radius [m] or reflection or resistance [s/m]
T	Temperature [K] or [$^{\circ}\text{C}$] or total transmittance
t	Time [s or hours] or thickness [m]
V	Volume-flow rate [m^3/s]
v	Velocity [m/s]
z	Depth in ground or axial height above ground level [m] or exponent

Greek symbols:

α	Absorptance
γ	Psychrometric constant
γ^*	Adjusted psychrometric constant
Δ	Differential
ϵ	Emissivity
ε	Roughness [m]
η	Efficiency [%]
θ	Angle [radians <i>or</i> degrees]
λ	Wavelength [m]
μ	Dynamic viscosity [kg/m·s]
ξ	Temperature gradient [K/m]
π	Pi
ρ	Density [kg/m ³] or reflectance
Σ	Sum
σ	Stefan-Boltzmann constant [5.67×10^{-8} W/m ² ·K ⁴]
τ	Shear stress [N/m ²] or transmittance
ϕ	Angle [radians <i>or</i> degrees] or relative humidity [%]
ω	Absolute humidity [kg H ₂ O/kg dry air]

Subscripts:

<i>a</i>	Ambient air
<i>avg</i>	Average
<i>b</i>	Beam
<i>bot</i>	Bottom
<i>bw</i>	Bracing wheel
<i>c</i>	Chimney or convection
<i>co</i>	Chimney outlet
<i>coll</i>	Collector
<i>cond</i>	Conduction
<i>D</i>	Drag or delta
<i>DG</i>	Double glazed
<i>d</i>	Diffuse or day
<i>dyn</i>	Dynamic
<i>e</i>	Effective or extinction or expansion
<i>eb</i>	Effective property for beam solar radiation component
<i>ed</i>	Effective property for diffuse solar radiation component
<i>er</i>	Effective property of collector roof
<i>er1</i>	Effective property of top sheet of double glazed main collector roof
<i>er2</i>	Effective property of bottom sheet of double glazed main collector roof
<i>es</i>	Effective property of secondary collector roof
<i>es1</i>	Effective property of top sheet of double glazed secondary collector roof

<i>es2</i>	Effective property of bottom sheet of double glazed secondary collector roof
<i>et</i>	Effective property of tertiary collector roof
<i>f</i>	Friction or plastic film
<i>fe</i>	Effective property of film or extinction of film
<i>feb</i>	Effective property of film for beam solar radiation component
<i>fed</i>	Effective property of film for diffuse solar radiation component
<i>fg</i>	Fluid to gas
<i>fh</i>	Film to air under collector roof
<i>fr</i>	Film to collector roof
<i>g</i>	Ground
<i>gbh</i>	Ground to air in bottom section of collector
<i>gh</i>	Ground to air under collector roof
<i>gr</i>	Ground to collector roof
<i>gs</i>	Ground to secondary roof
<i>gt</i>	Ground to tertiary roof
<i>H</i>	Collector height or heat transfer
<i>h</i>	Horizontal surface or air under collector roof or hydraulic
<i>hb</i>	Beam solar radiation component on horizontal surface
<i>hd</i>	Diffuse solar radiation component on horizontal surface
<i>i</i>	Inlet or node index or incident
<i>int</i>	Intersection
<i>j</i>	Node index
<i>k</i>	Node index
<i>m</i>	Mean or mixture
<i>max</i>	Maximum
<i>mid</i>	Middle
<i>net</i>	Net
<i>o</i>	Outlet
\parallel	Parallel
\perp	Perpendicular
<i>p</i>	Constant pressure or penetration
<i>po</i>	Pressure at outlet
<i>r</i>	Roof or radial or radiation
<i>r1</i>	Top sheet of double glazed main collector roof
<i>r2</i>	Bottom sheet of double glazed main collector roof
<i>ra</i>	Collector roof to ambient air
<i>re</i>	Refractive
<i>ref</i>	Reference
<i>rh</i>	Collector roof to air under collector roof
<i>rs</i>	Collector roof to sky
<i>rth</i>	Collector roof to air in top section of collector
<i>s</i>	Solar or secondary roof or stomata or saturated
<i>s1</i>	Top sheet of double glazed secondary collector roof

<i>s2</i>	Bottom sheet of double glazed secondary collector roof
<i>sat</i>	Saturated
<i>sbh</i>	Secondary roof to air in bottom section of collector
<i>sc</i>	Specific chimney or saturation commences
<i>sD</i>	Support drag
<i>sky</i>	Sky
<i>sl</i>	Sea level
<i>smh</i>	Secondary roof to air in middle section of collector
<i>sr</i>	Secondary roof to collector roof
<i>srD</i>	Support drag at a specific collector radius
<i>sth</i>	Secondary roof to air in top section of collector
<i>sup</i>	Support
<i>supports</i>	Collector roof supports
<i>T</i>	Temperature
<i>t</i>	Tangential or total or throat or tertiary
<i>tbh</i>	Tertiary roof to air in bottom section of collector
<i>tg</i>	Turbo-generator
<i>tmh</i>	Tertiary roof to air in middle section of collector
<i>top</i>	Top
<i>tot</i>	Total
<i>tr</i>	Tertiary roof
<i>ts</i>	Tertiary roof to secondary roof
<i>turb</i>	Turbine
<i>turb, i</i>	Turbine inlet
<i>V</i>	Vapor transfer
<i>v</i>	Constant volume or water vapor
<i>ve</i>	Vegetation
<i>veh</i>	Vegetation to air under collector roof
<i>ver</i>	Vegetation to collector roof
<i>w</i>	Wind or water
<i>wb</i>	Wet-bulb
<i>wt</i>	Water tanks

Chapter

1

Introduction

The global demand for energy is escalating while global greenhouse gas emissions increase incessantly.

1.1 Energy: consumption and availability

According to the U.S. Energy Information Administration (2001), the worldwide consumption of energy, especially petroleum related energy, is growing steadily (see figure 1.1). In addition, of the worldwide total energy consumption, approximately 86 % is generated from fossil fuels, just more than 13 % from nuclear and hydroelectricity, while only 0.8 % is supplied from other renewable energy sources (see figure 1.2). It is therefore clear that most of our energy needs, exploit the earth's natural resources, while electricity generation using nuclear facilities presents a big waste disposal problem.

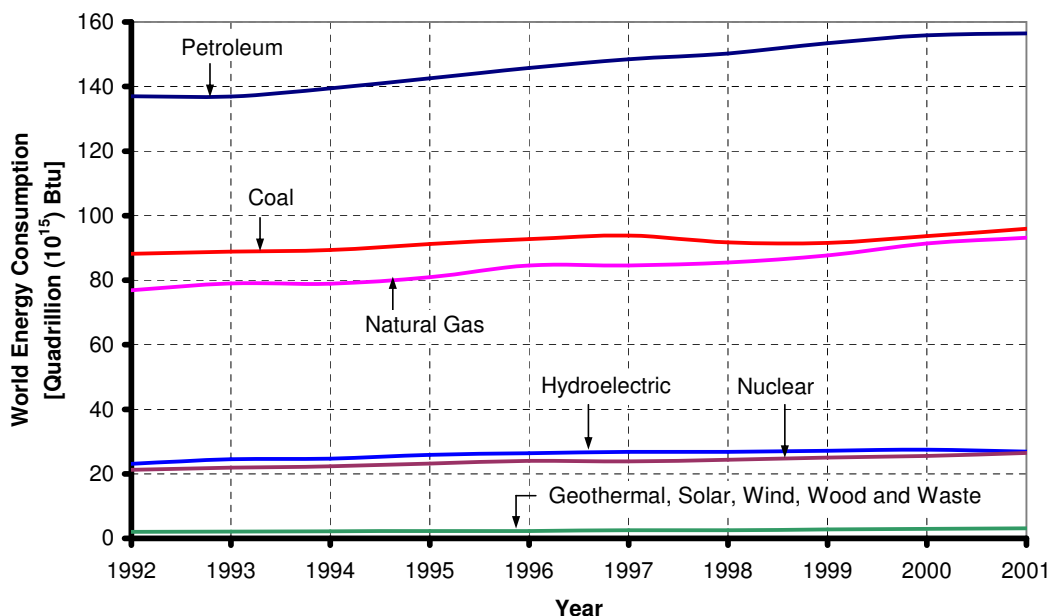
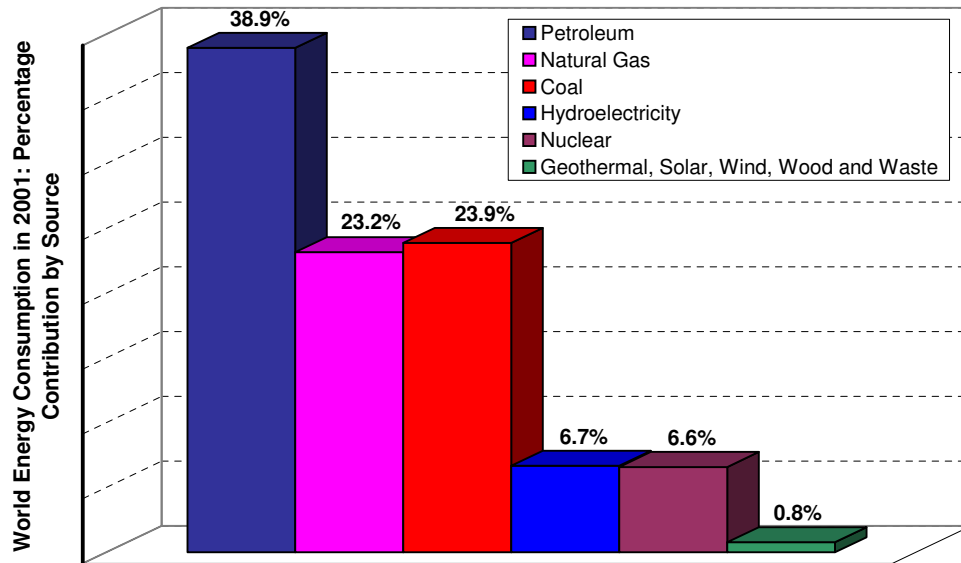


Figure 1.1: Global energy consumption by source (U.S. Energy Information Administration, 2001)



Source: USA Energy Information Administration

Figure 1.2: Energy sources: percentage contribution to global energy consumption (U.S. Energy Information Administration, 2001)

There is still widespread speculation over the future availability of the earth's natural resources. While some environmentalists claim that natural resources are running out, others claim that this is untrue. Bjorn Lomborg, a former Greenpeace member and current associate professor of political science at the University of Aarhus in Denmark, caused a major stir in environmental circles by turning his back on his previous beliefs, publishing arguments to contest the alleged degrading of the environment. In a news article in the UK newspaper *The Guardian*, Lomborg (2001) voiced his opinion that the earth's natural resources are not as scarce as claimed by some environmentalists, since technologies have improved on finding and utilizing new resources. Environmentalists have responded to this article with much criticism, commenting that while the earth's natural resources may not be diminishing as rapidly as some claim, they cannot be infinite.

On one aspect, however, both parties seem to reach a consensus: a move towards renewable energy will be beneficial for the planet and its inhabitants.

1.2 Global warming

Global warming remains a much debated topic. While it seems certain that greenhouse gas emissions resulting from human activities will increase the natural greenhouse effect of the planet, it is uncertain to which extent it does so.

Two facts remain largely unchallenged. Firstly, there exists definite evidence of a global warming trend. According to the U.S. Environmental Protection Agency (2000), average land surface temperatures have risen by 0.45 °C to 0.6 °C over the last century. Precipitation has increased by 1 % and sea level has risen by 15 cm to 20 cm in the last century. Secondly, proof also exists of radical climatic changes over past centuries in the earth's history.

However, scientists have not been able to substantiate whether the present global warming trends have occurred as part of a natural climatological cycle or as a result of human involvement.

1.3 The Kyoto Protocol

The concentration of carbon dioxide in the earth's atmosphere is steadily increasing, which can be partly attributed to the combustion of fuel, since emissions from fuel combustion have doubled globally since the mid 1960's.

Internationally, the world has acknowledged the need to cut global greenhouse gas emissions. The biggest step towards achieving this goal has been the establishment of the Kyoto Protocol agreement. After lengthy negotiations in 1997, contracting parties of the UN Framework Convention on Climate Change reached a consensus. The resulting agreement specified that a particular group of industrial countries should reduce their gas emissions by 5.2 % by the year 2012, from the reference year 1990. However, the agreement also foresees that emissions from developing countries should increase during this period. Therefore, the Kyoto Protocol only serves to lower the effective rate at which the greenhouse gases are being released into the atmosphere.

In the period after 1990, emissions from the USA have increased substantially more than expected. Since the USA is responsible for almost a quarter of worldwide greenhouse gas emissions, it has made the aims of the Kyoto Protocol for 2012 almost unattainable. Consequently, the USA has decided not to endorse the Kyoto Protocol, whereas most other countries involved have affirmed their commitments towards achieving the goals of the Kyoto Protocol. Figure 1.3 depicts the emission reduction commitments by the various contracting parties as well as their respective emission changes over the last few years.

Reduction commitments of the Kyoto protocol and emissions development					
Party	Reduction commitments	Emissions 1990 in Mt	Emissions 2000 in Mt	Emissions 2001 in Mt	Change 1990-2001
EU	-8 %	4 203	4 077	4 118	-2.0 %
Liechtenstein, Monaco, Switzerland	-8 %	53	53	54	+0.8 %
Bulgaria, Czech Republic, Estonia, Latvia, Lithuania, Romania, Slovakia, Slovenia	-8 %	816	478	485	-40.5 %
USA	-7 %	6 140	7 047	6 936	+13.0 %
Japan	-6 %	1 187	1 333	1 299	+9.5 %
Canada	-6 %	608	730	720	+18.5 %
Poland, Hungary	-6 %	666	470	461	-30.7 %
Croatia	-5 %	32	22	22	-30.3 %
New Zealand	0 %	62	70	72	+17.2 %
Russian Federation	0 %	3 040	1 877	1 877	-38.3 %
Ukraine	0 %	919	455	455	-50.5 %
Belarus	0 %	134	71	71	-46.6 %
Norway	+1 %	52	56	56	+8.1 %
Australia	+8 %	425	502	502	+18.2 %
Iceland	+10 %	3	3	3	-4.1 %
Total	-5.2 %	18 340	17 244	17 134	-6.6 %

Source: UNFCCC, these values refer to carbon dioxide equivalents excluding land-use change and forestry

Figure 1.3: Commitments to the Kyoto Protocol

The effectiveness of the Kyoto Protocol has come under scrutiny since its establishment. Many claim that the cost of implementing the measures set out by the Protocol is too high for the amount of emissions it will prevent. On the other hand, environmentalists believe that the cost of doing nothing may be far greater.

1.4 Renewable energy

Renewable energy sources are those which do not rely on stored energy resources. Various forms of renewable energy are currently used for the generation of electricity. As with most industries, the relative cost of a product becomes less expensive as technologies improve and product knowledge increases, with the renewable energy industry being no exception. The American Wind Energy Association (2006) states that the cost of electricity from wind energy systems has dropped by 80 % over the past twenty years, while Solarbuzz (2006) indicates that the price of photovoltaic solar modules have dropped by 85 % over the past twenty-five years. These cost reductions are making renewable energy much more competitive in the energy market. The following section lists some of the various types of renewable energy sources currently in use.

1.4.1 Biomass

Biomass energy is generated from the combustion of biofuels, which are renewable energy sources produced by living organisms. These fuels differ from fossil fuels due to the fact that fossil fuels are non-renewable. Biofuels are used in solid, gas and liquid form and when burning these fuels, chemical energy is converted to thermal energy or heat. Solid biofuels include materials such as wood, straw and different types of organic waste. The possibility of planting high energy crops for use as an energy source are also being explored. Liquid biofuels include fuels like methanol, ethanol and vegetable oils which are derived from biomass to produce a combustible liquid. Biogas is produced by the digestion of human and animal waste or by capturing methane gas from municipal landfill sites.



Figure 1.4: An example of a solid biofuel

1.4.2 Geothermal

Geothermal energy is derived from the natural heat of the earth. The earth's heat is stored within the rock and water beneath its surface, which can be extracted by drilling wells to these sources. These geothermal reservoirs are classified as either low temperature ($< 150\text{ }^{\circ}\text{C}$) or high temperature ($> 150\text{ }^{\circ}\text{C}$) sources. Low temperature reservoirs are used for heating purposes while high temperature sources are employed for the generation of electricity.

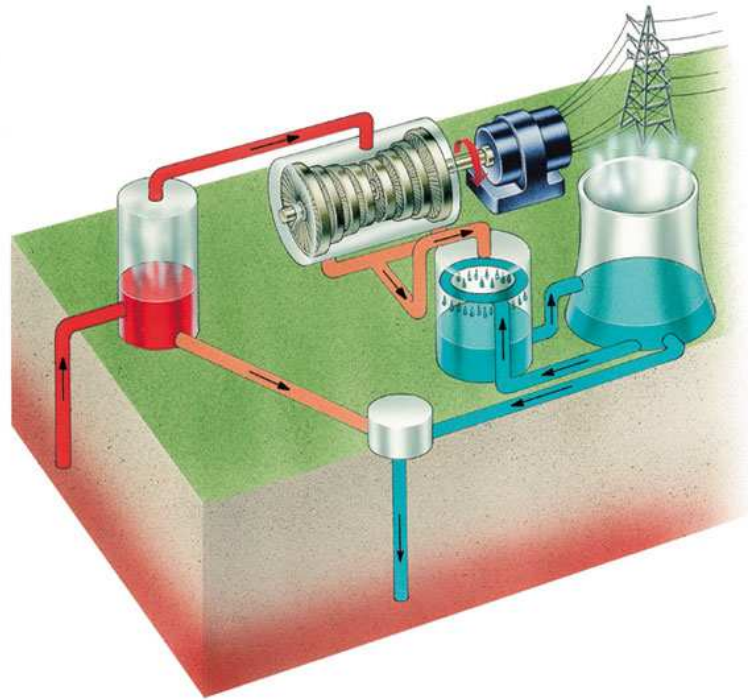


Figure 1.5: Generating electricity using the earth's natural heat (co2balance.com, 2006)

Figure 1.5 depicts the process of extracting geothermal energy from the earth. Hot liquid is pumped from within the earth to the surface. Due to its high temperature, the liquid releases steam which drives a steam turbine and consequently generates electricity. After moving through the turbine, the steam condenses and produces hot water which is cooled in a cooling tower before being returned to the geothermal reservoir within the earth.

1.4.3 Tidal

Tidal energy is generated by utilizing the natural rise and fall of the coastal tides, onshore or offshore. Onshore, seawater is allowed to fill an estuary through sluices, which are shut at peak high tide. The estuary is then drained through turbines, which generate electricity. Such a plant was constructed on the Rance river in St.Malo, France and generates up to 240 MW (see figure 1.6). Offshore, electricity generation by means of tidal flow over horizontal-axis turbines (similar to wind turbines) as well as over aerofoil-type generators are being researched (see figures 1.7 and 1.8).

1.4.4 Wave

Wave energy is a renewable source of energy which is based on the conversion of kinetic energy from ocean waves to electric energy. Various shoreline and offshore devices have been designed and installed worldwide.

The shoreline devices include the oscillating water column (OWC), tapered channel (TAPCHAN) and the Pendulator. The OWC is a partly submerged structure, with an opening at the bottom to the sea, which encloses a column of air situated above a column of water. As the waves strike the structure, the water level rises, thereby forcing the air out through a turbine which drives a generator. Unidirectional turbines are used to allow the air to flow back into the device from the atmosphere. The TAPCHAN design employs a



Figure 1.6: A 240 MW tidal power facility on the Rance river, France (Bigelow laboratory for ocean sciences, 2006)



Figure 1.7: A computer generated image of a proposed offshore tidal turbine (Atkins Power, 2006)

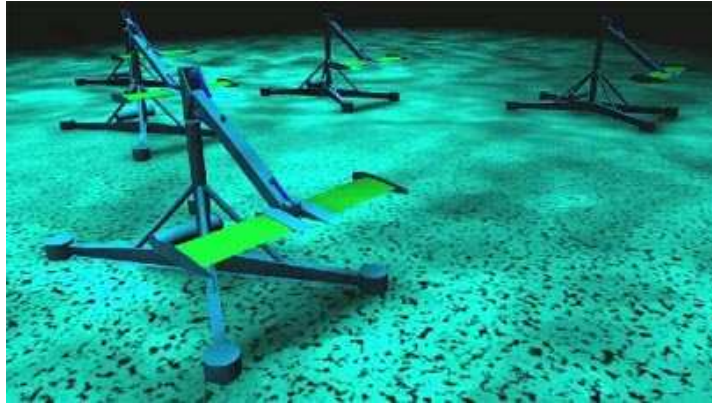


Figure 1.8: A computer generated image of a proposed offshore tidal aerofoil-type generator

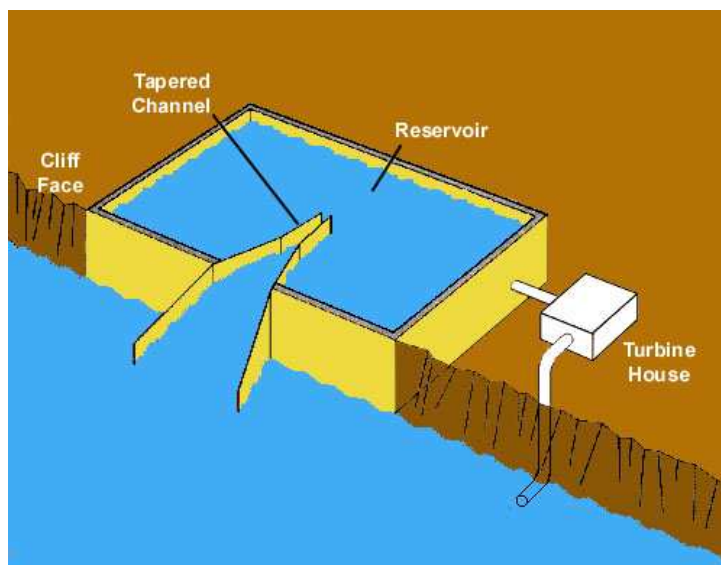


Figure 1.9: Schematic illustration of a tapered channel (TAPCHAN) wave energy device (UN atlas of the oceans, 2006)

tapered wall typically 3 m to 5 m above the mean sea level. Waves enter a narrowing channel which amplifies the wave amplitude until the water spills over the walls into a reservoir (see figure 1.9). The reservoir is then emptied through a turbine which drives an electric generator. The Pendulator consists of a rectangular box which is open to the sea at one end. The motion of the waves sway a pendulum flap which powers a hydraulic pump and generator.

The main offshore devices make use of a float which rises and falls with the waves. The float drives a pump which forces water through a turbine that is connected to a generator, thereby generating electricity.

1.4.5 Hydroelectric

Hydroelectric power is the most commonly used renewable energy source. It utilizes the energy released by water falling or flowing due to the effect of gravity. Two configurations for extracting renewable hydroelectric energy currently exist. The typical configuration

(such as the Aswan Dam scheme in Egypt) consists of a dam reservoir, from where the water can be released to flow through a power station. Within the power station, the flow of water drives a turbine which in turn drives an electric generator, after which the water is permitted to return to a nearby river.

Early hydroelectric schemes used the natural force of falling water from a waterfall to generate electricity, without the use of a dam. The most renowned example of such a scheme is the power station at Niagara Falls in the U.S.A., where some of the water flowing over the falls is diverted for electricity generation purposes.

1.4.6 Wind

Wind energy involves the conversion of the wind's kinetic energy into electric energy. The operational concept is simple: the wind drives a turbine that is connected to a generator, which generates electricity. Two configurations of wind turbines are in current use: horizontal (in current use onshore and offshore) and vertical axis turbines.

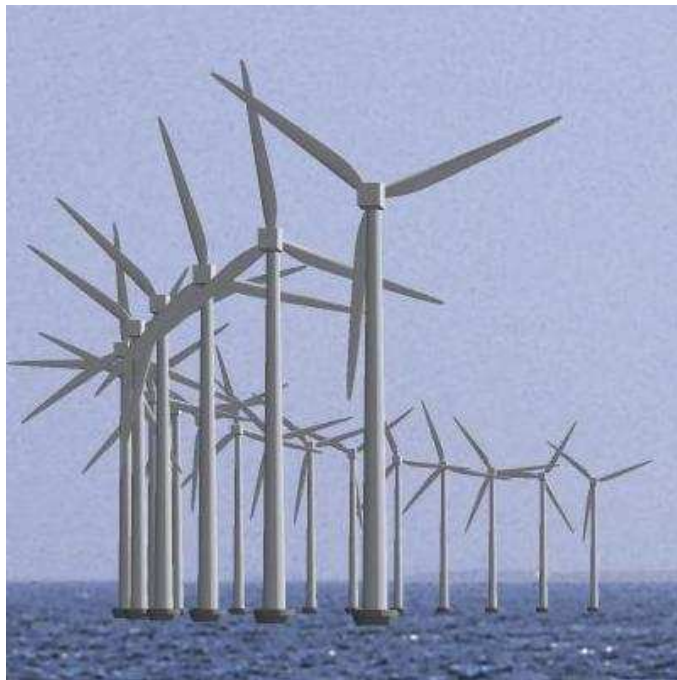


Figure 1.10: Offshore horizontal axis wind turbines

The most common configuration, the horizontal axis wind turbine, consists of a two or three blade rotor turned to face the wind on top of a tall tower, as shown in figure 1.10. Vertical axis turbines are not widely used, but two main types have been invented. Savonius turbines are S-shaped when viewed from above. These turbines rotate relatively slowly, but generate high torque and are typically employed for grinding grain and pumping water. A Darrieus-type wind turbine, on the other hand (as shown in figure 1.11), is shaped like an eggbeater. As the wind blows over the vertical blades of the Darrieus, the aerodynamic lift effect causes the turbine to rotate, thereby generating electricity.

As mentioned previously, due to technological advances the cost of wind energy has dropped by approximately 80 % in the past twenty years, making it much more competitive as a reliable energy source.



Figure 1.11: A Darrieus-type vertical axis wind turbine

1.4.7 Solar

Solar energy entails the conversion of thermal energy from the sun into electric energy. Many different concepts have been explored in an attempt to harness the sun's energy, with the most noteworthy being the following:

Central Receiver plants operate by focusing the sun's radiation on a central tower-mounted receiver by means of a multitude of reflectors (heliostats) which track the sun's path on two axes throughout the day (see figure 1.12). The concentrated radiation heats a fluid which passes through a heat exchanger in order to generate steam. The steam is passed through a turbine, which in turn drives an electric generator. Central Receiver power plants are also employed as part of hybrid combined cycle power plants. In such configurations the thermal heat from the Central Receiver plant is used to preheat air for the compressor of a gas cycle, while the exhaust gases of the gas cycle are used to generate steam for a steam turbine.

Photovoltaic Power Plants use photovoltaic solar panels to generate electricity. These panels consist of a multitude of photovoltaic cells which convert sunlight into electricity. The photovoltaic solar energy industry produces the largest share of solar electricity and is currently experiencing rapid growth, with the worldwide installed capacity increasing from 350 MW in 2001 to 1460 MW in 2005. Figure 1.13 illustrates photovoltaic solar panels.

Parabolic trough collectors are also employed as solar electricity generators. These troughs have linear parabolic-shaped reflectors which focus the sun's radiation on a receiver located at the focus line of the parabola. An example of a parabolic trough is illustrated by figure 1.14. Parabolic trough collectors are used for large scale electricity generation, such as the nine Solar Electric Generating Systems (SEGS) in the Mojave desert of California, which produce 354 MW in total. The collectors track the path of the sun during the day on one axis (from east to west) to ensure that the rays of the sun are constantly reflected onto the receiver. A working fluid inside the receiver is heated by the sun, then flows through a series of heat exchangers at a central location. Here, the fluid is used to generate superheated



Figure 1.12: A Central Receiver solar power plant (US Department of Energy, 2006)



Figure 1.13: Photovoltaic solar panels

steam which is passed through a steam turbine connected to a generator, which subsequently generates electricity. The fluid is then cooled and recirculated through the plant.

Linear Fresnel reflector power plants operate in a similar manner to parabolic trough plants. However, this technology uses angled plane mirrors to focus solar radiation onto a linear absorber.

Solar dish-engine systems employ one or more reflectors that form a dish to concentrate the sun's energy onto a focal point. A compressed working fluid in its cold state is then heated by the concentrated solar radiation and allowed to expand through a turbine or with a piston. The turbine or engine is coupled to a generator which then generates electricity.



Figure 1.14: A parabolic trough solar collector (Solar-Auto-Controller, 2006)

Figure 1.15 shows an example of a Solar dish-engine system.



Figure 1.15: A Solar dish-engine system with multiple reflectors (Innovative Power Systems, 2006)

As the sun strikes a lake or pond, the density of the heated water decreases and it rises. At the surface, the heated water again loses its energy to the atmosphere. In a Solar Pond (see figure 1.16), salt is dissolved in the water of a pond which inhibits the heated water from rising to the surface because of its added weight. The greater the concentration of the salt solution, the heavier it becomes, thus giving the pond a salinity gradient. This means that the heated water at the bottom of the pond cannot rise, thereby trapping the energy at the pond bed. This energy is used to evaporate a low boiling point fluid which, as a gas, is expanded through a turbo-generator to generate electricity.



Figure 1.16: Aerial view of a Solar Pond power plant (University of Texas El Paso, 2006)

1.5 Solar chimney power plants: concept and history

A solar chimney power plant consists of a circular transparent collector raised a certain height from the ground, with a chimney at the collector center, as illustrated by figure 1.17 (see Chapter 2 for dimensional details). A single turbine or multiple turbines are located at or near the base of the chimney and are connected to an electric generator or generators. Radiation from the sun penetrates the collector and strikes the ground surface beneath, which is heated and in turn heats the adjacent air, causing it to rise. The warm rising air is trapped underneath the collector, but rises up into the central chimney, causing the air under the collector to be sucked into the chimney as well. The air flowing into the chimney drives the turbine or turbines which subsequently generates electricity.

A prototype solar chimney power plant (shown in figure 1.18) was built in Manzanares, Spain in 1982 in a joint venture between the German structural engineering firm Schlaich Bergermann and the Spanish government. The plant had a collector diameter of 244 m and a 194.6 m high, 10 m diameter chimney and was designed to produce 50 kW. Although not achieving the maximum power as envisaged by the design, the plant operated successfully for seven years, proving that the concept is technically sound.

Since the pilot plant's introduction, various studies have been conducted investigating the possibility of building large-scale solar chimney power plants (see section 1.7). According to these studies, such plants will have collector diameters in the range of 4000 m to 7000 m, chimney heights of 1000 m to 1500 m with a chimney diameter in the order of 160 m and should generate a peak power of between 85 MW and 275 MW, depending on the size of

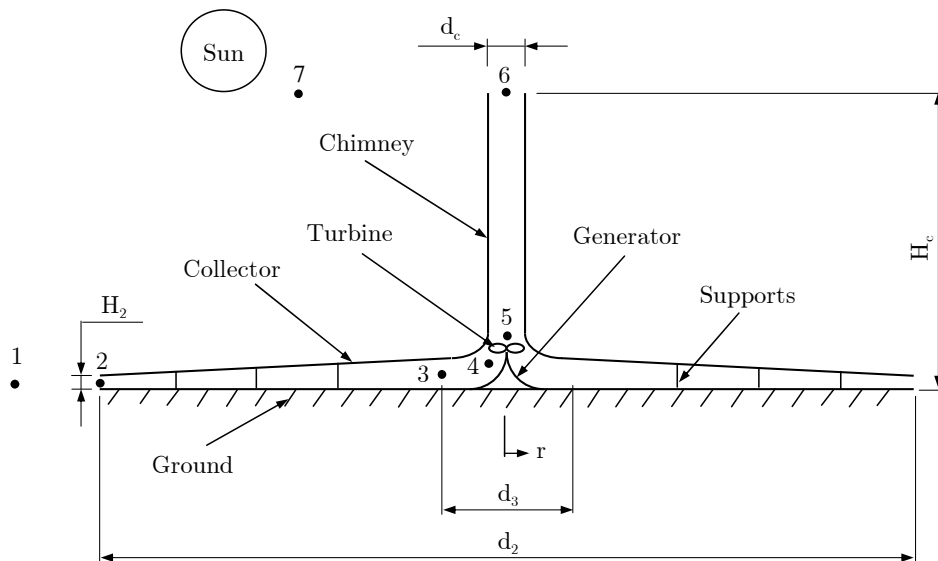


Figure 1.17: A schematic illustration of a solar chimney power plant (single turbine configuration)



Figure 1.18: The pilot solar chimney power plant in Manzanares, Spain

the plant. The most noteworthy commitment towards constructing such a plant is a current joint venture between an Australian based company, EnviroMission Ltd. and the German firm, Schlaich Bergermann und Partner. These companies are currently pursuing further investment opportunities and plan to build a large-scale solar chimney power plant (see figure 1.19) near Mildura, Australia in the near future.

1.6 Why use solar chimney power plants?

The following section lists the advantages of generating power using solar chimney power plant technology and also evaluates the disadvantages compared to other energy sources. Many of these factors have been mentioned by Schlaich (1994), Trieb *et al.* (1997) and



Figure 1.19: Computer generated image of a proposed large-scale solar chimney power plant (Schlaich Bergermann und Partner, 2006)

Gannon (2002).

1.6.1 Advantages

- Solar chimney power plants utilize beam and diffuse solar radiation. Therefore, although reduced, the plant still generates power under cloudy conditions.
- The ground (soil) underneath the collector of a solar chimney power plant acts as a natural energy storage mechanism. This means that, although reduced, the plant continues to generate power at night.
- Construction materials (mainly glass and concrete) for such a plant are relatively inexpensive and readily available.
- The plant operates using simple technology. Except for possibly the turbo-generator, the technology of a solar chimney power plant will not become outdated easily.
- The plant does not require any non-renewable fuels in order to operate and does not produce any emissions. This also means that the plant would never have to deal with escalating fuel costs.
- At suitable plant sites such as desert areas, solar radiation is a very reliable input energy source. Consequently, energy produced by solar chimney power plants will not produce power spikes which may occur with schemes such as wind energy generation.
- The plant has a long operating life (at least 80 to 100 years).
- Solar chimney power plants do not require any cooling water.
- Low maintenance cost.

The above-mentioned advantages are the primary advantages of a solar chimney power plant. Some secondary advantages of the construction of such a plant would include job creation during the construction period and boosted tourism to the area (due to the fact that a structure of such scale has never been built before).

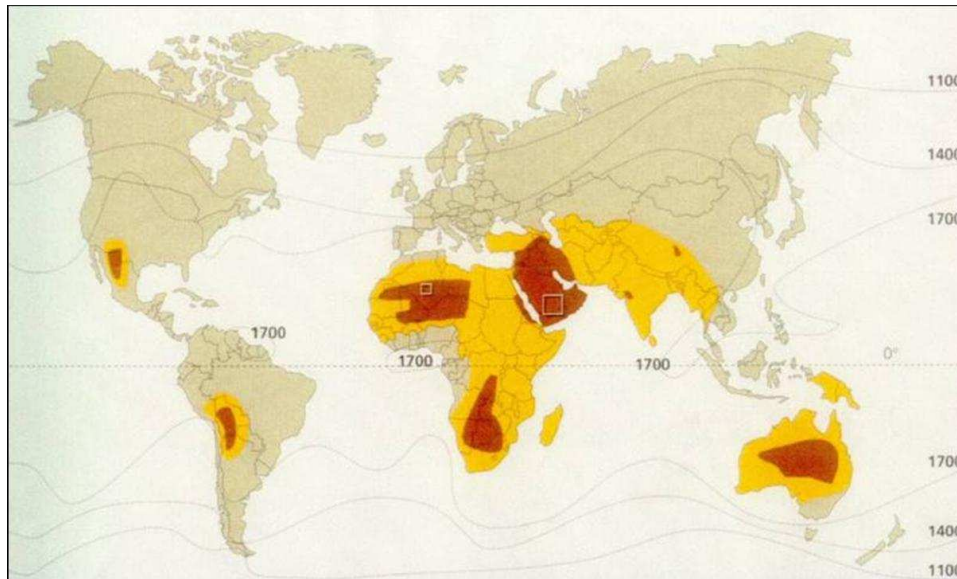


Figure 1.20: Annual global solar radiation

1.6.2 Disadvantages

- In order to be economically viable, solar chimney power plants have to be built on a very large scale. Due to its size, the initial capital cost of such a plant is high.
- The power output is not constant throughout the day or year. Output during peak energy demand times (early in the morning and early evening) are low while power production is at its peak in times of low electricity demand. Power generation is also much lower in the colder months of the year, when electricity demand is high. Further development may however reduce or even eliminate these disadvantages.
- The construction of the plant requires huge quantities of materials. Such quantities may cause logistical problems regarding the availability and transportation of the materials.
- No structures of similar scale have been built before.

Figure 1.20 depicts the regions of the world with high annual solar radiation, with the yellow areas receiving more than 1950 kWh/m^2 annually while the red areas receive more than 2200 kWh/m^2 per year. Either of the yellow or red regions are ideal locations for solar chimney power plants.

1.7 Literature review

The first contemporary citing of a solar chimney concept appears in a book by Günther (1931). In this book, reference is made to a proposal by B.Dubos on the potential of constructing a solar-powered updraught power plant. The plant would consist of a horizontal glass collector near the foot of a hill or mountain and a large duct running up the hillside to a turbo-generator. Heated air from underneath the collector would then flow via the duct up the hillside to the turbo-generator.

After the construction of the aforementioned experimental solar chimney power plant in Manzanares, Haaf *et al.* (1983) discuss the basic principles behind the operation, construction and power generation of a solar chimney power plant. Haaf also makes mention of a

similar notion used centuries before by Leonardo da Vinci, (according to his sketches of a barbecue-spit driven by an updraught through a chimney) as well as a previous study by Simon (1976). Following his publication in 1983, Haaf (1984) documents preliminary test results from the Manzanares prototype plant, with experimental findings which correspond well with model calculations.

Mullett (1987) presents an analysis for evaluating the overall efficiency of a solar chimney power plant. He deduces that solar chimney power plants have low overall efficiencies, making large scale ventures the only economically feasible option.

A publication by Padki and Sherif (1988) researched the chimney in particular, investigating the influence of various geometrical configurations on the performance and efficiency of the chimney.

Schlaich (1991) insists on urgent action regarding global problems such as energy demand, rapid population growth and pollution by the utilization of large scale solar energy generation. In a later publication by Schlaich (1994), he endorses the use of solar chimney power plants for future electricity generation. Schlaich also communicates details of the construction, construction materials, operation, tests and experimental data of the pilot solar chimney plant in Manzanares. Based on the experience gained from the experimental plant, rough investment and energy generation cost calculations are presented for developing large-scale solar chimney power plants. In a supplement to the book, water-filled black tubes are identified as a possible means to enhance the plant's natural energy storage capability.

Pasumarthi and Sherif (1998*a*) published an approximate mathematical model for a solar chimney, followed by a subsequent article (Pasumarthi and Sherif, 1998*b*) which validates the model against experimental results from a small scale solar chimney model.

A study by Kröger and Blaine (1999) investigates the driving potential of a solar chimney power plant. Various theoretical models are assessed and the effect of prevailing ambient conditions evaluated. The study also concludes that a higher humidity increases the driving potential while condensation may form in the chimney under certain conditions.

With its application to the solar chimney power plant collector, Kröger and Buys (1999) consider developing radial flow between two essentially parallel discs. They develop analytical relations which evaluate the heat transfer coefficient and the pressure differential due to frictional effects.

In a paper on tension structures, Schlaich (1999) discusses the performance, construction methods and cost of a variety of solar energy generation schemes, including the solar chimney power plant. A chimney design which incorporates spoked bracing wheels for enhanced chimney stiffness, especially under wind load, is also presented.

Hedderwick (2001) derives relevant conservation equations, including a draught equation, which approximates the heat transfer and flow in a solar chimney power plant. The equations are incorporated into a numerical model that evaluates the performance of a reference large-scale solar chimney power plant.

Von Backström and Gannon (2000*b*) follow an alternate approach by regarding the solar chimney power plant as an air standard thermodynamic cycle. Certain parameter relationships are also developed within this study. A further publication by Von Backström and Gannon (2000*a*) investigates the compressible air-flow through the chimney of a large-scale solar chimney power plant. The study evaluates all losses associated with the chimney, specifying relevant pressure drop contributions to the total pressure drop across the chimney. Gannon and Von Backström (2000) also present an analysis of the solar chimney that includes chimney friction, system, turbine and exit kinetic energy losses and a simple solar collector model.

Relevant equations for a solar chimney power plant are also developed by Kröger and Buys (2001). A numerical model is developed and simulation results shown.

Another paper by Gannon and Von Backström (2002) develops a collector model which is incorporated into a numerical model. The numerical model is used to simulate a small experimental plant and results are compared to actual measurements. The study also in-

investigates power limitation by varying the turbine pressure drop and performs simulations for a large-scale plant. Gannon (2002) and Gannon and Von Backström (2003) also studied the performance of turbines to be used in a solar chimney power plant. Turbine design and configuration proposals are made, while an experimental model is used to predict turbine performance and efficiency.

An analytical and numerical model is developed by Bernardes *et al.* (2003). A comparison between simulated results and experimental measurements from the pilot plant at Manzanares is given. Simulation results which predict the performance characteristics of large-scale plants are also presented.

Pastohr *et al.* (2004) conduct a basic temperature and flow field analysis using a numerical CFD package and compare their results to another simple numerical model.

Pretorius *et al.* (2004) present a study that evaluates the annual power output of a reference large-scale solar chimney power plant. A numerical simulation model solves the relevant equations using specified meteorological input data from a suitable plant site in South Africa. The dependency of the power output on plant size is verified while showing that greater power production is achievable by optimizing the collector shape and height. Pretorius (2004) also briefly presents the effects of the chimney shadow and prevailing winds on the power output of the same reference solar chimney power plant. It is shown that the chimney shadow should have a minor influence on power production while prevailing winds should cause a significant drop in annual power output.

A paper by Von Backström and Fluri (2004) conducts an analytical investigation into the maximum fluid power condition in solar chimney power plants. The study predicts that the maximum flow condition is available at much lower flow and higher turbine pressure drops than previously accepted.

A mathematical model is developed by Bilgen and Rheault (2005) for evaluating the performance of solar chimney power plants at high latitudes.

1.8 Objectives of current study

This study builds on the previous investigation into the performance characteristics of a solar chimney power plant (Pretorius, 2004). The main objectives of this dissertation are as follows. Firstly, to investigate the optimization of a large-scale solar chimney power plant, through the pursuit of obtaining thermo-economic optimal dimensions and evaluating plant specifications which enhance plant performance. Secondly, to explore dynamic and static control over plant power output. Some of the major milestones of this dissertation include:

- The incorporation of improved convective heat transfer equations (developed by Kröger and Burger (2004) and Burger (2004)) into the numerical model and subsequent investigation into the influence of these equations on the solar chimney power plant performance characteristics, especially the annual output.
- Conducting a sensitivity analysis on the influence of various operating and technical specifications on the performance of a solar chimney power plant.
- Performing a thermo-economic optimization of the solar chimney power plant with the inclusion of the aforementioned improvements. The goal will be to determine thermo-economic optimal plant configurations for varying cost structures.
- Evaluating the effect of wind, ambient temperature lapse rates and nocturnal temperature inversions on the power production of the plant.
- Investigating various possibilities of controlling the power delivered by the plant. The objective will be to achieve power generation according to specified demand patterns.
- Evaluating the effect of including vegetation in the collector of the plant.

Plant Model Specification

The following chapter presents a complete solar chimney power plant model specification on which all simulations and results are based. The specification considers a particular reference plant configuration and the relevant governing conservation equations, the convective heat transfer and corresponding momentum equations employed in the performance evaluation as well as the meteorological conditions at a reference location (Sishen, South Africa).

2.1 Reference plant configuration

This section defines a reference solar chimney power plant configuration on which all of the simulations are based. The listed dimensional details in table 2.1 apply to figure 2.1.

Table 2.1: Reference solar chimney power plant configuration

Collector Roof (Glass)	
Emissivity of glass	$\epsilon_r = 0.87$
Roughness of glass	$\epsilon_r = 0$ m
Extinction coefficient of glass	$C_e = 4$ m ⁻¹
Refractive index of glass	$n_r = 1.526$
Thickness of glass	$t_r = 0.004$ m
Roof shape exponent	$b = 1$
Perimeter (inlet) height	$H_2 = 5$ m
Outer diameter	$d_2 = 5000$ m
Inner diameter	$d_3 = 400$ m
Inlet loss coefficient	$K_i = 1$
Support diameter	$d_{sup} = 0.2$ m
Support drag coefficient	$C_{sD} = 1$
Supports tangential pitch	$P_t = 10$ m
Supports radial pitch	$P_r = 10$ m
Ground	
Type	Sandstone
Emissivity (treated surface)	$\epsilon_g = 0.9$
Absorptivity (treated surface)	$\alpha_g = 0.9$
Density	$\rho_g = 2160$ kg/m ³
Specific heat	$c_g = 710$ J/kgK
Thermal conductivity	$k_g = 1.83$ W/mK

2.2.1 Collector equations

Continuity equation

$$\frac{1}{r} \frac{\partial}{\partial r} (\rho v r H) = 0 \quad (2.1)$$

Momentum equation

$$-\left(H \frac{\partial p}{\partial r} + \tau_r + \tau_g + \frac{F_{\text{supports}}}{r \Delta \theta} \right) = \rho v H \frac{\partial v}{\partial r} \quad (2.2)$$

Roof energy equation

$$\alpha_{eb} I_{hb} + \alpha_{ed} I_{hd} + q_{gr} = q_{ra} + q_{rs} + q_{rh} \quad (2.3)$$

Ground energy equations

At $z = 0$ (Ground surface)

$$(\tau_e \alpha_g)_b I_{hb} + (\tau_e \alpha_g)_d I_{hd} = q_{gr} - k_g \left. \frac{\partial T_g}{\partial z} \right|_{z=0} + q_{gh} \quad (2.4)$$

At $z > 0$

$$-k_g \frac{\partial^2 T_g}{\partial z^2} + \rho_g c_g \frac{\partial T_g}{\partial t} = 0 \quad (2.5)$$

At $z = \infty$

$$\frac{\partial T_g}{\partial z} = 0 \quad (2.6)$$

Air stream energy equation

$$q_{rh} + q_{gh} = \frac{RT}{r} \frac{\partial}{\partial r} (\rho v r H) + \rho v H \frac{\partial}{\partial r} (c_p T) \quad (2.7)$$

2.2.2 Chimney equations

Continuity equation

$$\frac{\partial}{\partial z} (\rho_c v_c) = 0 \quad (2.8)$$

Momentum equation

$$-\frac{\partial p_c}{\partial z} - \left(\frac{\tau_c \pi d_c + F_{bw}}{A_c} \right) = \rho_c \left(g + v_c \frac{\partial v_c}{\partial z} \right) \quad (2.9)$$

Air stream energy equation

$$RT_c \frac{\partial}{\partial z} (\rho_c v_c) + \rho_c v_c \frac{\partial}{\partial z} (c_{pc} T_c) + \frac{\partial}{\partial z} (\rho_c v_c g z) = 0 \quad (2.10)$$

2.3 Convective heat transfer equations

In order to solve the various energy equations applicable to the solar chimney power plant model, relevant convective heat transfer coefficients need to be determined. The following section presents the various convective heat transfer equations that will be employed in the model for the calculation of these coefficients.

2.3.1 Convection to ambient

The term q_{ra} of equation (2.3) represents the convective heat flux from the collector roof of the solar chimney power plant to the ambient air. This convection heat flux may be expressed as

$$q_{ra} = h_{ra}(T_r - T_a) \quad (2.11)$$

where h_{ra} is the convective heat transfer coefficient from the roof to the ambient air, while T_r and T_a are the roof and ambient air temperatures respectively.

2.3.1.1 $T_r > T_a$

Work by Kröger and Burger (2004) has led to the development of a correlation for the local convective heat transfer coefficient from a smooth horizontal surface exposed to the natural environment. More recent work by Burger (2004) led to the development of an improved version of this correlation, represented by the following

$$h_{ra} = \left[0.2106 + 0.0026 v_w \left(\frac{\rho T_m}{\mu g \Delta T} \right)^{1/3} \right] / \left[\frac{\mu T_m}{g \Delta T c_p k^2 \rho^2} \right]^{1/3} \quad (2.12)$$

where T_m is the mean temperature between the collector roof and ambient air, g is the gravitational constant and ΔT is the difference between the roof and ambient air temperature. The variables ρ , μ , c_p and k symbolize the density, dynamic viscosity, specific heat capacity and thermal conductivity of the air respectively, all of which are evaluated at the mean temperature T_m .

Equation (2.12) applies to a heated horizontal surface facing upward or a cooled surface facing downward and considers both natural and forced convection heat transfer effects. The experimental work by Burger (2004) (in development of equation (2.12)) regards an energy balance which evaluates the various convective and radiative heat fluxes onto / from a smooth horizontal flat plate exposed to the natural environment. The radiative heat flux from the plate to the environment is based on the sky emissivity according to Berdahl and Fromberg (1982).

When substituting equation (2.12) into equation (2.11), the local convection heat flux from the collector roof to the environment can be accurately predicted if the corresponding local ambient air temperature (T_a) about one meter above the collector surface is known.

During times when the collector roof temperature only marginally exceeds the ambient temperature, a recent correlation developed by Burger (2004) becomes applicable. This equation is of the form:

$$h_{ra} = 3.87 + 0.0022 \left(\frac{v_w \rho c_p}{Pr^{2/3}} \right) \quad (2.13)$$

where Pr is the Prandtl number and all properties are evaluated at the mean of the collector roof and ambient air temperature. This correlation considers the heat transfer during relatively stable conditions. The heat transfer mechanisms present during these stable conditions include a combination of minor convective thermals, conduction in the stratified air and condensation heat transfer.

It is assumed that the dominant local heat transfer mechanisms present will determine the local heat transfer rate. Consequently, with $T_r > T_a$ the numerical model employs the higher of the h_{ra} values calculated by equation (2.12) and equation (2.13).

Due to the large collector surface and complex air-flow patterns above it due to natural convection and winds, considerable uncertainty exists concerning the local value of T_a and the local ambient wind velocity v_w . In the present analysis a conservative approach will be followed when employing specified ambient temperatures and wind speeds for T_a and v_w respectively.

2.3.1.2 $T_r < T_a$

During periods when the ambient temperature exceeds the collector roof temperature, the roof is approximated as a cooled horizontal surface facing up. As previously mentioned, equation (2.13) applies when the collector roof temperature is slightly greater than the ambient air temperature. However, the correlation also applies when $T_r < T_a$. Therefore, the numerical model employs only equation (2.13) during these times.

2.3.2 Convection from roof to collector air

The convection heat flux from the collector roof to the air in the collector (from equations (2.3) and (2.7)) may be found using

$$q_{rh} = h_{rh}(T_r - T) \quad (2.14)$$

where h_{rh} is the convective heat transfer coefficient from the roof to the collector air, with T_r the roof temperature and T the temperature of the air in the collector.

2.3.2.1 $T_r > T$

When the collector roof temperature is greater than the collector air temperature, the roof is approximated as a heated horizontal surface facing down. In this case, no significant natural convection mechanisms exist and the stable warm air layer which is formed underneath the collector roof is "swept away" by the air flowing in the collector.

By approximating the flow in the collector as flow between parallel plates, the convective heat transfer coefficient from the collector roof to the air in the collector may be determined using Gnielinski's equation for fully developed turbulent flow (Kröger, 2004)

$$h_{rh} = \frac{(f/8)(Re - 1000)Pr}{1 + 12.7(f/8)^{1/2}(Pr^{2/3} - 1)} \left(\frac{k}{d_h} \right) \quad (2.15)$$

where f is the friction factor, Re is the Reynolds number, Pr is the Prandtl number and k is the thermal conductivity of the air. The Reynolds number is based on the hydraulic diameter ($d_h = 2H$) and all properties and the Prandtl number are evaluated at the mean air temperature. Equation (2.15) considers forced convection heat transfer only, including the effect of the specific surface roughness.

During times when $T_r > T$, equation (2.16) (analogous to equation (2.13)) is valid and can also be used for the evaluation of h_{rh} , according to the following

$$h_{rh} = 3.87 + 0.0022 \left(\frac{v\rho c_p}{Pr^{2/3}} \right) \quad (2.16)$$

where the properties are evaluated at the mean of the roof and collector air temperature. It is again assumed that the dominant local heat transfer mechanisms present will determine the local heat transfer rate. The numerical model subsequently employs the higher of the h_{rh} values calculated by equation (2.15) and equation (2.16) during times when $T_r > T$.

2.3.2.2 $T_r < T$

During times when the collector air temperature exceeds the collector roof temperature, the roof is assumed to be a cooled horizontal surface facing down. Now, the adjacent air underneath the collector roof becomes unstable and forms cool thermals flowing downward (i.e. natural convection).

According to its definition, equation (2.17) (analogous to equation (2.12)) is applicable when $T_r < T$ and can be utilized for the calculation of h_{rh} , as follows

$$h_{rh} = \left[0.2106 + 0.0026 v \left(\frac{\rho T_m}{\mu g \Delta T} \right)^{1/3} \right] / \left[\frac{\mu T_m}{g \Delta T c_p k^2 \rho^2} \right]^{1/3} \quad (2.17)$$

where T_m is the mean temperature between the collector roof and collector air and ΔT is the difference between the roof and collector air temperature.

However, equation (2.15) remains applicable for determining a forced convective h_{rh} value when $T_r < T$. Furthermore, equation (2.16) also becomes applicable during times when the collector air temperature exceeds the roof temperature by only a slight margin.

Once again it is assumed that the dominant local heat transfer mechanisms present will determine the local heat transfer rate. Consequently, with $T_r < T$ the numerical model employs the higher of the h_{rh} values calculated by equations (2.15), (2.16) and (2.17).

2.3.3 Convection from ground to collector air

The convective heat flux from the ground surface to the air in the collector (from equations (2.4) and (2.7)) may be expressed as follows

$$q_{gh} = h_{gh}(T_g - T) \quad (2.18)$$

where h_{gh} is the convective heat transfer coefficient from the ground surface to the collector air, T_g is the ground surface temperature and T the temperature of the air in the collector.

2.3.3.1 $T_g > T$

For a ground surface temperature greater than the temperature of the air in the collector, the ground surface may be approximated as a heated horizontal surface facing up. The heated ground surface causes the adjacent air to become unstable and forms rising thermals, thereby effecting natural convection.

According to its definition, equation (2.19) (analogous to equation (2.12)) is applicable for the calculation of the convective heat transfer coefficient from the ground to the collector air (h_{gh}) when $T_g > T$. The correlation is rewritten for h_{gh} as

$$h_{gh} = \left[0.2106 + 0.0026 v \left(\frac{\rho T_m}{\mu g \Delta T} \right)^{1/3} \right] / \left[\frac{\mu T_m}{g \Delta T c_p k^2 \rho^2} \right]^{1/3} \quad (2.19)$$

with T_m the mean temperature between the ground surface and the collector air and where ΔT is the difference between the ground surface temperature and the collector air temperature.

Analogous to the evaluation of h_{rh} , h_{gh} may also be calculated using equation (2.20) (similar to equation (2.15))

$$h_{gh} = \frac{(f/8)(Re - 1000)Pr}{1 + 12.7(f/8)^{1/2}(Pr^{2/3} - 1)} \left(\frac{k}{d_h} \right) \quad (2.20)$$

when $T_g > T$.

It should be noted that equation (2.20) takes the ground roughness into account. In addition, analogous to the evaluation of h_{rh} , h_{gh} may also be calculated using equation (2.21) (similar to equation (2.13)) during times when the ground surface temperature is slightly greater than the collector air temperature. The correlation may be rewritten for h_{gh} as

$$h_{gh} = 3.87 + 0.0022 \left(\frac{v \rho c_p}{Pr^{2/3}} \right) \quad (2.21)$$

where the properties are evaluated at the mean temperature between that of the ground surface and collector air.

It is assumed that the dominant local heat transfer mechanisms present will determine the local heat transfer rate. Therefore, with $T_g > T$ the numerical model employs the higher of the h_{gh} values calculated by equations (2.19), (2.20) and (2.21).

2.3.3.2 $T_g < T$

In the unlikely case where the temperature of the air in the collector is greater than the ground surface temperature, the ground surface is approximated as a cooled horizontal surface, facing upwards. A cool, stable layer of air forms above the ground surface which, similar to the heated roof facing down, is "swept away" by the flowing collector air.

In situations where $T_g < T$, equation (2.20) is valid for the calculation of h_{gh} . Equation (2.21) is also applicable in such stable conditions. Thus the numerical model employs the higher of the h_{gh} values calculated by equations (2.20) and (2.21) during periods when $T_g < T$. It should be noted that $T_g < T$ is only considered a theoretical possibility, as simulations have never predicted such a case.

2.4 Momentum equations

Air flowing through the collector from the perimeter towards the chimney experiences frictional effects at the ground and roof surfaces. These effects are taken into account by the numerical model when solving the roof and ground shear stress terms of the collector momentum equation (equation (2.2)).

When considering the convective heat transfer equations of section 2.3, it is clear that equations (2.15) and (2.20) employ the Darcy friction factor f to compensate for a specific surface roughness. In addition, equations (2.12), (2.17) and (2.19) are defined for a smooth flat surface and all employ a constant skin friction coefficient of 0.0052. Furthermore, equations (2.13), (2.16) and (2.21) are defined for the same smooth horizontal surface under stable atmospheric conditions and all incorporate a constant skin friction coefficient of 0.0044.

In order to determine the respective shear stress terms of the collector momentum equation, corresponding friction coefficients should be employed as those used when determining the respective heat transfer coefficients. The following section presents the friction coefficient relations employed by the numerical model for the calculation of the convective heat transfer coefficients and shear stress terms.

2.4.1 Collector roof shear stress

By approximating the flow of air through the collector as flow between parallel plates, the collector roof shear stress may be determined (according to White (1999)) by the following

$$\tau_r = \frac{f\rho v^2}{8} \quad (2.22)$$

where f represents the Darcy friction factor. When approximating the flow underneath the collector roof as flow over an infinite horizontal flat plate, the roof shear stress is calculated using (according to White (1999))

$$\tau_r = \frac{c_f\rho v^2}{2} \quad (2.23)$$

where c_f represents the skin friction coefficient. The Darcy friction factor for smooth surfaces is obtained from the equation by Filonenko (Kröger, 2004)

$$f = (1.82 \log_{10} Re - 1.64)^{-2} \quad (2.24)$$

where Re is the Reynolds number. For rough surfaces, Haaland (1983) recommends the following equation

$$f = 0.3086 \left[\log_{10} \left(\frac{6.9}{Re} + \left(\frac{\varepsilon/d_h}{3.75} \right)^{1.11} \right) \right]^{-2} \quad \text{for } \varepsilon/d_h > 10^{-4} \quad (2.25)$$

where Re is again the Reynolds number and ε/d_h is the relative roughness of the surface, with d_h the hydraulic diameter. Haaland (1983) also suggests

$$f = 2.7778 \left[\log_{10} \left(\left(\frac{7.7}{Re} \right)^3 + \left(\frac{\varepsilon/d_h}{3.75} \right)^{3.33} \right) \right]^{-2} \quad \text{for } \varepsilon/d_h \leq 10^{-4} \quad (2.26)$$

for cases where ε/d_h is very small. As previously mentioned, equations (2.12), (2.17) and (2.19) employ a constant skin friction coefficient of 0.0052, while equations (2.13), (2.16) and (2.21) use a constant skin friction coefficient of 0.0044.

2.4.1.1 $T_r > T$

During periods when $T_r > T$, the numerical model employs the higher of the h_{rh} values determined from equations (2.15) and (2.16). When approximating the collector roof as a smooth surface, equation (2.24) is used to calculate f , which is then substituted into equation (2.15). Additionally, equation (2.16) employs a constant c_f value of 0.0044 (from experimental results for a smooth surface in stable atmospheric conditions).

The calculated f and c_f values are also substituted respectively into equation (2.22) and (2.23) to determine respective τ_r values. In order to generate a conservative solution, the higher of the τ_r values is employed in the collector momentum equation.

2.4.1.2 $T_r < T$

As discussed in section 2.3, the numerical model employs the higher of the h_{rh} values calculated by equations (2.15), (2.16) and (2.17) when $T_r < T$. When determining h_{rh} using equation (2.15), equation (2.24) is used to calculate the value of f (the roof is once again approximated as a smooth surface). When h_{rh} is evaluated according to equation (2.16), a constant c_f value of 0.0044 is used. For the calculation of h_{rh} using equation (2.17), a constant c_f value of 0.0052 is used (from experimental results for a smooth surface).

The calculated f and c_f values are also substituted respectively into equation (2.22) and (2.23) to determine respective τ_r values. Once again the aim is to generate a conservative solution. Therefore, the higher of the τ_r values is employed in the collector momentum equation.

2.4.2 Ground surface shear stress

Analogous to the evaluation for the collector roof surface, by approximating the flow of air through the collector as flow between parallel plates, the ground surface shear stress is determined using

$$\tau_g = \frac{f\rho v^2}{8} \quad (2.27)$$

where f once again represents the Darcy friction factor. When approximating the flow over the ground surface as flow over an infinite horizontal flat plate, the ground surface shear stress is calculated using

$$\tau_g = \frac{c_f \rho v^2}{2} \quad (2.28)$$

where c_f once again represents the skin friction coefficient. Analogous to the roof shear stress calculations, the Darcy friction factor is determined using either one of equations (2.24), (2.25) or (2.26), as appropriate.

2.4.2.1 $T_g > T$

As discussed in section 2.3, the numerical model employs the higher of the h_{gh} values calculated by equations (2.19), (2.20) and (2.21) when $T_g > T$. For the calculation of h_{gh} using equation (2.19), a constant c_f value of 0.0052 is used. When determining h_{gh} using equation (2.20), equation (2.24), (2.25) or (2.26) is used to calculate the value of f (depending on whether the ground surface is approximated as a smooth or rough surface). When h_{gh} is determined according to equation (2.21), a constant c_f value of 0.0044 is employed.

The determined f and c_f values are substituted respectively into equation (2.27) and (2.28), thereby calculating respective ground surface shear stress values. A conservative approach is followed, whereby the higher of the τ_g values is employed in the collector momentum equation. It is important to note that the equations employing the constant skin friction coefficients are defined for smooth surfaces and therefore do not take into account the possible roughness of the ground. This necessitates the mentioned conservative approach.

2.4.2.2 $T_g < T$

During periods when $T_g < T$, the numerical model employs the higher of the h_{gh} values determined from equations (2.20) and (2.21). Depending on whether the ground is approximated as a smooth or rough surface, equation (2.24), (2.25) or (2.26) is used to calculate f to be substituted into equation (2.20). Additionally, equation (2.21) employs a constant c_f value of 0.0044.

The calculated f and c_f values are also substituted respectively into equation (2.27) and (2.28) to determine respective τ_g values. In order to generate a conservative solution, the higher of the τ_g values is employed in the collector momentum equation.

2.5 Meteorological data of the reference location

When modelling the solar chimney power plant, environmental conditions must be specified over a period of one year. Due to the fact that the plant generates electricity by harnessing the sun's energy, solar radiation will obviously be a crucial input. Another important influence on the power plant's performance will be the ambient air temperature. Other influencing factors include the wind conditions and humidity.

The reference location selected is near Sishen, South Africa. This particular location is dry and hot and experiences predominantly clear sky days and nights. It is situated in a flat and open part of South Africa where a high quantity of solar irradiation is received annually. All of these factors contribute to making Sishen an ideal location for the construction of a large-scale solar chimney power plant. The specific location co-ordinates are:

Table 2.2: Reference location co-ordinates and Standard Time Zone

Latitude	27.67° South
Longitude	23.00° East
Standard Time Zone	30° East

2.5.1 Solar radiation

Solar radiation consists of two components, namely beam and diffuse radiation. The sum of these components is the total solar radiation. The solar radiation input data employed by the numerical model is given in table H.1 of Appendix H in the format of total and diffuse solar radiation (in W/m^2) on a horizontal surface for a specific solar time (sunshine) hour. These are average hourly values for an average day in that specific month. Negligible solar radiation is assumed for the hours not shown in the table.

2.5.2 Ambient temperature

The ambient air temperatures shown in table H.2 (Appendix H) are those air temperatures which occur at approximately 1.5 m above ground level at the specific location. The table displays ambient air temperatures (in $^{\circ}\text{C}$) for a specific solar time hour. These temperatures are average hourly values for an average day in that specific month. It is assumed that a dry adiabatic lapse rate (DALR) exists in the atmosphere of the reference location (during day and night-time). Night-time temperature inversions appear to be weak at this particular location.

2.5.3 Ambient wind speed

The ambient wind speeds are shown in table H.3 (Appendix H) and are those wind speeds measured at 10 m above ground level at the specific location. The table displays ambient wind speeds (in m/s) for a specific solar time hour. These speeds are average hourly values for an average day in that specific month.

2.5.4 Ambient humidity

The ambient humidities shown in table H.4 (Appendix H) are those which occur at approximately 1.5 m above ground level at the specific location. The table displays ambient relative humidities (in %) for a specific solar time hour. These humidities are average hourly values for an average day in that specific month.

2.5.5 Interpretation of input data

In order to find a smoother representation of the input data for its use in the numerical model, the input solar radiation, ambient air temperature, ambient wind speed and ambient humidity data is interpreted in the following way.

It is assumed that the values given in tables H.1, H.2, H.3 and H.4 are the specific values which occur on the stroke of the given solar time hour on the 15th of that particular month. The data is then interpolated between months to find values for specific days and then interpolated between hours to give specific minutely input values. Thus the input data to the numerical model are approximated values which occur at a specific minute of a particular day of the year.

2.6 Modelling ambient cross-winds

Previous studies have confirmed that windy ambient conditions affect the performance of cooling towers. It is therefore natural to investigate the performance of a solar chimney power plant in the presence of wind.

The following section presents equations which are used to model the wind effects at the top of the chimney.

2.6.1 Chimney outlet loss

The air exiting the chimney experiences a pressure differential due to the shape of the chimney outlet, and can be expressed as (see figure 2.1)

$$\Delta p_{co} = K_{co} \frac{1}{2} \rho_6 v_6^2 \quad (2.29)$$

where K_{co} is the chimney outlet loss coefficient.

2.6.1.1 No-wind conditions

According to Kröger (2004), during relatively quiet (no significant ambient winds) periods, for a hyperbolic cooling tower with a cylindrical outlet where $0.5 \leq d_o/d_i \leq 0.85$, the tower (in our case the chimney) outlet loss coefficient is given by

$$K_{co} = -0.28 Fr_D^{-1} + 0.04 Fr_D^{-1.5} \quad (2.30)$$

where d_o and d_i is the tower (chimney) outlet and inlet diameter respectively, while Fr_D is the densimetric Froude number, determined by

$$Fr_D = \left(\frac{\dot{m}}{A_6} \right)^2 / [\rho_6 (\rho_7 - \rho_6) g d_c] \quad (2.31)$$

The subscript 6 in equation (2.31) represents the chimney outlet, while 7 indicates the ambient air condition at a position some distance from, but at the same height as the chimney outlet (as shown in figure 2.1).

It is assumed that the solar chimney power plant has a chimney outlet to inlet diameter ratio of unity. Furthermore, it is assumed that equation (2.30) is applicable to the plant chimney, although the chimney has a diameter ratio larger than 0.85.

2.6.1.2 Windy conditions

During windy ambient conditions, the chimney outlet loss coefficient may be defined as follows (Buxmann, 1983):

$$K_{co} = \frac{(p_6 + \frac{1}{2} \rho_6 v_6^2) - (p_7 + \frac{1}{2} \rho_7 v_7^2)}{\frac{1}{2} \rho_6 v_6^2} = \frac{\Delta p_w}{\frac{1}{2} \rho_6 v_6^2} + 1 - \frac{\rho_7 v_7^2}{\rho_6 v_6^2} \quad (2.32)$$

where Δp_w is the static pressure difference in windy conditions. The velocity v_7 indicates the ambient wind velocity at the height of the chimney outlet (position 7 of figure 2.1), while v_6 is the velocity of the air exiting the chimney at position 6.

A fluid flowing across a cylinder causes the static pressure to vary circumferentially around the cylinder. A static pressure coefficient which describes this variation may be defined as

$$C_p = \frac{(p_\theta - p_a)}{\frac{1}{2} \rho_a v_a^2} \quad (2.33)$$

where p_θ is the local static pressure and the subscript a refers to the ambient conditions far from the cylinder.

Buxmann (1983) performed model tests to evaluate the performance characteristics of cooling towers in the presence of wind. He defines an outlet pressure coefficient in terms of the static pressure difference between the throat of the chimney and the ambient, as follows:

$$C_{po} = \frac{(\Delta p_w - \Delta p)}{\frac{1}{2}\rho_7 v_7^2} \quad (2.34)$$

where Δp_w is once again the static pressure difference in windy conditions and Δp is the static pressure difference during no-wind conditions. Equation (2.34) can be re-written as

$$C_{po} = \frac{\Delta p_w - (p_6 - p_7)}{\frac{1}{2}\rho_7 v_7^2} \quad (2.35)$$

In the case of no wind outside the chimney, it is assumed that $p_6 \approx p_7$ and therefore equation (2.35) simplifies to

$$C_{po} = \frac{\Delta p_w}{\frac{1}{2}\rho_7 v_7^2} \quad (2.36)$$

Substitute equation (2.36) into equation (2.32) and find the chimney outlet loss coefficient in windy conditions:

$$K_{co} = \frac{\rho_7 v_7^2}{\rho_6 v_6^2} (C_{po} - 1) + 1 \quad (2.37)$$

According to Du Preez (1992), the pressure coefficient at the outlet of a cooling tower may be represented by the empirical relation:

$$\begin{aligned} C_{po} = & -0.405 + 1.07 \left(\frac{v_7}{v_6} \right)^{-1} \\ & + 1.8 \log_{10} \left[\left(\frac{v_7}{2.7 v_6} \right) \left(\frac{A_o}{A_t} \right)^{1.65} \right] \left[\left(\frac{v_7}{v_6} \right) \left(\frac{A_o}{A_t} \right)^{1.65} \right]^{-2} \\ & + \left[-1.04 + 1.702 \left(\frac{A_o}{A_t} \right) - 0.662 \left(\frac{A_o}{A_t} \right)^2 \right] \left(\frac{v_7}{v_6} \right)^{-0.7} \end{aligned} \quad (2.38)$$

which is valid for $1.8 \leq (v_7/v_6) \leq 24$. The variables A_o and A_t represent the tower outlet and tower throat cross-sectional (in our case chimney) areas respectively. It is assumed that the ratio of (A_o/A_t) for the chimney of the solar chimney power plant is unity.

The numerical model evaluates the effect of wind at the top of the chimney in the following way. If the ratio $(v_7/v_6) < 1.8$, it is assumed that an insignificant ambient wind is present and the pressure differential at the chimney outlet (equation (2.29)) is evaluated according to subsection 2.6.1.1. When $1.8 \leq (v_7/v_6) \leq 24$, it is assumed that significant wind is present and the approach of subsection 2.6.1.2 is followed for the determination of Δp_{co} .

Chapter

3

Critical Evaluation of Plant Performance

This chapter presents a critical evaluation of the influence of recently developed convective heat transfer and momentum equations, the quality, thickness, reflectance, emissivity, shape and insulation of the collector roof glass, the cross-section of the collector roof supports, various ground types, ground surface roughness, absorptivity and emissivity, turbine inlet and bracing wheel loss coefficients and the ambient pressure and temperature lapse rate on the performance of a reference solar chimney power plant (defined in Chapter 2).

The general goal of this chapter is to reveal the sensitivity (on power output) to variation of certain specifications of a solar chimney power plant. A reference plant is selected as a realizable basis to work from. The specifications of the reference plant are assumed to be achievable without excessive (unrealistic) cost. Some of the following sections illustrate the sensitivity of varying parameters over a generally accepted range, while other sections investigate extreme cases of variation (which would most probably require substantially increased investments) for the purpose of illustrating a "best case" scenario and identifying possible areas of research or future improvements on the solar chimney power plant.

Multiple computer simulations are performed in order to evaluate the above-mentioned parameters. Simulations are performed using the complete specifications of a reference plant as discussed in Chapter 2 of this dissertation. When evaluating the effect of a specific parameter, only that parameter is varied. All simulations are repeated for a number of years after start-up to allow ground energy fluxes to reach a quasi-steady state.

3.1 Convective heat transfer and momentum equations

Recently obtained convective heat transfer and corresponding momentum equations are discussed in Chapter 2. These newly developed equations are implemented into the present numerical model at the conditions specified in Chapter 2 and simulations are performed.

3.1.1 Simulation and results

Comparative computer simulations were conducted for the reference solar chimney power plant, with one model employing the original strategy and equations for the calculation of the various convective heat transfer coefficients (Pretorius, 2004), while the other included the more recent heat transfer and momentum equations as given in Chapter 2.

A comparison between the electrical plant outputs for 21 June and 21 December is illustrated in figure 3.1.

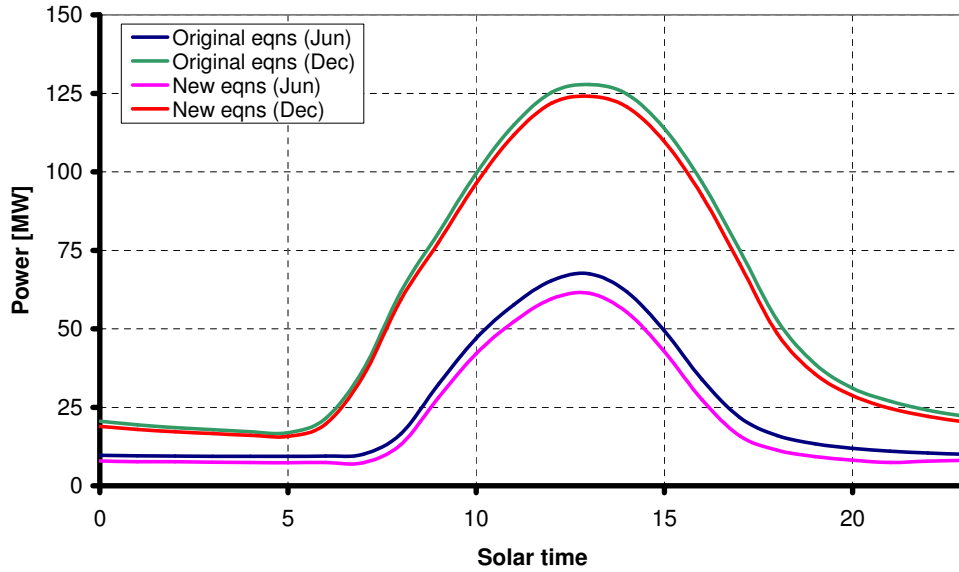


Figure 3.1: Effect of the convective heat transfer and momentum equations on daily plant power output

From figure 3.1 it is evident that the power production of the solar chimney power plant is markedly higher throughout a 24-hour period when employing the original convective heat transfer and momentum correlations when compared to the new equations. Table 3.1 confirms an increased output, showing a rise in annual power generation of 9.2 %. Figure 3.2 sheds some light on this power increase by presenting the values of various convective heat transfer coefficients at specific collector radii, at 13:00 on 21 December.

Table 3.1: Annual power output comparison, illustrating the effect of the convective heat transfer and corresponding momentum equations on plant performance

Plant configuration	Annual power output [GWh]
Incorporating new equations	336
Incorporating original equations	366.9

It is clear that the original value for h_{gh} (from model incorporating previous equations) is smaller than the new h_{gh} value (from model incorporating recently developed equations) over the entire radius of the collector. The original h_{gh} value decreases from approximately 19 W/m²K to 10 W/m²K while the new heat transfer coefficient remains virtually constant at 19 W/m²K as the air-flow approaches the chimney inlet. The lower (original) convection coefficient facilitates less energy to be extracted from the ground into the air, resulting in a higher ground surface temperature.

It is also clear that the original and new values for h_{rh} differ significantly. The original h_{rh} value decreases somewhat from 6 W/m²K to 4.4 W/m²K, while the new heat transfer coefficient increases slightly from approximately 15.2 W/m²K at the collector perimeter to 18.3 W/m²K at the collector outlet. Due to the fact that $T_r < T$ at 13:00, energy is transferred from the flowing collector air to the collector roof. The considerably lower (original) convective heat transfer coefficient results in a significantly smaller heat transfer from the collector air to the roof than predicted when employing the new equations.

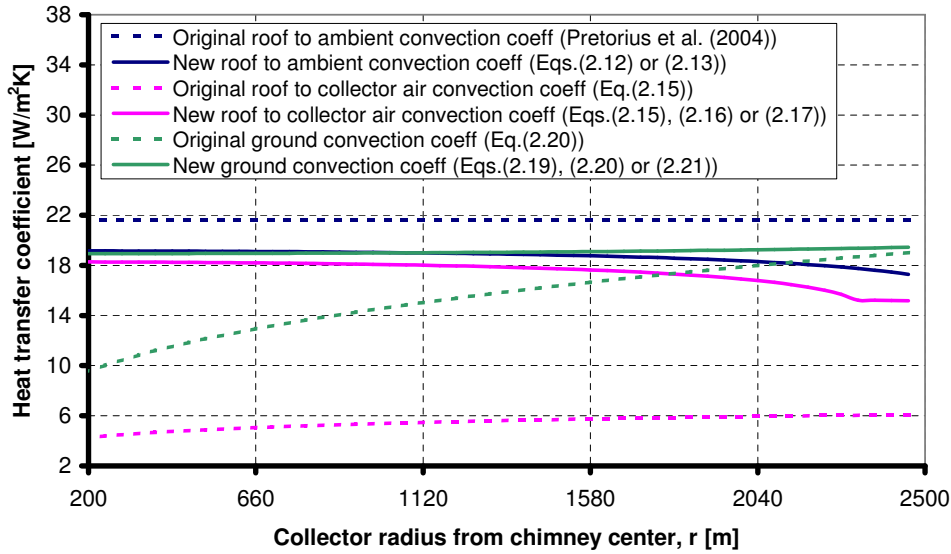


Figure 3.2: Comparison between the new and original convective heat transfer coefficients

From figure 3.2 it is also evident that the original h_{ra} value stays constant at $21.6 \text{ W/m}^2\text{K}$ (due to an ambient wind of 4.2 m/s) while the new value for h_{ra} is somewhat lower over the entire collector radius. The original, higher value of h_{ra} is therefore responsible for retaining less of the energy that is transferred to the roof from the collector air.

Despite a higher h_{ra} value, the greatly reduced heat transfer from the ground to the roof causes less energy to be lost through the collector roof to the environment (due to slightly cooler air under the collector roof) than predicted when incorporating the new equations, resulting in an overall power output increase.

3.2 Collector roof glass quality

The quality of glass can certainly be evaluated according to aspects such as strength, radiative properties (i.e. optical quality), stiffness, surface finish etc. However, in terms of solar chimney power plant performance, the optical quality is of greatest importance. The transmittance and absorptivity of glass depend on the solar radiation incidence angle, the refractive index of the glass, the thickness of the glass and its extinction coefficient. The refractive index of glass remains virtually unchanged for different types of glass, while glass thickness is unlikely to be changed significantly due to cost and strength considerations.

Previous studies (Hedderwick (2001), Kröger and Buys (2001), Bernardes *et al.* (2003) and Pretorius *et al.* (2004)) assumed a relatively poor quality glass as collector roof material. In terms of the current investigation, better quality glass implies a better transparency, thereby allowing more solar radiation transmittance. For partially transparent media, such as glass, a material constant known as the extinction coefficient partially determines the amount of radiation absorbed and consequently transmitted by the medium. According to Duffie and Beckman (1991), the extinction coefficient of glass varies from 32 m^{-1} for "greenish cast of edge" (having a somewhat greenish edge colour) to 4 m^{-1} for "water white" glass (having a whitish edge colour). Therefore the better the quality of the glass, the better its transparency, allowing more solar radiation to penetrate it.

3.2.1 Simulation and results

Once again comparative simulations were conducted for the reference plant, with one model incorporating the poorer quality collector roof glass (with extinction coefficient of $C_e = 32 \text{ m}^{-1}$) while the other included a better quality glass with extinction coefficient of $C_e = 4 \text{ m}^{-1}$. It is noted that both models now include the new convective heat transfer and momentum equations.

Figure 3.3 illustrates the electrical plant power on 21 June and 21 December, while table 3.2 compares the annual power output of the two models.

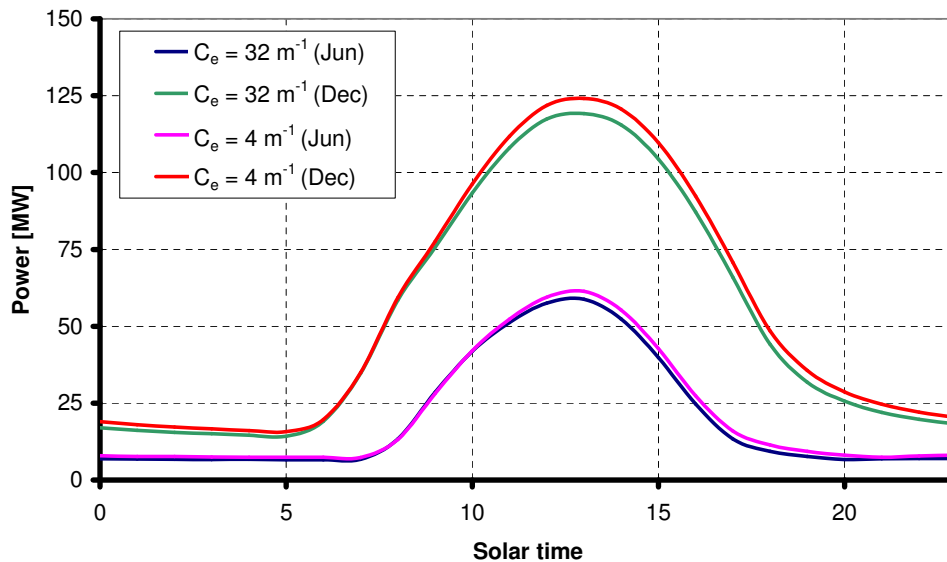


Figure 3.3: Effect of optical collector roof glass quality on the daily power output

When evaluating figure 3.3, it is clear that during the summer months the poorer quality glass causes a somewhat reduced plant power output throughout the day, with a lower peak value. The overall output during the colder months is also marginally lower.

Another noticeable trend is that the model incorporating the poorer quality glass produces a similar power output during the mornings as the plant employing the better quality glass. This is due to the fact that the poorer quality glass is less transparent than the better quality glass. A greater fraction of energy is absorbed by the poorer glass in the mornings, resulting in a higher collector roof temperature. Conversely, the better glass allows more of the solar radiation to penetrate (thus absorbing a smaller fraction of energy) and strike the ground, causing a lower roof temperature than with poor quality glass.

As a result, the temperature difference between the roof and the collector air is smaller when employing poor quality glass, while the value of h_{rh} is approximately similar for both plant configurations. The net result during mornings is that less heat is transferred from the collector air to the roof and less heat is lost to the environment when including a poorer

Table 3.2: Annual power output comparison, illustrating the influence of optical collector roof glass quality on solar chimney power plant performance

Plant configuration	Annual power output [GWh]
Good quality glass ($C_e = 4 \text{ m}^{-1}$)	336
Poor quality glass ($C_e = 32 \text{ m}^{-1}$)	317.8

quality glass roof. Note that generally the collector air is warmer than the collector roof. Table 3.2 substantiates the negative influence of a poorer quality glass on the annual power output of the solar chimney power plant, indicating a reduction of approximately 5.4 %.

It was decided to employ an improved glass ("white glass") collector roof with an extinction coefficient of $C_e = 4 \text{ m}^{-1}$ in the reference plant specifications of this study.

3.3 Collector roof thickness

Publications by Schlaich (1994) and Bernardes *et al.* (2003) employ a collector roof (glass) thickness of $t_r = 0.004 \text{ m}$, while studies by Hedderwick (2001), Kröger and Buys (2001) and Pretorius *et al.* (2004) assume a roof thickness of $t_r = 0.005 \text{ m}$.

According to data from the prototype plant in Manzanares, the 4 mm thick glass that was used for the collector of the plant proved strong enough to withstand the meteorological forces such as wind and even hail which prevailed on site. Also, as a huge area will be covered by the collector roof (for a large-scale plant), it is essential that the glass that is used for the roof be as cheap as possible.

This section determines the effect of collector roof (glass) thickness on the performance of a solar chimney power plant.

3.3.1 Simulation and results

Comparative simulations were conducted for the reference solar chimney power plant, with one model using a 5 mm glass thickness while the other model incorporated a 4 mm glass thickness.

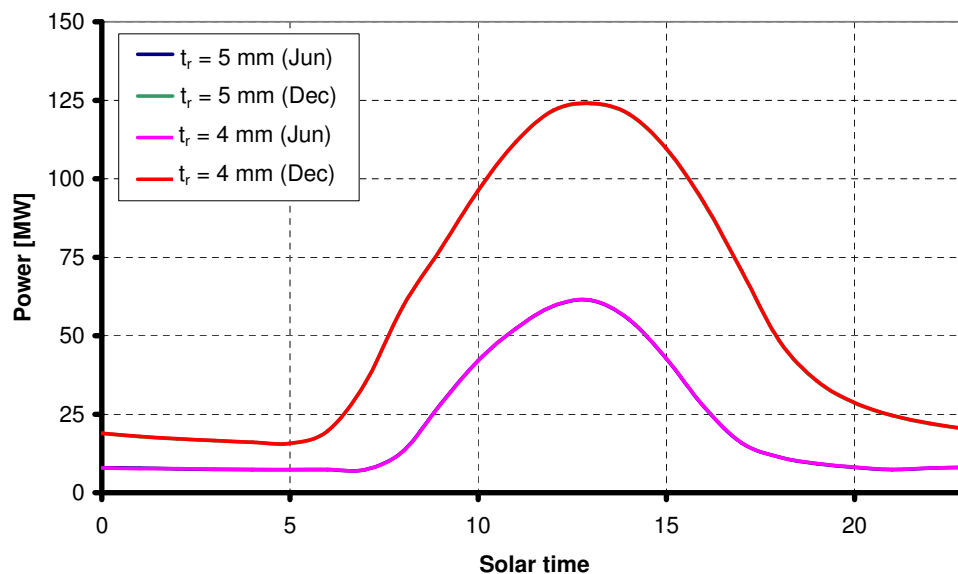


Figure 3.4: Effect of collector roof (glass) thickness on daily plant power output

From figure 3.4 (presenting electrical plant power outputs for 21 June and 21 December) it is clear that the collector roof (glass) thickness does not have a significant influence on the solar chimney plant power output. This is corroborated by table 3.3 which shows only a 0.2 % reduction in annual power output when employing 5 mm thick glass instead of the reference 4 mm glass. The minor reduction in power can be attributed to the fact that solar radiation is transmitted slightly less effectively through the thicker of the two roofs.

Table 3.3: Annual power output comparison, illustrating the influence of collector roof (glass) thickness on plant performance

Plant configuration	Annual power output [GWh]
Roof thickness: $t_r = 4$ mm	336
Roof thickness: $t_r = 5$ mm	335.3

Therefore, as 4 mm thick glass is generally accepted as very durable, and since 4 mm thick glass is cheaper than 5 mm glass, it was decided to introduce the thinner glass into the reference plant specifications of this study.

3.4 Collector roof reflectance

Throughout a typical clear sky day, solar radiation strikes the collector (glass) roof at varying incident angles. Depending on the time-dependent incident angle and glass properties, different fractions of solar energy are absorbed, transmitted and reflected by the roof.

Duffie and Beckman (1991) state that the solar reflectance of a single untreated glass pane is approximately 8 %. This was checked with the calculations of the numerical model. The numerical model calculates the beam solar reflectance of a single pane of untreated glass (the collector roof) to be between 8 % and 15 % for most of the day, throughout the year. Diffuse solar reflectance is calculated to be constant at 15.5 %.

If a film of low refractive index is deposited onto a glass pane at an optical thickness of $\lambda/4$, the radiation of wavelength λ that is reflected from the upper and lower surface of the film will have a phase difference of π . This phase difference will cause the reflected components to cancel, thereby decreasing the glass reflectance and increasing its transmittance. Duffie and Beckman (1991) also mention that reflection losses can be reduced to approximately 2 % when applying such a surface treatment to glass.

This section studies the effect that the collector roof reflectance has on the solar chimney power plant performance. It is assumed that the top surface of the whole collector roof is treated in order to lower its reflectance and effectively increase its transmittance. In light of the suggestion by Duffie and Beckman (1991) that a surface treatment may reduce the solar reflectance of glass to a quarter of its original value, the numerical model subsequently reduces the reflectance losses of the collector roof at each time step to a quarter of its untreated reflectance value.

3.4.1 Simulation and results

Comparative simulations were conducted for the reference solar chimney power plant, with one model incorporating an untreated collector (glass) roof, while the other employs a treated collector roof to decrease reflective losses.

Figure 3.5 illustrates clearly the increased daily power output delivered by a plant employing a treated collector roof surface versus a plant using an untreated roof. The increased transmittance as a result of the treatment allows more energy to pass through the roof and heat the ground surface beneath. More energy is subsequently transferred to the collector air, giving a greater power output during the day. Another product of better roof transmittance is that more energy is stored in the ground during daytime. Consequently, with more energy stored in the ground during the day, more energy is released during night-time, which explains the marginally higher plant power production at night.

It is also evident from table 3.4 that reduced reflectance has a very positive effect on annual solar chimney power output. Table 3.4 indicates a 13.9 % annual power output increase when employing a treated collector roof surface instead of an untreated roof.

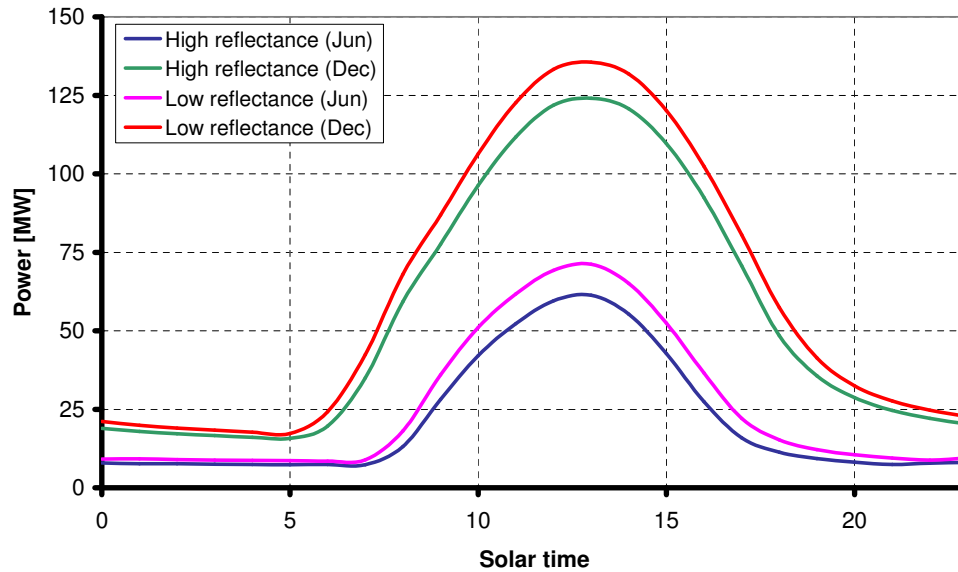


Figure 3.5: Effect of collector roof reflectance on daily plant power output

Table 3.4: Annual power output comparison, illustrating the effect of collector roof reflectance on the performance of the reference solar chimney power plant

Plant configuration	Annual power output [GWh]
High reflectance (untreated surface)	336
Low reflectance (treated surface)	382.7

Despite these findings, an untreated collector roof is employed in the reference plant specifications. When one considers the sheer size of the collector roof area and the cost of such film deposits, the increase in plant cost due to these treatments will be significant. It would require a specific cost / benefit investigation for an individual plant design to validate the economic viability of such surface treatments, a topic not covered in this study.

3.5 Collector roof emissivity

Studies by Hedderwick (2001), Kröger and Buys (2001) and Pretorius *et al.* (2004) employ a collector roof emissivity of $\epsilon_r = 0.87$ (for both the top and bottom surface), while Bernardes *et al.* (2003) uses $\epsilon_r = 0.9$ as cover emissivity. This section investigates the effect that roof emissivity has on solar chimney power plant performance.

According to Duffie and Beckman (1991), glass may be treated in order to decrease its emittance. This section therefore assumes that the top surface of the collector (glass) roof will be treated in order to lower the top surface emissivity. This will reduce (depending on value) the radiation losses of the collector to the atmosphere. It is assumed that the bottom surface emissivity remains unchanged.

Duffie and Beckman (1991) also mention that the above-mentioned treatments may decrease the glass transmittance. This study, however, assumes that the treatment of the collector (glass) roof does not affect its transmittance in any way.

3.5.1 Simulation and results

Comparative simulations were performed for the reference solar chimney power plant, using varying top collector roof surface emissivity values of $\epsilon_{r,top} = 0.87$, $\epsilon_{r,top} = 0.5$ and $\epsilon_{r,top} = 0.1$. The lower surface emissivity is kept constant at $\epsilon_r = 0.87$ for all cases.

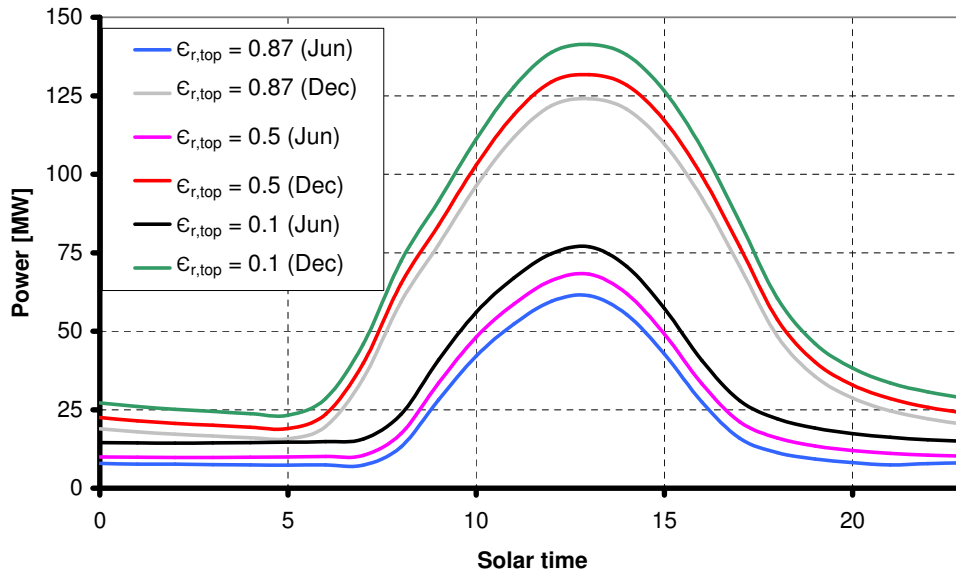


Figure 3.6: Effect of collector roof emissivity (top surface) on daily plant output

Figure 3.6 illustrates the major influence that the roof emissivity has on daily plant performance. It is evident that a lower emissivity value on the top collector roof surface enables the plant to generate more power throughout a typical day. Annually, the implementation of a collector roof with top surface emissivity of $\epsilon_{r,top} = 0.5$ or $\epsilon_{r,top} = 0.1$ produces respective increases in power output of 12.9 % and 29.7 % when compared to a plant with top surface roof emissivity of $\epsilon_{r,top} = 0.87$ (as shown in table 3.5).

Table 3.5: Annual power output comparison, illustrating the effect of collector roof emissivity (top surface) on plant performance

Plant configuration	Annual power output [GWh]
High emissivity ($\epsilon_{r,top} = 0.87$)	336
Intermediate emissivity ($\epsilon_{r,top} = 0.5$)	379.4
Low emissivity ($\epsilon_{r,top} = 0.1$)	435.8

The sizeable increase in power output can be attributed to much lower radiation losses from the collector roof to the environment. With the low emissivity value implemented ($\epsilon_{r,top} = 0.1$), the radiative losses are approximately reduced by an order of magnitude. Therefore, with less energy being lost to the environment, more is available to heat the collector air, giving an increased draught through the plant and subsequent greater power output.

Despite the results presented above, an untreated collector roof with emissivity (top and bottom surface) of $\epsilon_r = 0.87$ is employed in the reference plant specifications. If at all possible, it will be costly to achieve top surface emissivity values between 0.5 and 0.1 with a

surface treatment and the increase in plant cost due to these treatments will be significant. Future research to investigate the possibility of achieving such low emissivity values as well as a specific cost / benefit investigation for an individual plant design is required to validate the technical and economic viability of these surface treatments, a topic not covered in this study.

3.6 Collector roof insulation

During the night-time operation of the solar chimney power plant, large heat losses are incurred by means of convection and radiation from the collector roof to the environment. This section investigates the possibility of insulating the top collector roof surface during specific periods in order to reduce these losses.

The numerical model continuously calculates the heat fluxes into and out of the collector of the plant. It is assumed that the entire collector roof is covered with a specific insulation material during times when a net outflow of energy exists (mostly during night-time), while uncovering the roof during periods of net energy inflow (for most of the daytime). It is furthermore assumed that the covering material insulates the collector roof perfectly (it is not possible to achieve this extreme in practice), while also isolating the roof perfectly from incoming solar radiation during periods of net energy outflow in the daytime.

3.6.1 Simulation and results

Comparative simulations were conducted for the reference solar chimney power plant, with one model employing periodic thermal insulation while the other model incorporates no insulation. Figure 3.7 illustrates the substantial effect of insulation on daily plant power production.

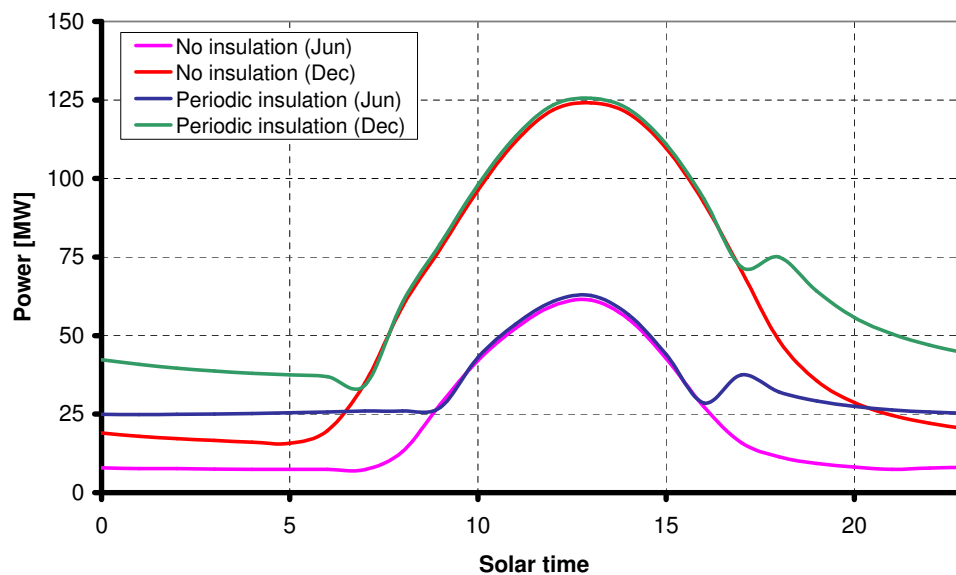


Figure 3.7: Effect of thermal collector roof insulation on daily plant output

It is clear that the insulation of the collector roof (mostly during night-time) enables much greater power production throughout the night, as well as a marginally higher peak output at midday.

In addition, small peaks in output late in the afternoon are also noticeable. During the late afternoon, heat losses through the roof to the environment start to exceed the incoming quantity of solar radiation energy. The heat losses experienced are large due to the high collector temperatures at these times. At this point in time it is assumed that the roof is covered in order to reduce these losses. Consequently, the combination of large heat losses which are retained due to the collector roof insulation and a rapidly cooling environment produces the observed peaks in power.

Table 3.6: Annual power output comparison, illustrating the effect of collector roof insulation on plant performance

Plant configuration	Annual power output [GWh]
No thermal insulation	336
Periodic thermal insulation	452.6

Table 3.6 affirms the considerable influence of periodic thermal insulation, showing a 34.7 % increase in annual power output compared to a plant employing no thermal insulation.

Despite these findings, an uninsulated collector roof is employed in the reference plant specifications. Once again, when one considers the sheer quantity of the insulation material needed to cover the entire collector area, it is clear that the increase in total plant cost will be significant. It would require a specific cost / benefit investigation for an individual plant design to validate the economic viability of thermally insulating the collector roof, a topic not covered in this study.

3.7 Collector roof shape

The numerical model defines the collector roof height at a specific collector radius according to the relation:

$$H = H_2 \left(\frac{r_2}{r} \right)^b \quad (3.1)$$

where H_2 and r_2 refer to the collector roof inlet (perimeter) height and collector perimeter radius respectively (see figure 2.1), while b is the roof shape exponent.

Work by Hedderwick (2001) employed a reference plant with a roof shape exponent of $b = 0.5$. Further publications by Kröger and Buys (2001) and Pretorius *et al.* (2004) also employed reference plants with shape exponents of $b = 0.5$, while also considering the effect of the roof shape exponent on solar chimney plant power production.

The inclusion of recently developed convective heat transfer correlations (section 2.3) into the numerical model significantly alters the performance characteristics of the solar chimney power plant (section 3.1). Previous publications only considered the effect of the roof shape exponent on plant performance based on previously employed heat transfer equations. Therefore this section investigates the effect of the roof shape exponent on plant performance based on the revised numerical model.

3.7.1 Simulation and results

Comparative simulations were conducted for the reference solar chimney power plant, employing collector roof shape exponents of $b = 0.5$, $b = 0.75$ and $b = 1$ (reference case).

Figure 3.8 illustrates the dependence of plant power output on the roof shape exponent. The figure indicates that the collector roof shape does have a significant effect on plant power

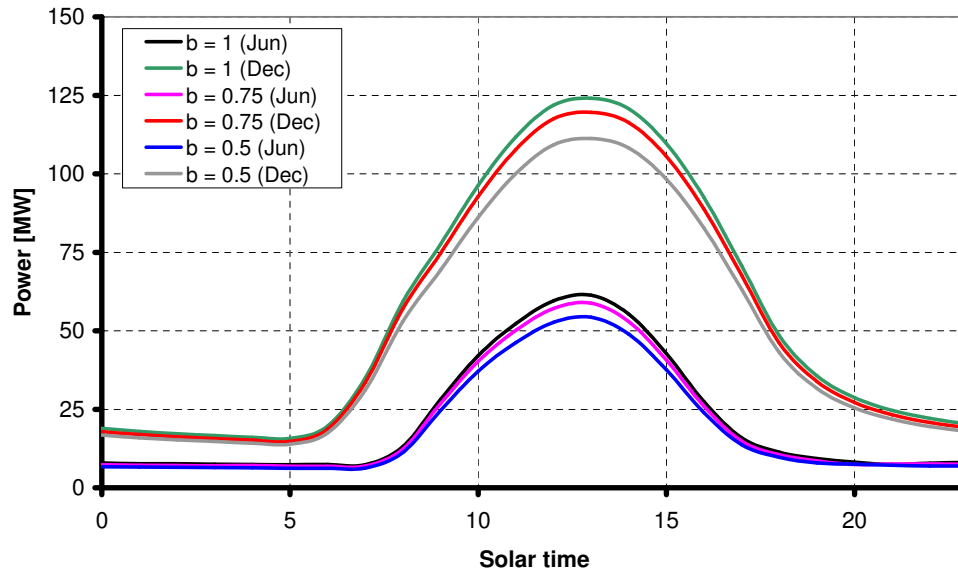


Figure 3.8: Effect of collector roof shape on daily plant power output

production. Table 3.7 confirms this, showing annual power output reductions of 4.3 % and

Table 3.7: Annual power output comparison, illustrating the influence of collector roof shape on plant performance

Plant configuration	Annual power output [GWh]
High exponent ($b = 1$)	336
Intermediate exponent ($b = 0.75$)	321.5
Low exponent ($b = 0.5$)	299.5

10.9 % (when compared to the reference case with $b = 1$) respectively when employing shape exponents of $b = 0.75$ and $b = 0.5$.

Assuming identical collector roof inlet heights, a larger roof shape exponent leads to a higher average collector roof height and thus to higher costs. Nevertheless, the incremental costs for longer collector roof supports are marginal. With one motivating factor being that there should be no significant difference in cost when employing different roof shapes in the solar chimney power plant, the current study employs a reference plant configuration with a roof shape exponent of $b = 1$. The exponent $b = 1$ also implies that since $H \propto r^{-1}$ the air velocity or pressure does not change measurably under the collector roof. Therefore, essentially no pressure differential exists between the air below and above the collector roof with $b = 1$. This eliminates leakage or large forces on the glass roof. It should also be noted that roof shape exponents larger than one may cause flow separation underneath the collector roof.

3.8 Collector roof support diameter

Studies by Hedderwick (2001), Kröger and Buys (2001) and Pretorius *et al.* (2004) assume a collector roof support diameter of $d_{sup} = 0.15$ m.

According to preliminary stress calculations by Van Dyk (2004-2006), the diameter of the collector supports should range from approximately 0.14 m at the collector perimeter

to 0.4 m (or even larger) near the chimney inlet. It should also be noted that, due to the shape of the collector roof, more of the collector roof area is supported by shorter supports than longer ones. Consequently, this study assumes an average collector support diameter of $d_{sup} = 0.2$ m, which is included in the reference plant specifications.

This section determines the influence of collector roof support diameter on solar chimney power plant performance.

3.8.1 Simulation and results

Comparative simulations were conducted for the reference solar chimney power plant, with one model using a collector roof support diameter of $d_{sup} = 0.15$ m while the other model employed a support diameter of $d_{sup} = 0.2$ m.

When regarding figure 3.9, it is evident that the power output curves for both plant configurations are very similar. At closer inspection we notice that the peak plant power output is slightly increased with the inclusion of collector roof supports with smaller diameters.

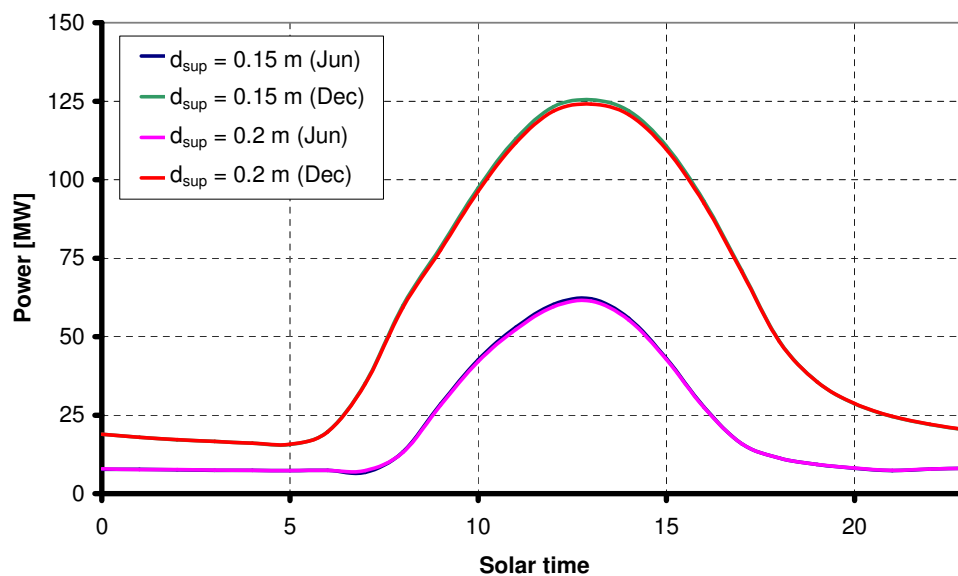


Figure 3.9: Effect of collector roof support diameter on daily solar chimney power plant output

From table 3.8 we see that the annual plant output is increased by approximately 0.7 % when introducing the smaller diameter supports. This minor power increase can be attributed to lower air-flow drag losses (due to the smaller support diameters) as the air under the collector roof flows across the supports towards the chimney inlet.

Table 3.8: Annual power output comparison, illustrating the influence of collector roof support diameter on plant performance

Plant configuration	Annual power output [GWh]
Support diameter: $d_{sup} = 0.2$ m	336
Support diameter: $d_{sup} = 0.15$ m	338.3

3.9 Various ground types

The previously mentioned studies by Hedderwick (2001), Kröger and Buys (2001) and Pretorius *et al.* (2004) employed Granite as the ground type for their solar chimney power plant simulations. However, many different ground types exist at locations around the world suitable for the construction of a solar chimney power plant. The following section evaluates the effect of three other dry ground types, as well as an extreme case of waterlogged ground on the power production of a solar chimney plant. Although ground properties may vary, average values are selected from literature. Also, despite the fact that in reality ground properties may vary with depth, water content, vapor diffusion, etc., this study assumes the ground properties to be uniform.

The ground properties of Granite used by the above-mentioned studies were selected from Holman (1992). Average properties for two other ground types, Limestone and Sandstone, are now selected from the same text and listed in table 3.9. The average properties of Sand are also included in the same table, as given by Incropera and DeWitt (2002).

Table 3.9: Average properties of Granite, Limestone and Sandstone according to Holman (1992); Average properties of Sand and water (at 300 K) according to Incropera and DeWitt (2002); Average properties of wet soil according to Mills (1995)

Ground type	Density [kg/m ³]	Specific heat capacity [J/kgK]	Thermal conductivity [W/mK]	Heat penetration coefficient b_p [Ws ^{1/2} /Km ²]
Granite	2640	820	1.73	1935
Limestone	2500	900	1.26	1684
Sandstone	2160	710	1.83	1675
Sand	1515	800	0.27	572
Wet soil	1900	2200	2.00	2891
Water	996	4179	0.613	1597

For the purpose of evaluating the effect of incorporating an extremely good energy storing mechanism, a plant configuration which includes waterlogged ground underneath the collector roof is investigated. In this instance, two sets of properties for waterlogged ground are investigated. Firstly, the properties of wet soil are introduced. Secondly, as an extreme case, the properties of waterlogged ground are assumed to be similar to those of water. Average properties for wet soil, as given by Mills (1995) and water, as presented by Incropera and DeWitt (2002), are listed in table 3.9. The investigation considers only simple one-dimensional conduction in the waterlogged ground (as with the other ground types) and neglects the effects of water evaporation. This should not be confused with a layer of pure water where radiation and convection effects in the water can have significant influences.

It is clear that, according to the practically identical heat penetration coefficients ($b_p = \sqrt{\rho c_p k}$) of Limestone, Sandstone and water (waterlogged ground) in table 3.9, simulations corresponding to these three ground types should produce virtually similar results.

This study assumes that the soil under the collector roof will have a composition similar to that of Sandstone and therefore employs Sandstone as soil type in the reference plant (as defined in Chapter 2).

3.9.1 Simulation and results

Comparative computer simulations were run for the reference solar chimney power plant, with the respective models incorporating Granite, Limestone, Sandstone, Sand and water-

logged ground (employing the properties of both wet soil and water) as ground type under the collector roof.

The results shown in figure 3.10 indicate the electrical plant power output for 21 June and 21 December for the various ground types investigated.

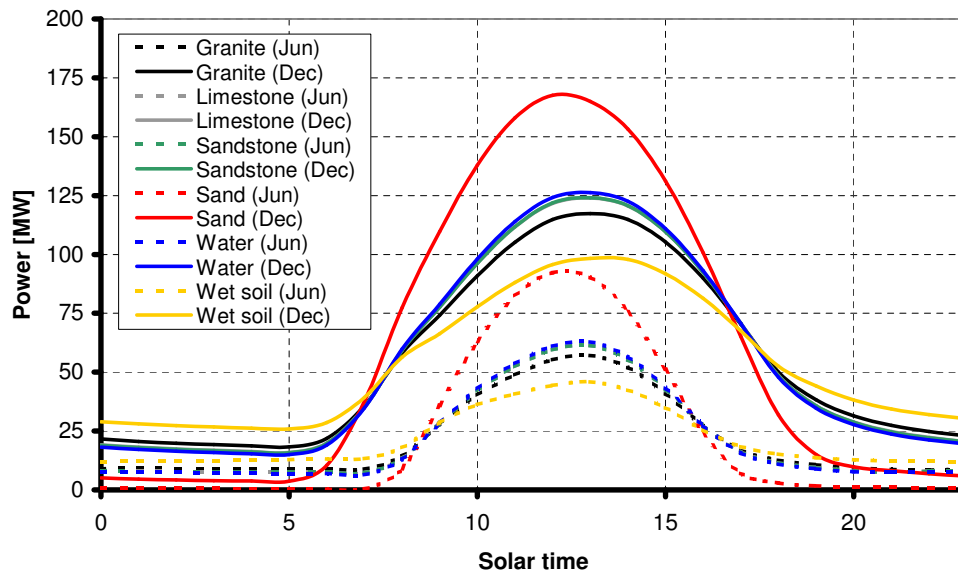


Figure 3.10: The influence of various ground types on the daily power output of a solar chimney power plant

Closer inspection of figure 3.10 reveals that the curves for Limestone and Sandstone are indistinguishable, both for June and December. Thus there is no marked difference between the power outputs of a plant employing Limestone versus a plant employing Sandstone as its soil type. It is also interesting to note that, despite the fact that the properties of water (waterlogged ground) differ significantly from that of Limestone and Sandstone, the daily power output profile produced by a plant incorporating water (waterlogged ground) is virtually similar to those of Limestone and Sandstone. This can be attributed to their comparable heat penetration coefficients, as previously mentioned.

Furthermore, the plants employing Limestone, Sandstone and water (waterlogged ground) indicate a lower power output during the night and greater power generation for most of the day, compared to the simulation model based on Granite.

The performance curves of a plant incorporating wet soil (waterlogged ground) show significantly greater power output during night-time and lower power output during daytime, compared to the other ground types. This is due to its large heat penetration coefficient, which provides wet soil (waterlogged ground) with a good capacity for storing energy. During the daytime, more of the solar radiation is stored in the soil, resulting in a decreased plant output. During night-time, the energy stored during the day is released, giving an increased nocturnal plant power production.

The power output profile of a plant employing Sand exhibits a very low output during night-time, with a much higher peak output than the other ground types during daytime. Once again the observed behavior may be attributed to the heat penetration coefficient of the employed ground type. The low thermal conductivity value of Sand causes very little energy to be conducted and eventually stored in the ground. Consequently, most of the solar radiation received during the day only heats the ground surface, giving high ground surface temperatures. In effect, higher ground surface temperatures mean more energy is available

to heat the collector air, which ultimately means a greater power output. However, because very little energy is stored in the ground during the day, very little power is produced at night.

An important adverse effect was discovered with the implementation of Sand as ground type in a solar chimney power plant. Figure 3.10 indicates a very low power output during a typical winter night. Closer inspection of the data revealed that a draught is only induced through the plant due to an ambient wind flowing across the chimney outlet. Therefore, no driving potential is generated during these times by the ground heating the collector air. An undesirable consequence of the observed behavior is that the solar chimney power plant may stall if no significant ambient winds are present.

Table 3.10: Annual power output comparison for a solar chimney power plant employing various ground types

Plant configuration	Annual power output [GWh]
Sandstone	336
Granite	334
Limestone	336.8
Sand	360.7
Wet soil	329.8
Water	337

Annually, table 3.10 confirms the comparable results of plants employing Limestone, Sandstone and water (waterlogged ground). Compared to the Sandstone-based reference solar chimney power plant, the plants employing Limestone and water (waterlogged ground) exhibit respective increases in annual power output of approximately 0.2 % and 0.3 %. The models employing Granite and wet soil (waterlogged ground) show respective annual output reductions of approximately 0.6 % and 1.8 % when compared to the reference plant. A plant employing Sand as ground type exhibits a 7.4 % increase in annual power output in comparison with a plant employing Sandstone. Even though the Sand-based plant does not generate much power at night, the enhanced output during the daytime produces a greater net annual output.

Bernardes *et al.* (2003) evaluate the influence of varying the ground heat penetration coefficient from $1000 \text{ W s}^{1/2}/\text{Km}^2$ to $2000 \text{ W s}^{1/2}/\text{Km}^2$ on solar chimney power plant performance, showing negligible influence on power output. This section seems to confirm these results, when considering the comparable annual power outputs predicted for the plants employing ground types with heat penetration coefficients from $1675 \text{ W s}^{1/2}/\text{Km}^2$ (Sandstone) to $1935 \text{ W s}^{1/2}/\text{Km}^2$ (Granite). However, the current results also predict that varying the heat penetration coefficient to lower values (e.g. $572 \text{ W s}^{1/2}/\text{Km}^2$ for Sand) will significantly influence plant performance.

3.10 Ground surface roughness

The most suitable locations for the construction of a solar chimney power plant are hot and dry desert-type areas. Therefore, it is safe to assume that the terrain under the collector roof of such a plant will probably be rough and rocky, smooth and sandy or a combination of both. Previous studies (Hedderwick (2001), Kröger and Buys (2001), Bernardes *et al.* (2003) and Pretorius *et al.* (2004)) assumed a conservative value of $\varepsilon_g = 0.05 \text{ m}$ for the ground surface roughness at the solar chimney power plant site.

Kröger (2004) lists some roughness lengths for various types of vegetation and natural surfaces. Table 3.11 gives an extract of the most relevant values by Kröger (2004).

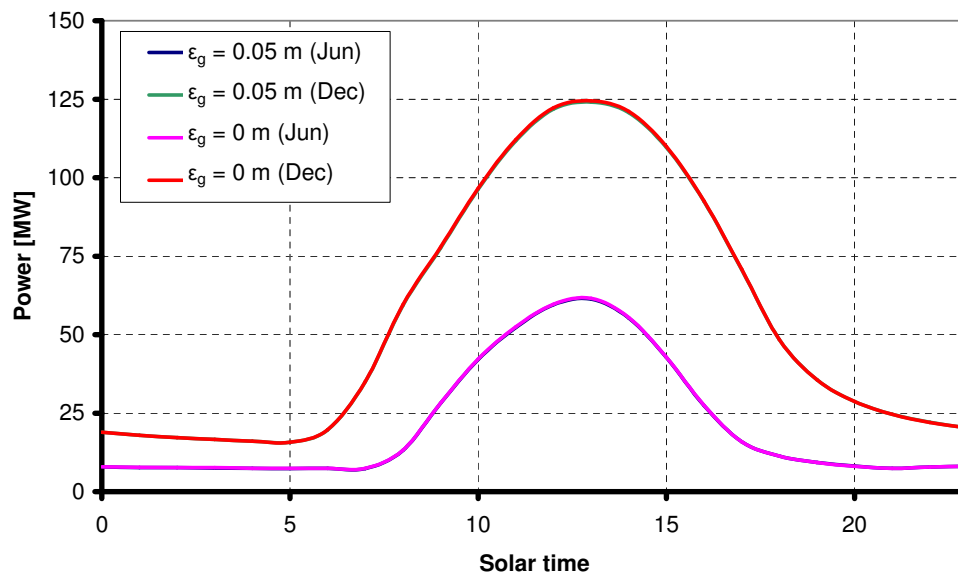
Table 3.11: Extract of some natural surface roughness lengths by Kröger (2004)

Surface Configuration	Roughness [m]
Uncut grass	0.07
Crop stubble	0.02
Short grass	0.002
Bare sand	0.0004

The following section evaluates the influence of ground surface roughness on solar chimney power plant performance.

3.10.1 Simulation and results

Comparative simulations were performed for the reference solar chimney power plant, with one model employing a rough ground surface ($\varepsilon_g = 0.05$ m) while the other assumed the ground surface to be smooth ($\varepsilon_g = 0$ m).

**Figure 3.11:** Effect of ground surface roughness on daily plant power output**Table 3.12:** Annual power output comparison, illustrating the effect of ground surface roughness on plant performance

Plant configuration	Annual power output [GWh]
Rough ground surface ($\varepsilon_g = 0.05$ m)	336
Smooth ground surface ($\varepsilon_g = 0$ m)	336.7

When considering figure 3.11 (showing electrical plant outputs for 21 June and 21 December) it is evident that the effect of ground roughness on solar chimney power output is virtually negligible. Table 3.12 confirms this fact, showing that a plant with a smooth ground surface only produces 0.2 % more power per annum than a plant with a rough ground

surface. This small increase in output can be attributed to the fact that the collector air in the plant employing the smooth ground surface experiences less frictional losses as it flows over the ground surface.

It is however assumed that the actual ground surface under the collector of the solar chimney power plant will have a certain roughness. Therefore, as it has been shown that the effect of ground roughness is very small, a conservative roughness length of $\epsilon_g = 0.05$ m is still incorporated in the reference plant specifications.

3.11 Ground absorptivity

Previous studies by Hedderwick (2001), Kröger and Buys (2001) and Pretorius *et al.* (2004) employ a ground absorptivity value of $\alpha_g = 0.9$. All of these assume that the ground will be treated and acts as a gray and diffuse surface.

The current study supports a (treated) ground absorptivity value of $\alpha_g = 0.9$ as a reasonable approximation, thus employing such a value in the reference plant specification of section 2.1. Once again a gray and diffuse ground surface is assumed. Therefore, the ground absorptivity value is assumed to be independent of the direction of incident radiation as well as equal to the ground emissivity value (only for the reference case).

This section investigates the effect of different ground absorptivity values on the power output of the reference solar chimney power plant. It must be noted that the ground emissivity value is kept constant at $\epsilon_g = 0.9$ for all simulations.

3.11.1 Simulation and results

Comparative simulations were performed for the reference solar chimney power plant, using varying ground absorptivity values of $\alpha_g = 0.8$, $\alpha_g = 0.9$ and $\alpha_g = 1$.

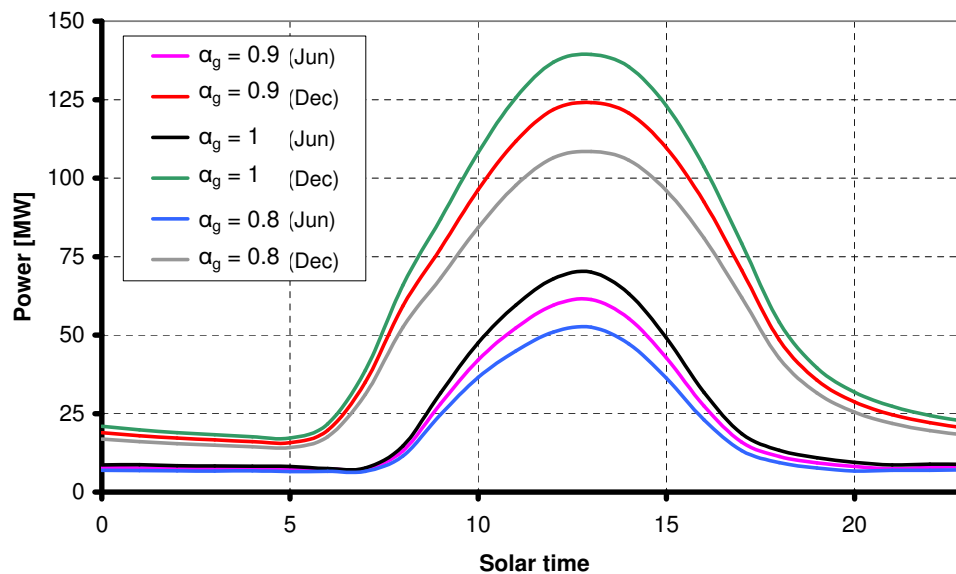


Figure 3.12: Effect of ground absorptivity on plant performance

From figure 3.12 it is clear that the ground absorptivity value has a major effect on the daily solar chimney power plant performance. It is evident that a higher ground absorptivity value causes a greater peak power output. With a greater absorptivity value, more energy is absorbed by the ground surface. This means that more energy is made available at the

ground surface which can be transferred to the collector air, thereby giving greater power production. Furthermore, as more energy is absorbed by the ground, more energy is stored deeper in the ground and released at night.

Table 3.13: Annual power output comparison, showing the influence of ground absorptivity on plant performance

Plant configuration	Annual power output [GWh]
Intermediate absorptivity ($\alpha_g = 0.9$)	336
Low absorptivity ($\alpha_g = 0.8$)	293.5
High absorptivity ($\alpha_g = 1$)	377.4

Table 3.13 substantiates the significant effect of ground absorptivity on plant performance, indicating a 12.6 % reduction and 12.3 % increase in annual power output (compared to the reference case with $\alpha_g = 0.9$) when employing respective ground absorptivity values of $\alpha_g = 0.8$ and $\alpha_g = 1$.

3.12 Ground emissivity

Previous studies by Hedderwick (2001), Kröger and Buys (2001) and Pretorius *et al.* (2004) employ a ground emissivity value of $\epsilon_g = 0.9$. All of these assume that the ground will be treated and acts as a gray and diffuse surface.

As mentioned in the previous section, the current study supports a (treated) ground emissivity value of $\epsilon_g = 0.9$ as a reasonable approximation, thus employing such a value in the reference plant specification of section 2.1. Once again a gray and diffuse ground surface is assumed. Therefore, the ground absorptivity is assumed equal to the ground emissivity value (only for the reference case).

This section investigates the effect that ground surface emissivity has on solar chimney power plant performance.

3.12.1 Simulation and results

Comparative simulations were performed for the reference solar chimney power plant, using varying ground emissivity values of $\epsilon_g = 0.9$, $\epsilon_g = 0.5$ and $\epsilon_g = 0.1$. It must be noted that the ground absorptivity value is kept constant at $\alpha_g = 0.9$.

Figure 3.13 illustrates the substantial effect that the ground emissivity value has on the daily power output of the solar chimney power plant. It is evident that a lower ground emissivity value enables the plant to consistently produce more power throughout a 24-hour period.

The significant increase in power output can be attributed to reduced radiation losses from the ground to the environment via the collector roof. With a low ground emissivity value incorporated, the ground surface radiates less energy to the roof and in turn the roof radiates less energy to the environment. With more energy available at the ground surface, more energy is transferred by convection to the collector air, giving an increased draught and ultimately greater power output.

Note that a lower ground emissivity value produces higher collector air temperatures and lower collector roof temperatures. Therefore, convection heat transfer losses from the collector air to the roof will be higher. However, even with these higher convection losses the net effect of a lower ground emissivity value is still increased power output due to the reduced radiation losses.

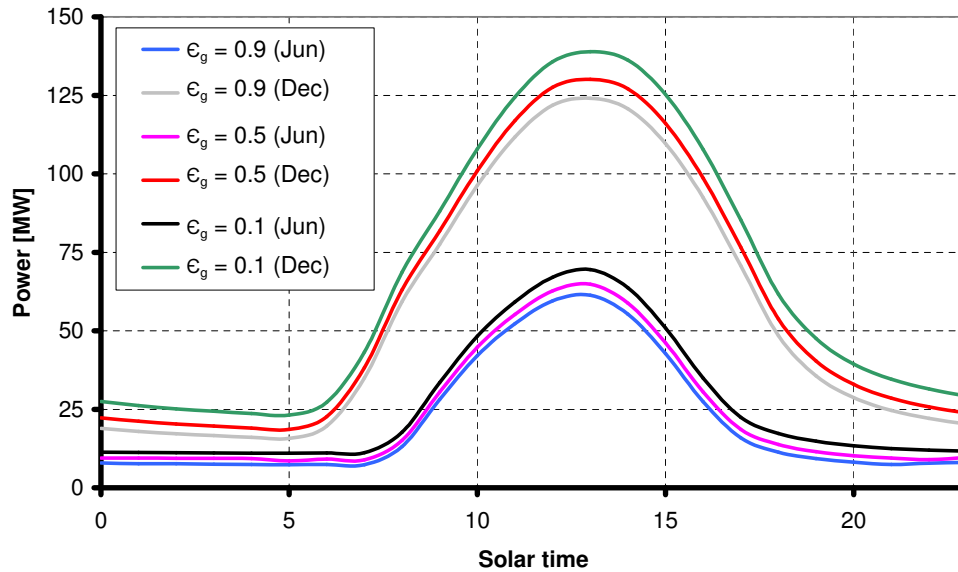


Figure 3.13: Effect of ground emissivity on plant performance

Table 3.14: Annual power output comparison, showing the influence of ground emissivity on plant performance

Plant configuration	Annual power output [GWh]
High emissivity ($\epsilon_g = 0.9$)	336
Intermediate emissivity ($\epsilon_g = 0.5$)	364.8
Low emissivity ($\epsilon_g = 0.1$)	408.1

Table 3.14 substantiates the significant effect of ground emissivity on plant performance, indicating respective increased annual power outputs of 8.6 % and 21.5 % when implementing ground emissivity values of $\epsilon_g = 0.5$ and $\epsilon_g = 0.1$, compared to a plant employing an emissivity value of $\epsilon_g = 0.9$.

Despite the results presented above, a ground surface with emissivity of $\epsilon_g = 0.9$ is employed in the reference plant specifications. If at all possible, it will be costly to achieve ground surface emissivity values between 0.5 and 0.1 with a surface treatment and the increase in plant cost due to these treatments will be significant. Future research to investigate the possibility of achieving such low emissivity values as well as a specific cost / benefit investigation for an individual plant design is required to validate the technical and economic viability of these surface treatments, a topic not covered in this study.

3.13 Turbine inlet loss coefficient

The collector air flowing into the turbine at the base of the chimney experiences a pressure drop. This pressure drop is based on a turbine inlet loss coefficient, $K_{turb,i}$. The previously used turbine inlet loss coefficient of 0.25, employed by Hedderwick (2001), Kröger and Buys (2001) and Pretorius *et al.* (2004) was originally selected as a conservative first approximation value. After consulting Von Backström *et al.* (2003b) and Von Backström (2004-2006) personally, it was decided to introduce a more realistic value of $K_{turb,i} = 0.14$ into the reference plant specifications. Recent work by Kirstein *et al.* (2005) indicates that

the turbine inlet loss coefficient may even be lower than 0.1 for certain plant configurations and inlet guide vane (IGV) stagger angles.

This section evaluates the influence of the turbine inlet loss coefficient on solar chimney power plant performance.

3.13.1 Simulation and results

Comparative simulations were performed using the reference solar chimney power plant, with one model including the higher turbine inlet loss coefficient ($K_{turb,i} = 0.25$) while the other incorporates the more realistic coefficient value of $K_{turb,i} = 0.14$.

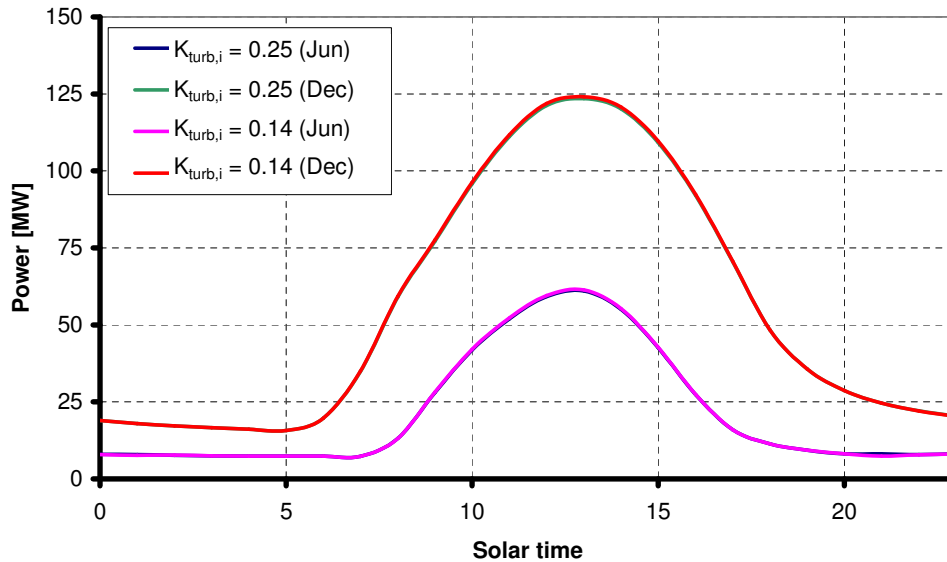


Figure 3.14: Effect of turbine inlet loss coefficient on daily plant power output

Figure 3.14 compares the electrical plant power generated throughout a 24-hour period on 21 June and 21 December, while table 3.15 presents an annual power output comparison.

Table 3.15: Annual power output comparison, showing the influence of the turbine inlet loss coefficient on plant performance

Plant configuration	Annual power output [GWh]
Low loss coefficient ($K_{turb,i} = 0.14$)	336
High loss coefficient ($K_{turb,i} = 0.25$)	334.8

Figure 3.14 indicates no major difference in plant power production following the introduction of the higher turbine inlet loss coefficient. Table 3.15 however, shows a slightly reduced annual power output. It follows that the inclusion of the larger turbine inlet loss coefficient is responsible for a 0.4 % reduction in annual plant power production.

3.14 Bracing wheel pressure loss coefficient

The chimney structure of the solar chimney power plant is reinforced internally using evenly spaced spoked bracing wheels. These bracing wheels exert a drag force on the buoyant air flowing upward through the chimney.

Von Backström *et al.* (2003a) state that a very conservative value for the bracing wheel pressure loss coefficient (for the whole supporting structure, based on a chimney with 10 bracing wheels) will be in the order of $K_{bw} = 0.1$, based on their experimental results. Studies by Hedderwick (2001), Kröger and Buys (2001) and Pretorius *et al.* (2004) all select a similar pressure loss coefficient of $K_{bw} = 0.1$ for the internal supporting chimney structure.

It should be noted that the calculations by all of the above-mentioned authors pertain to a reference chimney with a height of 1500 m and 160 m inside diameter.

Even though the chimney dimensions of the reference plant used in this study differs significantly from the above-mentioned dimensions, a similar bracing wheel pressure loss coefficient is assumed for this dissertation ($K_{bw} = 0.1$ for the whole structure, thus $K_{bw} = 0.01$ for each of the 10 bracing wheels, as noted in section 2.1).

This section investigates the effect of the bracing wheel pressure loss coefficient on the performance of the reference solar chimney power plant.

3.14.1 Simulation and results

Comparative simulations were performed for the reference solar chimney power plant, using varying bracing wheel pressure loss coefficient values (based on one bracing wheel) of $K_{bw} = 0.00$, $K_{bw} = 0.01$ and $K_{bw} = 0.02$.

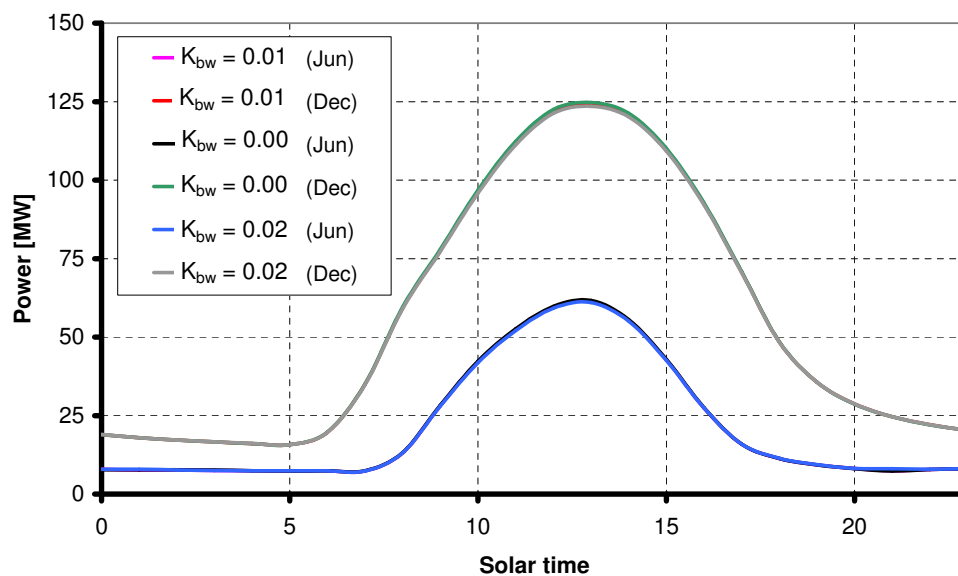


Figure 3.15: Effect of bracing wheel pressure loss coefficient on plant performance

Figure 3.15 indicates the insignificant effect of the bracing wheel pressure loss coefficient on daily plant power output, with the various curves being almost indistinguishable.

Table 3.16 substantiates the minor effect of the bracing wheel loss coefficient, indicating only a 0.3 % increase and 0.3 % reduction in annual power output (compared to the reference case using $K_{bw} = 0.01$) when employing respective bracing wheel pressure loss coefficient values of $K_{bw} = 0.00$ and $K_{bw} = 0.02$.

Table 3.16: The influence of the bracing wheel pressure loss coefficient on annual solar chimney power plant output (values displayed based on one bracing wheel)

Plant configuration	Annual power output [GWh]
Intermediate loss coefficient ($K_{bw} = 0.01$)	336
Low loss coefficient ($K_{bw} = 0.00$)	337
High loss coefficient ($K_{bw} = 0.02$)	334.9

These small power reductions are due to the higher air-flow drag losses experienced as the buoyant air in the chimney flows across the supporting bracing wheel structures.

3.15 Ambient pressure

Previous studies by Hedderwick (2001), Kröger and Buys (2001) and Pretorius *et al.* (2004) (all specifying the same reference location as the current study) as well as the current one employ an ambient pressure at ground level of $p_a = 90000 \text{ N/m}^2$, which is the approximate ground level pressure at the specified reference location.

Even though the ambient pressure employed in the numerical model depends on the specific reference location chosen, this section evaluates the role of ambient pressure on plant performance by decoupling it from the particular location.

3.15.1 Simulation and results

Comparative computer simulations were performed for the reference solar chimney power plant, using varying ambient pressures at ground level of $p_a = 80000 \text{ N/m}^2$, $p_a = 90000 \text{ N/m}^2$ and $p_a = 100000 \text{ N/m}^2$. It should be noted that, except for the varying ambient pressures, all of the above-mentioned simulations employ the meteorological conditions given in Appendix H.

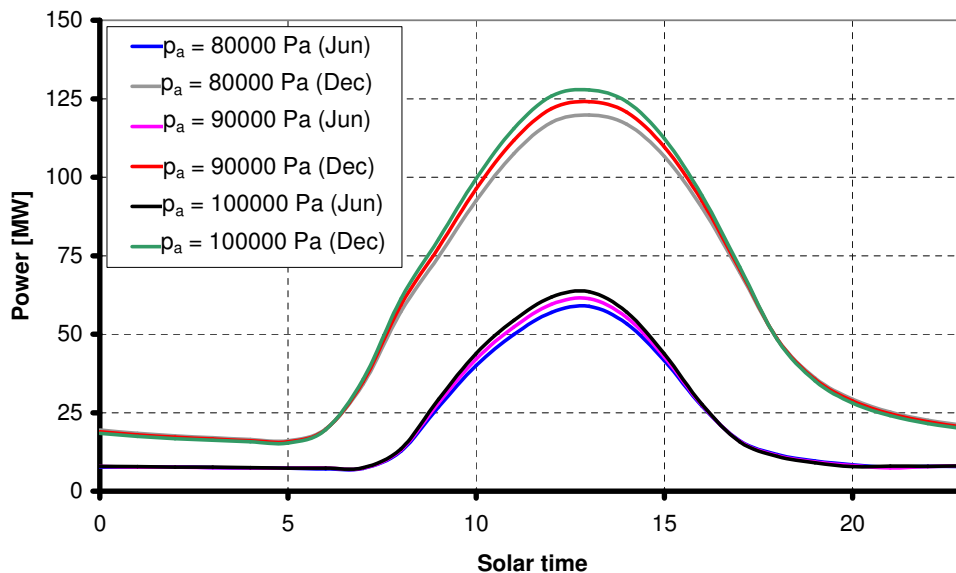
**Figure 3.16:** Effect of ambient pressure on plant performance

Table 3.17: The influence of ambient pressure on annual solar chimney power plant output

Plant configuration	Annual power output [GWh]
Intermediate pressure ($p_a = 90000 \text{ N/m}^2$)	336
Low pressure ($p_a = 80000 \text{ N/m}^2$)	328.2
High pressure ($p_a = 100000 \text{ N/m}^2$)	342.7

From figure 3.16 it is clear that a greater ambient pressure causes a slightly enhanced peak power output during the daytime operation of the solar chimney power plant.

When regarding table 3.17, we see that the differing peak outputs amount to a reduction of 2.3 % and an increase of 2 % in annual power output (compared to the reference case using $p_a = 90000 \text{ N/m}^2$) when employing respective ambient pressures of $p_a = 80000 \text{ N/m}^2$ and $p_a = 100000 \text{ N/m}^2$.

The following gives an explanation for the observed results, but first a brief background has to be given. The driving potential that causes air to flow through the solar chimney power plant is due to a pressure difference between a column of cold air outside and a column of hot air inside the chimney of the plant. When assuming a dry adiabatic lapse rate (DALR) outside and inside of the chimney, the following relation can be derived for the driving potential of the plant (Pretorius, 2004)

$$\Delta p = p_1 \left[1 - \left[\frac{\left(1 - 0.00975 \frac{H_c}{T_1}\right)}{\left(1 - 0.00975 \frac{H_c}{T_5}\right)} \right]^{3.5} \right] \quad (3.2)$$

where H_c is the chimney height and the numbered subscripts refer to the positions in figure 2.1.

From equation (3.2) it is evident that the greater the temperature rise in the collector, the greater the driving force or potential becomes. Consequently, during midday the temperature rise in the collector is at its greatest, which brings about the maximum daily driving potential and maximum daily power output. In addition, an increase in ambient pressure will also effect an increase in the driving potential.

The results illustrated in figure 3.16 can therefore be clarified as follows. An increased ambient pressure increases the plant's driving force (and ultimately power output). Additionally, this effect becomes more pronounced as the temperature rise in the collector increases, with the ambient pressure acting as a "multiplying factor" to the driving force caused by the particular temperature differential.

Kröger and Blaine (1999) also evaluated the effects of ambient pressure on the driving potential of a large solar chimney power plant. They find an increase of 11 % in plant driving potential when employing an ambient pressure of $p_a = 100000 \text{ N/m}^2$, compared to the driving potential of a plant employing $p_a = 90000 \text{ N/m}^2$. This would suggest that the plant power output would also be approximately 11 % higher, which does not concur with the predicted 2 % increase as presented above.

The reason for the seeming discrepancy between the results of Kröger and Blaine (1999) and the results presented here is as follows. The results of Kröger and Blaine (1999) are based on a constant temperature differential across the collector. The current numerical model however does not specify a constant temperature differential, but rather calculates the temperature rise in the collector based on the given ambient conditions and air-flow through the plant. When employing a higher ambient pressure, the density of the air increases. This produces a greater mass-flow through the plant, thereby increasing the heat transfer rate from the ground, but also increasing the heat transfer rate from the collector air to the collector roof. Effectively, this causes a slightly decreased temperature differential

across the collector and a lower driving potential (and ultimately power output) increase than the expected 11 %.

3.16 Ambient temperature lapse rate

Previous studies by Hedderwick (2001), Kröger and Buys (2001) and Pretorius *et al.* (2004) as well as the current one employ a dry adiabatic lapse rate (DALR) to describe the temperature and pressure gradients in the atmosphere surrounding the solar chimney power plant.

This section investigates the effect on plant performance of employing a lapse rate with temperature gradient equal to that of the International Standard Atmosphere (ISA) as atmospheric model for the environment surrounding the solar chimney power plant. Note that this section does not employ the standard (constant) ISA for temperate latitudes, but merely a time-dependent lapse rate with a temperature gradient equal to that of the ISA. All mention to "ISA" in this section also refers to this particular ambient lapse rate.

It should be noted that all simulations assume a dry adiabatic lapse rate inside the chimney of the plant.

3.16.1 Simulation and results

Comparative computer simulations were conducted for the reference solar chimney power plant, with one model employing a DALR for the atmosphere surrounding the plant, while the other model employed an ISA lapse rate.

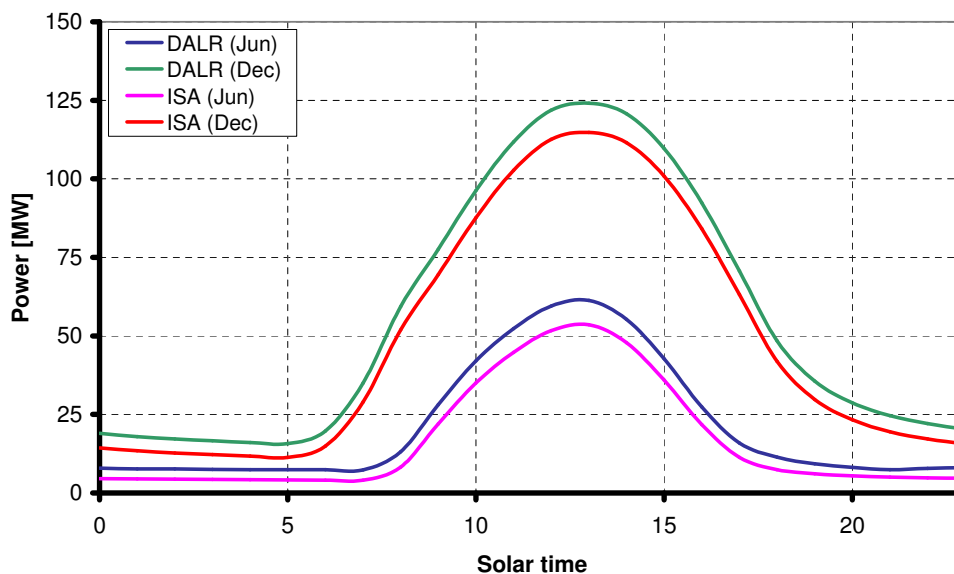


Figure 3.17: Effect of ambient lapse rate on solar chimney plant performance

From figure 3.17 it is clear that the plant simulation model employing the ISA lapse rate performs consistently worse throughout a typical day in winter or summer than the model incorporating the DALR. Table 3.18 also predicts a much lower annual power output (14.4 %) for the plant using the ISA lapse rate versus the plant using a DALR.

The much lower annual power output produced by the plant employing the ISA lapse rate can be explained as follows. The DALR predicts a greater negative temperature gradient in the atmosphere than the ISA lapse rate. Therefore, the atmospheric air temperature

Table 3.18: Effect of the ambient lapse rate on the annual power output of the reference solar chimney power plant

Plant configuration	Annual power output [GWh]
Dry adiabatic lapse rate (DALR)	336
International standard atmosphere (ISA) gradient	287.5

predicted over the height of the chimney will consistently be somewhat higher when using an ISA lapse rate assumption than when assuming a DALR. The higher temperatures predicted by the ISA lapse rate subsequently predicts less dense atmospheric air outside the chimney, resulting in a smaller pressure difference between the air inside the chimney and the atmospheric air outside it.

This pressure difference acts as the driving potential of the plant. Analogous to equation (3.2), when assuming an ISA lapse rate outside and a DALR inside the chimney of the plant, the following relation can be derived for the driving potential of the plant

$$\Delta p = p_1 \left[1 - \frac{\left(1 - 0.0065 \frac{H_c}{T_1}\right)^{5.255}}{\left(1 - 0.00975 \frac{H_c}{T_5}\right)^{3.5}} \right] \quad (3.3)$$

Thus when employing an ISA lapse rate the solar chimney power plant experiences a consistently smaller driving potential than when employing a DALR, which ultimately results in a lower power output.

Kröger and Blaine (1999) also used equation (3.3) to evaluate the influence on solar chimney driving potential of employing an atmospheric temperature gradient equal to that of the ISA outside and DALR inside the chimney of the plant. Compared to using a DALR inside and outside the chimney, they obtain an 11.5 % reduction in driving potential. A publication by Von Backström *et al.* (2003b) confirms this result.

Note that the driving potential defined by equation (3.3) is dependent on the specific chimney height and collector temperature differential and that the result of Kröger and Blaine (1999) is based on a chimney height of $H_c = 1500$ m and a constant collector temperature differential of 20 °C. Therefore, the significant reduction (14.4 %) in annual plant power output presented in this section confirms the results of Kröger and Blaine (1999) and Von Backström *et al.* (2003b) but cannot be directly compared, as the current study employs a chimney height of $H_c = 1000$ m and a collector temperature differential that varies throughout the day and year.

In order to determine the actual ambient lapse rate, experimental temperature measurements need to be taken at various heights above ground level at the proposed solar chimney power plant site. It should be noted that the effects of possible nocturnal temperature inversions were neglected in the above analysis.

Chapter

4

Thermo-Economic Plant Optimization

Many different solar chimney power plant dimensions have been suggested in the available literature. However, no study has ever attempted to find a "thermo-economically optimized" dimensional configuration.

It is a fact that no physical optimum solar chimney power plant exists (as mentioned by Schlaich (1994)) when only considering the dimensions of the plant. This means that the larger the plant dimensions are, the more power it will produce. However, if construction costs are introduced and compared to annual plant power output, it is possible to determine an "optimal" solar chimney power plant configuration.

This chapter determines thermo-economically optimal solar chimney power plant configurations, where such optima are defined as those plants which present the minimum plant cost per annual power output unit. Initially, relevant dimensions are selected which are to be optimized. An approximate plant cost model is then developed, giving the capacity for finding optimum plant dimensions for different cost structures. Multiple simulations are performed and results are compared to the approximated cost of each specific plant. All simulations are repeated for a number of years to allow ground energy fluxes to reach a quasi-steady state.

4.1 Selecting dimensions for optimization

As a multitude of variables constitute the specification of a solar chimney power plant, it would require a major task to optimize for all of the independent variables. Each set of specification values requires a single computer simulation to be run, which takes several hours to complete. Therefore it was decided to select only the most prominent plant dimensions and optimize for them.

4.1.1 Selected dimensions, limits and intervals

The most relevant solar chimney power plant dimensions were selected and are presented in table 4.1. The goal was to keep the number of dimensions as few as possible in order to minimize the number of simulations to be run. In addition, the intervals were selected to be as large as possible to minimize the number of simulations, but small enough to give a reasonable degree of accuracy in finding the optimum plant.

It was decided to optimize for a 500 m, 1000 m and 1500 m high chimney, while not limiting the other dimensions.

Table 4.1: Selected solar chimney plant dimensions for optimization

Dimension	Dimensional limits [m]	Interval [m]
Chimney height (H_c)	500-1500	500
Chimney diameter (d_c)	unlimited	10
Collector diameter (d_{coll})	unlimited	1000
Collector inlet height (H_2)	unlimited	1

4.2 Approximate cost model

In order to determine optimal plant dimensions, it was decided to introduce the following approximate solar chimney power plant cost model. The purpose of the model is not to ascertain an accurate plant cost, but to give a first approximation for comparing plant dimensions in terms of cost.

4.2.1 Assumptions

All costs are defined in terms of a currency unit C . The idea behind this assumption is to keep the plant cost independent of a specific currency. The specific cost (C_{sc}) of the chimney (materials and construction) is defined as one C per cubic meter volume of the chimney ($C_{sc} = 1 C/m^3$). The cost model can approximate the cost of a solar chimney power plant in any international currency by substituting any true cost for C_{sc} .

It is assumed that the average chimney thickness is one millimeter for every one meter that it is tall (based on design calculations by Van Dyk (2004-2006)). Thus the total chimney cost is simply determined as the volume of the chimney multiplied by the specific chimney cost:

$$C_c = 0.001 \pi d_c H_c^2 C_{sc} \quad (4.1)$$

Furthermore, it is assumed that the base cost of the collector per square meter will be $(pt)_{coll}$ % of the cost of C_{sc} plus an additional $(pt)_H$ % for every one meter height at the collector inlet (as the roof shape exponent is constant at $b = 1$, all roofs will have the same shape). The total collector cost is therefore given by:

$$C_r = \frac{\pi}{4} d_r^2 (0.01 (pt)_{coll} C_{sc}) (1 + 0.01 (pt)_H H_2) \quad (4.2)$$

It is assumed that additional costs including the turbo-generator equal 10 % of the total collector and chimney cost. Therefore, the total solar chimney power plant cost is given by:

$$C_{tot} = 1.1(C_c + C_r) \quad (4.3)$$

4.2.2 Selected values for optimization

In order to optimize the solar chimney power plant for various plant cost structures, it was decided to select certain varying parameters in the cost model. Analogous to the selection of the plant dimensions to optimize, these varying parameters were kept to a minimum. The varying parameters of the cost model which were selected and their various values are listed in table 4.2.

4.3 Simulation and results

Multiple computer simulations were conducted based on the reference solar chimney power plant configuration (as listed in section 2.1 of Chapter 2), however incorporating each of

Table 4.2: Varying cost parameters

Cost parameter	Symbol	Values for parameter [%]
Collector cost per sqm as percentage of C_{sc}	$(pt)_{coll}$	2, 5, 8
Additional collector cost as percentage of H_2	$(pt)_H$	2, 5, 8

the possible dimensional combinations of table 4.1. All other plant specifications, equations, meteorological conditions, etc. that were utilized are those presented in Chapter 2 of this dissertation.

4.3.1 Approximate yield and specific cost curves

Figures 4.1, 4.2 and 4.3 present nomograms for ascertaining the approximate annual power output for any combination of the given plant dimensions. In addition, figures 4.4, 4.5 and 4.6 present corresponding nomograms for determining the approximate specific plant cost for any combination of the given dimensions and the specified cost parameters (presented in the order $(pt)_{coll}$ %, $(pt)_H$ %). The specific plant cost is calculated in terms of the currency unit (C) as C_{tot} /annual power output, with units C/GWh.

These curves present trend lines from the simulation results of the current numerical model and the calculations according to the approximate cost model, with all other specifications being those of the reference plant in section 2.1. The dimensional limits for each nomogram were chosen to include all the optimal plant configurations for each specific chimney height (see table 4.6).

Figures 4.1 to 4.6 are evaluated as follows. A specific collector diameter is selected from the horizontal axis at the bottom of the figure. By drawing a line upwards from the horizontal collector diameter axis, one may select a specific chimney diameter where the line intersects one of the given curves. From this point of intersection, when drawing a line to the left-hand-side of the figure, one may select a particular collector inlet height where the line intersects one of the curves. Then, when drawing a line upwards from this intersection point, either the approximate annual power output or the approximate specific cost is determined (value read from vertical axis on left-hand-side of figure) at the intersection point with the annual power output or specific cost curves.

Note that the above-mentioned curves should be evaluated in conjunction with the tables in section 4.3.2.

4.3.2 Cold inflow

During the operation of natural draught cooling towers, a mass of slowly moving air flows upward through the tower. According to Kröger (2004) it is not unusual that, during times of very slow upward air velocities, these towers may experience the inflow of cold air into the top of the tower. Under these conditions, significant reductions in performance are observed.

Analogous to cooling towers, it is believed that cold inflow may also exist in the chimney of the solar chimney power plant, especially when air velocities through the plant are low. Therefore the analysis for predicting cold inflow in the solar chimney is approximated to be similar to the one employed for cooling towers.

According to Moore and Garde (1981), a cooling tower (and therefore the solar chimney) will experience cold inflow when $1/Fr > 2.8$, where the densimetric Froude number is represented by equation (2.31).

Tables 4.3, 4.4 and 4.5 present actual annual power output values as approximated by the curves of figures 4.1, 4.2 and 4.3. The values of tables 4.3, 4.4 and 4.5 in bold represent those plant configurations for which the numerical model predicts cold inflow. It is clear that

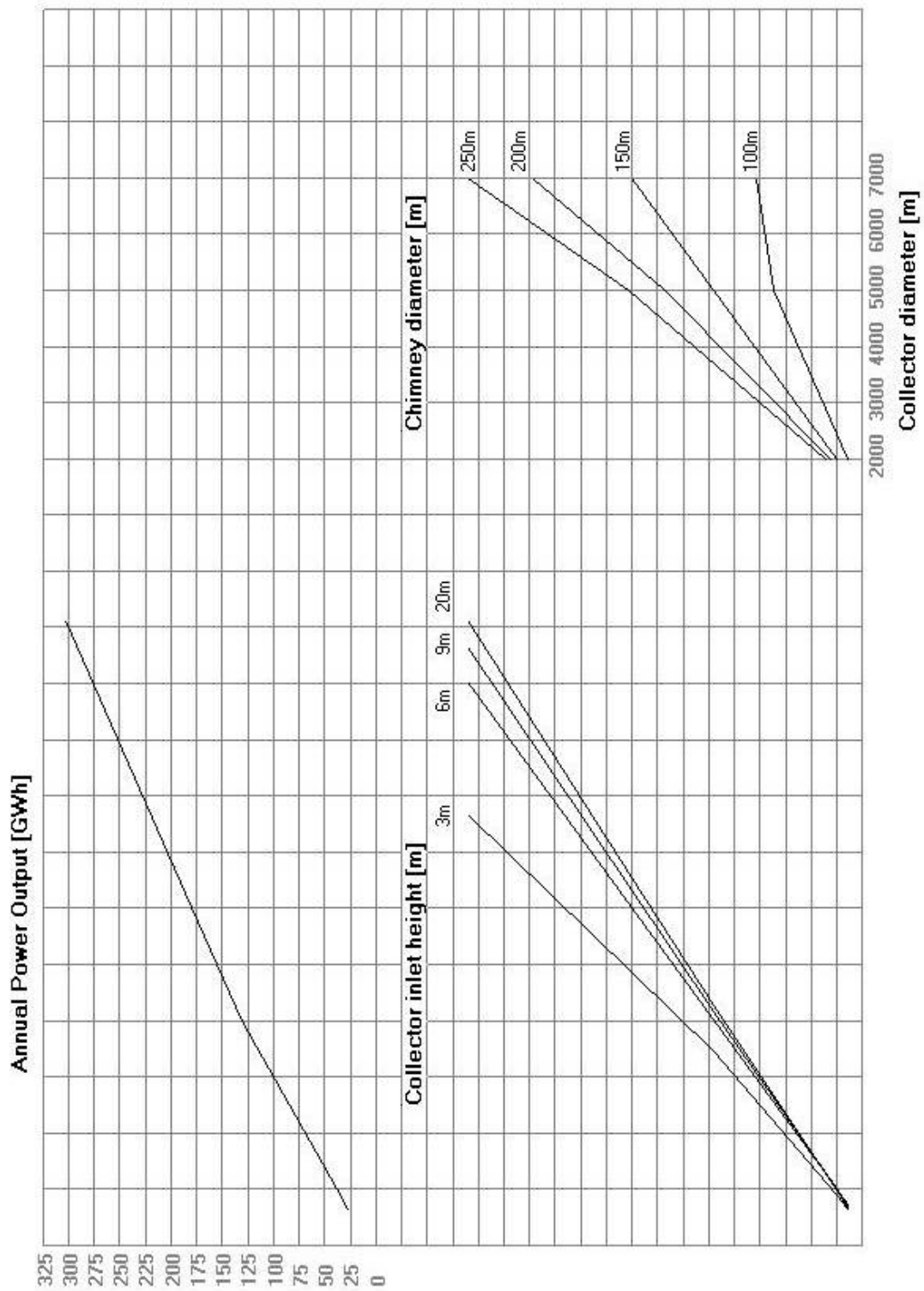


Figure 4.1: Approximate annual power output for various solar chimney power plant configurations, for plants with a chimney height of $H_c = 500$ m

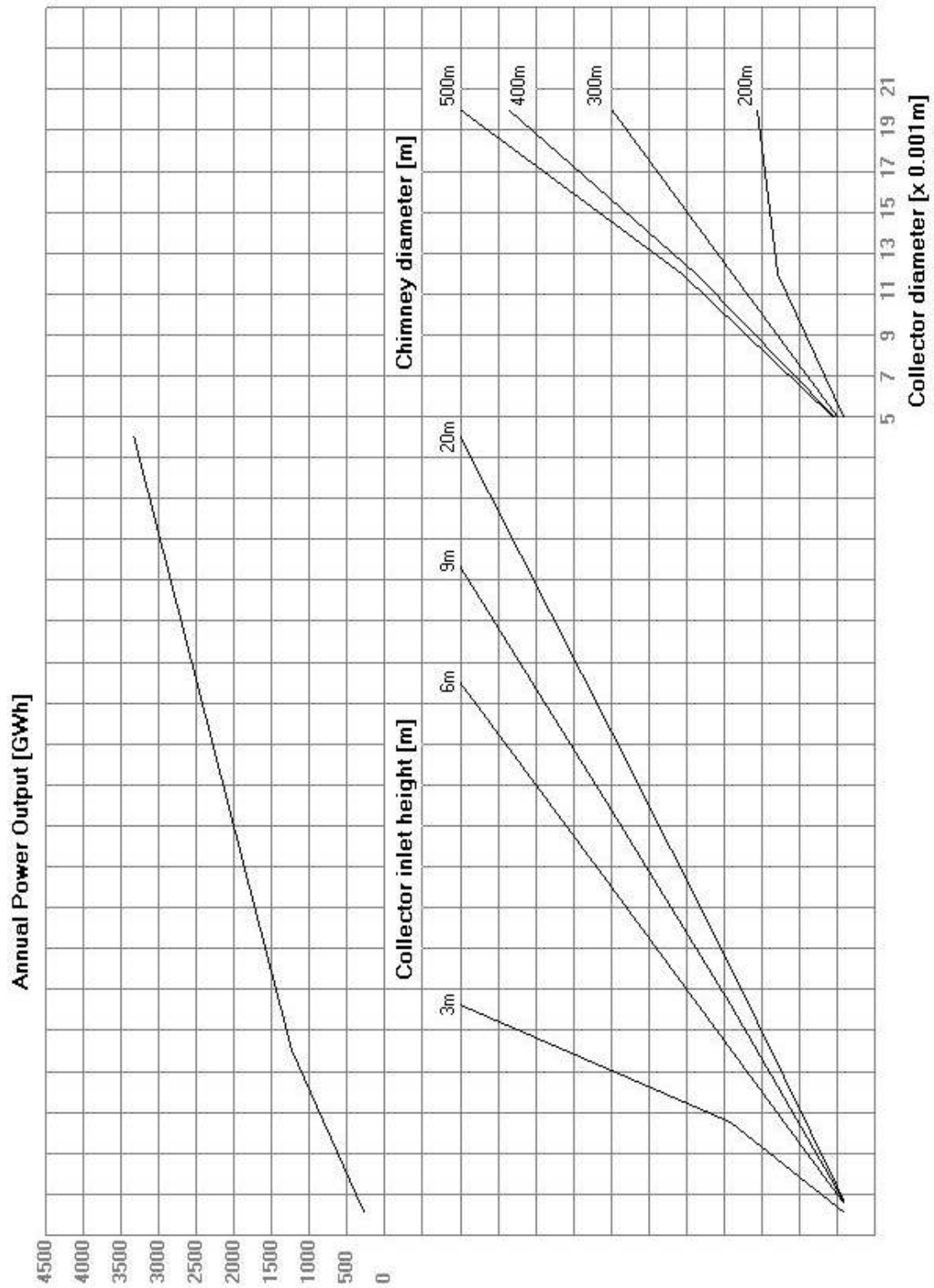


Figure 4.2: Approximate annual power output for various solar chimney power plant configurations, for plants with a chimney height of $H_c = 1000$ m

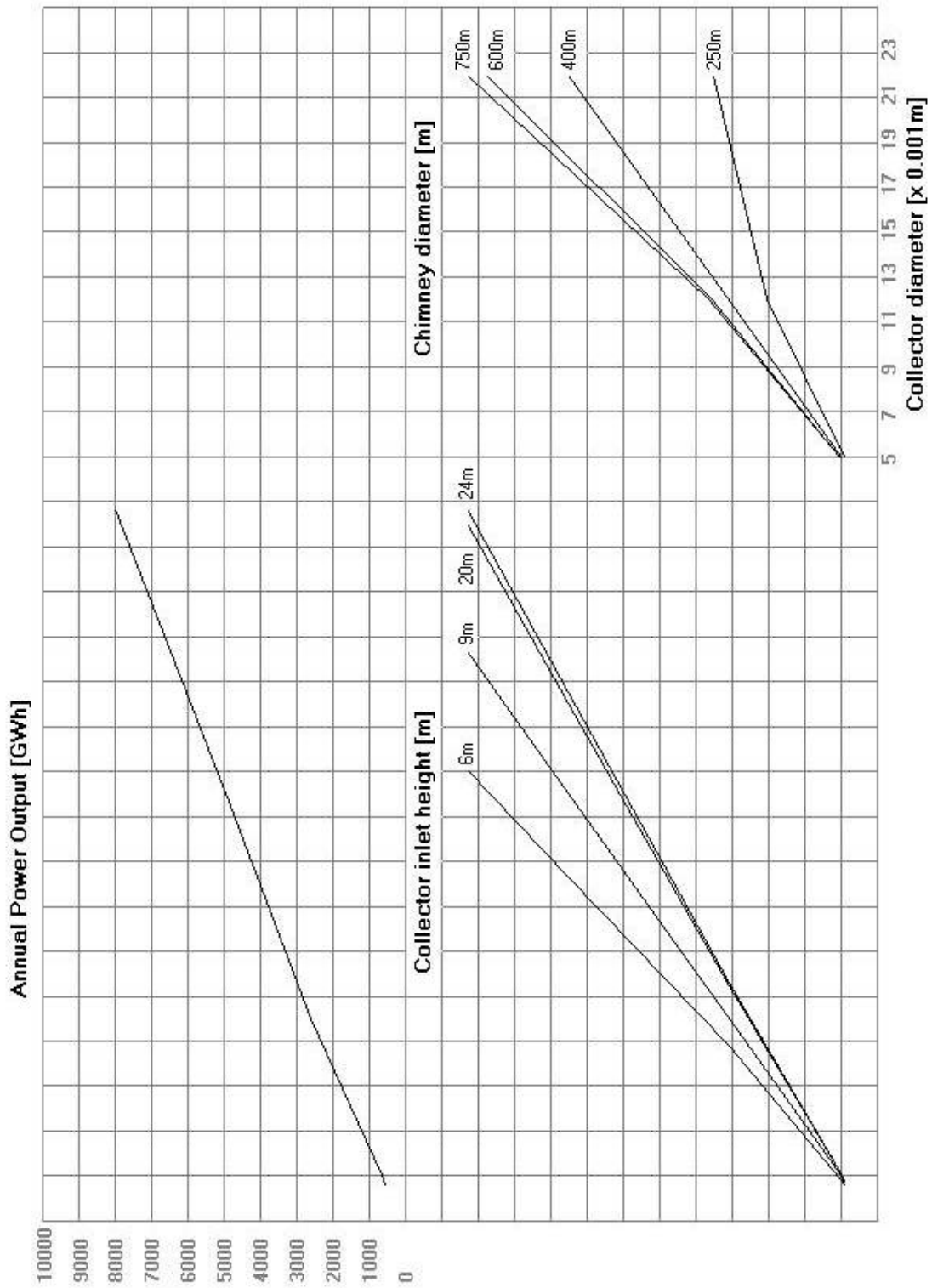


Figure 4.3: Approximate annual power output for various solar chimney power plant configurations, for plants with a chimney height of $H_c = 1500$ m

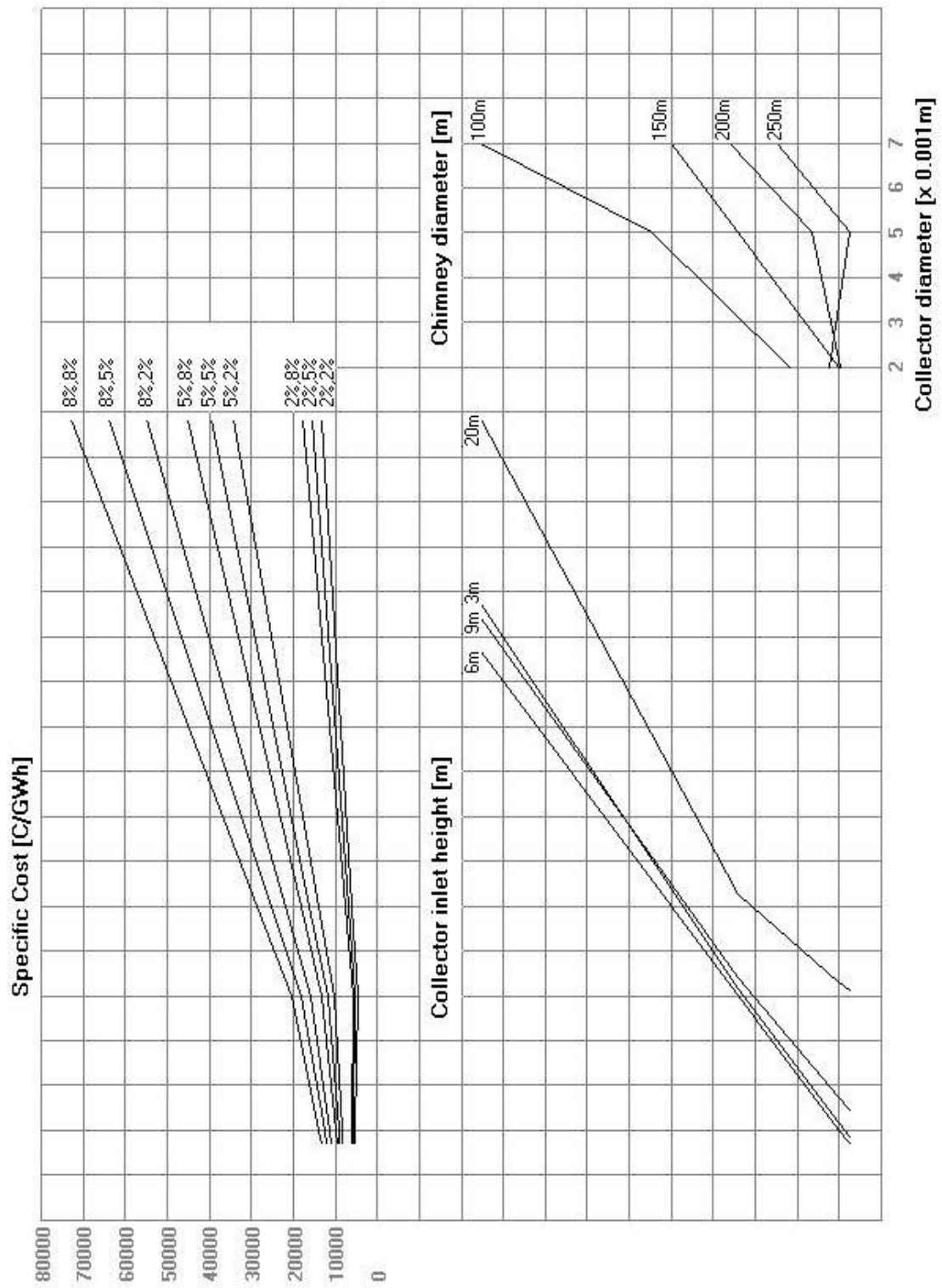


Figure 4.4: Approximate specific cost for various solar chimney power plant configurations, for plants with a chimney height of $H_c = 500$ m

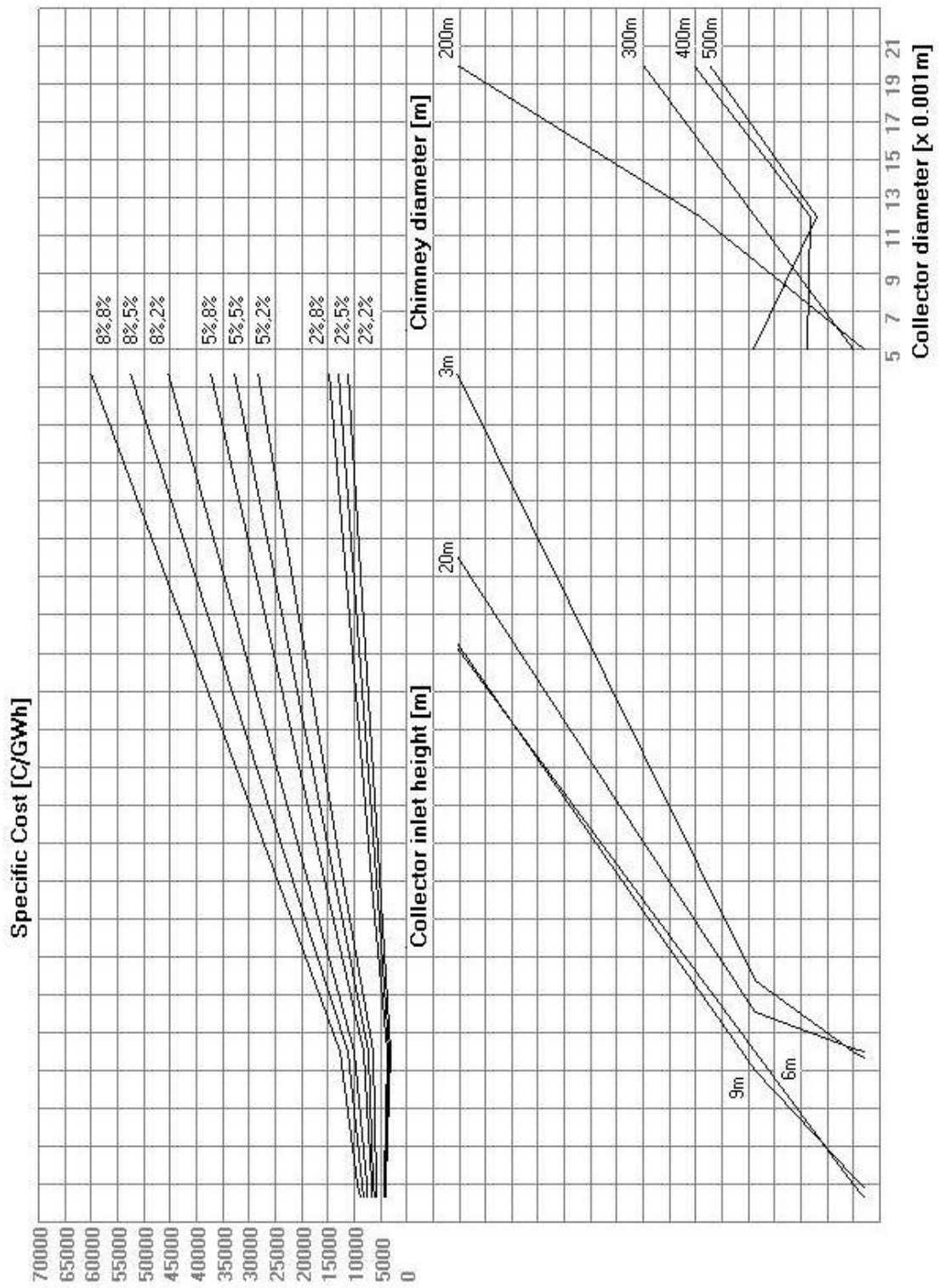


Figure 4.5: Approximate specific cost for various solar chimney power plant configurations, for plants with a chimney height of $H_c = 1000$ m

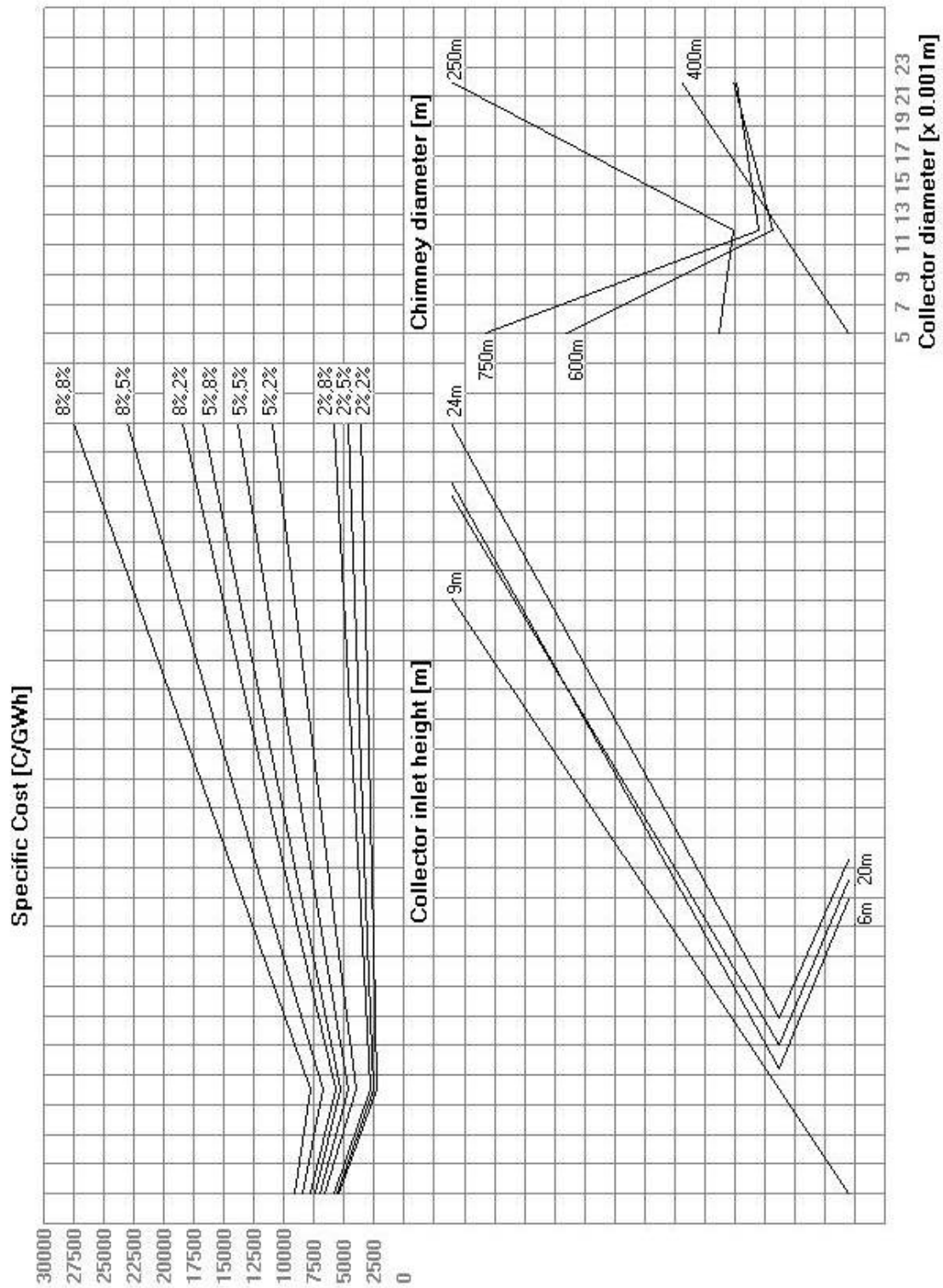


Figure 4.6: Approximate specific cost for various solar chimney power plant configurations, for plants with a chimney height of $H_c = 1500$ m

Table 4.3: Annual power output (in GWh) of various plant configurations for a chimney height of $H_c = 500$ m, with values in bold indicating which configurations experience cold inflow

d_{coll} [m]	H_2 [m]	d_c [m]			
		100	150	200	250
2000	3	29.55	35.34	37.51	38.65
	6	29.89	38.71	43.64	46.94
	9	29.89	38.95	44.94	49.58
	20	29.81	38.45	45.06	51.07
5000	3	78.86	114.38	134.51	144.53
	6	85.98	131.28	160.2	181.94
	9	88.04	135	166.86	190.11
	20	89.39	137.92	170.63	196.84
7000	3	91.09	151.89	187.12	208.85
	6	99.88	179.6	238.21	276.83
	9	102.39	187.01	251.32	298.05
	20	105.09	192.98	261.51	312.79

Table 4.4: Annual power output (in GWh) of various plant configurations for a chimney height of $H_c = 1000$ m, with values in bold indicating which configurations experience cold inflow

d_{coll} [m]	H_2 [m]	d_c [m]			
		200	300	400	500
5000	3	284.19	309.77	316.45	317.93
	6	339.47	388.75	410.83	419.62
	9	352.74	410.73	450.79	462.88
	20	360.73	429.38	478.3	514.72
12000	3	662.17	819.17	865.7	890.7
	6	866.24	1241.83	1404.4	1468.86
	9	928.34	1398.85	1639.62	1757.71
	20	989.11	1529.6	1874.19	2091.71
20000	3	814.23	1126.94	1233.76	1276.37
	6	1028.58	1802.15	2279.23	2504.46
	9	1097.84	2065.52	2795.03	3221.08
	20	1170.76	2336.31	3345.88	4093.2

a large number of these plant configurations may experience cold inflow, thereby making them unsuitable as optimum plant candidates.

From tables 4.3 to 4.5 we also see that the probability of a plant experiencing cold inflow increases with decreasing collector diameter, chimney height and collector inlet height as well as increasing chimney diameter.

It is important to note that the annual power output and specific cost nomograms (figures 4.1 to 4.6) do not take into consideration the effects of cold inflow. Therefore, these figures should always be evaluated in conjunction with their corresponding table in this section in order to ensure that a specific plant configuration does not experience cold inflow.

Table 4.5: Annual power output (in GWh) of various plant configurations for a chimney height of $H_c = 1500$ m, with values in bold indicating which configurations experience cold inflow

d_{coll} [m]	H_2 [m]	d_c [m]			
		250	400	600	750
5000	6	564.09	617.52	625.33	623.04
	9	591.54	664.71	686.86	688.72
	20	610.51	696.66	766.93	786.27
	24	609.76	698.28	779.37	801.95
12000	6	1792.05	2251.17	2383.56	2431.11
	9	1946.75	2592.05	2837.62	2897.26
	20	2091.67	2933.49	3420.35	3569.99
	24	2106.17	2965.3	3491.08	3668.84
22000	6	2549.3	4089.7	4725.76	4811.93
	9	2812.46	4972.8	6208.84	6485.34
	20	3098.22	5928.47	8217.68	9078.68
	24	3134.86	6041.27	8475.55	9462.51

4.3.3 Optimal plant configurations

The present optimal plant configurations are found in the following way. First, a computer simulation calculates the annual power output for a specific plant configuration. Second, the total cost for the same plant is calculated by the approximate cost model for a specific cost parameter combination (see table 4.2). Third, the numerical model must predict no cold inflow for the same plant at any stage of its annual operation. The plant configuration which predicts the minimum specific cost, as well as no cold inflow, is considered the optimal plant.

Table 4.6 presents the optimal solar chimney power plant configurations determined for the varying cost parameters, while table 4.7 lists the corresponding annual power output, total plant cost (according to the approximate cost model) and specific plant cost of these plants. The various configurations are numbered for easy reference between the two tables.

From table 4.6 it is clear that the more expensive the construction costs of the plant become, the smaller the dimensions of the predicted optimal plant becomes. Furthermore, the optimal chimney diameters are much larger than the dimensions presented in literature thus far. Note that even with these larger diameters, the presented optimal plants do not experience cold inflow. In addition, when considering the relatively inexpensive construction cost parameters, results predict much larger (optimal) collector diameters and collector inlet heights than the largest dimensions mentioned in literature.

From table 4.7 it is evident that for the same cost parameters a larger optimum plant, i.e. with greater chimney height, is consistently more cost-effective than the smaller optimum plant.

As a final remark it is noted that the optimal plant with $H_c = 1000$ m, $(pt)_{coll} = 8\%$ and $(pt)_H = 8\%$ was selected in Chapter 2 as the reference plant.

Table 4.6: Optimal solar chimney power plant configurations

No.	H_c [m]	$(pt)_{coll}$ [%]	$(pt)_H$ [%]	d_{coll} [m]	d_c [m]	H_2 [m]
1	500	2	2	6000	220	15
2		2	5	4000	140	5
3		2	8	4000	140	5
4		5	2	3000	130	7
5		5	5	2000	100	4
6		5	8	2000	100	4
7		8	2	2000	100	4
8		8	5	2000	100	4
9		8	8	2000	100	4
10	1000	2	2	16000	510	17
11		2	5	11000	350	10
12		2	8	9000	290	8
13		5	2	10000	350	14
14		5	5	6000	240	6
15		5	8	6000	240	6
16		8	2	6000	250	9
17		8	5	5000	220	6
18		8	8	5000	210	5
19	1500	2	2	22000	720	24
20		2	5	18000	590	14
21		2	8	15000	490	11
22		5	2	16000	620	19
23		5	5	12000	440	10
24		5	8	10000	360	8
25		8	2	13000	510	15
26		8	5	9000	350	9
27		8	8	7000	280	6

Table 4.7: Annual power output, total cost and specific cost for the optimal solar chimney power plant configurations of table 4.6

No.	Annual power output [GWh]	Total plant cost [C]	Specific plant cost [C/GWh]
1	231.7	998 712	4 311
2	94.2	466 527	4 954
3	94.2	507 996	5 394
4	62.5	555 512	8 887
5	29.8	293 739	9 874
6	29.8	314 473	10 571
7	29.8	384 971	12 940
8	29.8	418 146	14 055
9	29.8	451 321	15 170
10	3 083.8	7 689 739	2 494
11	1 413.8	4 345 608	3 074
12	948.6	3 297 478	3 476
13	1 310.5	6 738 716	5 142
14	475.3	2 850 995	5 998
15	475.3	3 130 911	6 587
16	512.2	3 799 945	7 419
17	352.7	3 006 504	8 525
18	336	3 144 734	9 360
19	9 308	17 975 439	1 931
20	5 789.6	14 104 651	2 436
21	3 972.8	11 118 882	2 799
22	5 345.6	20 081 374	3 757
23	2 750.7	12 751 725	4 636
24	1 886.3	9 883 450	5 240
25	3 532.4	19 150 049	5 421
26	1 648.1	10 838 966	6 577
27	975.3	7 189 346	7 371

Ambient Wind, Temperature Lapse Rate and Temperature Inversion Effects

Previous publications have confirmed that windy ambient conditions, ambient temperature lapse rates and atmospheric temperature inversions measurably affect the performance of natural draft cooling towers (Kröger, 2004). These findings subsequently prompt the following investigation into the effect of ambient wind, temperature lapse rates and nocturnal temperature inversions on the performance of a solar chimney power plant.

Computer simulations are performed for a reference solar chimney power plant defined in Chapter 2 of this dissertation. All simulations are repeated for a number of years to allow ground energy fluxes to reach a quasi-steady state.

5.1 Wind effects

Ambient winds affect the operation of a solar chimney power plant in a number of ways. Convection losses from the collector roof to the environment are increased as cross-winds blow over the roof. The air-flow through the plant is also altered by winds blowing across the chimney outlet. In addition, ambient cross-winds which blow in under the collector roof also affect the air-flow through the plant.

A publication by Serag-Eldin (2004) conducts a simple study into the effect of atmospheric winds on the flow patterns under the collector roof of a small-scale solar chimney power plant. The numerical model developed in the present study however considers the effect of prevailing winds on top of the collector roof surface and at the top of the chimney, while neglecting any flow pattern distortions under the collector roof as a result of ambient winds.

As previously mentioned, the chosen location of the reference solar chimney power plant is near Sishen, South Africa. The prevailing ambient wind speeds at this location is given in Appendix H of this study and are those wind speeds measured at 10 m above ground level.

5.1.1 Wind profiles

This section evaluates the effect of three different wind profiles on the performance of a solar chimney power plant. It should be noted that the numerical model assumes that the wind speed over the entire top collector roof surface is equal to the particular wind speed at 10 m above ground level at that specific time. Chapter 2 discusses how ambient cross-winds at the chimney outlet are modelled by the numerical simulation model.

5.1.1.1 Simulation and results

Comparative simulations are performed for the reference solar chimney power plant, with two of the models incorporating the following well-known power-law profile

$$\frac{v_w}{v_{w,ref}} = \left(\frac{z}{z_{ref}} \right)^{1/n} \quad (5.1)$$

where v_w is the wind velocity at a specific height z above ground level, $v_{w,ref}$ is the wind velocity at a reference height above ground level z_{ref} and n is the power-law exponent. These two models employ respective exponents of $n = 5$ and $n = 7$ for the power-law wind profile. Another model assumes a linear wind profile, approximating the ambient wind speed at the chimney outlet as twice the value at 10 m above ground level. Simulations are repeated for chimney heights of $H_c = 500$ m, 1000 m and 1500 m.

The author realizes that no standard wind profile exists and that the fluid dynamic analysis of the earth's boundary layer is an extremely complex exercise. Previous simple attempts at modelling the atmospheric boundary layer have yielded the power-law profile of equation (5.1). It is not the aim of this analysis to model wind profiles accurately, but instead to present trends of solar chimney power plant performance in the presence of ambient winds. It should also be noted that the effects of cold inflow are neglected in the analysis of this section.

Figures 5.1, 5.2 and 5.3 depict the three mentioned wind profile approximations for chimney heights of $H_c = 500$ m, 1000 m and 1500 m respectively. For purposes of illustration, a typical wind speed of $v_w = 2$ m/s is chosen at 10 m above ground level. It is clear that all the profiles employ equal wind velocities at 10 m above ground level, while differing wind velocities are predicted at the chimney outlet height.

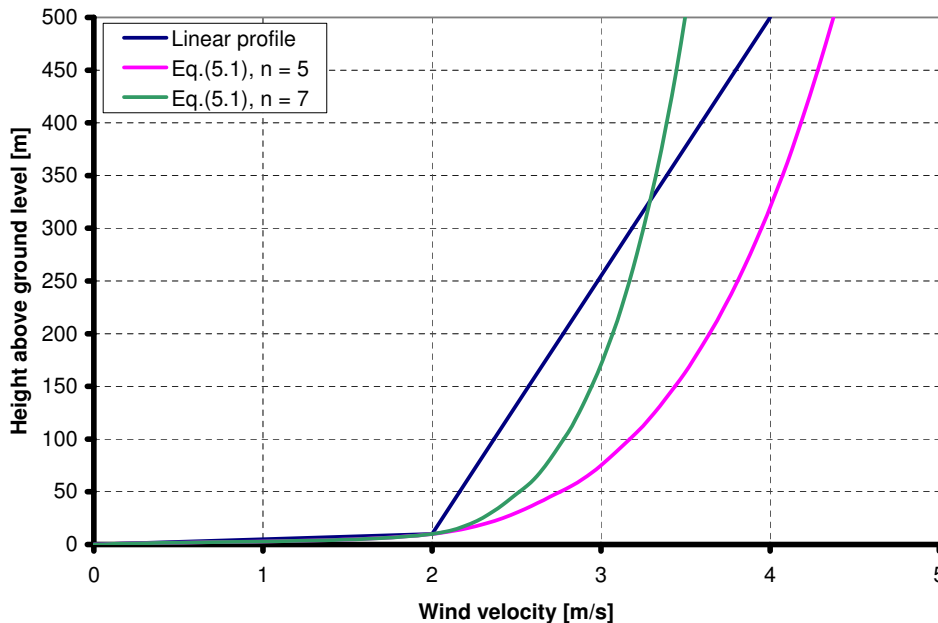


Figure 5.1: The linear and power-law wind profiles for a 500 m high chimney ($v_w = 2$ m/s at 10 m above ground level)

Table 5.1 illustrates the insignificant difference in annual output between the models employing the various approximated wind profiles.

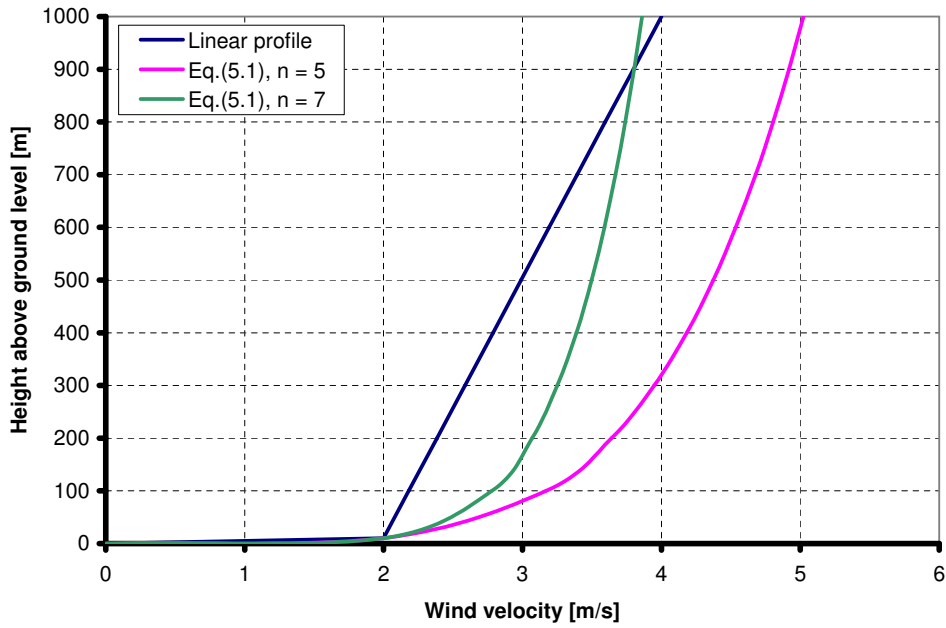


Figure 5.2: The linear and power-law wind profiles for a 1000 m high chimney ($v_w = 2$ m/s at 10 m above ground level)

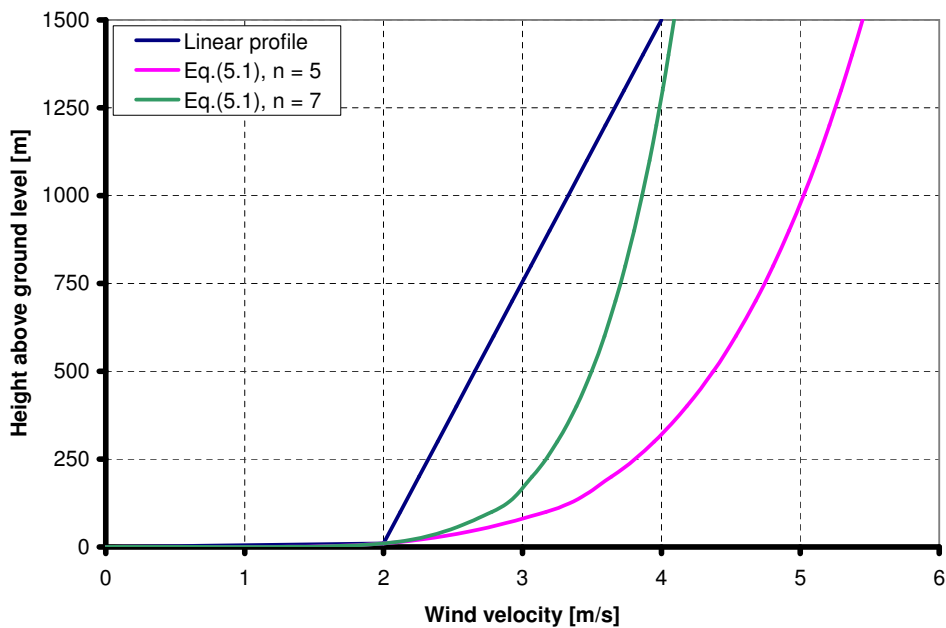


Figure 5.3: The linear and power-law wind profiles for a 1500 m high chimney ($v_w = 2$ m/s at 10 m above ground level)

In addition, when comparing table 5.1 and figures 5.1, 5.2 and 5.3 it is evident that in each case the plant model that employs the wind profile which predicts the greatest wind velocity at the height of the chimney outlet also predicts the highest annual power output. For example, consider figure 5.1. The power-law wind profile with $n = 5$ predicts the greatest wind velocity at a chimney height of 500 m. Now consider table 5.1, where for a chimney

Table 5.1: Annual solar chimney power plant performance for various wind profile approximations

Chimney height [m]	Wind profile	Annual power output [GWh]
500	Linear	159.2
	Eq. (5.1), $n = 5$	164.5
	Eq. (5.1), $n = 7$	157
1000	Linear	336
	Eq. (5.1), $n = 5$	343.6
	Eq. (5.1), $n = 7$	335.6
1500	Linear	521.1
	Eq. (5.1), $n = 5$	528.5
	Eq. (5.1), $n = 7$	521.5

height of $H_c = 500$ m the plant model employing the power-law profile with $n = 5$ gives the highest annual power output (compared to the other models with $H_c = 500$ m). The plant model employing the wind profile which predicts the second highest wind velocity at the chimney outlet height also predicts the second highest annual power output, etc. Similar findings are presented for $H_c = 1000$ m and $H_c = 1500$ m.

An in-depth evaluation of the simulation data reveals the following. All of the above-mentioned plant models experience periods in the winter months where the ambient winds generate a suction effect of air through the chimney, which is ultimately responsible for a slightly enhanced power production. This is caused due to a pressure rise (Δp_{co}) at the chimney outlet, as discussed in Chapter 2 of this study. During the winter months (mostly during night-time) the driving potential of the plant is relatively low and thus more sensitive to suction due to wind. During the summer months the driving potential is much greater, causing the suction effect to have a negligible influence on plant performance.

Therefore, the plants modelling the highest wind velocity at the chimney outlet also predicts the greatest annual power output as a result of predicting the greatest suction effect.

5.1.2 Influence of wind on plant performance

5.1.2.1 Simulation and results

Comparative computer simulations were run for the reference solar chimney power plant. Figure 5.4 compares the power output curves of the reference plant model (which includes windy ambient conditions) with that of the reference plant model which assumes quiet ambient conditions (no wind). It should be noted that the numerical model employs the linear wind profile, as mentioned in the previous section.

From figure 5.4 it is clear that the prevailing winds significantly decrease the plant power output. This is primarily due to the convective heat losses from the collector roof to the environment. Notwithstanding higher suction effects at the chimney outlet which would cause greater power production, the windy conditions result in an increased convective heat transfer coefficient, facilitating a greater heat flux from the collector roof to the environment and ultimately lower power output.

When regarding figure 5.4 more closely, one finds that during the mornings and evenings of June (winter), the plant generates a slightly higher power output during windy conditions than during no-wind conditions. Two factors contribute to this phenomenon. Firstly, the ambient temperatures at these times are marginally higher than the corresponding collector roof temperatures. Therefore, the windy conditions actually cause a minor convective heat

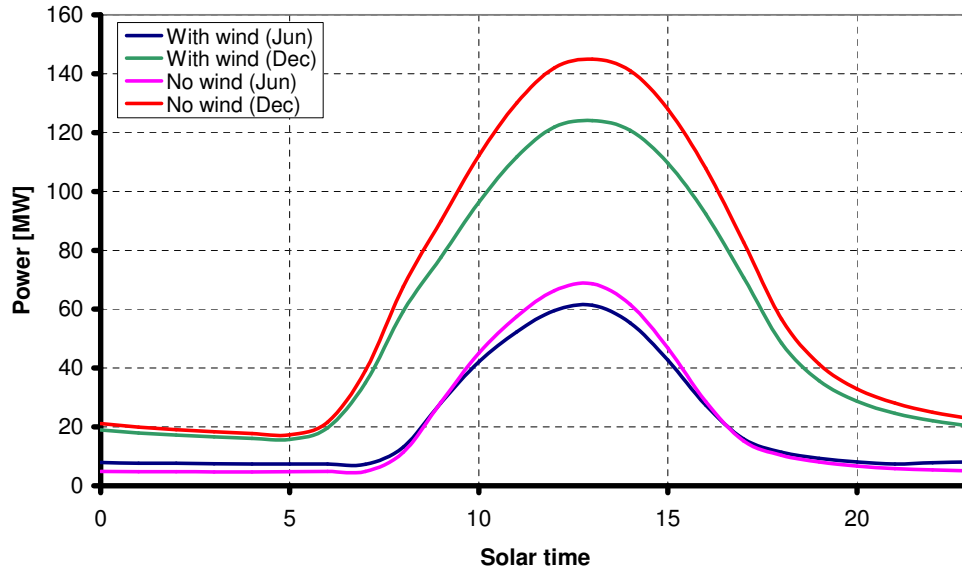


Figure 5.4: Effect of ambient wind on plant power output

flux from the environment to the collector roof, resulting in a slightly increased plant power output. Secondly, as mentioned in the previous section, a slight suction effect due to ambient winds is experienced at the top of the chimney during these times, which boosts the power output somewhat.

We can also further analyze the influence of ambient winds by regarding its effect on the annual power output of the solar chimney power plant. Table 5.2 gives an annual power output comparison of the two models which were simulated.

Table 5.2: Annual power output comparison, illustrating the effect of ambient winds on solar chimney power plant performance

Plant configuration	Annual power output [GWh]
Windy ambient conditions	336
Quiet ambient conditions	373.2

From table 5.2 it is clear that if the quiet ambient conditions are assumed at the proposed site, the annual power output of the plant increases by approximately 11.1 %.

5.2 Ambient temperature lapse rate effects

The reference plant of this dissertation assumes a dry adiabatic lapse rate (DALR) for the air inside the chimney and the atmosphere surrounding the solar chimney power plant. These are believed to be good approximations of the experienced temperature gradients in these regions.

Chapter 3 also briefly investigated the effect on plant performance when employing an atmospheric temperature gradient equal to that employed by the International Standard Atmosphere (ISA) for the air surrounding the plant (while still employing a DALR inside of the chimney). Note that this model did not consider the standard (constant) ISA for all temperate latitudes, but instead employed a time-dependent lapse rate with similar

temperature gradient. The purpose of this investigation was to evaluate the effect on plant performance if a different ambient temperature lapse rate existed than the specified DALR.

The following section evaluates the performance of a solar chimney power plant when combining a modified version of the standard ISA with the assumed DALR as atmospheric models to the plant.

5.2.1 Assumptions by the numerical model

In the analysis of this section, the numerical model makes two assumptions:

- The DALR and ISA should predict a similar atmospheric temperature and pressure at the intersection point of the two lapse rates.
- The higher ambient temperature predicted at any height (by either the DALR or ISA) is always employed as the atmospheric temperature at that height.

5.2.2 Implementation into the numerical model

According to Kröger (2004), the standard ISA for temperate latitudes is a time-independent temperature lapse rate having a mean sea level pressure of 101325 N/m², corresponding temperature of 288.15 K and a temperature gradient of 0.0065 K/m. In light of the fact that the reference location (Sishen, South Africa) is situated in a slightly warmer climate, the modified version of the standard ISA is approximated to be a time-independent lapse rate having a mean sea level pressure of 101325 N/m², corresponding temperature of 290.65 K and a temperature gradient of 0.0065 K/m. Figure 5.5 illustrates this modified linear ISA temperature line.

The following modified versions of the equations by Kröger (2004) present the temperature and pressure variation with height above sea level (according to the ISA)

$$T = T_{sl} - \frac{dT}{dz} z_{sl} = 290.65 - 0.0065 z_{sl} \quad (5.2)$$

$$p = p_{sl} \left[1 - 0.0065 \left(\frac{z_{sl}}{T_{sl}} \right) \right]^{5.255} = 101325 \left[1 - 0.0065 \left(\frac{z_{sl}}{290.65} \right) \right]^{5.255} \quad (5.3)$$

where T_{sl} and p_{sl} refer to the temperature and pressure at sea level respectively, while z_{sl} is the height above sea level. It should be noted that the reference site (Sishen, South Africa) is located at 1187 m above sea level. The DALR is used as normally (time-dependent) with a temperature gradient of 0.00975 K/m.

Figure 5.5 depicts the linear DALR temperature line at two different positions, which represents the DALR for two different times of the day and year. Kröger (2004) also presents the following equations for the DALR

$$T = T_a - \frac{dT}{dz} z = T_a - 0.00975 z \quad (5.4)$$

$$p = p_a \left[1 - 0.00975 \left(\frac{z}{T_a} \right) \right]^{3.5} \quad (5.5)$$

where T_a and p_a are the respective ambient temperature and pressure near ground level, while z is the altitude above ground level.

It should be mentioned that experimental daytime temperature measurements by Kröger (2004) reveal that, due to a non-linear temperature distribution within a few meters (10 m to 20 m) above ground level, actual ambient air temperatures may effectively be between 1 °C and 2 °C lower than those measured near ground level (1 m to 2 m) and thus predicted

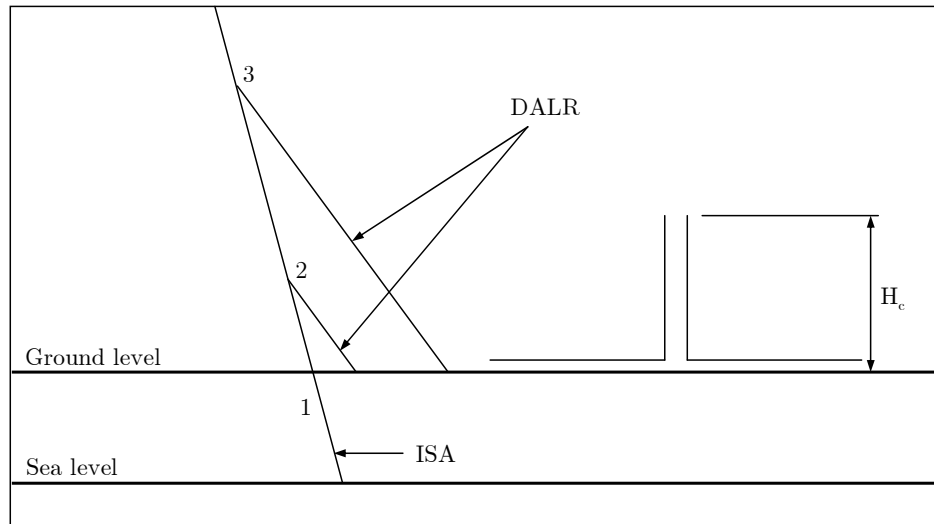


Figure 5.5: Graphical illustration of the modified ISA (Eq.(5.2)) and DALR (Eq.(5.4)) and their implementation into the numerical model

by the specified DALR of equation (5.4). This is illustrated clearly by figure 5.6. The figure shows the DALR according to equation (5.4), where T_a is the ambient temperature value near ground level. The actual atmospheric temperature distribution is also indicated, showing the non-linear region near ground level, followed (at a height in the order of 10 m above ground level) by a temperature gradient equal to the specified DALR.

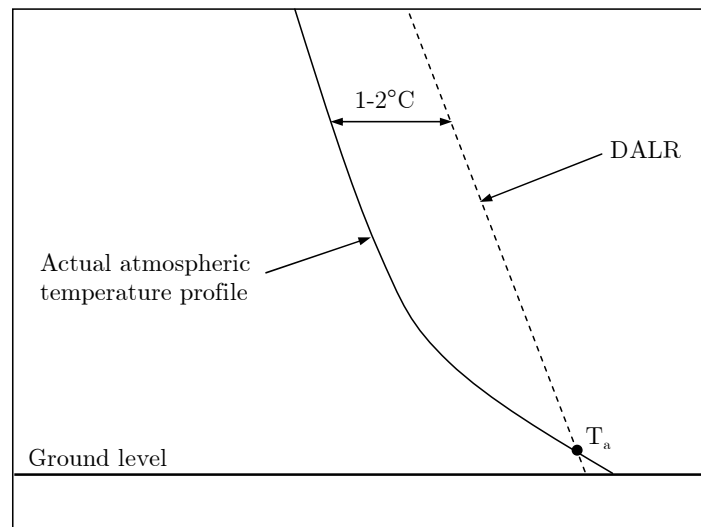


Figure 5.6: The specified DALR and actual atmospheric temperature distribution

These actual lower atmospheric temperatures would mean a greater driving potential and subsequent greater power output for the solar chimney power plant. For the reference plant of section 2.1, a lower ambient air temperature of 1 °C over the chimney height results in an annual power output increase in the order of 10 %. This suggests that the current numerical model predicts a conservative yield.

Since the temperature gradients of the DALR and ISA differ, the profiles will intersect at a specific height, depending on the time of day and day of the year. Consider the first assumption of this section. The main implication of this assumption is that the ambient pressure employed at ground level will vary with time, which is in contrast with the normal constant ambient pressure assumption ($p_a = 90000 \text{ N/m}^2$ in the reference plant specification of Chapter 2). The intersection height above ground level of the two lapse rates is determined by equating equation (5.2) and equation (5.4) (since the atmospheric temperature is assumed equal at the intersection point) and simplifying

$$z_{int} = \frac{(T_a - 282.9345)}{0.00325} \quad (5.6)$$

where $z_{sl} = z + 1187$ in equation (5.2). The atmospheric pressure at the intersection height may then be determined by

$$p_{int} = 101325 \left[1 - 0.0065 \left(\frac{z_{int} + 1187}{290.65} \right) \right]^{5.255} \quad (5.7)$$

according to the ISA.

Consider the second assumption of this section. This assumption produces a conservative solution. Therefore, if the calculated intersection point is above ground level (e.g. positions 2 and 3 in figure 5.5) then the ambient pressure at ground level is given by

$$p_a = \frac{p_{int}}{[1 - 0.00975(z_{int}/T_a)]^{3.5}} \quad (5.8)$$

as predicted by the DALR. However, if the intersection point is below ground level (e.g. position 1 in figure 5.5) the ambient pressure at ground level is

$$p_a = 101325 \left[1 - 0.0065 \left(\frac{1187}{290.65} \right) \right]^{5.255} \quad (5.9)$$

as predicted by the ISA. In addition to determining the ambient pressure at ground level, the temperature and pressure at the height of the chimney outlet must also be determined in order to calculate the Froude number and driving potential of the plant. Once again the second assumption is used by employing the higher temperature predicted by either the DALR or ISA at the chimney outlet height. Consequently, if the intersection height is higher than the chimney height (position 3 in figure 5.5), the atmospheric temperature and pressure at the chimney outlet height is determined by equations (5.4) and (5.5) respectively (by substituting the chimney height H_c for z). However, if the calculated intersection height is lower than the chimney height (position 2 in figure 5.5), the ambient temperature and pressure at the chimney outlet height is given by equations (5.2) and (5.3) (by substituting $H_c + 1187$ for z_{sl}).

5.2.3 Simulation and results

Comparative simulations were conducted for the reference solar chimney power plant with one model employing a combination of the DALR and ISA (according to the strategy mentioned above) while the other model uses only the DALR to model the atmosphere surrounding the solar chimney power plant. Both models employ the DALR inside the chimney of the plant.

Figure 5.7 indicates a slightly reduced peak power output during the summer months when introducing the DALR/ISA combination atmospheric model. This trend is due to the somewhat reduced (and varying) ambient pressure employed by the DALR/ISA combination model in comparison to the assumption of a constant ground level ambient pressure of

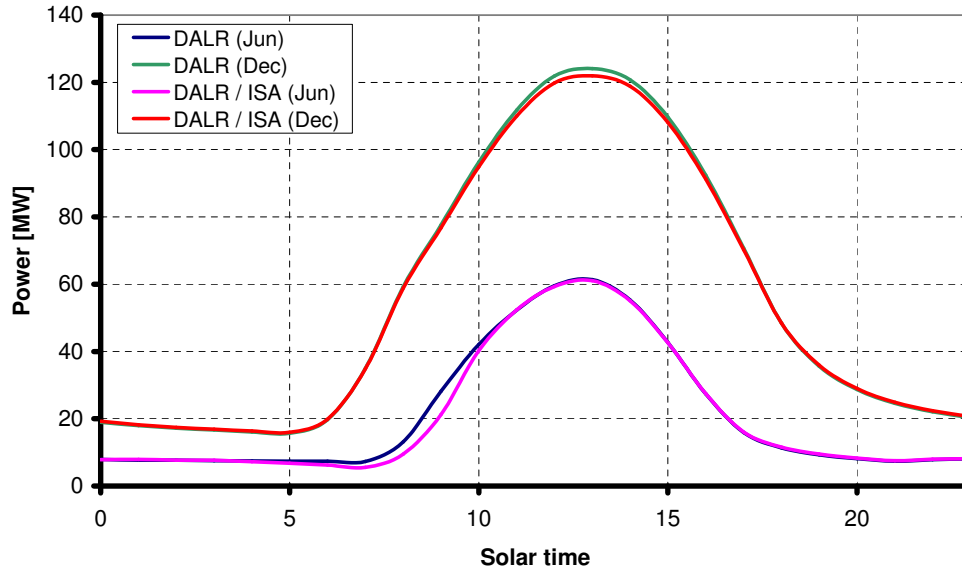


Figure 5.7: The effect of two atmospheric lapse rate models on daily power output

$p_a = 90000 \text{ N/m}^2$ employed by the DALR model. This is also consistent with the results of section 3.15 in Chapter 3.

Another noticeable trend is a decreased power output during most of the morning of the winter months when employing the DALR/ISA combination model. This occurrence is caused by the fact that the DALR/ISA combination model always employs the higher ambient temperature predicted by either the DALR or ISA at any height. During these winter morning periods, the ISA predicts higher ambient temperatures at the chimney outlet height than the DALR and is therefore used by the numerical model. The higher temperatures predicted over the height of the chimney causes a lower driving potential which ultimately results in a lower power output.

Table 5.3: Annual power output comparison, showing the influence of employing a DALR/ISA combination versus only a DALR to model the environment surrounding a solar chimney power plant

Plant configuration	Annual power output [GWh]
Dry adiabatic lapse rate (DALR)	336
DALR/ISA combination	333.1

Annually, table 5.3 shows a marginally reduced power output of 0.9 % when incorporating the DALR/ISA combination model in comparison with the DALR atmospheric model.

5.3 Nocturnal temperature inversion effects

The air near the surface of the earth experiences significant daily temperature variations as a result of radiative heating and cooling of the earth's surface. Previous sections have mentioned the linear temperature gradients (DALR and ISA) which exist in the atmosphere (figure 5.5). Under certain conditions, it is possible that temperature inversions may occur in the atmosphere above ground level, as a result of rapid surface cooling.

Normally, in the time just after sunset, the earth's surface cools down rapidly through radiation. This may cause the ground surface to have a lower temperature than the lowest parts of the atmosphere above ground level, which in turn produces a heat flux from these parts of the atmosphere to the ground. This process initiates the formation of a stable layer of air above the ground surface. With sunrise, the ground surface is reheated and the DALR is reinstated in the atmosphere. Certain geographical regions may also experience stronger temperature inversions than others. Strong inversions have been observed in arid and desert areas where solar chimney power plants are most likely to be located.

The following section evaluates the performance of a solar chimney power plant by combining the DALR and ISA as atmospheric models, while also considering inversion effects during the night-time operation of the plant. During the daytime, the numerical model approximates the atmosphere surrounding the solar chimney power plant according to the analysis of section 5.2. During the night-time however, this analysis is modified.

5.3.1 Assumptions by the numerical model

In the analysis of this section, the numerical model makes three assumptions:

- The nocturnal DALR (equation (5.12)) and ISA should predict a similar atmospheric temperature and pressure at the intersection point of the two lapse rates.
- The temperature inversion profile (equation (5.10)) and nocturnal DALR should predict an equal atmospheric temperature and pressure at their intersection point.
- The inversion profile predicts the atmospheric temperature and pressure until it intersects the nocturnal DALR. Thereafter, the nocturnal DALR predicts the ambient conditions until intersecting the modified ISA. After this point, the ISA predicts the atmospheric conditions.

5.3.2 Implementation into the numerical model

Kloppers (2003) presents the following approximate temperature inversion profile during night-time

$$T = T_{ref} \left(\frac{z}{z_{ref}} \right)^b \quad (5.10)$$

where T_{ref} refers to a reference air temperature (in Kelvin) measured at a reference height z_{ref} , which is approximately 1 m above ground level. Thus with $z_{ref} = 1$ m, T_{ref} may be referred to as T_a . The exponent b is given by

$$b = 0.0035 \sin(0.0177n_d - 2.32392) + 0.0065 \quad (5.11)$$

where n_d is the number of the day of the year. Equation (5.11) is applicable to a fully developed inversion at a particular location and was developed by fitting it to measured nocturnal temperature data. It should be noted that b actually changes as the temperature inversion develops. These changes are neglected in this analysis.

Kloppers (2003) also suggests that the nocturnal temperature distribution above the inversion gradient may be approximated by

$$T = T_{a,max} - 0.00975 z - 0.43 t \quad (5.12)$$

where $T_{a,max}$ is the maximum daily ambient temperature at approximately 1 m above ground level, z is the height above ground level and t is the time after sunset, in hours.

Figure 5.8 illustrates the modified linear ISA profile (equation (5.2)) as well as the inversion (equation (5.10)) and nocturnal DALR (equation (5.12)) profiles at two different

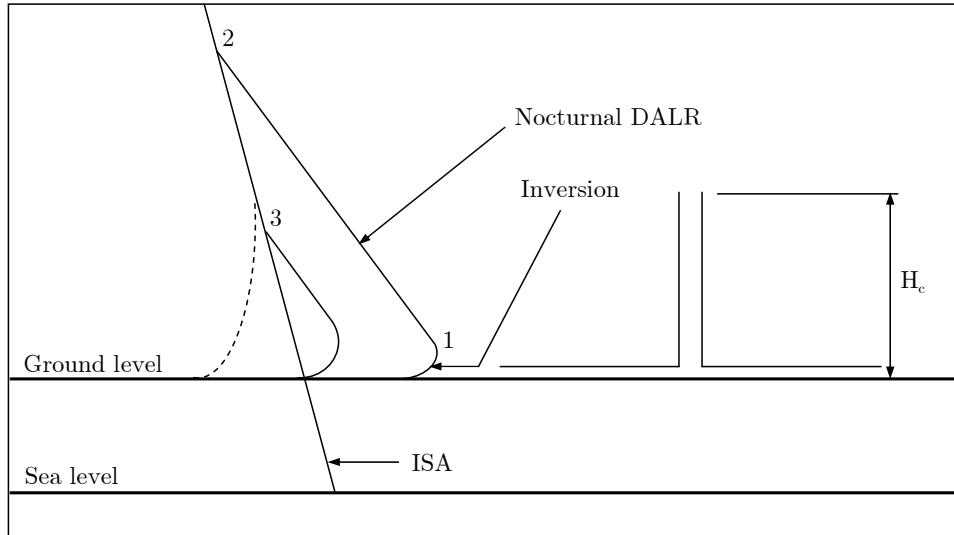


Figure 5.8: Graphical illustration of the modified ISA (Eq. (5.2)), temperature inversion profile (Eq. (5.10)) and nocturnal DALR (Eq. (5.12)) and their implementation into the numerical model for modelling the night-time atmosphere

positions representing two different times after sunset. Note that the inversion height grows throughout the night. Although such a condition is not experienced according to the meteorological conditions at the reference site, the dashed line in figure 5.8 indicates that certain geographical areas may experience much lower night-time ambient temperatures and thus inversion profiles reaching to much greater altitudes.

According to Kröger (2004), when assuming the atmospheric air to be a perfect gas, the pressure gradient in a gravity field may be expressed as

$$\frac{dp}{p} = \frac{-g dz}{RT} \quad (5.13)$$

where p and T refer to the respective atmospheric pressure and temperature at any altitude z above ground level, while g is the gravitational acceleration and R is the specific gas constant. By substituting equation (5.10) into equation (5.13) and integrating, we find

$$p = p_a \cdot \exp \left[- \left(\frac{gz^{1-b}}{RT_a(1-b)} \right) \right] \quad (5.14)$$

for the pressure during night-time at any height z above ground level according to the specified temperature inversion profile, where p_a and T_a refer to the ground level ambient pressure and temperature. Similarly, when substituting equation (5.12) into equation (5.13) and integrating, we find

$$p = p_a \left[1 - \frac{0.00975 z}{(T_{a,max} - 0.43 t)} \right]^{3.5} \quad (5.15)$$

for the pressure at any height z above ground level according to the modified nocturnal DALR of Kloppers (2003).

Since the temperature gradients of the nocturnal DALR, inversion profile and ISA differ, the profiles will intersect at specific heights, depending on the time of day and day of the year. Consider the first two assumptions of this section. The main implication of these assumptions is that the ambient pressure employed at ground level will vary with time, which is in contrast with the normal constant ambient pressure assumption ($p_a = 90000 \text{ N/m}^2$ in the reference

plant specification of Chapter 2). The intersection height above ground level of the nocturnal DALR and ISA is determined by equating equation (5.2) and equation (5.12) (since the atmospheric temperature is assumed equal at the intersection point) and simplifying

$$z_{int} = \frac{(T_{a,max} - 282.9345 - 0.43 t)}{0.00325} \quad (5.16)$$

where $z_{sl} = z + 1187$ in equation (5.2). The atmospheric pressure at the intersection height (p_{int}) may then be determined according to equation (5.7). When considering the first assumption of this section, the ambient pressure at ground level as predicted by the nocturnal DALR is

$$p_a = \frac{p_{int}}{[1 - (0.00975 z_{int}) / (T_{a,max} - 0.43 t)]^{3.5}} \quad (5.17)$$

The intersection height above ground level of the inversion profile and the nocturnal DALR (e.g. position 1 in figure 5.8) is determined by equating equation (5.10) and equation (5.12) (since the atmospheric temperature is assumed equal at the intersection point) and simplifying

$$T_a z^b = T_{a,max} - 0.00975 z - 0.43 t \quad (5.18)$$

where the intersection point ($z_{int,2}$) is determined by solving equation (5.18) iteratively. At this intersection height, the ambient pressure $p_{int,2}$ is determined according to equation (5.15), where $z_{int,2}$ is substituted into z and p_a is taken from equation (5.17). When considering the second and third assumption of this section, the ambient pressure as predicted by the inversion profile can be calculated as follows

$$p_a = (p_{int,2}) / \exp \left[- \left(\frac{g z_{int,2}^{1-b}}{R T_a (1-b)} \right) \right] \quad (5.19)$$

This pressure is employed as the ambient pressure for the DALR/ISA/Inversion atmospheric model. The temperature and pressure at the height of the chimney outlet must also be determined in order to calculate the Froude number and driving potential of the plant. Once again we consider the third assumption of this section. Consequently, if the intersection height from equation (5.16) is higher than the chimney height (e.g. position 2 in figure 5.8), the atmospheric temperature and pressure at the chimney outlet height is determined by equations (5.12) and (5.15) respectively (by substituting the chimney height H_c for z). However, if the calculated intersection height is lower than the chimney height (e.g. position 3 in figure 5.8), the ambient temperature and pressure at the chimney outlet height is given by equations (5.2) and (5.3) (by substituting $H_c + 1187$ for z_{sl}).

5.3.3 Simulation and results

Comparative computer simulations were conducted for the reference solar chimney power plant. One model employs a combination of the DALR and ISA during the daytime and a combination of the nocturnal DALR, ISA and inversion profile during the night-time. The other model uses only the DALR to model the atmosphere surrounding the solar chimney power plant. Both models employ the DALR inside the chimney of the plant.

Figure 5.9 illustrates a considerably lower night-time power output throughout the year for the DALR/ISA/Inversion model compared to the DALR model. This phenomenon can be ascribed to the nocturnal temperature inversions. In effect, such temperature inversions near the ground surface cause higher atmospheric air temperatures over the height of the chimney than predicted by the DALR model. This leads to a reduced driving potential and a subsequently reduced power output.

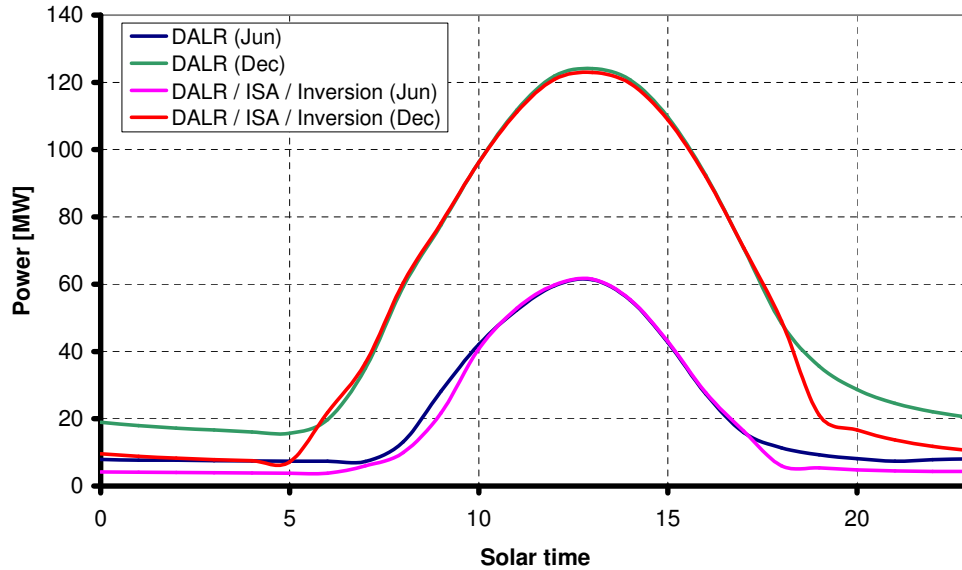


Figure 5.9: The effect of two atmospheric lapse rate models on daily power output

Analogous to the results of section 5.2, figure 5.9 also indicates a marginally reduced peak power output during the summer months when introducing the DALR/ISA/Inversion combination atmospheric model. This is due to the somewhat reduced (and varying) ambient pressure employed by the DALR/ISA/Inversion model.

Table 5.4: The influence on annual power output of employing a DALR/ISA/Inversion combination versus only a DALR to model the environment surrounding a solar chimney power plant

Plant configuration	Annual power output [GWh]
Dry adiabatic lapse rate (DALR)	336
DALR/ISA/Inversion combination	310.1

Also similar to the results of section 5.2 is a decreased power output during most of the morning of the winter months when employing the DALR/ISA/Inversion combination model. This is caused by the fact that the DALR/ISA/Inversion model employs the higher temperature predicted by either the DALR or ISA during these times. During winter mornings, the ISA predicts higher temperatures at the chimney outlet height than the DALR and is therefore employed by the numerical model. The higher temperatures over the height of the chimney causes a lower driving potential which ultimately results in a lower power output.

Table 5.4 indicates a significantly reduced power output of 7.7 % when incorporating the DALR/ISA/Inversion combination model in comparison with the DALR atmospheric model.

It should be noted that inversion effects at the reference location are relatively weak, yet the effect thereof on the power production of the solar chimney power plant is already measurable. In areas where stronger inversions occur this effect will be correspondingly more pronounced.

Regulating Plant Power Output According to Demand

Results of previous studies regarding the performance of solar chimney power plants have shown that the plant power output varies considerably during the day. No control is involved over the power generated by the plant and therefore it simply produces the maximum power at each moment in time, as determined by the prevailing ambient conditions.

This chapter investigates ways to control the power output of a solar chimney power plant in order to be able to deliver power according to specified demand patterns. This is achieved through the inclusion of some new technologies. Firstly, it is shown that double glazing the collector roof improves plant performance. Secondly, instead of double glazing the main collector roof, the glass is employed to form a secondary collector roof. Thirdly, double glazing of the secondary roof is investigated. Then, a secondary and tertiary roof are implemented under the main roof. Furthermore, the chapter also ascertains the influence on plant power output when incorporating plastic covered water tanks under the main canopy. Lastly, the effect of a delta ground configuration on plant performance is evaluated.

Relevant conservation equations for the introduction of a secondary collector roof are derived in Appendix A. Conservation equations are also derived in Appendix B for the double glazing of the main or secondary roof. Appendix C derives relevant equations for the inclusion of a secondary and tertiary roof under the main canopy, while Appendix D derives equations for the introduction of plastic covered water tanks under the main roof. Governing equations are also developed in Appendix E for the inclusion of a delta ground configuration in place of the original flat ground surface.

It is obvious that the inclusion of the following technologies (devices) into the solar chimney power plant will significantly impact the overall plant cost. The aim of this chapter is not to determine the cost-effectiveness of these technologies, but to ascertain what may be possible in terms of control of solar chimney power plant output. Future studies should consider whether the implementation of such devices are cost-effective.

All simulations conducted in this chapter are repeated for a number of years after start-up to allow ground energy fluxes to reach a quasi-steady state. Also, for the sake of simplicity and illustration, it is assumed that South African local time corresponds with solar time.

6.1 Base and peak load power stations

Two main categories of power stations exist: base load stations and peak load stations. Base load power stations operate continuously at near full capacity, in order to satisfy the average

amount of electricity consumed at any given time. Peak load power stations only operate at full capacity during peak periods, in order to satisfy the additional demand over and above the normal base load requirements.

Through the inclusion of the above-mentioned technologies and two control strategies, this chapter investigates the ability of the solar chimney power plant to operate as either a base load or peak load facility.

In each case, the control strategy employed for the solar chimney power plant to act as a base load station is called "Control strategy: base load", while the strategy used for the plant to act as peak load facility is called "Control strategy: peak load".

6.1.1 Peak demand patterns

According to Eskom (2006) (the main supplier of electricity in Southern Africa), peak electricity demand times in South Africa are between 07:00 and 12:00 in the morning and between 17:00 and 22:00 in the evening. Figure 6.1 presents a typical electricity demand pattern for South Africa.

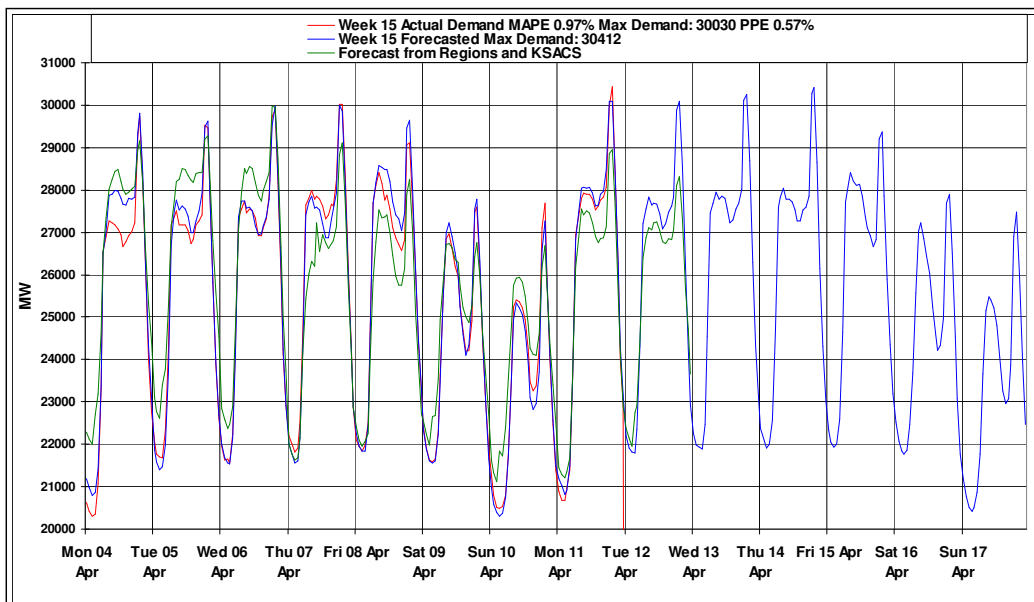


Figure 6.1: Typical electricity demand pattern for South Africa

6.2 Including a double glazed main collector roof

The inclusion of a double glazed main collector roof is as such not a method of controlling the power production of the solar chimney power plant. It is simply a technology which is implemented to achieve improved plant performance.

Previous studies regarding the double glazing of the collector roof have been performed, with varying results. Schlaich (1994) presents results indicating that, for a plant with similar dimensions to those of the reference plant employed in this dissertation, the double glazing of the collector roof increases annual plant output by approximately 28.6 %, compared to the same plant using a single glazed roof. Conversely, Bernardes *et al.* (2003) state that, for a plant of similar scale to the reference plant referred to here, output is only increased by approximately 5.6 %.

6.2.1 Modification of plant collector

The single glazed glass collector roof is replaced by a double glazed glass roof (for the case where the full collector area is replaced by double glazing). Another alternative is studied, where only a certain part of the collector roof consists of double glazing, while the rest of the roof is single glazed.

For the case of partial double glazing, the collector roof is double glazed over the inner part of the collector (from the chimney outwards), while the outer part is single glazed. The idea behind this approach is that by double glazing the section near the chimney, heat losses to the environment will more effectively be reduced than if double glazing were implemented on the outer parts of the collector. Due to the higher collector temperatures experienced near the chimney inlet, higher heat losses occur in this region. Double glazing in this inner region will reduce these losses.

6.2.2 Plant specifications

The solar chimney power plant model of this section is based on the reference plant specifications in Chapter 2. A full or partially double glazed collector roof is included in the model, having similar properties and dimensions to that of the collector roof as specified in table 2.1, except for the dimensions listed in table 6.1.

According to information from vendors, the individual sheets of double glazing are normally spaced between 6 mm and 30 mm apart, where the gap between them are usually filled with air or some inert gas. It is assumed that each of the sheets of the double glazing employed here are 4 mm thick, with spacing in the above-mentioned range, while the gap between the sheets are filled with air.

Table 6.1: Full or partially double glazed collector roof specifications for each of the following simulations (DG = Double glazed)

DG Collector Roof (Glass) - Full Area	
Glazing sheet spacing	$L = 0.006 \text{ m}, 0.01 \text{ m or } 0.03 \text{ m}$
DG Collector Roof (Glass) - 1/4 Area	
Outer diameter	$d_{DG} = 2516 \text{ m}$
Glazing sheet spacing	$L = 0.01 \text{ m}$
DG Collector Roof (Glass) - 1/2 Area	
Outer diameter	$d_{DG} = 3528 \text{ m}$
Glazing sheet spacing	$L = 0.01 \text{ m}$
DG Collector Roof (Glass) - 3/4 Area	
Outer diameter	$d_{DG} = 4356 \text{ m}$
Glazing sheet spacing	$L = 0.01 \text{ m}$

6.2.3 Simulation and results

Two sets of simulations are performed in this section, employing the above-mentioned plant specifications. Firstly, the performance of a plant employing a double glazed roof over the full collector area is simulated, having varying spacing between the double glazing sheets of $L = 0.006 \text{ m}$, $L = 0.01 \text{ m}$ and $L = 0.03 \text{ m}$. Secondly, the performance of a plant employing

a double glazed roof over a quarter, a half and three-quarters of the total collector area is evaluated, using double glazed spacing of $L = 0.01$ m.

Figures 6.2 and 6.3 depict the daily performances (for 21 June and 21 December), while tables 6.2 and 6.3 compare the annual power outputs of the above-mentioned simulated plants.

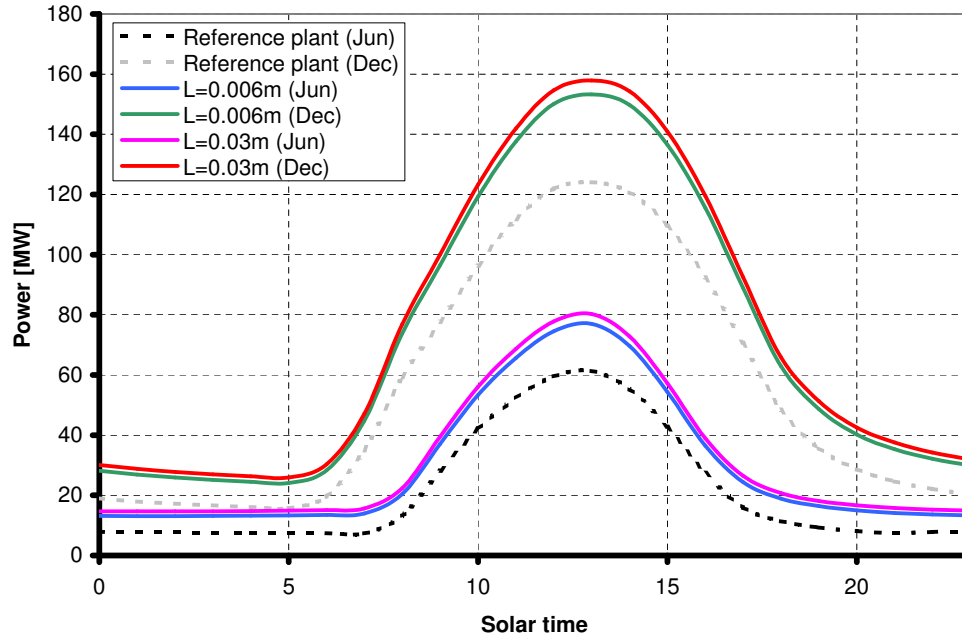


Figure 6.2: Effect on plant performance of including a double glazed collector roof over the entire collector area; effect of spacing between double glazing sheets

From figure 6.2 it is clear that the double glazing of the collector roof has a major impact on daily power output. When compared to the reference plant which incorporates a single glazed collector roof, the plant models that include double glazed roofs show significantly higher power production throughout a 24-hour period. Annually, table 6.2 indicates at least a 32.3 % increase (for the plant employing $L = 0.006$ m) in power output when incorporating a double glazed collector roof. The double glazing of the main collector roof restricts the heat losses through the roof to the environment, which increases the effective plant output. These results confirm the findings of Schlaich (1994), while differing significantly from those of Bernardes *et al.* (2003).

Table 6.2: Annual power output comparison, illustrating the effect of incorporating a double glazed collector roof over the full collector area and the effect of varying spacing between double glazing sheets

Plant configuration	Annual power output [GWh]
Reference plant	336
$L = 0.006$ m	444.6
$L = 0.01$ m	463.6
$L = 0.03$ m	466.8

Furthermore, results also indicate that the greater the spacing between the double glazed sheeting is, the higher the plant power output becomes. This is due to the fact that the larger the air gap between the sheets are, the better its insulation of the warm collector air from the environment, and consequently the smaller the heat losses through the roof.

However, the effect of increasing sheet spacing beyond $L = 0.01$ m becomes less significant. Refer to figure 6.2, where the daily output curves for $L = 0.01$ m are not indicated, as they are indistinguishable from the curves of $L = 0.03$ m. Table 6.2 confirms this, showing only a 0.7 % rise in annual power output for a plant incorporating double glazing sheet spacing of $L = 0.03$ m compared to a plant using $L = 0.01$ m. This is much less than the rise in annual output of 4.3 % of a plant incorporating spacing of $L = 0.01$ m versus a plant employing $L = 0.006$ m.

When evaluating figure 6.3 one finds that even partially double glazing the collector roof of the solar chimney power plant has a significant positive impact on plant power generation (when compared to the reference plant which only utilizes a single glazed collector roof).

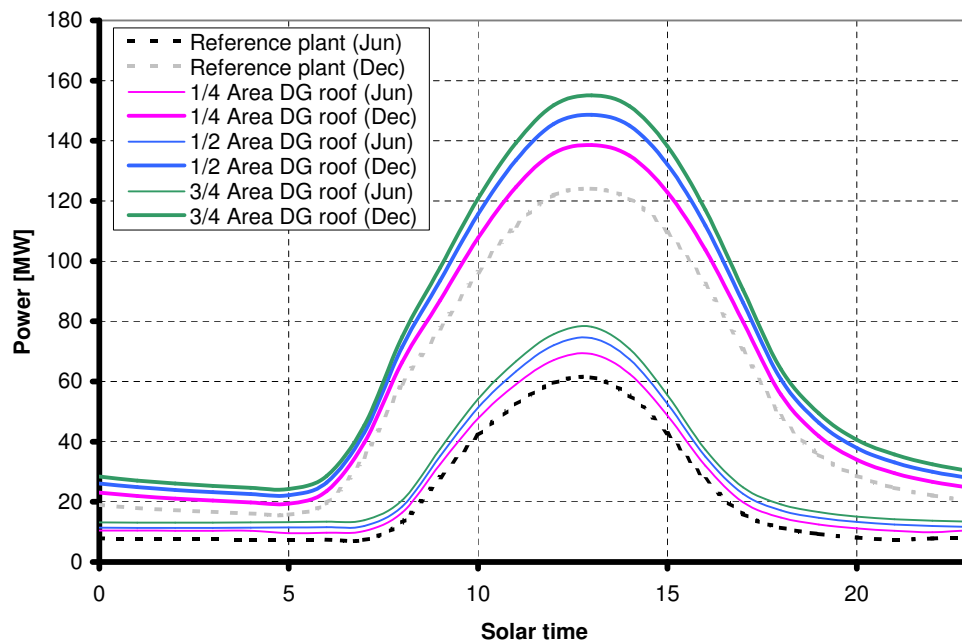


Figure 6.3: Effect on plant performance of including a partially double glazed collector roof ($L = 0.01$ m, DG = Double glazed)

Table 6.3: Annual power output comparison, illustrating the effect of incorporating a partially double glazed collector roof (with $L = 0.01$ m)

Plant configuration	Annual power output [GWh]
Reference plant	336
1/4 Area double glazed	387.4
1/2 Area double glazed	423.8
3/4 Area double glazed	449.7
Full Area double glazed	463.6

In terms of annual power output, table 6.3 reveals that double glazing a quarter, half or three-quarters of the collector roof area (with the rest single glazed) produces respective increased power outputs of 15.3 %, 26.1 % or 33.8 % compared to a fully single glazed reference plant collector roof. Compared to the reference roof, double glazing the entire collector roof increases the annual power output by (in this case) 38 %.

6.3 Including a secondary collector roof

In order to control the daily power output of the solar chimney power plant, a mechanism is necessary which controls the flow of air through the plant. Personal communication with Kröger (2004-2006) revealed that the introduction of a secondary collector roof under the main canopy could facilitate some effective control of plant output.

6.3.1 Modification of plant collector

The inclusion of a secondary collector roof divides the collector into a top and bottom section, as illustrated schematically by figure 6.4.

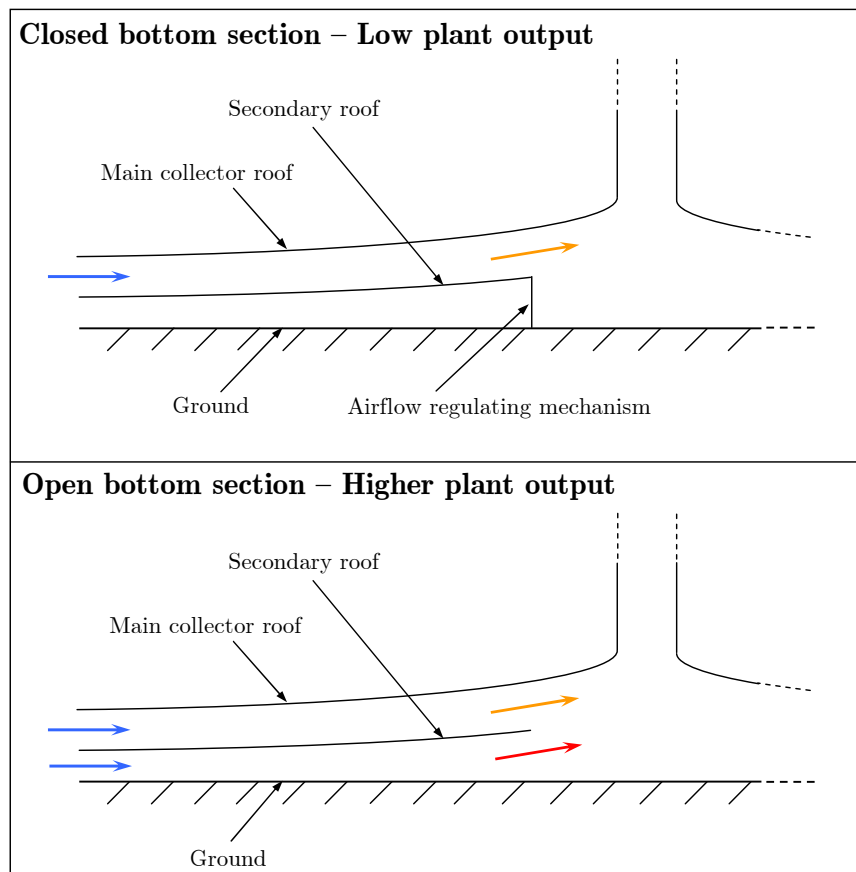


Figure 6.4: Controlling plant power output by regulating the collector air-flow

Air flows constantly through the top section, without being regulated, while an air-flow regulating mechanism at the bottom section outlet controls the mass-flow through the bottom section of the collector. The control of air-flow through the bottom section is

effectively achieved by incrementally increasing or decreasing the pressure drop across the regulating mechanism. The secondary roof gives the plant the ability to store and release energy from the bottom section of the collector in order to regulate the plant power output. At times when less power is required, the bottom section is closed and energy is stored in the ground. If more power is required, the bottom section is opened in a controlled manner, which causes an air-flow under the secondary roof. This air-flow extracts energy from the ground and subsequently boosts plant power output. Figure 6.4 illustrates schematically the operation of the plant when introducing a secondary roof.

A further refinement to achieve additional control which may be considered is the implementation of multiple radial channels underneath the secondary roof in the collector, as illustrated by figure 6.5. These channels can be fully opened or closed off at the bottom section outlet, thereby incrementally increasing or decreasing the collector air-flow area.

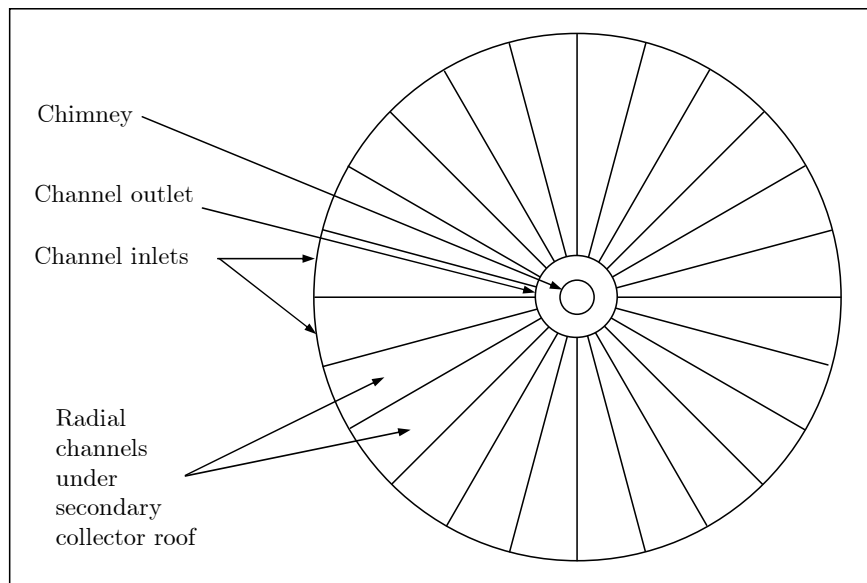


Figure 6.5: Schematic plan view of the solar chimney power plant collector, showing the proposed radial channels under the secondary collector roof

6.3.2 Plant specifications

The solar chimney power plant model of this section is based on the reference plant specifications in Chapter 2. In addition, a secondary collector roof is included in the model, having similar properties and dimensions to that of the main collector roof (as specified in table 2.1), except for the dimensions listed in table 6.4. In this particular example the perimeter height of the secondary collector roof ($H_{2,s}$) is simply taken as half of the reference plant's main roof perimeter height. The inner diameter of the secondary collector roof ($d_{3,s}$) is somewhat greater than the reference plant's main roof inner diameter, due to the inclusion of a transitional (mixing section) and single section in the collector of the plant (see figure A.1). The numbered subscripts of the specified dimensions apply to figure 2.1.

Table 6.4: Secondary collector roof specifications

Secondary Collector Roof (Glass)	
Perimeter (inlet) height	$H_{2,s} = 2.5$ m
Inner diameter	$d_{3,s} = 584$ m

6.3.3 Control strategy: base load

The plant model is controlled to act as a base load power generating facility. The air-flow through the bottom section of the collector is regulated (by the proposed air-flow regulating mechanism) to keep the generated power as constant as possible, while maximizing the total electrical energy produced.

It is important to note the difference between the words "objective" and "target" as it is used in the following discussion. The "objectives" of the base load control strategy are to keep the generated power as uniform as possible, while maximizing the power delivered. In the quest for achieving these objectives, a theoretical "target" power is specified within the numerical model, which the plant must try to attain. This target power acts as a theoretical control mechanism which ensures that the power produced by the plant is as close as possible to constant, as well as the maximum deliverable power under the strategy.

The following explains the physical method of modelling the above-mentioned base load control strategy. At the outset, a target power is specified (with a tolerance of 1 %) which the plant model must try to achieve. At first, air only flows through the top section of the collector, while the air-flow regulating mechanism at the bottom section outlet is fully closed (i.e. infinite pressure drop across the mechanism), making no air-flow possible through this section. If the plant model cannot achieve the specified target with air flowing only through the top section, the pressure drop across the regulating mechanism in the bottom section is incrementally decreased (causing an air-flow through the bottom section) to the point where the target power is attained. If the target power is reached without it being necessary that the mechanism be fully opened (i.e. zero pressure drop across it), the next time step is simulated. The pressure drop across the mechanism is then incrementally increased or decreased to maintain the target power output.

If the target power cannot be achieved even with the regulating mechanism fully open (zero pressure drop across it), the target power is decreased to the point where the target can be reached with the mechanism fully opened. The next time step is then modelled, where it may be necessary to further decrease the target power.

During some periods the target power cannot be maintained with the regulating mechanism fully closed (no air-flow in bottom section). During these times, the target is increased to a point where it can be achieved before simulating the next time step, where it may be necessary to further increase the target.

Note that the incremental regulation of the pressure drop across the air-flow regulating mechanism is defined in terms of percentages. This refers to the pressure drop across the mechanism as a percentage of the total pressure drop across the collector section (i.e. from the collector perimeter to the outlet at the end of the secondary roof). The plant model employs percentage increments of 1 % for effective air-flow regulation.

6.3.3.1 Simulation and results

A computer simulation is performed, employing the above-mentioned plant specifications and base load control strategy.

Consider the performance curve for 21 December in figure 6.6 for the plant incorporating a secondary roof. At solar midnight, the air-flow regulating mechanism at the bottom section outlet is controlled to have no pressure drop across it. At this time the plant is running at

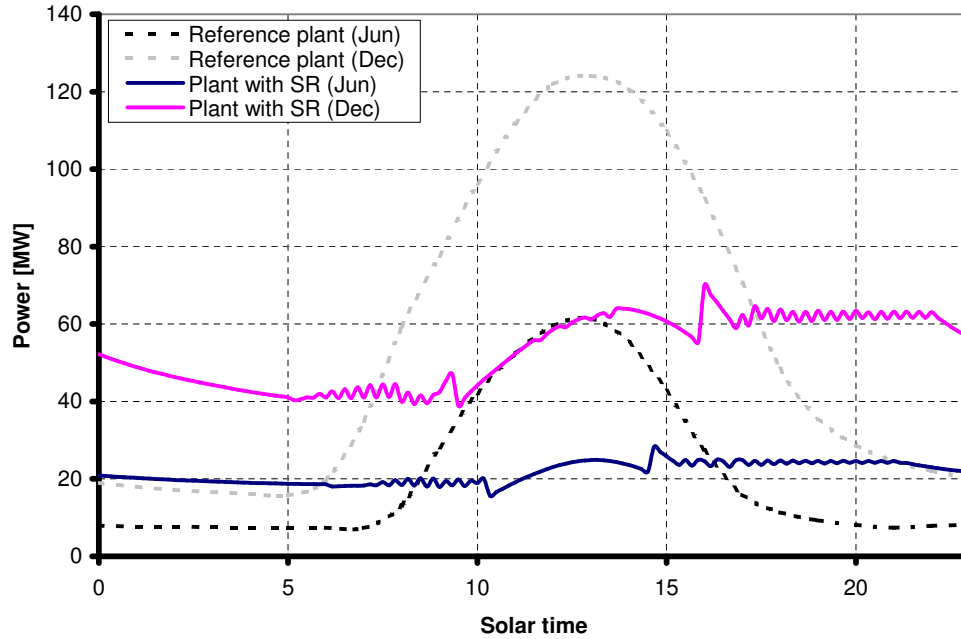


Figure 6.6: Daily solar chimney power plant performance as base load facility - controlled power output through the inclusion of a secondary collector roof (SR = Secondary roof)

full capacity in order to achieve the theoretical target power. Between 22:00 and 05:00 the plant cannot deliver the target power and therefore the target is consistently decreased to a level which can be attained.

As the sun rises the plant is increasingly able to achieve the target power. Between 05:00 and 08:00 the control system incrementally increases the pressure drop across the bottom section's regulating mechanism, thereby steadily decreasing the air-flow through the bottom collector section. In this way the delivered power is kept as constant as possible (the target remains constant for this period).

At this point there is a jump in the plant power output, where the highest point is the plant output with a 99 % pressure drop across the air-flow regulating mechanism (minimal air-flow through the bottom section), while the lowest point is the plant output with a 100 % pressure drop across the mechanism (no air-flow in the bottom section). This considerable difference in power generation is due to the following. During the morning period after sunrise, the ground surface of the solar chimney power plant is heated considerably by solar radiation, especially with restricted air-flow through the bottom section. Therefore, even with minimal flow through the bottom collector section, a significant amount of heat is transferred from the ground surface to the collector air, resulting in a strong driving potential and ultimately high plant power output. Conversely, with no air-flow through the bottom section, only the cooler top airstream contributes to the plant's driving potential, producing a significantly lower plant power output.

In addition, at this point the control system must also decide whether to enforce a 99 % or 100 % pressure drop across the air-flow regulating mechanism in order to maintain the target power output. However, neither of the options delivers a power output within the specified tolerance of the target power. In such a case, the control option which produces an output closest to the target, is selected. Therefore, due to the significant difference in power output between the two options, a jump in the power generation results. Finer control of the air-flow in the bottom section can reduce the magnitude of these fluctuations.

From approximately 10:00 to 14:00 the plant model is able to produce a greater power

output (minimum operating capacity, with air-flow through only the top section) than the specified target power and therefore the target power is consistently increased during this period.

Between 14:00 and 16:00 the control system must once again evaluate whether to enforce a pressure drop of 99 % or 100 % across the regulating mechanism at the bottom section outlet. Once again neither option produces an output within the specified tolerance of the target power and the closest power output is subsequently selected at each time step. It is clear that during this period, a 100 % pressure drop is maintained, giving no flow through the bottom section. Thereafter a similar jump in output is experienced, as explained previously, when a pressure drop of 99 % is instated.

As the sun sets the plant is increasingly unable to achieve the target power and the control system incrementally decreases the pressure drop across the air-flow regulating mechanism. Thus between 17:00 and 22:00 the control system continuously increases the air-flow through the bottom section of the collector in order to keep the delivered power as constant as possible (the target remains constant for this period).

From figure 6.6 it is also clear that the base load plant power output during winter-time, although reduced, exhibits the same characteristics to that of the output during summertime.

Table 6.5: Annual power output comparison, illustrating the effect of incorporating a secondary collector roof for the purpose of base load electricity generation

Plant configuration	Annual power output [GWh]
Reference plant	336
Plant with secondary roof	330.9

Table 6.5 shows a decrease of 1.5 % in annual output for a plant incorporating a secondary collector roof compared to the reference plant. In an effort to keep the delivered power as constant as possible, the plant is not always able to produce its maximum power, resulting in a somewhat reduced annual power output.

Lastly, it is clear that including a secondary collector roof facilitates good control over the plant power output when subjected to a base load control strategy. This is evident when considering that the predicted summertime base load power output is between 31 % and 56 % of the peak summer output of the reference plant, while the predicted winter-time base load power output is between 26 % and 46 % of the peak winter output of the reference plant. Note that the ground surface under the secondary collector roof may reach temperatures of up to 95 °C in summer.

6.3.4 Control strategy: peak load

The plant model is controlled to act as a peaking power facility. Consider the particular case when, during peak demand times, the air-flow regulating mechanism at the bottom section outlet is fully opened (zero pressure drop across it) and the plant operates at full capacity. In off-peak periods the plant operates at minimum capacity, without having to shut down the plant. During these times, the mechanism is fully closed (no air-flow in the bottom section) and most of the available energy is stored by the plant (for use during peak times). It should be noted that shutting down the plant completely during non-peak times is inefficient, with large quantities of energy being lost to the environment. This has been confirmed by simulation.

The author realizes that in practice a peaking power facility would not necessarily operate at full capacity during peak demand periods, but may however operate to generate power according to a certain demand pattern within the peak period. By regulating the air-flow

through the bottom section of the collector, the solar chimney power plant has the ability to produce peak power according to different demand patterns. This fact is not further evaluated in this study as the purpose of the "Control strategy: peak load" sections are simply to illustrate what is possible in terms of peak load power output by a solar chimney power plant.

6.3.4.1 Simulation and results

A computer simulation is performed, employing the above-mentioned plant specifications and peak load control strategy.

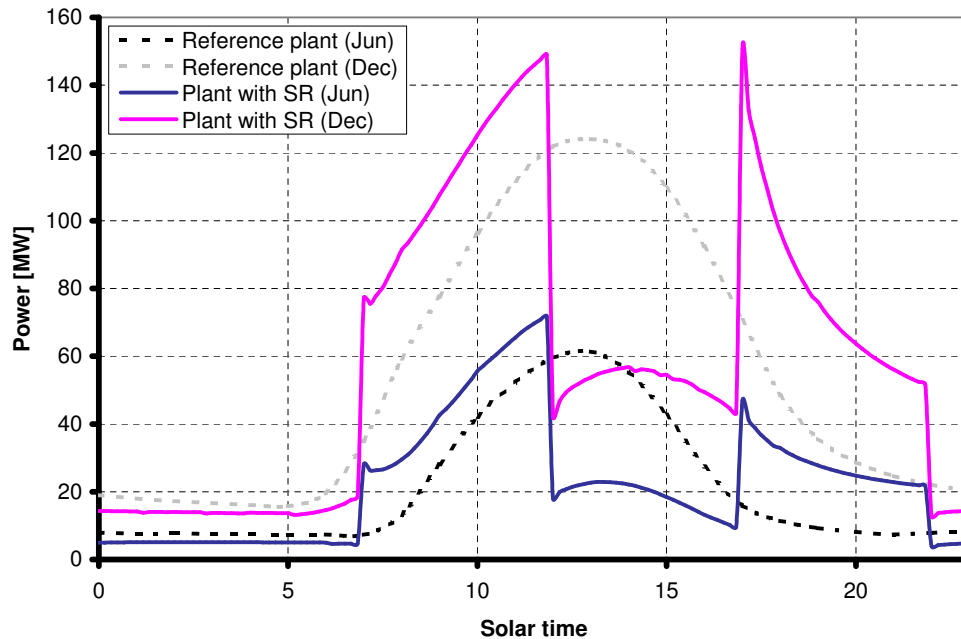


Figure 6.7: Daily solar chimney power plant performance as peak load facility - controlled power output through the inclusion of a secondary collector roof (SR = Secondary roof)

Consider the performance curves in figure 6.7 for the plant incorporating a secondary roof. It is evident that the plant power output rises sharply with the bottom section's air-flow regulating mechanism fully opened (no pressure drop across it) at 07:00 (start of morning peak time). Thereafter, as the sun heats the ground surface under the collector roof, the power produced by the plant continues to rise steadily until 12:00. At 12:00 (end of morning peak time) the regulating mechanism is fully closed (no air-flow through the bottom section), resulting in a sudden drop in power output during midday.

Between 12:00 and 17:00 the plant output at first increases and then decreases steadily. This is due to the corresponding solar radiation profile during this period of the day, i.e. the plant power output profile corresponds to the amount of solar radiation received.

At 17:00 (start of evening peak time) the pressure drop across the regulating mechanism at the bottom section outlet is again decreased to zero, allowing air-flow and giving a sharp rise in power output. The output then decreases rapidly as the sun sets and the plant has to start tapping the energy stored in the ground during the day, in order to produce the maximum amount of power for evening peak time.

The regulating mechanism is once again fully closed at 22:00 (end of evening peak time), thereby obstructing any air-flow through the bottom collector section and causing a sudden

drop in power production. The power produced during the night (off-peak time) remains virtually constant.

Another noticeable trend from figure 6.7 is that the power produced throughout the day during winter-time is considerably lower than during summertime.

Table 6.6: Annual power output comparison, illustrating the effect of incorporating a secondary collector roof for the purpose of peak load electricity generation

Plant configuration	Annual power output [GWh]
Reference plant	336
Plant with secondary roof	342.7

Table 6.6 indicates a slightly higher annual power output of 2 % for a plant incorporating a secondary roof in comparison with the reference plant of section 2.1. This is predominantly due to better insulation (provided by the inclusion of a secondary collector roof) of the solar energy stored in the ground, resulting in reduced heat losses to the environment.

Thus, in terms of peak load electricity production, it is clear that the inclusion of a secondary collector roof shows the potential for significant control of the solar chimney power plant output. Note that the ground surface under the secondary collector roof may reach temperatures of up to 92 °C in summer.

6.4 Including a double glazed secondary collector roof

6.4.1 Modification of plant collector

Similar modifications are made to the reference plant collector as discussed in section 6.3.1, with the exception that the secondary collector roof employs double glazing instead of single glazing over the full secondary roof area.

6.4.2 Plant specifications

The solar chimney power plant model of this section is based on the reference plant specifications in Chapter 2. A double glazed secondary collector roof is included in the plant model, having similar properties and dimensions to that of the main collector roof (as specified in table 2.1), except for the dimensions listed in table 6.7. In this particular example the perimeter height of the double glazed secondary collector roof ($H_{2,s}$) is simply taken as half of the reference plant's main roof perimeter height. The inner diameter of the double glazed secondary collector roof ($d_{3,s}$) is somewhat greater than the reference plant's main roof inner diameter, due to the inclusion of a transitional and single section in the collector of the plant (see figure A.1). The numbered subscripts of the specified dimensions apply to figure 2.1.

Table 6.7: Double glazed secondary collector roof specifications (DG = Double glazed)

DG Secondary Collector Roof (Glass)	
Perimeter (inlet) height	$H_{2,s} = 2.5$ m
Inner diameter	$d_{3,s} = 584$ m
Glazing sheet spacing	$L = 0.01$ m

It is assumed that each individual sheet of the double glazing employed for the secondary roof are 4 mm thick, while the gap between the sheets is filled with air.

6.4.3 Control strategy: base load

A similar control strategy to that of section 6.3.3 is followed.

6.4.3.1 Simulation and results

A computer simulation is performed, employing the above-mentioned plant specifications and base load control strategy.

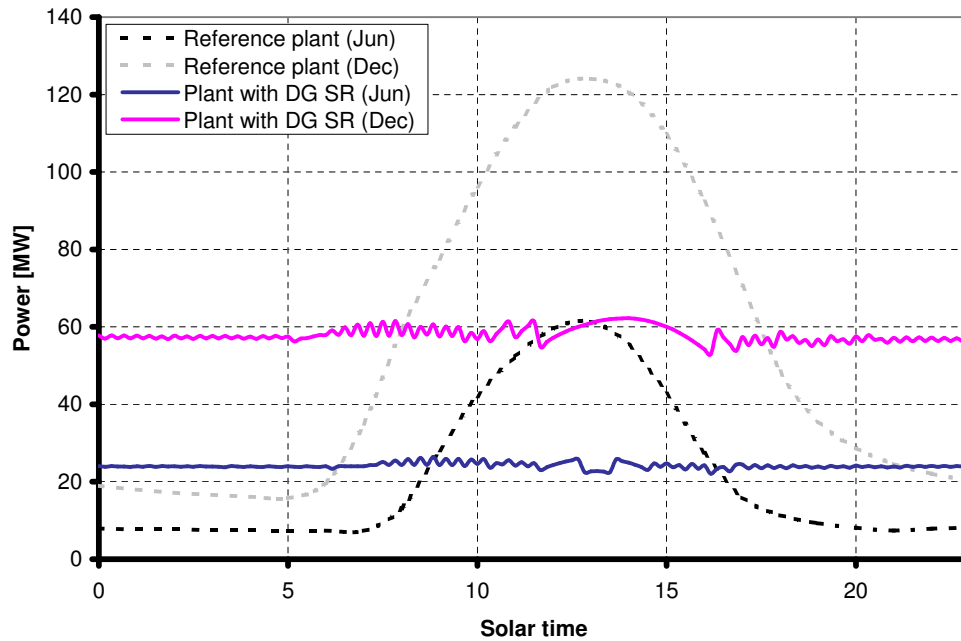


Figure 6.8: Daily solar chimney power plant performance as base load facility - controlled power output through the inclusion of a double glazed secondary collector roof (DG = Double glazed; SR = Secondary roof)

Consider the performance curves in figure 6.8 for the plant incorporating a double glazed secondary roof. By incrementally increasing or decreasing the air-flow through the bottom section of the collector, the plant is able to deliver an almost constant power output. Throughout the year, the achievable target power is reduced from summer to winter-time and again increased from winter to summer, as is evident when comparing the illustrated performance curves.

By incorporating a double glazed secondary roof, the plant is able to deliver a more constant power output than when including only a single glazed secondary roof (see figure 6.6). This is due to the fact that less heat is transferred from the bottom section to the top section during operation. During night-time the plant uses the energy from the bottom section more efficiently, while during daytime less energy is transferred into the top airstream.

With a more efficient collector, heat losses to the environment are reduced and the plant produces a 9.6 % greater annual power output (see table 6.8) than when incorporating a single glazed secondary roof.

Therefore, for the goal of base load electricity generation, the incorporation of a double glazed secondary collector roof seems to be an excellent mechanism for controlling plant

Table 6.8: Annual power output comparison, illustrating the effect of incorporating a double glazed secondary collector roof for the purpose of base load electricity generation (DG = Double glazed)

Plant configuration	Annual power output [GWh]
Plant with secondary roof	330.9
Plant with DG secondary roof	362.7

power output. Note that the ground surface under the double glazed secondary collector roof may reach temperatures of up to 105 °C in summer.

6.4.4 Control strategy: peak load

A similar control strategy to that of section 6.3.4 is followed.

6.4.4.1 Simulation and results

A computer simulation is performed, employing the above-mentioned plant specifications and peak load control strategy.

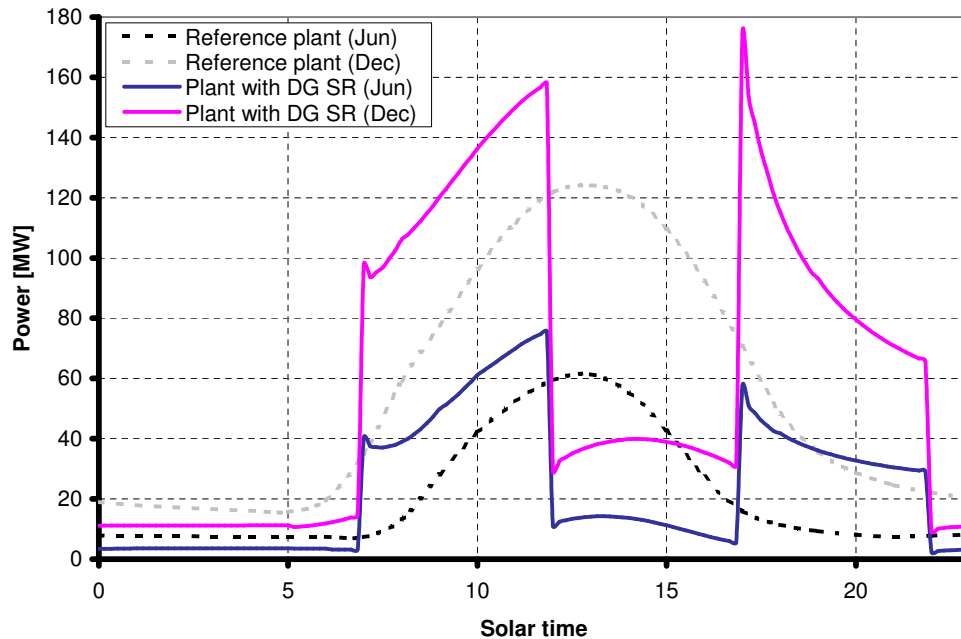


Figure 6.9: Daily solar chimney power plant performance as peak load facility - controlled power output through the inclusion of a double glazed secondary collector roof (DG = Double glazed; SR = Secondary roof)

Consider the performance curves in figure 6.9 for the plant incorporating a double glazed secondary roof. A similar daily power output profile to that of a plant with single glazed secondary roof is evident (figure 6.7). However, the power delivered during peak times are higher, while the power produced during off-peak times are lower when incorporating the double glazed secondary roof. These effects are due to better insulation of the warm collector air in the bottom section of the plant.

During off-peak times, the double glazing of the secondary roof causes less heat to be transferred from the bottom to the top section. The cooler air in the top section causes a reduced plant potential and ultimately reduced power output. With less heat being transferred to the top section, more heat is effectively stored in the ground during off-peak times. As such, more energy is available in the ground to be utilized during peak times, which explains the increased power delivered during peak times.

Table 6.9: Annual power output comparison, illustrating the effect of incorporating a double glazed secondary collector roof for the purpose of peak load electricity generation (DG = Double glazed)

Plant configuration	Annual power output [GWh]
Plant with secondary roof	342.7
Plant with DG secondary roof	356.8

Table 6.9 indicates that the net result of the higher daily peaks and lower lows is a somewhat higher annual power output of 4.1 % for a plant incorporating a double glazed secondary roof in comparison with a plant that employs a single glazed secondary roof.

In terms of peak load electricity generation, it is clear that the incorporation of a double glazed secondary roof provides greater control of the heat fluxes in the collector and ultimately greater control over the plant power output than when including a single glazed secondary roof. Note that the ground surface under the double glazed secondary collector roof may reach temperatures of up to 102 °C in summer.

6.5 Including a secondary and tertiary collector roof

The incorporation of a secondary and tertiary collector roof under the main collector canopy will split the airstream flowing through the collector into three different airstreams (see figure C.1 in Appendix C). It is believed that by controlling the flow of these airstreams, it will be possible to control plant power output more efficiently than with only two airstreams (when including only a secondary collector roof).

6.5.1 Modification of plant collector

The operation of the solar chimney power plant that includes a secondary and tertiary roof will be similar to the operation of a plant including only a secondary or double glazed secondary roof. With the inclusion of a tertiary roof, air will flow from the collector perimeter through three sections in the collector, namely the top, middle and bottom sections (figure C.1).

Air will flow constantly through the top section, while air-flow regulating mechanisms will control the air-flow at the outlet of both the middle and bottom sections, analogous to the idea illustrated by figure 6.4. Also, similar to the design in figure 6.5, it is proposed that multiple radial channels between the secondary and tertiary roofs, as well as between the tertiary roof and the ground surface will be able to facilitate the required collector air-flow regulation. These channels can be fully opened or closed off at the middle and bottom section outlets, thereby incrementally increasing or decreasing the collector air-flow area.

6.5.2 Plant specifications

The solar chimney power plant model of this section is based on the reference plant specifications in Chapter 2. A secondary and tertiary collector roof are included in the plant

model, having similar properties and dimensions to that of the main collector roof (as specified in table 2.1), except for the dimensions listed in table 6.10. In this particular example the perimeter height of the secondary ($H_{2,s}$) and tertiary ($H_{2,tr}$) collector roofs were chosen arbitrarily to fit under the reference main roof perimeter height. The inner diameter of both the secondary ($d_{3,s}$) and tertiary ($d_{3,tr}$) collector roofs is somewhat greater than the reference plant's main roof inner diameter, due to the inclusion of a transitional and single section in the collector of the plant (see figure C.1). The numbered subscripts of the specified dimensions apply to figure 2.1, while the subscript tr refers to properties of the tertiary collector roof.

Table 6.10: Secondary and tertiary collector roof specifications

Secondary Collector Roof (Glass)	
Perimeter (inlet) height	$H_{2,s} = 3.5$ m
Inner diameter	$d_{3,s} = 584$ m
Tertiary Collector Roof (Glass)	
Perimeter (inlet) height	$H_{2,tr} = 2$ m
Inner diameter	$d_{3,tr} = 584$ m

6.5.3 Control strategy: base load

A similar control strategy to that of section 6.3.3 is followed. However, the airflows through the middle and bottom sections are regulated (by the proposed air-flow regulating mechanisms) to keep the generated power as constant as possible, while maximizing the power produced.

At the outset, a target power is specified (with a tolerance of 1 %) which the plant model must try to achieve. At first, air only flows through the top section of the collector, while the air-flow regulating mechanisms at the middle and bottom section outlets are fully closed (i.e. infinite pressure drop across each of the mechanisms), making no air-flow possible through these sections. If the plant model cannot achieve the specified target with air flowing only through the top section, the pressure drop across the regulating mechanism in the middle section is incrementally decreased (causing an air-flow through the middle section) to the point where the target power is attained. If the target is not reached even with a zero pressure drop across the middle section's air-flow mechanism, the pressure drop across the air-flow regulating mechanism at the bottom section outlet is incrementally decreased (while still employing the maximum air-flow through the middle section) until the target power is attained. If the target cannot be achieved even with unrestricted air-flow through all three sections, the target power is decreased to a point where the plant can deliver the desired output.

When the plant is able to deliver more than the target power with unrestricted air-flow through all three sections, the same process follows in reverse. First, the pressure drop across the bottom section's air-flow mechanism is incrementally increased (until there is no air-flow in the bottom section) and thereafter the pressure drop is increased over the air-flow mechanism of the middle section. If the plant can still produce more than the target power with air-flow through only the top section, the target is increased.

Note that the incremental regulation of the pressure drops across the air-flow regulating mechanisms are defined in terms of percentages. This refers to the pressure drop across each mechanism as a percentage of the total pressure drop across the particular collector section (i.e. from the collector perimeter to the outlet at the end of the secondary and tertiary roof). The plant model employs percentage increments of 1 % for effective air-flow regulation.

6.5.3.1 Simulation and results

A computer simulation, employing the above-mentioned plant specifications and base load control strategy, is performed.

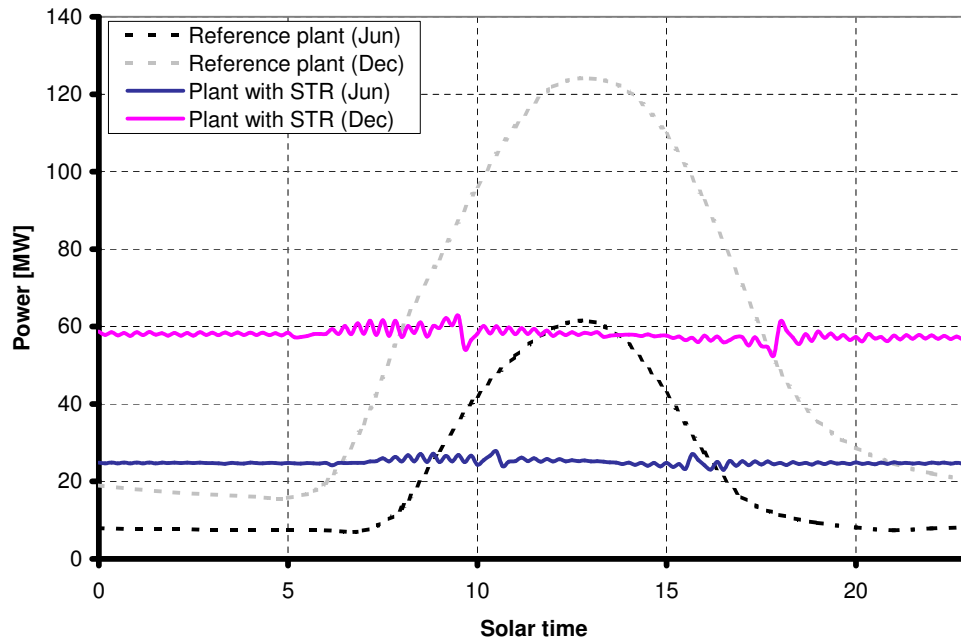


Figure 6.10: Daily solar chimney power plant performance as base load facility - controlled power output through the inclusion of a secondary and tertiary collector roof (STR = Secondary and tertiary roof)

Consider the performance curves for the plant that incorporates a secondary and tertiary collector roof. It is clear that such a plant, when subjected to the above-mentioned base load control strategy, produces an almost constant daily power output respectively for both winter and summer.

Though smoother, the daily power output profiles are very similar to those of a plant which only includes a double glazed secondary roof (see figure 6.8). With three airstreams, the plant is better able to control the required mass flows and heat fluxes necessary to generate the specified target power. Consequently, a somewhat smoother power generation profile is produced.

The illustrated small spikes in power production are incurred when, as mentioned before, a transition is made between a 99 % (minimal air-flow through the bottom section) and a 100 % (no air-flow through the bottom section) pressure drop across the air-flow regulating mechanism at the bottom section outlet. Finer control of the air-flow in the bottom section can reduce the magnitude of these fluctuations.

Table 6.11: Annual power output comparison, illustrating the effect of incorporating a secondary and tertiary collector roof for the purpose of base load electricity generation (DG = Double glazed)

Plant configuration	Annual power output [GWh]
Plant with DG secondary roof	362.7
Plant with secondary and tertiary roof	367.5

Another noticeable result is the comparable annual plant power output (approximately 1.3 % higher), compared to a plant that incorporates a double glazed secondary collector roof.

Note that the author realizes that the plant incorporating a secondary and tertiary roof employs respective top, middle and bottom section inlet heights of only 1.5 m, 1.5 m and 2 m, while the simulated plant with a double glazed secondary roof uses equal inlet heights of 2.5 m. It should be noted that the specification of the tertiary and secondary roof inlet heights were done arbitrarily, as to include a main collector roof with inlet height of $H_{2,r} = 5$ m (similar to reference plant). In actual fact, for the purpose of this chapter, the height of each section is not of greatest importance as the main focus is the controllability of the power output and not the optimization of the multi-sectioned solar chimney power plant. Note however that the performance of the solar chimney power plant will improve when greater roof heights are implemented.

In terms of base load electricity generation, the inclusion of a secondary and tertiary collector roof still seems to be a better method of controlling solar chimney power plant output compared to a plant which uses a double glazed secondary roof. However, the benefit (producing a more constant daily output) of including a secondary and tertiary roof into the solar chimney power plant is marginal. Yet the inclusion of a secondary and tertiary roof will be more expensive than only including a double glazed secondary roof. Therefore, the inclusion of a secondary and tertiary roof into the solar chimney power plant may not be very cost-effective. Additionally, take note that the ground surface under the tertiary collector roof may reach temperatures of up to 102 °C in summer.

6.5.4 Control strategy: peak load

A similar control strategy to that of section 6.3.4 is followed. However, during peak demand times the air-flow regulating mechanisms at the middle and bottom section outlets are fully opened (zero pressure drop across each mechanism) and the plant operates at full capacity, while during off-peak times these mechanisms are fully closed (causing no air-flow in the middle and bottom sections) and the plant operates at minimum capacity.

6.5.4.1 Simulation and results

A computer simulation, employing the above-mentioned plant specifications and peak load control strategy, is performed.

Consider the performance curves in figure 6.11 for the plant incorporating a secondary and tertiary collector roof. We see that the curves closely resemble those of a plant employing only a double glazed secondary roof (figure 6.9). However, figure 6.11 illustrates marginally higher output during peak times and more significantly lower output during off-peak times.

The somewhat reduced output during off-peak times are largely as a result of a lower mass-flow rate predicted through the top section of the plant. This is due to the fact that a smaller top section inlet height of 1.5 m is employed, compared to the top section inlet height of 2.5 m used by the plant incorporating a double glazed secondary roof. With a smaller top section flow area, the plant model predicts a lower mass-flow rate through the top section in order to achieve optimal performance. Please refer to section 6.5.3.1, where these dimensional selections are discussed.

The slightly higher output during peak times are due to the fact that less heat is extracted (compared to a plant employing a double glazed secondary roof) from the ground during off-peak times, making it available to be utilized during peak times.

From table 6.12 it is apparent that the net effect of the above-mentioned daily power differences is a slightly lower annual power output (3.2 %) for a plant that employs a secondary and tertiary roof, compared to a plant incorporating a double glazed secondary roof.

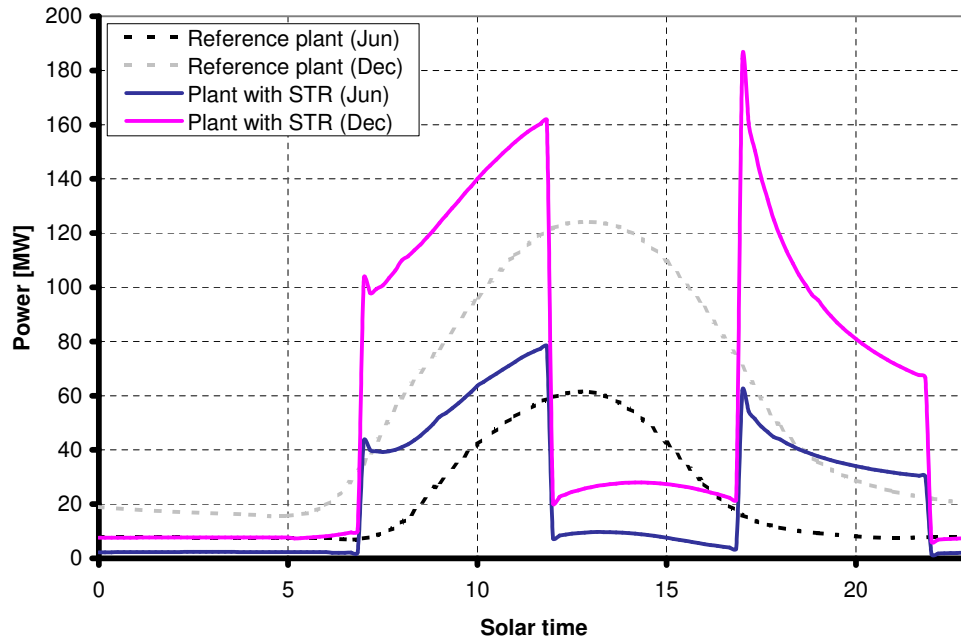


Figure 6.11: Daily solar chimney power plant performance as peak load facility - controlled power output through the inclusion of a secondary and tertiary collector roof (STR = Secondary and tertiary roof)

Table 6.12: Annual power output comparison, illustrating the effect of incorporating a secondary and tertiary collector roof for the purpose of peak load electricity generation (DG = Double glazed)

Plant configuration	Annual power output [GWh]
Plant with DG secondary roof	356.8
Plant with secondary and tertiary roof	345.3

When considering peak load power generation, this section reveals that even greater control over daily power output is possible through the inclusion of a secondary and tertiary roof instead of a double glazed secondary roof. Note that the ground surface under the tertiary collector roof may reach temperatures of up to 101 °C in summer.

6.5.5 Control strategy: Seasonal base load

Section 6.5.3 investigates a strategy of controlling the solar chimney power plant output to keep the generated power as constant as possible, while also maximizing the delivered power. This strategy, however, does not attempt to minimize the seasonal variation in the power produced by the plant. This section now investigates a control strategy which minimizes seasonal output variation, which involves the storage of energy during the warmer months of the year in order to utilize (extract) it during the colder months. This is done in an effort to keep the power delivered by the plant constant throughout an entire year, irrespective of the season.

A similar control strategy to that of section 6.5.3 is followed here. However, during the warmer half of the year the air-flow regulating mechanism at the bottom section outlet remains fully closed throughout this time. During these months, air flows constantly through the top section, while the air-flow through the middle section is regulated (by the air-flow

regulating mechanism at the middle section outlet) to keep the generated power as constant as possible, while maximizing the power produced. With no air-flow through the bottom section during these months, energy is effectively stored in the ground.

During the colder half of the year, air flows constantly through the top section of the collector, while air-flow is again regulated through the middle and bottom sections in order to keep the generated power as constant as possible, while maximizing output. In these months, the energy stored in the ground during the warmer months is systematically extracted and utilized.

6.5.5.1 Simulation and results

A computer simulation, employing the above-mentioned plant specifications and seasonal base load control strategy, is performed.

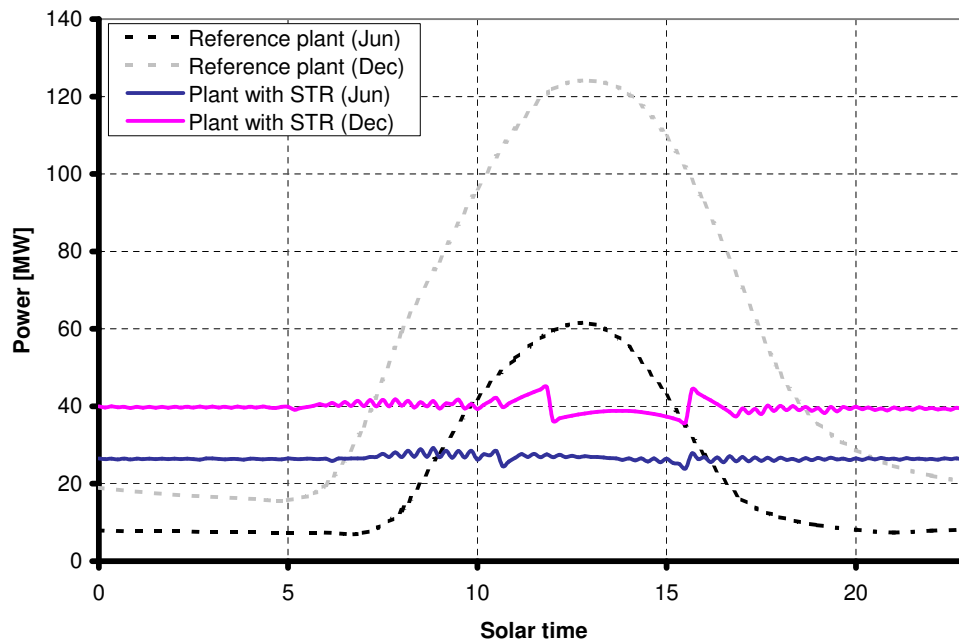


Figure 6.12: Daily solar chimney power plant performance as base load facility - controlled power output through the inclusion of a secondary and tertiary collector roof (STR = Secondary and tertiary roof), while minimizing seasonal output variations

Consider the performance curves for the plant that incorporates a secondary and tertiary collector roof. It is clear that such a plant, when subjected to the above-mentioned seasonal base load control strategy, produces an almost constant daily power output respectively for both winter and summer.

It is evident, when compared to figure 6.10, that the difference between the summer and winter power production is significantly reduced. However, this is primarily due to the drastically reduced summer output, as a direct result of the plant not being able to utilize the hot air in the bottom section during this season. Figure 6.12 clearly shows an insignificant increase in winter power production, compared to the winter output in figure 6.10. Therefore, the energy stored during the warmer months of the year does not make a substantial impact (when extracted) on the plant power production during the colder months.

Table 6.13 indicates an annual power output reduction of 19.1 % for a plant incorporating a secondary and tertiary collector roof and subjected to a base load control strategy, while

Table 6.13: Annual power output comparison, illustrating the effect of employing a control strategy to minimize seasonal output variations; each plant model incorporates a secondary and tertiary collector roof and both models are subject to a base load control strategy

Plant configuration	Annual power output [GWh]
Plant with secondary and tertiary roof	367.5
Plant with secondary and tertiary roof (seasonal)	297.2

minimizing seasonal output variations, compared to the same plant that is only subjected to a base load control strategy. This major decline in annual output is due to the significantly decreased summer power output, as mentioned previously.

The results of this section suggest that seasonal energy storage in order to facilitate a constant power output throughout an entire year is ineffective. Note that the ground surface under the tertiary collector roof may reach temperatures of up to 114 °C in summer.

6.6 Including plastic covered water tanks

Due to the high specific heat capacity of water, the incorporation of water tanks under the main collector roof will increase the energy (heat) storage capability of the solar chimney power plant significantly. This means that the inclusion of these tanks into the plant should alter the daily power output profile measurably, thereby facilitating static control over plant output.

In a supplement to his book, Schlaich (1994) indicates that, through the inclusion of water filled black tubes under the collector roof of the solar chimney power plant, the plant output can be controlled to be much more uniform. For a water depth of 0.2 m, he predicts a daily plant output between approximately 30 % and 42 % of the peak output for the same plant not incorporating water filled tubes.

Bernardes *et al.* (2003) also studied the effects of water storage on the solar chimney power plant output. They predict that, for a water depth of 0.1 m employed over the total collector area, daily plant output can be controlled to within (approximately) 10 % and 75 % of the peak output of the same plant employing no water storage. They also find that varying the area employed for water storage has a negligible effect on the total daily power output produced (therefore, also on the annual output produced).

This section also investigates the possibility of facilitating a more uniform daily solar chimney power plant output through the inclusion of transparent plastic covered water tanks into the plant model.

Note that the inclusion of water tanks is a static and not a dynamic method of controlling the power production of the solar chimney power plant. However, it may be utilized in conjunction with other devices discussed in this chapter to more effectively control plant output. The plant evaluated in this section does not include a secondary or tertiary collector roof, only a main roof. Therefore, no dynamic control over output is practiced by the regulation of air-flow underneath the collector roof. The plant simply produces the maximum power output possible throughout the day.

6.6.1 Modification of plant collector

A multitude of relatively shallow water tanks are arranged on the ground surface under the collector roof, thereby replacing the ground upon which it rests as the energy storage mechanism. The tanks are filled to the brim with water and each tank is covered by a thin transparent plastic film to suppress evaporation. The inner bottom surface of each tank is black, while the bottom and sides are insulated. The inner sides of the tanks are covered by

a highly reflective material to minimize the effects of these surfaces on the convective heat transfer and subsequent water temperature distribution in the tanks.

This section investigates the incorporation of water tanks for various fractions of the total ground surface area under the collector roof. For the case where only part of the ground surface area is covered by water tanks, the tanks are arranged over the inner collector area (see figure D.1).

6.6.2 Plant specifications

The solar chimney power plant model of this section is based on the reference plant specifications in Chapter 2. In addition, plastic covered water tanks are arranged under the main collector roof over part or the entire ground surface area (see figure D.1), with dimensions as specified in table 6.14. All dimensional details and solar properties of the plastic covered water tanks are taken from a study performed by Lombaard (2002), while the refractive index of water is taken from Duffie and Beckman (1991).

Table 6.14: Water tanks specifications for each of the following simulations

Water tanks (Plastic film and water)	
Thickness of film	$t_f = 0.0002$ m
Refractive index of film	$n_f = 1.6$
Emissivity of film	$\epsilon_f = 0.8$
Roughness of film	$\varepsilon_f = 0$ m
Extinction coefficient of film	$C_{fe} = 200$ m ⁻¹
Refractive index of water	$n_w = 1.333$
Depth of water tanks	$t_w = 0.2$ m, 0.5 m or 1 m
1/2 Area outer diameter	$d_{wt} = 3528$ m
3/4 Area outer diameter	$d_{wt} = 4356$ m
Full Area outer diameter	$d_{wt} = 5000$ m

6.6.3 Assumptions

The simulations of this section are based on the following assumptions concerning the implemented water tanks:

- No water is evaporated from the water tanks.
- No air gap exists between the plastic film and the water surface.
- No heat is lost to the environment through the water tank bottom or sides.
- No heat is stored in the ground underneath the water tanks.
- The water inside the tank is a bulk of water at a mean temperature T_w .
- The thermal capacity of the plastic film is negligible. Therefore, the plastic film and mean water temperature are assumed to be approximately equal.
- Water tanks cover the entire collector area specified. Therefore, the numerical model essentially models the covered area as one large water tank.

6.6.4 Simulation and results

Two sets of simulations are performed in this section, employing the above-mentioned plant specifications. Firstly, the performance of a plant incorporating water tanks over a half, three-quarters and total collector area is investigated, using a tank depth of 0.2 m. Secondly, the performance of a plant that incorporates water tanks over the entire collector area is evaluated for tank depths of 0.2 m, 0.5 m and 1 m.

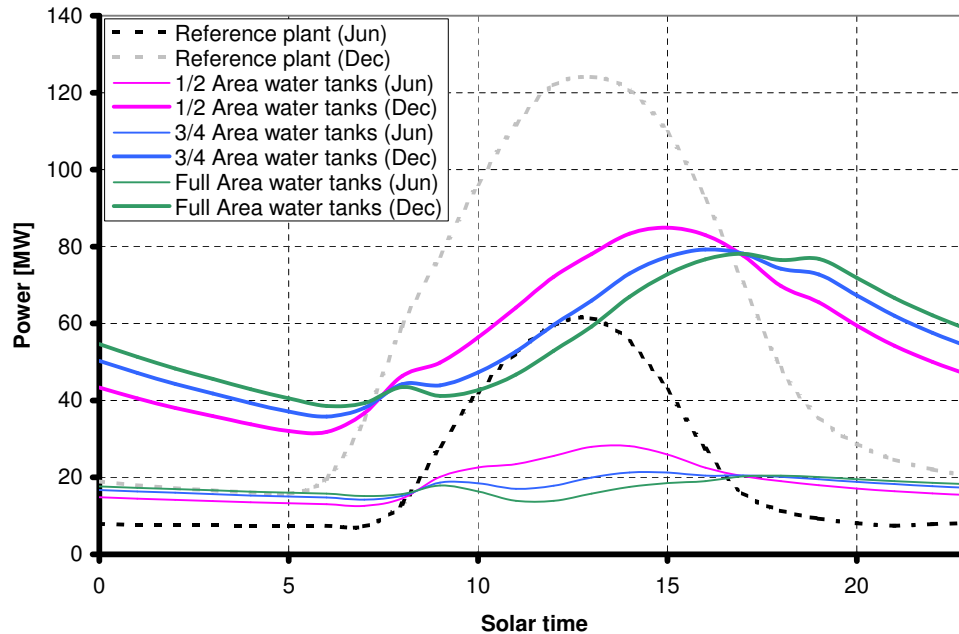


Figure 6.13: Daily solar chimney power plant performance for a plant incorporating water tanks over various fractions of the collector ground surface area ($t_w = 0.2$ m)

From figure 6.13 it is evident that the inclusion of water tanks into the solar chimney power plant has a significant influence on the daily power output profile of the plant, compared to the profile of the reference plant. The plant model incorporating water tanks predicts much lower power production during the daytime, while predicted output during night-time is much higher (for all the presented cases). Due to the high heat capacity of water, a significantly increased fraction of the daily solar radiation is stored in the water, compared to the ground storage of the reference plant. The increased storage means that less heat is transferred to the collector air, which in turn produces a lower power output during the day. The greater amount of energy stored during the day is then again released at night, facilitating an increased nocturnal power output.

It is also clear from figure 6.13 that the greater the area covered by water tanks, the greater the overall energy storage, giving increasingly lower power output during the daytime and increasingly greater power output during night-time.

For a collector area fully covered by water tanks, results predict a daily summertime plant output of between 31 % and 63 % of the peak output of the reference plant, which employs no water storage. Thus the predicted output is not as uniform as the results presented by Schlaich (1994). This difference is presumably due to the fact that Schlaich (1994) employs water filled black tubes, while this study uses plastic covered water tanks as storage mechanism. It is difficult to compare the particular results presented here to the publication of Bernardes *et al.* (2003), as they employ a different maximum water depth and do not specify whether the entire collector area employs water storage at that depth. However, an

additional simulation was performed, based on the reference plant that incorporates water storage over the total collector area and employing a water tank depth of 0.1 m. Results (not shown here) predict a daily summertime power output between 13 % and 90 % of the peak output of the reference plant, which does not incorporate water storage. Therefore, the predicted output is also not as uniform as the mentioned results by Bernardes *et al.* (2003). It is believed that this discrepancy is due to the different methods employed for modelling the water storage mechanisms.

Another trend which is noticeable from figure 6.13 is the initial rise and then slight drop in power output between 08:00 and 09:00 on summer mornings. Alternatively, there is also a power decrease followed by a slight increase in output between 18:00 and 19:00 during summer evenings. These trends become more pronounced the greater the collector area is that is covered by water tanks. These occurrences are explained by the fact that the meteorological data for the reference site predict a significant ambient temperature rise from 08:00 to 09:00 and a significant ambient temperature drop from 18:00 to 19:00 during summertime. The sudden ambient temperature rise at 09:00 reduces the driving potential of the plant considerably, thereby causing a slight drop in power output. Conversely, the sudden ambient temperature drop at 19:00 increases the driving potential, causing a somewhat increased power output.

The greater the collector area covered by water tanks, the more sensitive the plant system becomes to these sudden temperature changes. This can be explained as follows. The reference plant, for example, experiences much higher collector air temperatures and mass-flow rates at 09:00 in summertime than the plant models incorporating water tanks. These temperatures and flow rates are so high that the sudden rise in ambient temperature at 09:00 has a negligible effect on the power output profile of the plant (note that all plant models experience similar meteorological conditions). Similarly, the reference plant also experiences much lower collector air temperatures and mass-flow rates at 19:00, compared to the plant models employing water tanks. As such, the temperatures and flow rates are so low that the sudden decrease in ambient temperature at 19:00 has a negligible effect on the plant performance.

The presence of an exposed ground surface is the cause of the insensitivity to the sudden ambient temperature fluctuations. Due to the lower heat capacity of the ground to that of water, more energy is transferred to the collector air during the morning periods, while less energy is available during the early evening periods. Therefore, the greater the exposed ground surface area, the less sensitive the plant is to the mentioned ambient temperature fluctuations.

Table 6.15: Annual power output comparison, illustrating the effect of incorporating water tanks over various fractions of the collector ground surface area ($t_w = 0.2$ m)

Plant configuration	Annual power output [GWh]
Reference plant	336
1/2 Area water tanks	327.9
3/4 Area water tanks	327
Full Area water tanks	327.4

Table 6.15 indicates that water is a very good storage mechanism. Almost all of the energy that is stored in the water during the day is released at night, giving at most only a 2.7 % (for the case where three-quarters of the collector area is covered by water tanks) decrease in annual power output, compared to the reference plant. This compares well with the findings of Bernardes *et al.* (2003).

Note that for the plant that incorporates water tanks over the entire collector area, with a tank depth of 0.2 m, the water temperature may reach temperatures of up to 60 °C in summer.

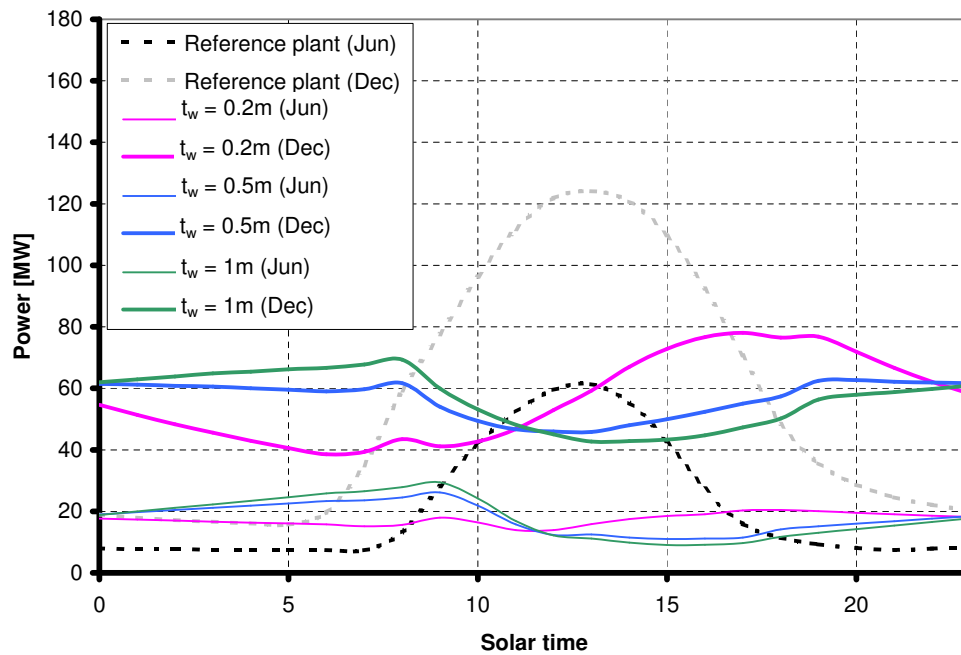


Figure 6.14: Daily solar chimney power plant performance for a plant incorporating water tanks over the entire collector ground surface area; effect of varying water tank depths

Figure 6.14 indicates that by increasing the depth of the water tanks, it is even possible for the solar chimney power plant to produce more power during the night-time than during the daytime. With more water in the tanks, more energy is stored during the day, resulting in a decreased daytime output. The enhanced storage during daytime means that more energy is available to be released at night, giving increased nocturnal power production. It is also clear that by increasing the water tank depth from 0.2 m to 0.5 m facilitates a more uniform daily summertime power output profile, while a further increase to 1 m produces a less uniform output.

Table 6.16: Annual power output comparison, illustrating the effect of varying water tank depths (total collector area covered by water tanks)

Plant configuration	Annual power output [GWh]
Reference plant	336
$t_w = 0.2$ m	327.4
$t_w = 0.5$ m	329.2
$t_w = 1$ m	331

Table 6.16 shows that an increased water tank depth does not affect the annual power output of the plant significantly. This is illustrated by the fact that increasing the tank depth from 0.2 m to 1 m only produces a 1.1 % rise in annual yield.

In conclusion therefore, it seems that the inclusion of water tanks under the collector roof is a good mechanism for statically controlling the output of the solar chimney power plant. In the quest for the plant to act as a base load electricity generating facility, a plant incorporating water tanks are able to facilitate a significantly more uniform power output than that of the reference plant.

Note that the drag effect that the water tanks will have on the air-flow under the collector roof is expected to be small and is therefore not accounted for by the numerical model.

6.7 Including a delta ground surface configuration

A key factor in controlling the power output of the solar chimney power plant is the rate at which heat is stored in and extracted from the ground. Therefore the higher the heat transfer rate at the ground, the more control is possible over the plant's power output.

Personal communication with Kröger (2004-2006) revealed the possibility of including a delta ground surface configuration under the collector roof, which will enhance the heat transfer rate at the ground.

The inclusion of a delta ground configuration is a static and not a dynamic method of controlling the power production of the solar chimney power plant. However, it may be utilized in conjunction with other devices discussed in this chapter to more effectively control plant output. The plant evaluated in this section does not include a secondary or tertiary collector roof, only a main roof. Therefore, no dynamic control over output is practiced by the regulation of air-flow underneath the collector roof. The plant simply produces the maximum power output possible throughout the day.

Consequently, the main objective of this section is to investigate the possible facilitation of a more uniform daily solar chimney power plant output through the inclusion of a delta ground configuration in the plant model.

6.7.1 Implication of a delta ground configuration

We firstly consider the case of energy extraction from the ground. The energy extracted from the ground must be utilized. Therefore, as the radiation from the ground surface only heats the collector roof, the main contributor to the power output of the plant is the convective heat transfer from the ground surface to the collector air. The variables determining the magnitude of this convective heat transfer is the convective heat transfer coefficient, the temperature difference between the ground surface and the collector air and the area of the exposed ground surface.

Secondly, the storage of energy in the ground is facilitated by conduction. The magnitude of the conduction heat transfer is determined by the thermal conductivity of the ground, the ground temperature gradient and the area of the exposed ground surface.

As previous studies and the current one have already, for the most part, investigated the convective heat transfer coefficient and evaluated various efforts of increasing the ground temperature, the only other logical step would be to increase the exposed ground surface area. After consulting Kröger (2004-2006) personally, it was decided to modify the originally flat ground surface to have a delta configuration. Practically, this would require earth moving equipment to change the face of the ground surface to have a triangular shape, as shown in figure 6.15.

The delta configuration ground surface increases the ground area exposed to convection and conduction heat transfer compared to the flat ground surface area (Note that radiation heat transfer considers essentially only the projected area of the ground). This enhances the rate at which energy is stored and extracted from the ground, thereby providing a mechanism to control the power output of a solar chimney power plant. Personal communication with Coetzee (2004) revealed that the maximum realistic angle at which Sand can be heaped

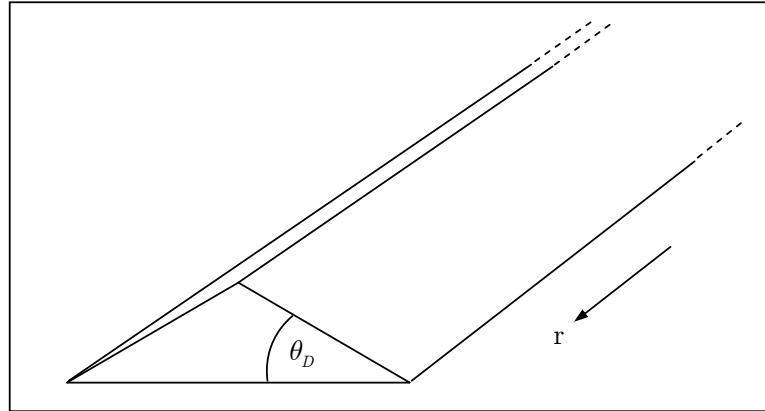


Figure 6.15: Delta ground surface configuration

(angle of repose) will be approximately $\theta_D = 35^\circ$, although other angles are possible depending on material characteristics. With the ground surface arranged at this angle, the exposed ground surface area increases by approximately 22 %.

However, another factor has to be considered. The implementation of a delta ground configuration will effectively decrease the through-flow area under the collector roof, unless the roof is raised. With a smaller area through which to flow, the air mass-flow rate through the plant will be altered, which may have significant implications.

6.7.2 Modification of plant collector

A possible design for incorporating a delta ground configuration in the solar chimney power plant is to arrange the ground under the collector roof to form multiple radial "strips" of ground, as shown in figure 6.16. In order to arrange multiple strips while keeping the angle of repose (see figure 6.15) constant, these strips will decrease in height and width from the perimeter inwards toward the chimney, while the percentage of increased ground surface (exposed) area will remain constant throughout.

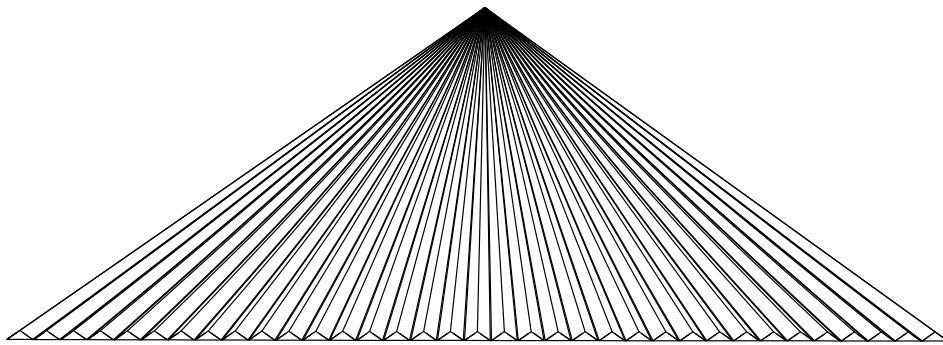


Figure 6.16: A section of the collector, showing the proposed idea of arranging the collector ground surface to have a delta configuration

This type of ground configuration can be incorporated in a solar chimney power plant that includes only a main collector roof or one which includes a secondary or even tertiary collector roof. Ultimately, the cost of shaping such a large ground surface to have a delta

configuration will have serious cost implications. However, these costs should be weighed against the benefit that the configuration provides in terms of plant output control.

6.7.3 Plant specifications

The solar chimney power plant model of this section is based on the reference plant specifications in Chapter 2. A delta ground configuration is included in the plant model, with dimensions as given by table 6.17. The numbered subscripts of the specified dimensions apply to figure 2.1, while the subscript D refers to properties of the delta ground configuration.

Table 6.17: Delta ground configuration specifications

Delta Ground Configuration (Sandstone)	
Perimeter (inlet) height	$H_{2,D} = 1 \text{ m}, 3 \text{ m or } 5 \text{ m}$
Outer diameter	$d_{2,D} = 2500 \text{ m}$
Inner diameter	$d_{3,D} = 400 \text{ m}$
Angle of repose	$\theta_D = 15^\circ, 35^\circ \text{ or } 60^\circ$

6.7.4 Assumptions

The simulations of this section are based on the following assumptions concerning the delta ground configuration:

- Despite the angle of the ground surface it should be noted that, for the sake of simplicity, simple one-dimensional conduction into the ground (perpendicular to the ground surface) is still assumed.
- Although added costs will be incurred in order to arrange a delta ground surface configuration with angle of repose greater than 35° , this section investigates the possibility as a theoretical exercise.
- This section assumes an ideal case where the entire specified ground surface area is utilized for increased heat transfer through the inclusion of a delta configuration. However in reality, due to the fact that earth moving is not such an exact science and that access roads would be required for such earth moving equipment, less than the entire area will be usable.

6.7.5 Simulation and results

Two sets of simulations are performed for a plant that incorporates a delta ground configuration (over the entire collector area), employing the above-mentioned plant specifications. Firstly, the effect on plant performance of varying the angle of repose (see figure 6.15) between 15° and 60° is investigated. For these simulations, a constant delta perimeter height of 1 m is assumed. Secondly, the performance of a plant with varying delta perimeter heights of 1 m, 3 m and 5 m is evaluated. These simulations assume a constant angle of repose of 35° .

Figure 6.17 illustrates the effect on daily power production of increasing the angle of repose for the delta ground surface configuration. Results predict that a greater angle of repose increases the nocturnal and decreases the daytime power production. This phenomenon can be explained as follows. The larger the angle of repose, the larger the exposed ground surface area. Due to the larger exposed surface area, ground surface temperatures are lower throughout a 24-hour period in comparison to a plant incorporating a flat ground

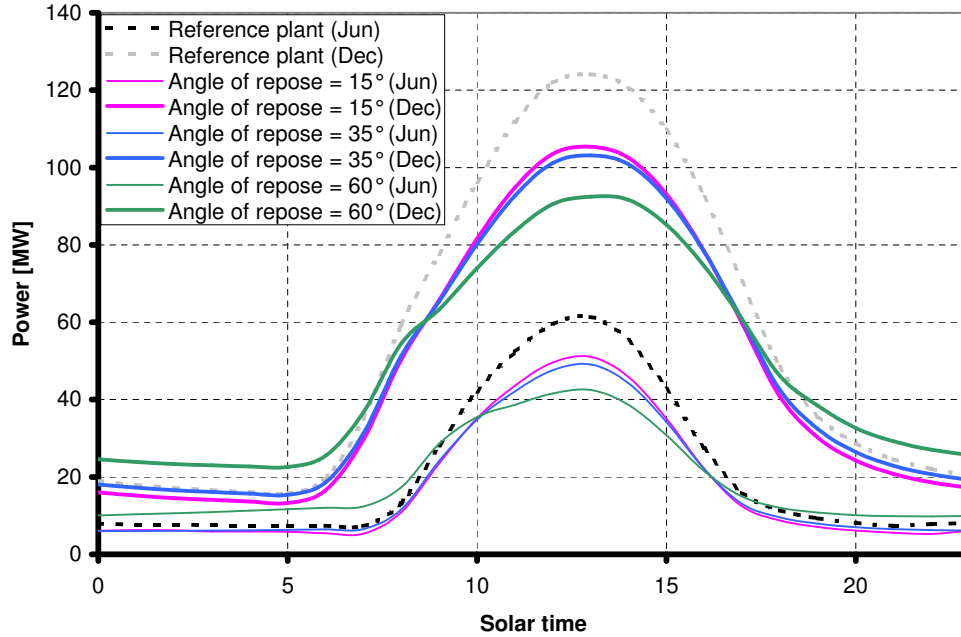


Figure 6.17: Daily solar chimney power plant performance for a plant incorporating a delta ground surface configuration with varying angles of repose ($H_{2,D} = 1$ m)

surface. It is important to note that the heat transfer rate from the ground to collector air is strongly dependent on two variables, namely the exposed surface area and the ground surface temperatures. During night-time, the net effect of an increased surface area and lower ground temperatures is an increased heat transfer rate from the ground to the collector air, resulting in a subsequent increased power output. During the daytime however, the net effect is a decreased plant output, predominantly due to significantly lower ground surface temperatures.

Figure 6.17 indicates another occurrence clearly. In the early mornings, a plant incorporating an angle of repose of $\theta_D = 60^\circ$ experiences a net increased heat transfer rate at the ground surface. Consequently, the solar energy striking the ground surface is immediately transferred to the collector air, giving a slight power production increase over the early morning period.

Table 6.18: Annual power output comparison, illustrating the effect of incorporating a delta ground configuration under the collector roof and the effect of varying angles of repose ($H_{2,D} = 1$ m)

Plant configuration	Annual power output [GWh]
Reference plant	336
$\theta_D = 15^\circ$	280.6
$\theta_D = 35^\circ$	286
$\theta_D = 60^\circ$	299.6

Table 6.18 shows decreased annual power outputs for the plant models incorporating delta ground configurations compared to the reference plant (with flat ground surface). These reductions are a result of a decreased through-flow area under the collector roof. The construction of a delta ground surface configuration obstructs some of the air flowing under the collector roof. The effect of a smaller through-flow area is an increased air velocity

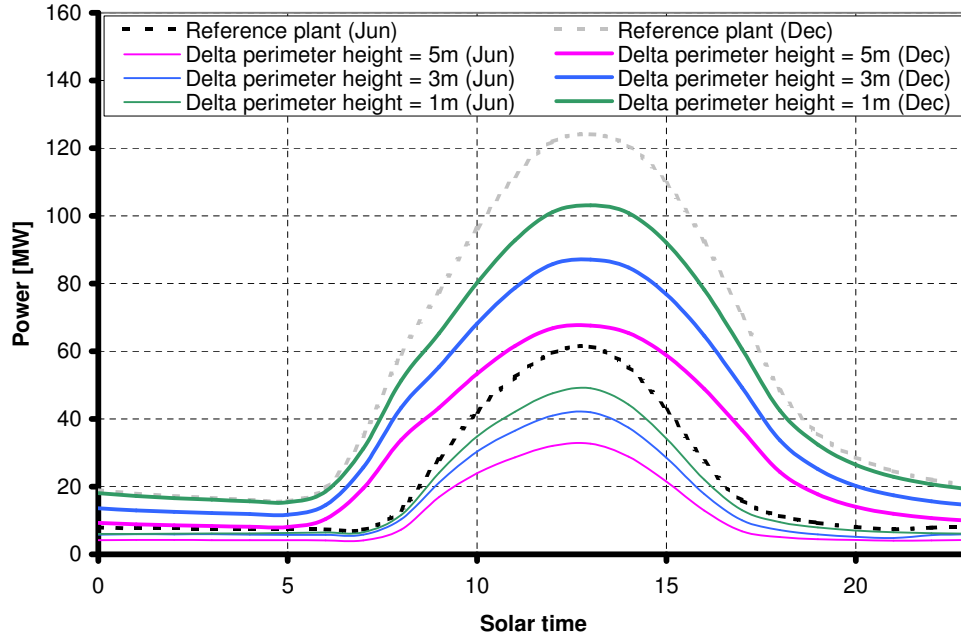


Figure 6.18: Daily solar chimney power plant performance for a plant incorporating a delta ground surface configuration with varying perimeter heights ($\theta_D = 35^\circ$)

Table 6.19: Annual power output comparison, illustrating the effect of incorporating a delta ground configuration under the collector roof and the effect of varying the delta perimeter height ($\theta_D = 35^\circ$)

Plant configuration	Annual power output [GWh]
Reference plant	336
$H_D = 1$ m	286
$H_D = 3$ m	236.3
$H_D = 5$ m	182.9

through the plant, which increases the heat transfer rate from the ground to the collector air, but also from the collector air to the roof. With greater heat transfer to the roof, more energy is lost to the environment which subsequently reduces the power generated by the plant. This trend is clearly indicated by figure 6.18 and table 6.19, showing reductions in plant performance with increasing delta perimeter heights.

Table 6.18 also reveals that increasing the angle of repose increases the exposed ground surface area, which in turn increases the effective heat transfer rate from the ground to the collector air, causing increased annual power output.

In conclusion therefore, it is clear that the incorporation a delta ground surface configuration does not facilitate a significantly more uniform daily plant output. However, if such a configuration is to be included, the greatest possible angle of repose and smallest possible perimeter height should be employed (as an alternative, the collector roof perimeter height can also be increased). This is advantageous when considering the delta height, as it is less expensive for ground moving equipment to construct smaller delta configurations.

Vegetation Under the Collector Roof

The question of whether a large-scale solar chimney power plant is financially viable solely as a power generating facility remains unanswered. The idea of adding value to the solar chimney system through the pursuit of secondary ventures has in recent times come to the fore. One such venture involves the solar collector taking on a secondary function as a greenhouse for agricultural purposes. If found to be viable, farmers could grow their crops in certain areas under the collector roof.

Appendix F derives relevant conservation equations necessary for the inclusion of vegetation in the existing numerical solar chimney model.

This chapter investigates the possibility of including vegetation under the collector roof of the solar chimney power plant. Equations are derived for determining the rate of evapotranspiration from the vegetation surface. The discretization scheme employed for the vegetation and ground energy equations in the vegetation section (at $z > 0$) is presented. Simulations are then performed, evaluating the effect on plant performance when incorporating vegetation. In addition, the influence on plant performance is evaluated when modelling the air (with certain vapor content) inside the chimney and atmosphere surrounding the plant according to different temperature lapse rates.

7.1 Modification under collector roof

With the inclusion of vegetation in the collector of the solar chimney power plant, the existing numerical model must be modified. As is evident from figure F.1 in Appendix F, the collector is effectively divided into two sections, namely the vegetation and ground section. It is assumed that the vegetation will be planted around the entire circumference (360°) of the collector, inwards from the collector perimeter to a specified radius, r_{ve} . Planting vegetation nearer to the perimeter of the collector allows vegetation to be included under the collector roof, while eliminating the possibility that the vegetation may be scorched by the high collector temperatures near the chimney.

7.2 Determining the rate of evapotranspiration

As the air under the collector roof flows over and through the vegetation, it will absorb moisture from the plants and the accompanying ground surface (in which they grow). In order to evaluate the effect of vegetation on the performance of a solar chimney power plant, it is necessary to determine the rate at which the water vapor is absorbed. This rate is known

as the rate of evapotranspiration. Note that all thermophysical properties are evaluated for an air-vapor mixture, from the relations by Kröger (2004).

According to Monteith and Unsworth (1990), the rate of evapotranspiration can be evaluated using

$$\left(\frac{\dot{m}_v}{A}\right) i_{fg} = \frac{\Delta_{avg} I_{net} + (vpd) h_{veh}}{\Delta_{avg} + \gamma^*} \quad (7.1)$$

known as the Penman-Monteith equation, where (\dot{m}_v/A) is the rate of water evaporation from the transpiring surface per unit area, i_{fg} is the latent heat of evaporation, Δ_{avg} is the average slope of the saturated vapor pressure line, I_{net} is the net radiation absorbed by the vegetation, vpd is the vapor pressure depression, h_{veh} is the convective heat transfer coefficient from the transpiring surface to the collector air and γ^* is the adjusted psychrometric constant. The latent heat of evaporation on the left-hand-side of equation (7.1) is determined at the vegetation surface temperature. By assuming the collector air and water vapor to be ideal gases, the Clapeyron-Clausius equation can be used to find the average slope of the saturated vapor pressure line, as follows (Çengel and Boles, 1998)

$$\Delta_{avg} \approx \left(\frac{dp}{dT}\right)_{sat} = \frac{i_{fg} p_{sat}}{T_{avg}^2 R_v} \quad (7.2)$$

where R_v is the gas constant for water vapor. The terms i_{fg} and p_{sat} of equation (7.2) represent the latent heat of evaporation and the saturated vapor pressure respectively and both are evaluated at the average between the dry-bulb and wet-bulb air temperatures:

$$T_{avg} = \frac{1}{2} (T + T_{wb}) \quad (7.3)$$

The saturated vapor pressure is calculated from an equation by Kröger (2004), as follows

$$p_{sat} = 10^z \quad (7.4)$$

where

$$\begin{aligned} z = & 10.79586(1 - 273.16/T_{avg}) + 5.02808 \log_{10}(273.16/T_{avg}) \\ & + 1.50474 \times 10^{-4} \left[1 - 10^{-8.29692((T_{avg}/273.16)-1)} \right] \\ & + 4.2873 \times 10^{-4} \left[10^{4.76955(1-(273.16/T_{avg}))} - 1 \right] + 2.786118312 \end{aligned} \quad (7.5)$$

The net radiation absorbed by the vegetation is calculated as follows:

$$I_{net} = (\tau_e \alpha_{ve})_b I_{hb} + (\tau_e \alpha_{ve})_d I_{hd} - q_{ver} - q_{cond} \quad (7.6)$$

where τ_e is the effective transmittance of the glass collector roof, α_{ve} is the absorptivity of the vegetation surface under the collector roof, I_h is the solar radiation on a horizontal surface, q_{ver} is the radiation exchange of the vegetation with the collector roof and q_{cond} is the energy conducted into or out of the ground. The subscripts b and d denote the beam and diffuse solar radiative components respectively while the brackets in equation (7.6) represent the transmittance-absorptance product of the vegetation. The vapor pressure depression is defined as the difference between the actual vapor pressure and the saturation pressure at the same dry-bulb air temperature and is given by

$$vpd = p_{sat} - p_v \quad (7.7)$$

The saturated vapor pressure (p_{sat}) of equation (7.7) is determined from equation (7.4) and (7.5) at the dry-bulb collector air temperature. According to Çengel and Boles (1998), the actual vapor pressure is ascertained by

$$p_v = \phi p_{sat} \quad (7.8)$$

where ϕ is the relative humidity of the collector air. Çengel and Boles (1998) also present the following relation for evaluating the relative humidity

$$\phi = \frac{\omega p}{(0.622 + \omega)p_{sat}} \quad (7.9)$$

where p is the total air pressure under the collector roof and ω is the absolute air humidity, which is determined from the water vapor continuity equation (equation (F.3) in Appendix F).

The convective heat transfer coefficient h_{veh} is evaluated according to the strategy in Chapter 2 for evaluating h_{gh} . The heat transfer equations in Chapter 2 by Burger (2004) were developed for a smooth flat surface and employ respective skin friction coefficients of $c_f = 0.0052$ and $c_f = 0.0044$. However, according to Westdyk (2005-2006), by substituting an equivalent friction coefficient of 0.023971 for these skin friction values, h_{veh} can be more accurately calculated for air-flow over a particular vegetation surface (short grass). This equivalent friction coefficient is also employed in the calculation of the vegetation surface shear stress term. When implementing these changes, we find the following alternative forms of the equations by Burger (2004):

$$h_{veh} = \left[0.2106 + 0.011986 v \left(\frac{\rho T_m}{\mu g \Delta T} \right)^{1/3} \right] / \left[\frac{\mu T_m}{g \Delta T c_p k^2 \rho^2} \right]^{1/3} \quad (7.10)$$

$$h_{veh} = 3.87 + 0.011986 \left(\frac{v \rho c_p}{Pr^{2/3}} \right) \quad (7.11)$$

where T_m is the mean of the vegetation surface and dry-bulb collector air temperature, while ΔT is the difference between these two temperatures. All properties of equations (7.10) and (7.11) are evaluated for an air-vapor mixture at the mean temperature. It should be noted that these two equations do not necessarily represent the physics of evapotranspiration, but do however satisfy the Penman-Monteith equation and also compare well with the heat transfer coefficient values found by other researchers.

Conradie (1989) gives the following relation for the determination of the psychrometric constant

$$\gamma = \frac{c_{p,ma} p}{0.622 i_{fg,wb}} \quad (7.12)$$

where $c_{p,ma}$ is the specific heat capacity of the air-vapor mixture (evaluated at the dry-bulb collector air temperature) and $i_{fg,wb}$ is the latent heat of evaporation evaluated at the wet-bulb collector air temperature.

According to Monteith and Unsworth (1990), the resistance to vapor transfer experienced by plant leaves are the sum of a boundary layer resistance r_V and a stomatal surface resistance r_s . The boundary layer resistance depends on the leaf dimensions and wind speed over them, while the stomatal resistance depends on the geometry, size and spacing of stomatal pores on the leaves. Monteith and Unsworth (1990) consider r_V equal to the resistance to heat transfer (r_H) of the leaf, giving the following equation for the adjusted psychrometric constant

$$\gamma^* = \left(\frac{r_V + r_s}{r_H} \right) \gamma = \left(1 + \frac{r_s}{r_H} \right) \gamma \quad (7.13)$$

The resistance to heat transfer of the leaves is determined by

$$r_H = \frac{\rho c_{p,ma}}{h_{veh}} \quad (7.14)$$

where ρ is the density of the air-vapor mixture. Both the density and specific heat of equation (7.14) are evaluated at the mean of the vegetation surface and dry-bulb air temperatures. According to the FAO (2006), the value of r_s for a reference grass crop is 70 s/m. The numerical model assumes a similar value for the stomatal surface resistance of the vegetation under the collector roof.

7.3 Temperature lapse rates for moist air

The reference plant of this dissertation assumes a dry adiabatic lapse rate (DALR) for the air inside the chimney and the atmosphere surrounding the solar chimney power plant. These are believed to be good approximations of the experienced temperature gradients in these regions when dry atmospheric air is assumed. Equations (5.4) and (5.5) describe the temperature and pressure distributions for dry air with respect to height as predicted by the DALR. When vegetation is included under the collector roof, the air flowing through the solar chimney power plant will absorb moisture from the vegetation surface. Therefore, the assumption of a DALR inside the chimney becomes invalid. According to Kröger (2004), the respective atmospheric temperature and pressure distributions for air containing water vapor are

$$T = T_1 - \frac{0.00975(1 + \omega)z}{(1 + 1.9\omega)} \quad (7.15)$$

$$p = p_1 \left[1 - \frac{0.00975(1 + \omega)z}{(1 + 1.9\omega)T_1} \right]^{2.1778(1+1.9\omega)/(\omega+0.622)} \quad (7.16)$$

where T and p represent the respective air temperature and pressure at a specific height z above ground level, with T_1 and p_1 the temperature and pressure at ground level. The symbol ω is the absolute humidity of the air.

When moist air is raised in a gravitational field, the air cools down adiabatically until it reaches the saturation point. If the air should rise even further, cooling will cause the vapor in the air to condense and precipitate. The energy removed from the condensate then heats the surrounding air. Kröger (2004) gives the following temperature and pressure distribution relations for moist air that experiences condensation at a certain height above ground level

$$T_s = T_{sc} + \xi_T z_s \quad (7.17)$$

$$p_s = p_{sc} \left(1 + \frac{\xi_T z_s}{T_{sc}} \right)^{-0.021233(1+\omega_{sc})/[\xi_T(\omega_{sc}+0.622)]} \quad (7.18)$$

where T_s and p_s represent the temperature and pressure at a specific height z_s , which is the height above the elevation where condensation commences. The terms T_{sc} , p_{sc} and ω_{sc} refer to the respective temperature, pressure and absolute humidity of the air at the point above ground level where condensation commences. The symbol ξ_T is the air temperature gradient after condensation commences and is given by

$$\xi_T = \frac{dT_s}{dz} = \frac{-(1 + \omega_s)g \{0.42216 \times 10^{-11} \omega_s^2 p_s \exp(5406.1915/T_s) i_e / [(\omega_s + 0.622)RT_s]\}}{c_{p,ma} + 3.6693 \times 10^{-8} \omega_s^2 p_s \exp(5406.1915/T_s) i_e / T_s^2} \quad (7.19)$$

where T_s , p_s and ω_s indicate the respective temperature, pressure and absolute humidity of the air after condensation has occurred. The term $c_{p,ma}$ refers to the specific heat capacity of the air-vapor mixture and is determined by

$$c_{p,ma} = c_{pa} + \omega_s c_{pv} \quad (7.20)$$

where c_{pa} and c_{pv} are the specific heats of dry air and saturated water vapor respectively. Furthermore, i_e of equation (7.19) is determined from

$$i_e = i_{fgw0} - (c_{pw} - c_{pv})(T_s - 273.15) \quad (7.21)$$

where i_{fgw0} is the latent heat of water at 273.15 K and c_{pw} is the specific heat capacity of saturated water liquid. All specific heats of equations (7.20) and (7.21) are determined at $T_s/2$.

Note that equation (7.19) cannot be analytically integrated. However, Kröger (2004) states that this temperature gradient, determined at a particular pressure and temperature, hardly changes at higher elevations where both the pressure and temperature will be lower, i.e. the temperature gradient is approximately constant.

7.4 Vegetation/Ground discretization scheme

When omitting vegetation in the solar chimney power plant model, the ground under the collector roof is assumed to be uniform and have constant properties. In this case, the conduction heat fluxes under the ground surface are defined by equation (2.5). An accurate implicit scheme, derived specifically (in the study by Pretorius (2004)) for one-dimensional heat conduction in a uniform medium with constant properties, is used for the discretization of this equation.

With the inclusion of vegetation under the collector roof, the collector model of the numerical model is modified as discussed in Appendix F of this dissertation. A section of the collector (defined as the vegetation section in Appendix F) now incorporates a non-uniform ground which simulates separate vegetation and ground properties. The heat fluxes within the vegetation and ground layers of this section are represented respectively by equations (F.11) and (2.5), while equations (F.16) and (F.21) relate the boundary energy flows.

The implicit scheme used in the study by Pretorius (2004) does not allow for the simple implementation of a non-uniform medium in the numerical model. Consequently, it was decided to use the following alternative scheme (originally employed by Hedderwick (2001)) for the discretization of equations (F.11) and (2.5) in the defined vegetation section. The collector finite difference grid employed for the ground/vegetation control volumes are constructed as in figure 7.1. The convention of Appendix F is kept, whereby all vegetation and ground temperatures are referred to as T_g .

The general one-dimensional heat conduction equation

$$\frac{\partial T_g}{\partial t} = \frac{k}{\rho c} \frac{\partial^2 T_g}{\partial z^2} \quad (7.22)$$

can be approximated using the following Crank-Nicholson implicit finite difference method

$$\frac{T_{g,k} - T_{g,k}^{old}}{\Delta t} = \frac{k}{2\rho c} \left[\frac{T_{g,k+1} - 2T_{g,k} + T_{g,k-1}}{\Delta z^2} + \frac{T_{g,k+1}^{old} - 2T_{g,k}^{old} + T_{g,k-1}^{old}}{\Delta z^2} \right] \quad (7.23)$$

where k , ρ and c respectively represent the thermal conductivity, density and specific heat of the medium. The subscript k denotes the node position (from figure 7.1). This scheme approximates the temperature gradient at a node by taking the average of the current and old values of the finite difference between the specific node and the two adjacent nodes.

The Crank-Nicholson method can also be modified as follows to account for varying control volume thicknesses. The second order derivative of equation (7.22) is approximated using a central difference and an average between the current and old temperature values

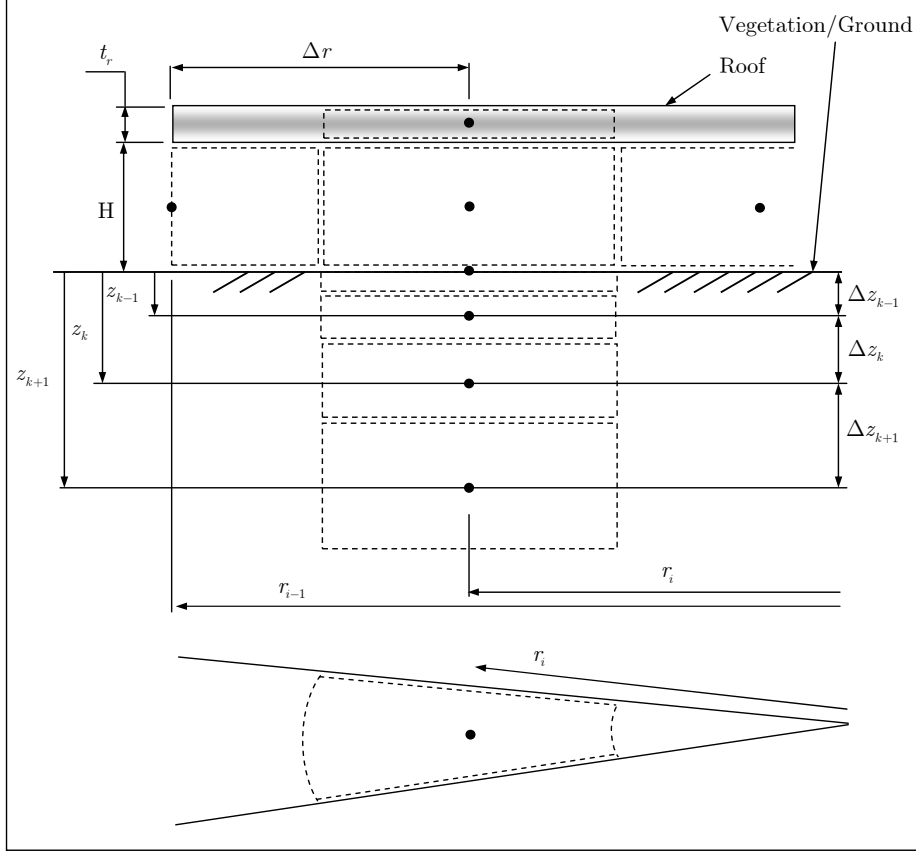


Figure 7.1: Collector finite difference grid for the ground/vegetation control volumes

$$\frac{\partial^2 T_g}{\partial z^2} = \frac{1}{2} \left[\frac{\frac{\partial T_{g,k+1/2}}{\partial z} - \frac{\partial T_{g,k-1/2}}{\partial z}}{\frac{1}{2}(\Delta z_k + \Delta z_{k+1})} + \frac{\frac{\partial T_{g,k+1/2}^{old}}{\partial z} - \frac{\partial T_{g,k-1/2}^{old}}{\partial z}}{\frac{1}{2}(\Delta z_k + \Delta z_{k+1})} \right] \quad (7.24)$$

When applying the derivatives, we find

$$\frac{\partial^2 T_g}{\partial z^2} = \frac{1}{2} \left[\left(\frac{T_{g,k+1} - T_{g,k}}{\frac{1}{2}(\Delta z_k + \Delta z_{k+1})\Delta z_{k+1}} - \frac{T_{g,k} - T_{g,k-1}}{\frac{1}{2}(\Delta z_k + \Delta z_{k+1})\Delta z_k} \right) + \left(\frac{T_{g,k+1}^{old} - T_{g,k}^{old}}{\frac{1}{2}(\Delta z_k + \Delta z_{k+1})\Delta z_{k+1}} - \frac{T_{g,k}^{old} - T_{g,k-1}^{old}}{\frac{1}{2}(\Delta z_k + \Delta z_{k+1})\Delta z_k} \right) \right] \quad (7.25)$$

Substituting equation (7.25) into equation (7.22) and employing the finite difference gives

$$\frac{T_{g,k} - T_{g,k}^{old}}{\Delta t} = \frac{k}{2\rho c} \left[\left(\frac{T_{g,k+1} - T_{g,k}}{\frac{1}{2}(\Delta z_k + \Delta z_{k+1})\Delta z_{k+1}} - \frac{T_{g,k} - T_{g,k-1}}{\frac{1}{2}(\Delta z_k + \Delta z_{k+1})\Delta z_k} \right) + \left(\frac{T_{g,k+1}^{old} - T_{g,k}^{old}}{\frac{1}{2}(\Delta z_k + \Delta z_{k+1})\Delta z_{k+1}} - \frac{T_{g,k}^{old} - T_{g,k-1}^{old}}{\frac{1}{2}(\Delta z_k + \Delta z_{k+1})\Delta z_k} \right) \right] \quad (7.26)$$

When solving this equation for $T_{g,k}$, we find

$$T_{g,k} = \left[\frac{k \Delta t}{\rho c} \left(\frac{T_{g,k+1} + T_{g,k+1}^{old} - T_{g,k}^{old}}{(\Delta z_k + \Delta z_{k+1}) \Delta z_{k+1}} + \frac{T_{g,k-1} + T_{g,k-1}^{old} - T_{g,k}^{old}}{(\Delta z_k + \Delta z_{k+1}) \Delta z_k} \right) + T_{g,k}^{old} \right] / \left(1 + \frac{k \Delta t}{\rho c (\Delta z_k + \Delta z_{k+1})} \right) \quad (7.27)$$

By substituting the appropriate properties into equation (7.27), the temperatures within the respective vegetation and ground layers under the collector roof can be determined.

7.4.1 Discretization of vegetation/ground interface equations

Appendix F derives relevant energy equations concerning the interface conduction heat fluxes between the vegetation and ground layers under the collector roof of the solar chimney power plant.

7.4.1.1 Vegetation side

Equation (F.16) presents a semi-discretized form of the heat conduction equation for the boundary control volume in the vegetation layer (see figure F.5). This equation is now fully discretized by taking an average between the current and old temperature values

$$\begin{aligned} \frac{T_{g,k} - T_{g,k}^{old}}{\Delta t} = \frac{1}{2\rho_{ve}c_{ve}\Delta z_k} \left\{ \left[\left(\frac{2k_{ve}k_g}{\Delta z_k k_g + \Delta z_{k+1} k_{ve}} \right) (T_{g,k+1} - T_{g,k}) \right. \right. \\ \left. \left. - \frac{k_{ve}}{\Delta z_k} (T_{g,k} - T_{g,k-1}) \right] + \left[\left(\frac{2k_{ve}k_g}{\Delta z_k k_g + \Delta z_{k+1} k_{ve}} \right) (T_{g,k+1}^{old} - T_{g,k}^{old}) \right. \right. \\ \left. \left. - \frac{k_{ve}}{\Delta z_k} (T_{g,k}^{old} - T_{g,k-1}^{old}) \right] \right\} \quad (7.28) \end{aligned}$$

Solving and simplifying this equation for $T_{g,k}$ gives

$$\begin{aligned} T_{g,k} = \left[\frac{k_{ve}k_g\Delta t}{\rho_{ve}c_{ve}\Delta z_k (\Delta z_k k_g + \Delta z_{k+1} k_{ve})} (T_{g,k+1} + T_{g,k+1}^{old} - T_{g,k}^{old}) \right. \\ \left. + \frac{k_{ve}\Delta t}{2\rho_{ve}c_{ve}\Delta z_k^2} (T_{g,k-1} + T_{g,k-1}^{old} - T_{g,k}^{old}) + T_{g,k}^{old} \right] \\ / \left[1 + \frac{k_{ve}k_g\Delta t}{\rho_{ve}c_{ve}\Delta z_k (\Delta z_k k_g + \Delta z_{k+1} k_{ve})} + \frac{k_{ve}\Delta t}{2\rho_{ve}c_{ve}\Delta z_k^2} \right] \quad (7.29) \end{aligned}$$

7.4.1.2 Ground side

Equation (F.21) presents a semi-discretized form of the heat conduction equation for the boundary control volume in the ground layer (see figure F.6). Analogous to the vegetation side, this equation is now fully discretized and rearranged to give

$$\begin{aligned}
T_{g,k} = & \left[\frac{k_{ve}k_g\Delta t}{\rho_g c_g \Delta z_k (\Delta z_{k-1}k_g + \Delta z_k k_{ve})} (T_{g,k-1} + T_{g,k-1}^{old} - T_{g,k}^{old}) \right. \\
& \left. + \frac{k_g\Delta t}{2\rho_g c_g \Delta z_k \Delta z_{k+1}} (T_{g,k+1} + T_{g,k+1}^{old} - T_{g,k}^{old}) + T_{g,k}^{old} \right] \\
& / \left[1 + \frac{k_{ve}k_g\Delta t}{\rho_g c_g \Delta z_k (\Delta z_{k-1}k_g + \Delta z_k k_{ve})} + \frac{k_g\Delta t}{2\rho_g c_g \Delta z_k \Delta z_{k+1}} \right]
\end{aligned} \tag{7.30}$$

7.5 Plant specifications

The solar chimney power plant model of this section is based on the reference plant specifications in Chapter 2. In addition, vegetation is included under the collector roof over part of the ground surface area (see figure F.1), with dimensions as specified in table 7.1.

The numerical model assumes the following vegetation properties. The vegetation density, specific heat and thermal conductivity are assumed to be similar to those of wet soil and are presented in table 7.1, as given by Mills (1995). The vegetation emissivity and absorptivity are assumed to be similar to the properties of relatively short grass and are included in the same table, as given respectively by Dong *et al.* (1992) and Hsu (1963).

Table 7.1: Average properties of wet soil according to Mills (1995), emissivity of relatively short grass (0.1 m to 0.15 m) according to Dong *et al.* (1992) and absorptivity of grass (80 % to 90 % new, green grass) according to Hsu (1963)

Vegetation	
Density	$\rho_{ve} = 1900 \text{ kg/m}^3$
Specific heat	$c_{ve} = 2200 \text{ J/kgK}$
Thermal conductivity	$k_{ve} = 2 \text{ W/mK}$
Emissivity	$\epsilon_{ve} = 0.98$
Absorptivity	$\alpha_{ve} = 0.77$
Surface roughness	$\epsilon_{ve} = 0.1 \text{ m}$
Depth	$z_{ve} = 0.55 \text{ m}$
Radial distance from perimeter	$r_{ve} = 1978 \text{ m or } 1012 \text{ m}$

7.6 Assumptions

The simulations of this section are based on the following assumptions:

- The vegetation in the collector is approximated as wet soil.
- It is assumed that the depth of the vegetation reaches approximately 0.5 m deep into the ground. Therefore, properties are assumed to be that of vegetation from the surface to 0.5 m and that of dry ground deeper than 0.5 m (for the vegetation section of the collector as illustrated by figure F.1).
- The vegetation is assumed to be constantly wet (by irrigation), thereby approximating the water vapor mass-flow to the collector air as a source term.
- No water is transferred from the vegetation to the collector air during night-time.

- If condensation occurs in the collector, the addition of water to the vegetation or ground through condensation is assumed to be negligible.
- The maximum temperature at which vegetation can function without impairing the photosynthetic processes is assumed to be 40 °C (assumed somewhat lower to values found by Taiz and Zeiger (1998)).
- Unless stated otherwise, the numerical model employs an atmosphere outside the solar chimney power plant that considers the effect of water vapor in the air. Therefore, equations (7.15) and (7.16) are implemented for the air outside the plant. It is assumed that no condensation takes place in the atmosphere surrounding the plant.
- Unless stated otherwise, the numerical model considers the effects of water vapor and possible condensation for the air inside the chimney of the solar chimney power plant. Therefore, equations (7.15) and (7.16), together with equations (7.17) and (7.18) (should condensation occur) are implemented for the air inside the chimney of the plant.

7.7 Simulations and results

Two computer simulations are performed, employing the above-mentioned plant specifications, vegetation properties and assumptions. The section investigates the incorporation of vegetation under the collector roof from the collector perimeter to respective radii of $r_{ve} = 1978$ m and $r_{ve} = 1012$ m.

When incorporating vegetation in the solar chimney power plant, the numerical model employs the discretization scheme discussed in section 7.4 for the vegetation section, while the discretization scheme of Pretorius (2004) is used for the ground section of the collector (refer to figure F.1). Note that the inclusion of the alternative discretization scheme (of section 7.4) in the numerical model may have an effect on the accuracy of the results.

7.7.1 Including vegetation over approximately 2000m of the collector radius

From figure 7.2 it is clear that the inclusion of vegetation in the collector over a radial distance of 1978 m has a major effect on the power output of the solar chimney power plant. This is confirmed by table 7.2, which shows a reduction of 45.1 % in annual power output for the plant incorporating vegetation, compared to the reference plant.

As air flows under the collector roof from the perimeter to the chimney, water from the vegetation surface is evaporated. The evaporation process cools the vegetation surface as well as the collector air. With lower collector air temperatures, a lower plant driving potential results, ultimately causing a lower power output compared to the reference plant.

Figure 7.2 also presents less smooth power output curves for the plant incorporating vegetation compared to the curves for the reference plant. As mentioned, the inclusion of vegetation lowers the collector air temperatures and driving potential. This makes the plant susceptible to variations in ambient conditions, which cause the illustrated small fluctuations in power output. Note that both plant models (reference plant model and model incorporating vegetation) are subject to the same ambient conditions. However due to the fact that the reference plant operates at much higher driving potentials (as a result of higher collector air temperatures), the reference plant is less sensitive to changes in the ambient conditions.

Two other factors which contribute to the uneven output profiles are the heat transfer due to evaporation from the vegetation surface and the fact that the plant model incorporating vegetation implements temperature lapse rates which consider the variable humidity of the air inside and outside the plant.

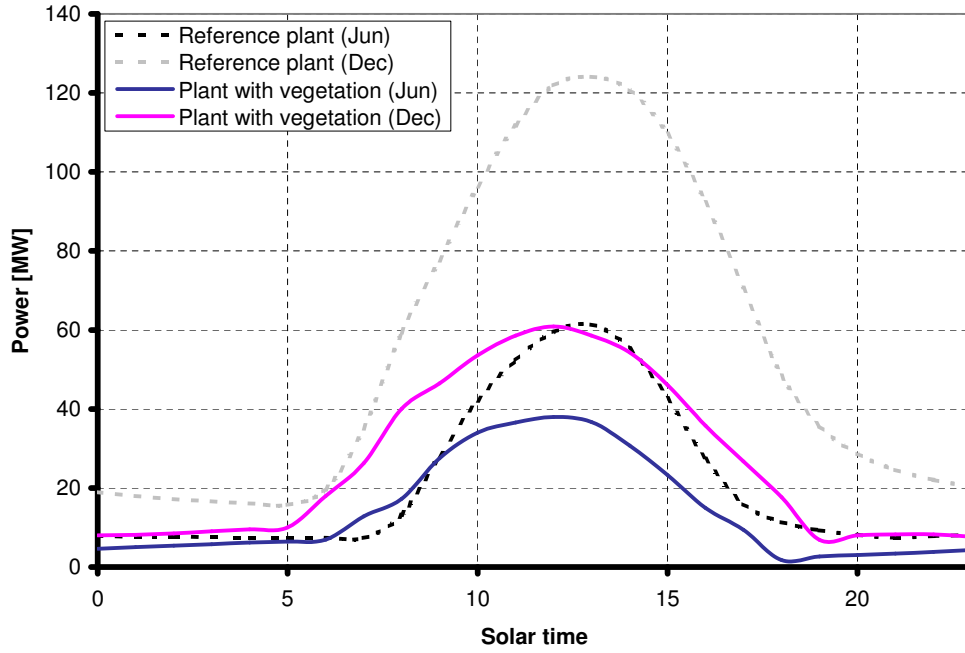


Figure 7.2: Daily solar chimney power output profile, illustrating the influence of including vegetation under the collector roof, over a radial distance of 1978 m from the collector perimeter

Table 7.2: Annual power output comparison, illustrating the effect of incorporating vegetation under the collector roof, over a radial distance of 1978 m from the collector perimeter

Plant configuration	Annual power output [GWh]
Reference plant	336
Plant with vegetation	184.4

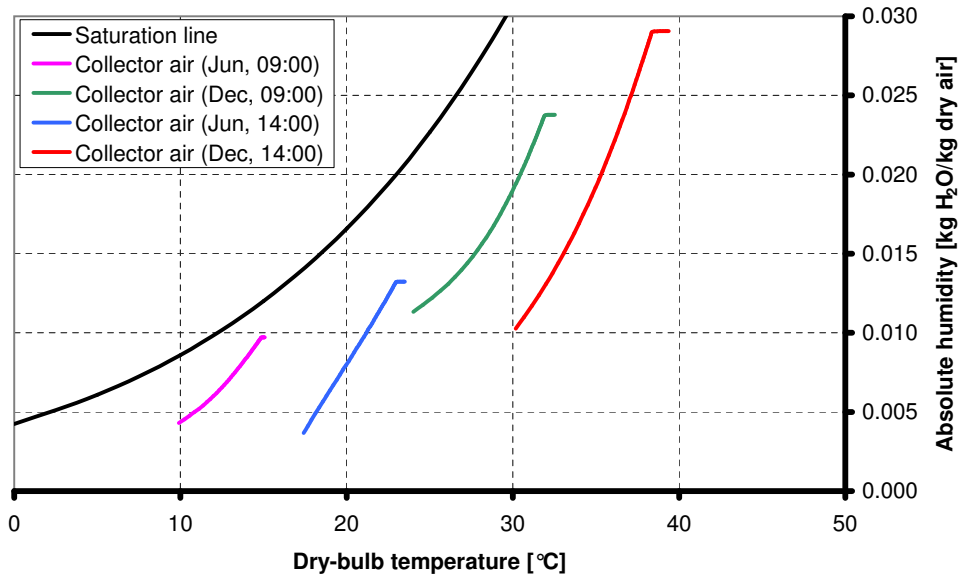


Figure 7.3: The psychrometric chart, illustrating the heating and humidification and simple heating of the collector air at 09:00 and 14:00 on 21 June and 21 December, for $r_{ve} = 1978$ m

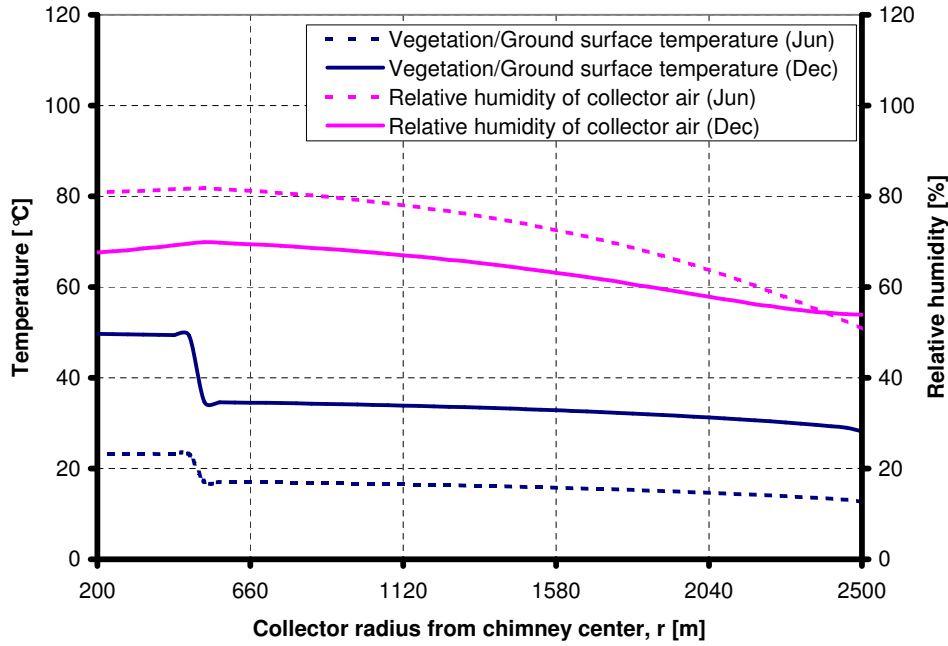


Figure 7.4: Vegetation or ground surface temperature and relative humidity of the collector air throughout the collector at 09:00 on 21 June and 21 December, for $r_{ve} = 1978$ m

Figure 7.3 illustrates, on a psychrometric chart, how the air flowing under the collector roof is heated and humidified in the vegetation section and simply heated in the ground section of the collector. The curves indicate the conditions in the collector at 09:00 and 14:00 on a typical day in June and December. As a large part of the collector employs vegetation ($r_{ve} = 1978$ m), heating and humidification takes place over a substantial radius from the collector perimeter. Simple heating of the collector air takes place over a small section of the collector (where a ground surface is employed) and is indicated by the small horizontal sections at the tips of the curves in figure 7.3.

The curves of figure 7.4 represent the vegetation or ground surface temperature and relative humidity of the collector air throughout the collector at 09:00 on 21 June and 21 December. The temperature curves indicate a slight rise in vegetation surface temperature from the perimeter of the vegetation section (also perimeter of collector, at $r = 2500$ m) to the end of the vegetation section ($r = 522$ m). Thereafter, a jump in temperature results, indicating the start of the ground section. A minor increase in temperature is evident from this point on to the end of the ground section ($r = 200$ m). It is clear that the average ground surface temperature is significantly higher than the average vegetation surface temperature.

Figure 7.4 also shows that the relative humidity of the collector air increases steadily over the vegetation section, as water from the vegetation surface is evaporated and absorbed by the flowing air. In the ground section, higher air temperatures are experienced due to higher (ground) surface temperatures and no water vapor is added to the collector air in this section. This causes a subsequent steady decrease in the relative humidity of the air over the ground section. In addition, the average relative humidity of the collector air is somewhat higher during winter than the average humidity during summer. During winter the collector air is cooler than during summer and consequently cannot hold as much moisture as the warmer collector air during summer, which explains the higher relative humidity values during winter.

The curves of figure 7.5 represent the vegetation or ground surface temperature and relative humidity of the collector air throughout the collector at 14:00 on 21 June and 21

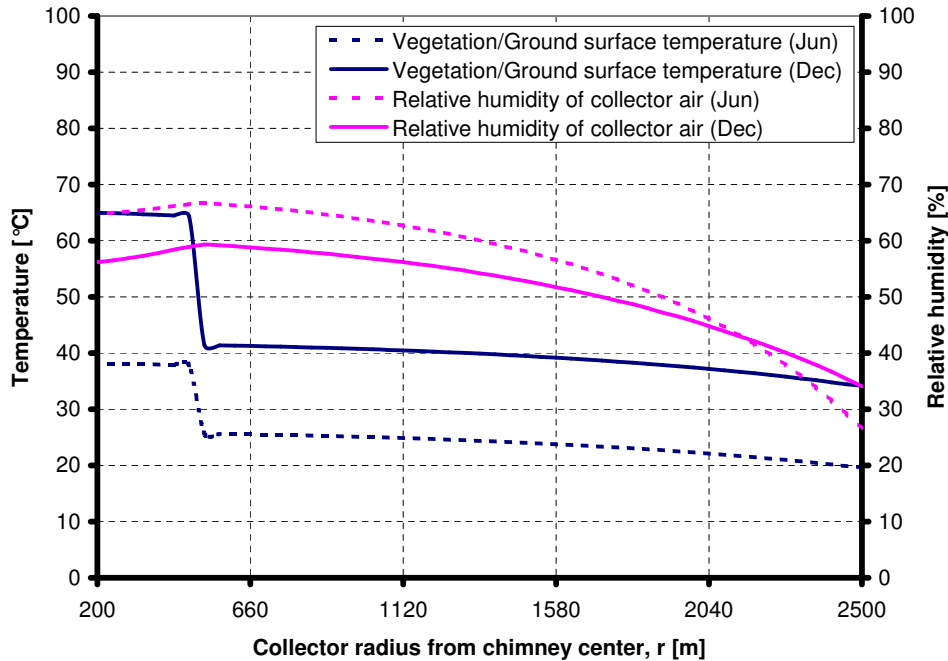


Figure 7.5: Vegetation or ground surface temperature and relative humidity of the collector air throughout the collector at 14:00 on 21 June and 21 December, for $r_{ve} = 1978$ m

December. Similar trends are visible to those in figure 7.4. Furthermore, surface temperatures are notably higher and relative humidities are somewhat lower at 14:00, compared to their corresponding values at 09:00 (from figure 7.4).

It is very important to note from figure 7.5 that the vegetation surface temperature reaches 40 °C (at 14:00 in December) at a collector radius of approximately $r = 1300$ m and rises even further to the end of the vegetation section. As mentioned in section 7.6, a rise in vegetation temperature above 40 °C is assumed to adversely affect the photosynthetic and other processes of the plants. This suggests that, for the given location, vegetation should not be incorporated to a collector radius beyond $r = 1300$ m from the collector perimeter.

From figure 7.6 it is evident that a substantial amount of water is removed from the vegetation via evapotranspiration during the daytime operation of the solar chimney power plant. Figure 7.6 follows the form of the daily solar radiation profile. The higher the solar radiation, the higher the collector air temperatures become, thereby increasing the ability of the air to absorb moisture and causing an increased rate of water vapor mass-flow from the vegetation to the air. It is also clear that significantly less water is removed from the vegetation during winter than during summer.

7.7.2 Including vegetation over approximately 1000m of the collector radius

Though significantly reduced compared to the results of figure 7.2 and table 7.2, figure 7.7 indicates that the inclusion of vegetation in the collector over a radial distance of 1012 m still has a major effect on the power output of the solar chimney power plant. Table 7.3 confirms this, showing a reduction of 29.8 % in annual power output for the plant incorporating vegetation, compared to the reference plant.

The performance curves of figure 7.7 are also smoother than the curves presented in figure 7.2, for the plant models incorporating vegetation. With a greater section of the collector employing a ground surface, higher air temperatures are experienced in the collector, giving

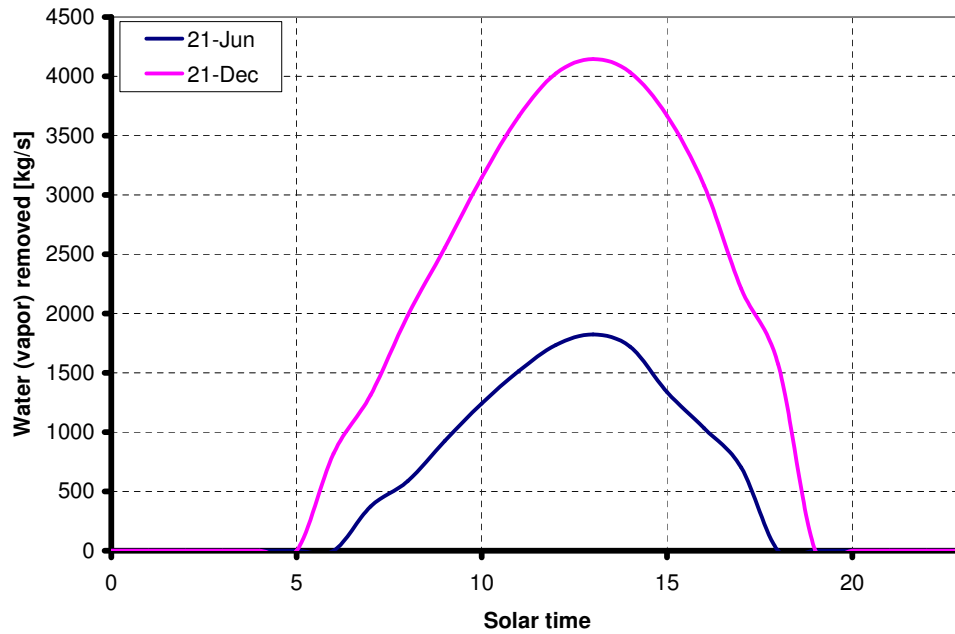


Figure 7.6: Mass-flow rate of water removed from the vegetation through evapotranspiration, throughout a typical day in June and December, for $r_{ve} = 1978$ m

an increased plant driving potential. This makes the plant less sensitive to fluctuations in ambient temperatures and causes smoother power output profiles.

Figure 7.8 presents similar trends to those in figure 7.3. However, as vegetation is only employed over a radial distance of $r_{ve} = 1012$ m from the collector perimeter, heating and humidification takes place over a smaller section of the collector, while simple heating in the ground section is significantly more prominent (represented by the horizontal sections of the curves).

Figures 7.9 and 7.10 also present similar trends to those of figures 7.4 and 7.5. It is however clear that vegetation is employed over a smaller collector section. The temperature curves of figures 7.9 and 7.10 indicate a slight rise in vegetation surface temperature from the perimeter of the vegetation section (also perimeter of collector, at $r = 2500$ m) to the end of the vegetation section ($r = 1488$ m). Thereafter, a jump in temperature results, indicating the start of the ground section. A steady increase in temperature is evident from this point on to the end of the ground section ($r = 200$ m). Correspondingly, the relative humidity of the collector air increases steadily over the vegetation section and decreases over the ground section.

Note from figure 7.10 that when incorporating vegetation to a collector radius of only $r_{ve} = 1012$ m, the vegetation surface temperature always remains below 40 °C.

Figure 7.11 exhibits the same trends to those of figure 7.6. Although somewhat reduced compared to the results presented by figure 7.6, figure 7.11 illustrates that a significant amount of water is still removed from the vegetation via evapotranspiration during the daytime operation of the solar chimney power plant.

7.8 Temperature lapse rates effects

This section evaluates the influence of employing various temperature lapse rates for the atmosphere outside and the air inside the chimney of the solar chimney power plant. As mentioned in section 7.3, the reference solar chimney power plant of this dissertation employs

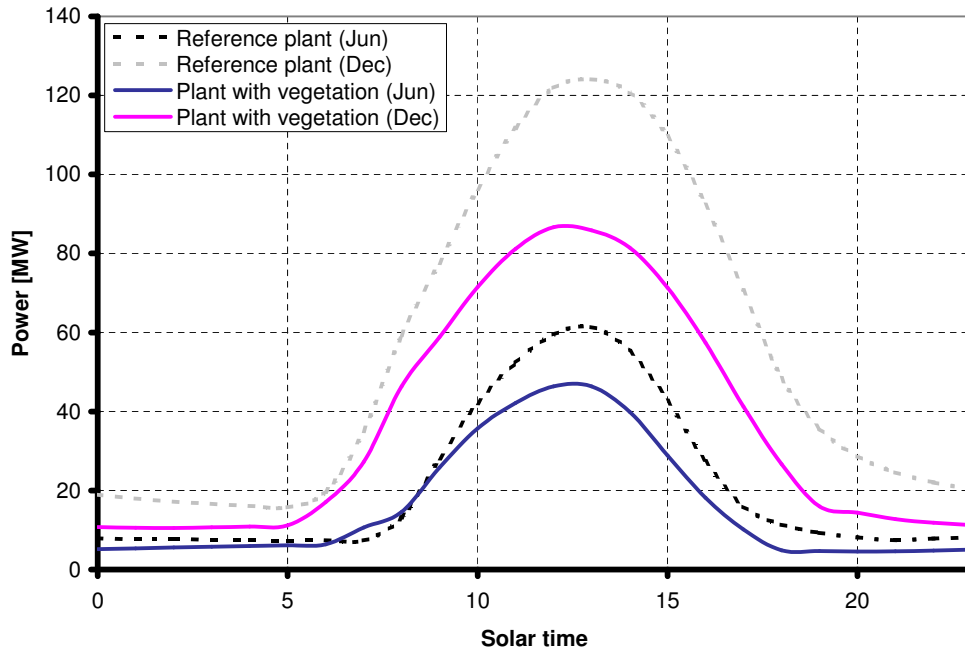


Figure 7.7: Daily solar chimney power output profile, illustrating the influence of including vegetation under the collector roof, over a radial distance of 1012 m from the collector perimeter

Table 7.3: Annual power output comparison, illustrating the effect of incorporating vegetation under the collector roof, over a radial distance of 1012 m from the collector perimeter

Plant configuration	Annual power output [GWh]
Reference plant	336
Plant with vegetation	236

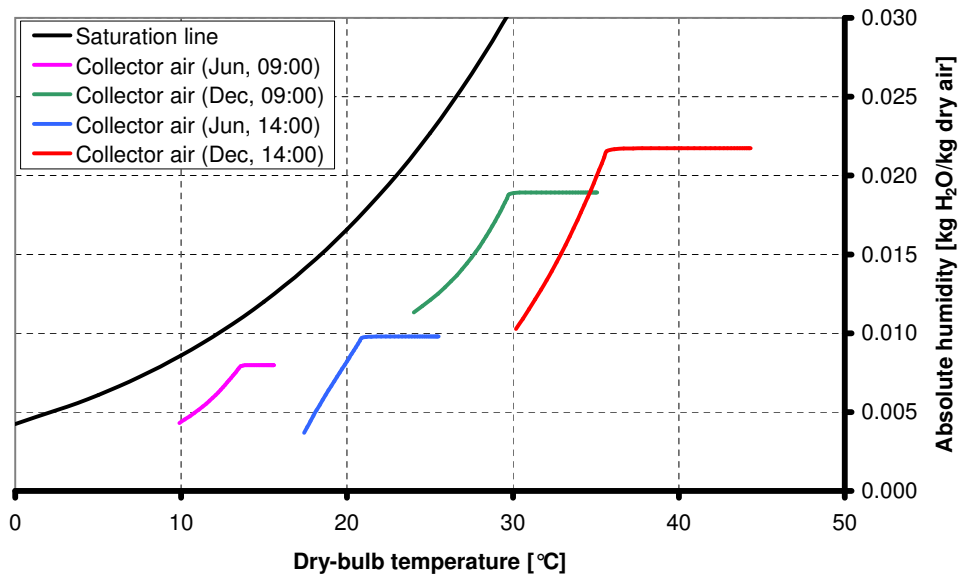


Figure 7.8: The psychrometric chart, illustrating the heating and humidification and simple heating of the collector air at 09:00 and 14:00 on 21 June and 21 December, for $r_{ve} = 1012$ m

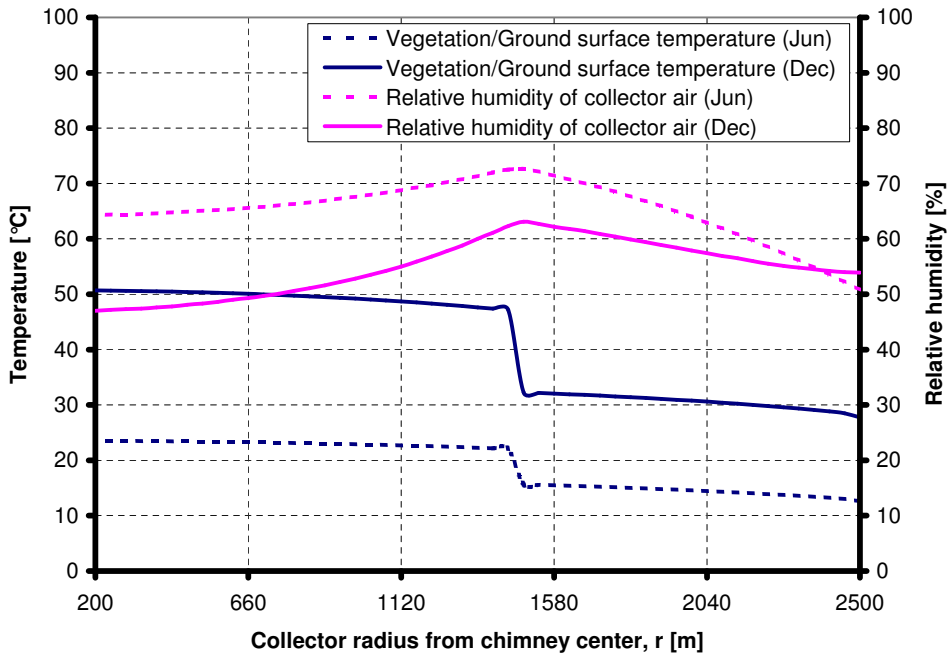


Figure 7.9: Vegetation or ground surface temperature and relative humidity of the collector air throughout the collector at 09:00 on 21 June and 21 December, for $r_{ve} = 1012$ m

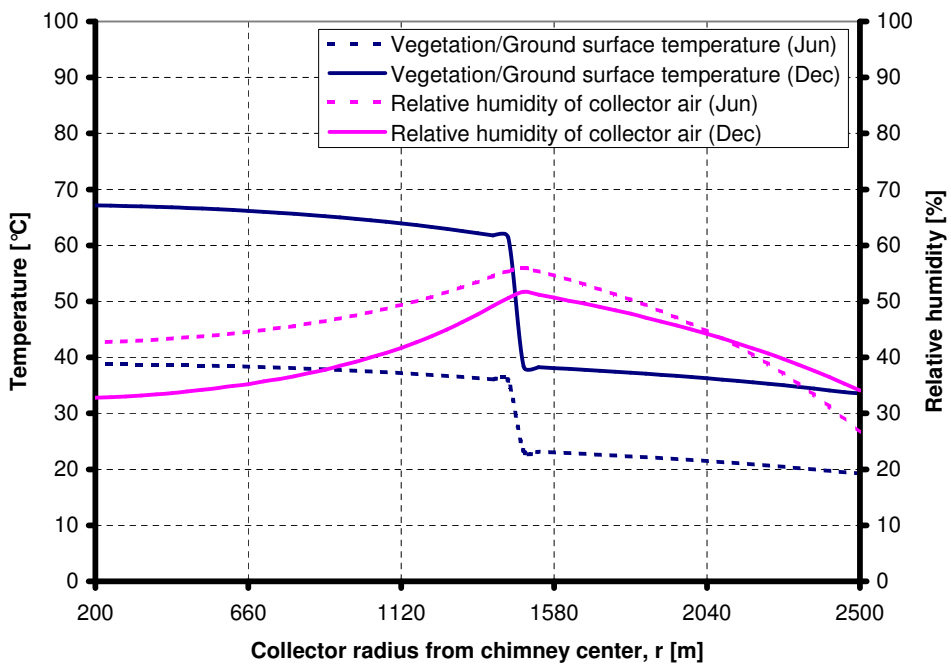


Figure 7.10: Vegetation or ground surface temperature and relative humidity of the collector air throughout the collector at 14:00 on 21 June and 21 December, for $r_{ve} = 1012$ m

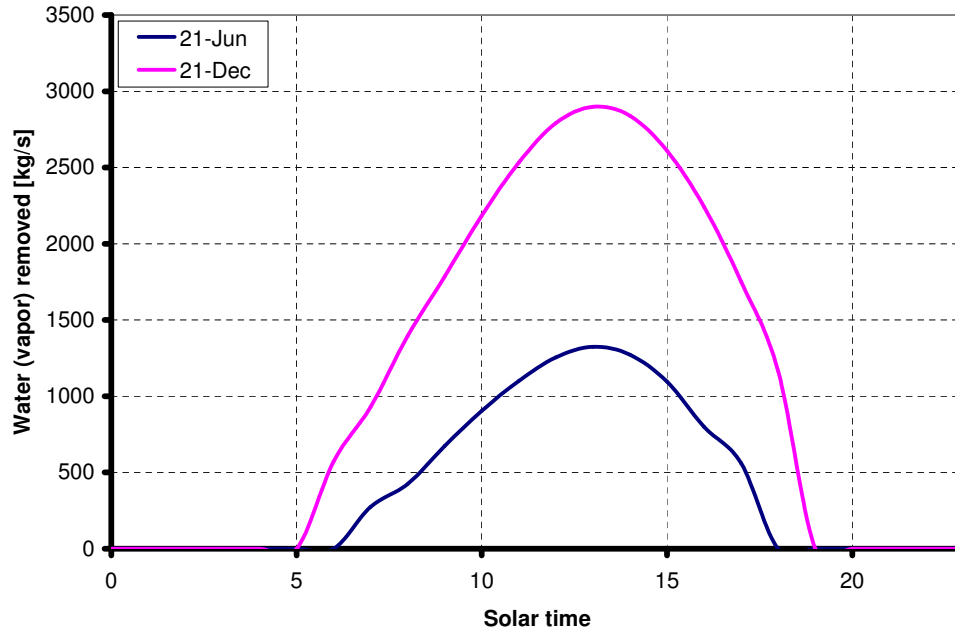


Figure 7.11: Mass-flow rate of water removed from the vegetation through evapotranspiration, throughout a typical day in June and December, for $r_{ve} = 1012$ m

a dry adiabatic lapse rate (DALR) for the atmosphere outside and air inside the chimney of the plant. However, when incorporating vegetation under the collector roof of the plant the effects of water vapor in air have to be taken into account, a factor which the DALR does not consider. This necessitates the inclusion of temperature lapse rates which do consider the effects of water vapor. Two such lapse rates are discussed in section 7.3.

A publication by Kröger and Blaine (1999) also investigated the effects of water vapor and possible condensation in a large solar chimney power plant (using the equations of section 7.3). The authors conclude that moist air improves plant driving potential and that condensation may occur inside the chimney of the plant under certain conditions.

7.8.1 Simulation and results

Numerical simulations are performed for three plant models, all employing the previously mentioned plant specifications, vegetation properties and assumptions (except for the last two assumptions, which are varied here) of this chapter. The first model employs a DALR for the outside atmosphere and the air inside the chimney (according to equations (5.4) and (5.5)). The second model takes the effect of water vapor in air into account, for the ambient air as well as for the air inside the chimney of the plant (according to equations (7.15) and (7.16)). The third plant model also takes into account the effect of water vapor in the air inside and outside the plant, while additionally considering the possible condensation of the air inside the chimney of the plant (according to equations (7.15), (7.16), (7.17) and (7.18)). Simulations are performed for a plant employing vegetation over a radial distance of $r_{ve} = 1978$ m and $r_{ve} = 1012$ m from the collector perimeter.

The results of the first plant model are referred to as "DALR", those of the second model as "Moisture" and those of the third as "Moisture and Condensation". It should be noted that all of the above-mentioned models employ vegetation under the collector roof of the plant and consider the transfer of water vapor from the vegetation to the collector air. Thus, their only distinction lie in the way which the respective temperature (and corresponding pressure) lapse rates are modelled.

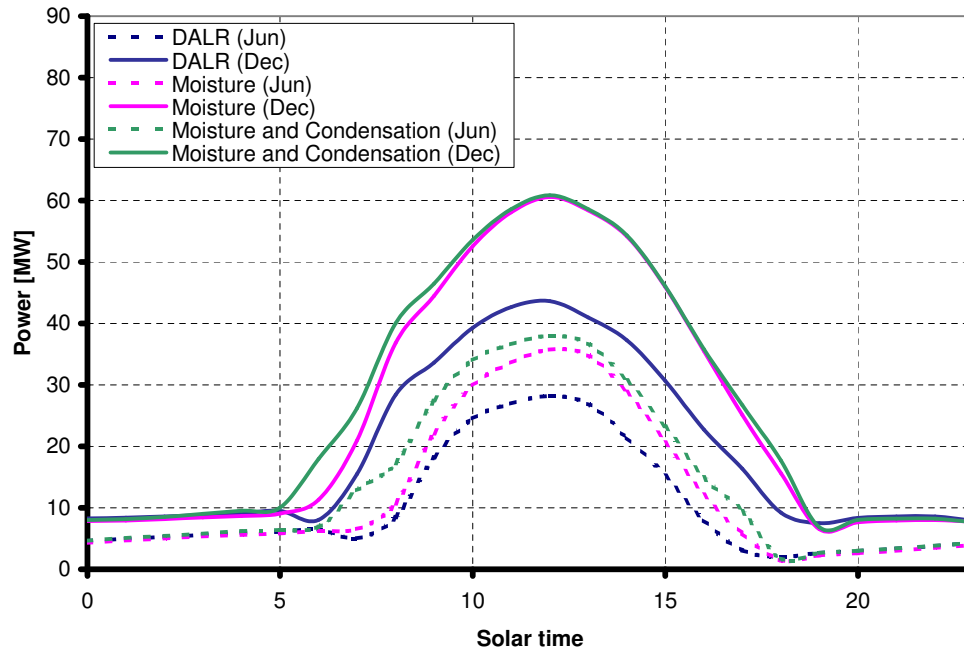


Figure 7.12: Daily solar chimney power output for a plant employing vegetation under the collector roof over a radial distance of $r_{ve} = 1978$ m; effect of different temperature lapse rate models on plant performance

Table 7.4: Annual power output comparison for a plant incorporating vegetation under the collector roof over a radial distance of 1978 m; effect of different temperature lapse rate models on plant performance

Plant configuration	Annual power output [GWh]
DALR	131.8
Moisture	168.6
Moisture and Condensation	184.4

From figure 7.12 it is clear that all the plant models predict similar power outputs during night-time, while the models considering the effects of water vapor predict significantly higher plant power production during the day. During the night, the lapse rates which consider water vapor employ the same absolute humidity for the air outside and inside the chimney of the plant. Consequently, during night-time driving potentials are predicted which are similar to the driving potentials of the plant model employing a DALR. During the day however, the air flowing under the collector roof absorbs moisture from the vegetation, thereby significantly altering the vapor content of the air inside the chimney of the plant (while the humidity of the outside air is assumed constant). The increased vapor content of the air inside the chimney alters the pressure distribution of the chimney air, causing an increased plant driving potential and ultimately power output. This corresponds to the findings of Kröger and Blaine (1999).

Another noticeable trend from figure 7.12 is the increased power output of the "Moisture and Condensation" plant model during early mornings in summer and for most of the day during winter. During these times, condensation occurs inside the chimney of the plant. Again, this corresponds to the findings of Kröger and Blaine (1999). When the water vapor in the chimney air condenses, heat is transferred to the air, thereby altering the chimney

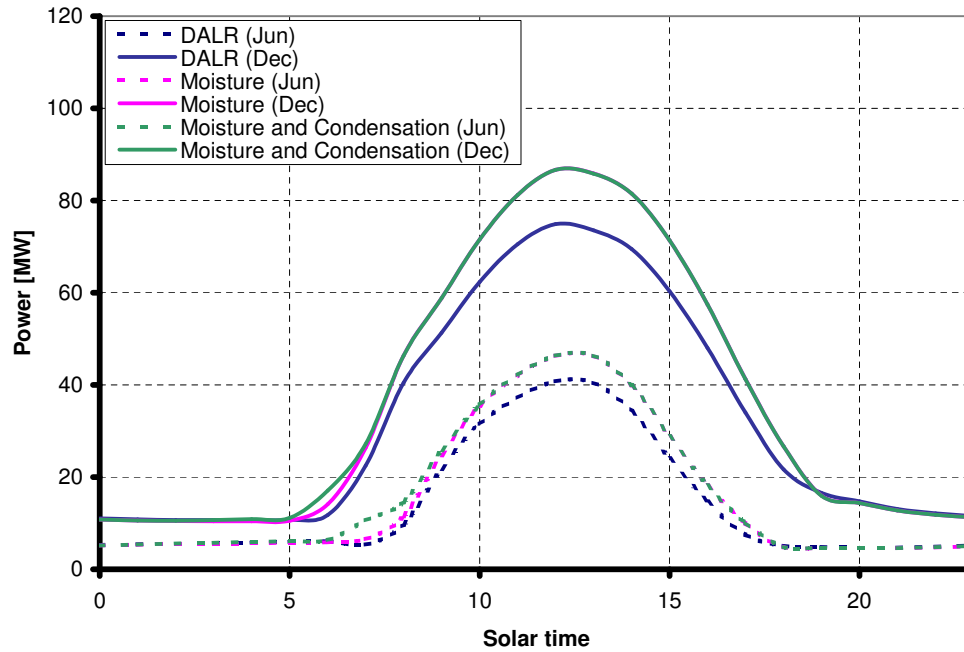


Figure 7.13: Daily solar chimney power output for a plant employing vegetation under the collector roof over a radial distance of $r_{ve} = 1012$ m; effect of different temperature lapse rate models on plant performance

Table 7.5: Annual power output comparison for a plant incorporating vegetation under the collector roof over a radial distance of 1012 m; effect of different temperature lapse rate models on plant performance

Plant configuration	Annual power output [GWh]
DALR	205
Moisture	232.5
Moisture and Condensation	236

air temperature and corresponding pressure distribution. This causes an increased plant driving potential and ultimately power output. Annually, table 7.4 confirms these results.

Figure 7.13 and table 7.5 present results for a plant incorporating vegetation over a smaller radial distance (1012 m). Similar trends, though much reduced, are visible compared to figure 7.12 and table 7.4. With less vegetation implemented under the collector of the plant, less moisture is transferred to the collector air via evapotranspiration. This results in a smaller difference in vapor content between the air outside and inside the chimney of the plant. Consequently, a smaller difference in driving potential and subsequent power output is predicted for the "Moisture" and "Moisture and Condensation" models, compared to the "DALR" model. This explains the more comparable daily and annual power output of the models.

Chapter

8

Conclusion

The main objectives of this dissertation were firstly to investigate the optimization of a large-scale solar chimney power plant, through the pursuit of obtaining thermo-economic optimal dimensions and evaluating plant specifications which enhance plant performance and secondly to explore dynamic and static control over plant power output.

This study builds on previous research (Pretorius, 2004), which investigated the basic performance characteristics of a large-scale solar chimney power plant. The previous study derived and discretized the relevant draught and conservation equations for an elementary control volume in the collector and chimney of the plant. These equations were implemented into a complete numerical computer model, taking into account factors such as the global site location, the position of the sun on a specific day of the year and all frictional, inlet, outlet, support and heat losses. Simulations were based on a defined reference plant, using specified meteorological input data for a particular site in South Africa.

A refined version of this numerical model, which includes improved convective heat transfer equations developed by Kröger and Burger (2004) and Burger (2004), is employed in this study and simulations are performed for a more relevant reference plant configuration at the same reference site. Results indicate, with an 8.4 % reduction in annual plant output, that the incorporation of these improved heat transfer equations does have a significant influence on solar chimney power plant performance.

A sensitivity analysis was performed on the influence of various operating and technical specifications on plant performance. Simulation results show that by the treatment of the top surface of the collector roof to reduce its reflectance or emissivity, major enhancements (in the order of 13 % to 30 %) in plant performance are potentially possible. Through the periodic thermal insulation of the collector roof in order to reduce heat losses to the environment, large improvements (up to approximately 35 %) on annual yield may also be established. It should also be noted that the shape and optical quality of the collector roof both have a significant effect (between 4 % and 11 %) on plant performance. The sensitivity analysis also shows that plant performance is very sensitive to the variation of the ground surface absorptivity value, indicating either an increase or decrease of approximately 12.5 % on the annual power output of the reference plant with a variation of 0.1 on the absorptivity value. To a slightly lesser extent, the possible treatment of the ground surface in order to reduce its emissivity will also have a significant positive effect on the annual plant output. Furthermore, an important adverse effect was discovered with the implementation of Sand as ground type in the solar chimney power plant. Due to the low heat storage capability of Sand, very low power production is observed for the plant during winter nights. This observation presents the danger that the plant may stall during these periods, making Sand

unsuitable as ground type to be employed under the collector roof. In effect, this rules out some locations around the world for the construction of a solar chimney power plant. Specifications which were found to have insignificant effects (less than 2.5 %) on annual yield when varied are the collector roof thickness (i.e. thickness of glass), cross-section of the collector roof supports, ground type (except Sand), ground surface roughness, turbine inlet loss coefficient, bracing wheel pressure loss coefficient and the ambient pressure. Lastly, the sensitivity analysis reveals that the temperature lapse rate of the atmosphere surrounding the solar chimney power plant may also have a significant effect on plant power production. Should an atmospheric temperature lapse rate with a similar temperature gradient to the International Standard Atmosphere (ISA) be assumed instead of a dry adiabatic lapse rate (DALR), predicted annual plant output is reduced by 14.4 %.

A thermo-economic optimization of the solar chimney power plant was performed, based on the results of numerical simulations and calculations according to an approximate plant cost model. Multiple computer simulations were performed and the results compared to the approximated cost of each specific simulated plant. Thermo-economically optimal plant configurations were obtained (at the reference location) for various plant cost structures. These optimal plant configurations represent those configurations that give a minimum specific plant cost, i.e. minimum plant cost per annual power unit. Simulations were based on the selected reference plant, while the optimization process only considered the most prominent plant dimensions, namely the chimney height, chimney diameter, collector diameter and collector inlet height. Approximate yield and specific plant cost curves are given, illustrating certain trends regarding the optimized dimensions. An important factor, the possible existence of cold inflow in the chimney of the plant, was considered in the optimization process. Cold inflow is considered an adverse effect, as it may cause the solar chimney power plant to stall. As such, the objective function for a thermo-economically optimal plant configuration was modified to represent those configurations that give a minimum specific plant cost, without experiencing cold inflow. Results indicate that a large number of the simulated plant configurations may experience cold inflow. Furthermore, for comparable cost structures, larger thermo-economically optimal plants are more cost-effective than the smaller optimal plants. In general, for relatively inexpensive cost structures, predicted optimal plant dimensions are much greater than any values presented in literature thus far. Predicted optimal chimney diameters are larger than any values from literature, irrespective of cost structure.

The effects of wind, ambient temperature lapse rates and nocturnal temperature inversions on plant performance were evaluated. Results show that the prevailing ambient winds at the reference site does have a considerable influence, by reducing annual plant output by approximately 10 %, compared to the same plant experiencing no-wind conditions throughout the year. Moreover, simulations indicate that the existence of nocturnal temperature inversions will also have a significant negative effect on plant performance. The variation of the ambient wind profile and the existence of an International Standard Atmosphere (without nocturnal temperature inversions) in the atmosphere surrounding the plant illustrate minor effects (less than 2.5 %) on annual plant yield.

Various techniques were investigated to control the power output of the solar chimney power plant, in order to deliver power according to specified demand patterns. As a preface and in the quest to simply achieve improved plant performance, a partial or fully double glazed collector roof is included in the plant model, with results showing major increases in annual plant output (in the order of 15 % to 40 %). The ability of the solar chimney power plant to act as either a base or peak load power generation facility was investigated. In order to investigate this, the reference plant model was modified to include a secondary, double glazed secondary or secondary and tertiary collector roof under the existing main collector canopy. The inclusion of these roofs effectively splits the solar collector into two or three horizontal sections, producing a plant which utilizes two or three airstreams (flowing under the main collector roof), at different temperatures, to produce a specific power out-

put. Through the inclusion of air-flow regulating mechanisms, the flow rates of the various airstreams can be controlled. This gives the plant the ability to store or release energy on demand to ultimately control the power produced by the plant.

In terms of base load electricity generation, the inclusion of a secondary collector roof produces good control over plant output, while the incorporation of a double glazed secondary or secondary and tertiary collector roof facilitates excellent control over plant output. This is demonstrated by the fact that the summertime plant power delivered is between 31 % and 56 % of the peak summertime output of the reference plant when including a secondary collector roof, between 43 % and 50 % when employing a double glazed secondary roof and between 42 % and 51 % when incorporating a secondary and tertiary collector roof. For the purpose of peak load power generation, all the above-mentioned configurations facilitate good control over plant output. In addition, all the mentioned plant configurations produce comparable annual yields to that of the selected reference solar chimney power plant, both under a base or peak load power generation strategy.

The ability of the solar chimney power plant to produce a constant power output throughout an entire year, irrespective of season, was also explored. This evaluation involved the minimization of seasonal plant output variations through the storage of energy during the warmer months of the year and the extraction thereof during the colder months. A plant model incorporating a secondary and tertiary collector roof was employed and subjected to a base load control strategy, while seasonal energy storage and extraction were implemented. Results suggest that seasonal energy storage and extraction are ineffective, with a decline of approximately 12 % in annual plant yield, compared to the output of the reference plant.

The inclusion of plastic covered water tanks under the main collector roof were investigated as a means of static plant control to produce a more uniform daily power output profile. Simulations were conducted for a plant incorporating relatively shallow water tanks over a part or the entire collector ground surface. Results show that the inclusion of water tanks under the collector roof is a good mechanism for controlling plant output, where an increase in the area covered by water tanks produces an increasingly uniform daily power output profile. For a collector area fully covered by (relatively shallow) water tanks, simulations predict a daily summertime plant output of between 31 % and 63 % of the peak output of the reference plant. Other simulations were also performed employing deeper water tanks over the entire collector area. Here results indicate that increasing the tank depth will produce a more uniform daily power output profile up to a point, after which a further increase in tank depth will cause the power output profile to become inverted and less uniform. Comparable annual yields to that of the selected reference plant are predicted for all the above-mentioned plant configurations, indicating that the inclusion of water tanks does not significantly affect solar chimney power plant performance.

The incorporation of a delta ground surface configuration was also studied as a possible method to statically control the solar chimney plant power output. Simulations were performed which investigated the effects of a varying angle of repose as well as a varying delta perimeter height. Results indicate insignificant control over plant power output when incorporating a delta ground configuration. Additionally, annual power output reductions of between 10 % and 46 % are predicted when including a delta ground surface configuration, compared to the output of the reference plant.

Lastly, the dissertation studied the incorporation of vegetation under the collector roof for possible agricultural purposes. Firstly, vegetation is included over a collector radius of approximately 2000 m and results predict that the maximum allowable vegetation surface temperature of 40 °C is exceeded over this distance. Furthermore, a major reduction in annual power output of approximately 45 % is shown when incorporating vegetation under the collector roof over such a large collector radius. Secondly, vegetation is included in the model over a collector radius of approximately 1000 m. In this particular case, results indicate that vegetation surface temperatures never exceed 40 °C, while a major reduction in annual yield of approximately 30 % is still experienced, compared to the output of the

reference plant. The effect on plant performance of modelling the atmosphere outside and air inside the chimney of the solar chimney power plant according to different temperature lapse rates is evaluated. Three different lapse rates, the dry adiabatic lapse rate (DALR), a lapse rate which considers the vapor content of air and a combination of the lapse rate considering vapor content and a lapse rate which takes the effects of condensation into account, are implemented in the numerical model. Results predict (depending on the total collector area covered by vegetation) improved plant performance when considering the effects of air vapor content, compared to the same plant employing a DALR. Further improvement on plant performance is experienced when condensation effects inside the chimney of the plant are taken into account. Despite the improved plant performance when incorporating lapse rates other than the DALR, simulations still predict major reductions in annual plant output of between 30 % and 50 % (compared to output of the reference plant) as a result of the inclusion of vegetation under the collector roof.

8.1 Discussion and future work

This study successfully identified some areas of possible improvement and possible concern regarding the performance of the solar chimney power plant, while areas of possible future development were also discovered. Plant specifications which could potentially have a major positive impact on plant performance include the collector roof reflectance, collector roof emissivity, ground surface absorptivity and ground surface emissivity. Potential improvements on plant performance would require the treatment of these surfaces. Furthermore, through the thermal insulation or double glazing of the collector roof major enhancements in plant performance are also possible. Future work should investigate the technical, practical and financial viability of the above-mentioned treatments and modifications. Areas which may cause major reductions in plant output include the ground surface absorptivity, atmospheric temperature lapse rates with less steep gradients compared to the DALR, windy ambient conditions and the incorporation of vegetation under the collector roof of the plant. Other interesting findings of this study are that Sand is unsuitable as a ground type under the collector roof of the plant and that optimal large-scale solar chimney plant dimensions may possibly be larger than generally employed in previous studies.

In light thereof that this study presents trends which suggest that larger diameter chimneys (than presented in previous literature) should be constructed to obtain a more optimal solution, future work should investigate the specific construction methods and economics of these larger structures, as they may differ from those of smaller diameter chimneys.

Future research on the solar chimney power plant should continue investigating all aspects regarding dynamic control of plant power output through the inclusion of a secondary collector roof and air-flow regulating mechanisms. Through the inclusion of these technologies, the plant may be able to operate as a base or peak load electricity generation facility, depending on the required demand. Should effective peak load power generation be confirmed, a solar chimney power plant could financially become a much more attractive option, due to the high selling price of peak load electricity. In reference to the above, the development of a complete three-dimensional computer simulation model of the solar chimney power plant would be a powerful tool in the evaluation of possible dynamic control.

Experimental studies should be conducted in future to evaluate the effect of including different types of vegetation under the collector roof of the plant. These experiments should consider the influence on plant performance while also examining the viability of incorporating vegetation - in terms of plant growth and survivability in a harsh environment.

Finally, a valuable future contribution would be the development of a complete solar chimney power plant cost model for a full scale plant design, specific to an actual location and based on actual quotes for construction, material, transportation, operation, maintenance, return on investment, insurance and land costs.

List of References

- American Wind Energy Association (2006). Available at: http://www.awea.org/faq/wwt_costs.html. (Cited on page 4.)
- Atkins Power (2006). Available at: <http://www.co2balance.com>. (Cited on pages ix and 6.)
- Berdahl, P. and Fromberg, R. (1982). The thermal radiance of clear skies. *Solar Energy*, vol. 29, no. 4, pp. 299–314. (Cited on page 21.)
- Bernardes, M.A.d.S., Voß, A. and Weinrebe, G. (2003 December). Thermal and technical analyses of solar chimneys. *Solar Energy*, vol. 75, no. 6, pp. 511–524. (Cited on pages 17, 32, 34, 36, 44, 82, 84, 101, 103, and 104.)
- Bigelow laboratory for ocean sciences (2006). Available at: http://www.bigelow.org/virtual/handson/water_level.html. (Cited on pages ix and 6.)
- Bilgen, E. and Rheault, J. (2005). Solar chimney power plants for high latitudes. *Solar Energy*, vol. 79, no. 5, pp. 449–458. (Cited on page 17.)
- Burger, M. (2004). *Prediction of the Temperature Distribution in Asphalt Pavement Samples*. Master's thesis, University of Stellenbosch, Stellenbosch, South Africa. (Cited on pages 17, 19, 21, 113, and 129.)
- Buxmann, J. (1983). Strömungsverteilung und Wärmeübertragung bei unterschiedlichen Elementanordnungen im Trockenkühlturm. Tech. Rep. 61, Subproject E10, Report nr. 54, Universität Hannover. (Cited on page 28.)
- Çengel, Y.A. and Boles, M.A. (1998). *Thermodynamics: An Engineering Approach*. 3rd edn. McGraw-Hill. (Cited on pages 112 and 113.)
- co2balance.com (2006). Available at: <http://www.co2balance.com>. (Cited on pages ix and 5.)
- Coetzee, C.J. (2004). Personal Communication, University of Stellenbosch, Stellenbosch, South Africa. (Cited on page 106.)
- Conradie, P.J. (1989 February). Psigrometrie. Unpublished notes, University of Stellenbosch. (Cited on page 113.)
- Dong, A., Grattan, S.R., Carroll, J.J. and Prashar, C.R.K. (1992). Estimation of daytime net radiation over well-watered grass. *Journal of Irrigation and Drainage Engineering*, vol. 118, no. 3, pp. 466–479. (Cited on pages xvi and 118.)
- Du Preez, A.F. (1992 November). *The Influence of Cross-winds on the Performance of Natural Draft Dry-cooling Towers*. Ph.D. thesis, University of Stellenbosch, Stellenbosch, South Africa. (Cited on page 29.)
- Duffie, J.A. and Beckman, W.A. (1991). *Solar Engineering of Thermal Processes*. 2nd edn. John Wiley and Sons, Inc., New York. (Cited on pages 32, 35, 36, and 102.)
- Eskom (2006). Available at: <http://www.eskom.co.za/zqf/process.asp>. (Cited on page 82.)
- FAO (2006). Available at: <http://www.fao.org/docrep/x0490e/x0490e06.htm>. (Cited on page 114.)

- Gannon, A.J. (2002). *Solar Chimney Turbine Performance*. Ph.D. thesis, University of Stellenbosch, Stellenbosch, South Africa. (Cited on pages 14 and 17.)
- Gannon, A.J. and Von Backström, T.W. (2000). Solar chimney cycle analysis with system loss and solar collector performance. *Journal of Solar Energy Engineering*, vol. 122, no. 3, pp. 133–137. (Cited on page 16.)
- Gannon, A.J. and Von Backström, T.W. (2002 April). Controlling and maximising solar chimney power output. 1st International Conference on Heat Transfer, Fluid Mechanics and Thermodynamics, Kruger Park, South Africa. (Cited on page 16.)
- Gannon, A.J. and Von Backström, T.W. (2003). Solar chimney turbine performance. *Journal of Solar Energy Engineering*, vol. 125, pp. 101–106. (Cited on page 17.)
- Günther, H. (1931). *Die künftige Energieversorgung der Welt*. Franck'sche Verlagshandlung, Stuttgart. (Cited on page 15.)
- Haaf, W. (1984). Solar chimneys, part II: Preliminary test results from the Manzanares pilot plant. *International Journal of Solar Energy*, vol. 2, pp. 141–161. (Cited on page 16.)
- Haaf, W., Friedrich, K., Mayr, G. and Schlaich, J. (1983). Solar chimneys, part I: Principle and construction of the pilot plant in Manzanares. *International Journal of Solar Energy*, vol. 2, pp. 3–20. (Cited on page 15.)
- Haaland, S.E. (1983). Simple and explicit formulas for the friction factor in turbulent pipe flow. *Transactions of the ASME, Journal of Fluids Engineering*, vol. 185, no. 3, pp. 89–90. (Cited on page 25.)
- Hedderwick, R.A. (2001). *Performance Evaluation of a Solar Chimney Power Plant*. Master's thesis, University of Stellenbosch, Stellenbosch, South Africa. (Cited on pages 16, 32, 34, 36, 39, 40, 42, 44, 46, 47, 48, 50, 51, 53, 115, 154, and 186.)
- Holman, J.P. (1992). *Heat Transfer*. 7th edn. McGraw-Hill. (Cited on pages xiv and 42.)
- Hsu, S.T. (1963). *Engineering Heat Transfer*. D. Van Nostrand Company, Inc., Princeton, New Jersey. (Cited on pages xvi and 118.)
- Incropera, F.P. and DeWitt, D.P. (2002). *Fundamentals of Heat and Mass Transfer*. 5th edn. John Wiley and Sons, Inc. (Cited on pages xiv and 42.)
- Innovative Power Systems (2006). Available at: <http://www.ips-solar.com/links.htm>. (Cited on pages ix and 11.)
- Kirstein, C.F., Kröger, D.G. and Von Backström, T.W. (2005). Flow through a solar chimney power plant collector-to-chimney transition section. ISES 2005 Solar World Congress, Orlando, USA. (Cited on page 48.)
- Kloppers, J.C. (2003). *A Critical Evaluation and Refinement of the Performance Prediction of Wet-Cooling Towers*. Ph.D. thesis, University of Stellenbosch, Stellenbosch, South Africa. (Cited on pages 77 and 78.)
- Kröger, D.G. (2004). *Air-cooled Heat Exchangers and Cooling Towers*. Pennwell Corp., Tulsa, Oklahoma. (Cited on pages xiv, 22, 24, 28, 44, 45, 57, 68, 73, 78, 112, 114, 115, 149, 168, and 169.)
- Kröger, D.G. (2004-2006). Personal Communication, University of Stellenbosch, Stellenbosch, South Africa. (Cited on pages 86 and 106.)
- Kröger, D.G. and Blaine, D. (1999). Analysis of the driving potential of a solar chimney power plant. *South African Institution of Mechanical Engineering, R & D Journal*, vol. 15, pp. 85–94. (Cited on pages 16, 52, 54, 126, and 127.)

- Kröger, D.G. and Burger, M. (2004 June). Experimental convection heat transfer coefficient on a horizontal surface exposed to the natural environment. Proceedings of the ISES EuroSun2004 International Sonnenforum, vol. 1, pp. 422-430, Freiburg, Germany. (Cited on pages 17, 19, 21, and 129.)
- Kröger, D.G. and Buys, J.D. (1999). Radial flow boundary layer development analysis. *South African Institution of Mechanical Engineering, R & D Journal*, vol. 15, pp. 95–102. (Cited on page 16.)
- Kröger, D.G. and Buys, J.D. (2001). Performance evaluation of a solar chimney power plant. ISES 2001 Solar World Congress, Adelaide, South Australia. (Cited on pages 16, 32, 34, 36, 39, 40, 42, 44, 46, 47, 48, 50, 51, and 53.)
- Lombaard, F. (2002). *Performance of a Solar Air Heater incorporating Thermal Storage*. Master's thesis, University of Stellenbosch, Stellenbosch, South Africa. (Cited on page 102.)
- Lomborg, B. (2001). Running on empty? Available at: <http://www.guardian.co.uk/globalwarming/story/0,7369,537537,00.html>. (Cited on page 2.)
- Mills, A.F. (1995). *Heat and Mass Transfer*. Richard D. Irwin Inc., Chicago. (Cited on pages xiv, xvi, 42, 118, 184, and 185.)
- Modest, M.F. (1993). *Radiative Heat Transfer*. McGraw Hill Inc., New York. (Cited on pages 150, 189, 190, and 197.)
- Monteith, J.L. and Unsworth, M.H. (1990). *Principles of Environmental Physics*. Arnold, London. (Cited on pages 112 and 113.)
- Moore, F.K. and Garde, M.A. (1981). Aerodynamic losses of highly flared natural draft cooling towers. 3rd Waste Heat Management and Utilization Conference, Miami. (Cited on page 57.)
- Mullett, L.B. (1987). The solar chimney - overall efficiency, design and performance. *International Journal of Ambient Energy*, vol. 8, pp. 35–40. (Cited on page 16.)
- Padki, M.M. and Sherif, S.A. (1988). Fluid dynamics of solar chimneys. *Proceedings of the ASME Winter Annual Meeting*, pp. 43–46. (Cited on page 16.)
- Pastohr, H., Kornadt, O. and Gürlebeck, K. (2004). Numerical and analytical calculations of the temperature and flow field in the upwind power plant. *International Journal of Energy Research*, vol. 28, pp. 495–510. (Cited on page 17.)
- Pasumarthi, N. and Sherif, S.A. (1998a). Experimental and theoretical performance of a demonstration solar chimney model - part I: Mathematical model development. *International Journal of Energy Research*, vol. 22, pp. 277–288. (Cited on page 16.)
- Pasumarthi, N. and Sherif, S.A. (1998b). Experimental and theoretical performance of a demonstration solar chimney model - part II: Experimental and theoretical results and economic analysis. *International Journal of Energy Research*, vol. 22, pp. 443–461. (Cited on page 16.)
- Pretorius, J.P. (2004). *Solar Tower Power Plant Performance Characteristics*. Master's thesis, University of Stellenbosch, Stellenbosch, South Africa. (Cited on pages iii, iv, 17, 19, 30, 52, 115, 119, 129, 138, 153, 155, 164, 174, 175, 177, 178, 179, 182, 187, 188, 189, 191, 196, and 198.)
- Pretorius, J.P., Kröger, D.G., Buys, J.D. and Von Backström, T.W. (2004 June). Solar tower power plant performance characteristics. Proceedings of the ISES EuroSun2004 International Sonnenforum, vol.1, pp. 870-879, Freiburg, Germany. (Cited on pages 17, 32, 34, 36, 39, 40, 42, 44, 46, 47, 48, 50, 51, and 53.)
- Schlaich, J. (1991). World energy demand, population explosion and pollution: could solar energy utilisation become a solution? *The Structural Engineer*, vol. 69, no. 10, pp. 189–192. (Cited on page 16.)

- Schlaich, J. (1994). *The Solar Chimney: Electricity from the Sun*. Deutsche Verlags-Anstalt, Stuttgart. (Cited on pages 13, 16, 34, 55, 82, 84, 101, and 103.)
- Schlaich, J. (1999). Tension structures for solar electricity generation. *Engineering structures*, vol. 21, pp. 658–668. (Cited on page 16.)
- Schlaich Bergermann und Partner (2006). Available at: <http://www.sbp.de/en/fla/mittig.html>. (Cited on pages ix and 14.)
- Serag-Eldin, M.A. (2004 July). Computing flow in a solar chimney plant subject to atmospheric winds. Proceedings of HT-FED04 2004 ASME Heat Transfer/Fluids Engineering Summer Conference, Charlotte, North Carolina, USA. (Cited on page 68.)
- Siegel, R. and Howell, J.R. (1992). *Thermal Radiation Heat Transfer*. 3rd edn. Taylor & Francis, Washington, DC. (Cited on pages 191 and 192.)
- Simon, M. (1976). Konzept der atmosphärischen Nutzung, in AGS/ASA-study energiequellen für morgen? *Nichtfossile/nichtnukleare Energiequellen, Teil II: Nutzung der solaren Strahlungsenergie*, pp. 555–564. Umschau-Verlag. (Cited on page 16.)
- Solar-Auto-Controller (2006). Available at: http://www.egis-rotor.de/sac_us.html. (Cited on pages ix and 11.)
- Solarbuzz (2006). Available at: <http://www.solarbuzz.com/StatsCosts.htm>. (Cited on page 4.)
- Taiz, L. and Zeiger, E. (1998). *Plant Physiology*. 2nd edn. Sinauer Associates Inc., Sunderland, USA. (Cited on page 119.)
- Trieb, F., Langniß, O. and Klaiß, H. (1997). Solar electricity generation - a comparative view of technologies, costs and environmental impact. *Solar Energy*, vol. 59, no. 1-3, pp. 88–99. (Cited on page 13.)
- UN atlas of the oceans (2006). Available at: <http://www.oceanatlas.com/unatlas/uses/EnergyResources/Background/Wave/W2.html>. (Cited on pages ix and 7.)
- University of Texas El Paso (2006). Available at: <http://www.solarpond.utep.edu>. (Cited on pages ix and 12.)
- US Department of Energy (2006). Available at: http://www1.eere.energy.gov/solar/solar_time_1900.html. (Cited on pages ix and 10.)
- U.S. Energy Information Administration (2001). International energy annual. Available at: <http://eia.doe.gov>. (Cited on pages ix, 1, and 2.)
- U.S. Environmental Protection Agency (2000). Available at: <http://yosemite.epa.gov>. (Cited on page 2.)
- Van Dyk, C. (2004-2006). Personal Communication, University of Stellenbosch, Stellenbosch, South Africa. (Cited on pages 40 and 56.)
- Von Backström, T.W. (2004-2006). Personal Communication, University of Stellenbosch, Stellenbosch, South Africa. (Cited on page 48.)
- Von Backström, T.W., Bernhardt, A. and Gannon, A.J. (2003a). Pressure drop in solar power plant chimneys. *Transactions of the ASME, Journal of Solar Energy Engineering*, vol. 125, pp. 1–5. (Cited on page 50.)
- Von Backström, T.W. and Fluri, T.P. (2004 June). Maximum fluid power condition in solar chimney power plants - an analytical approach. 5th ISES Europe Solar Conference, Freiburg, Germany. (Cited on page 17.)
- Von Backström, T.W. and Gannon, A.J. (2000a). Compressible flow through solar power plant chimneys. *Transactions of the ASME, Journal of Solar Energy Engineering*, vol. 122, pp. 1–8. (Cited on page 16.)

- Von Backström, T.W. and Gannon, A.J. (2000*b*). The solar chimney air standard thermodynamic cycle. *South African Institution of Mechanical Engineering, R & D Journal*, vol. 16, no. 1, pp. 16–24. (Cited on page 16.)
- Von Backström, T.W., Kirstein, C.F. and Pillay, L.A. (2003*b*). The influence of some secondary effects on solar chimney power plant performance. 2003 ISES Solar World Congress, Göteborg, Sweden. (Cited on pages 48 and 54.)
- Westdyk, D. (2005-2006). Personal Communication, University of Stellenbosch, Stellenbosch, South Africa. (Cited on page 113.)
- White, F.M. (1999). *Fluid Mechanics*. 4th edn. McGraw-Hill, Singapore. (Cited on page 24.)

Appendix

A

Conservation Equations: Including a Secondary Collector Roof

Results of previous studies regarding the performance of solar chimney power plants have shown that the plant power output varies considerably during the day.

This appendix investigates the possibility of including a secondary collector roof under the main collector canopy for the purpose of controlling the plant power output according to certain demand patterns. Relevant conservation equations for a collector incorporating a secondary roof are derived. These equations are discretized (not presented) according to the schemes discussed by Pretorius (2004) before their inclusion into the existing computer simulation model.

Chapter 6 discusses the modifications to the collector as well as the operation of the solar chimney power plant with the inclusion of a secondary collector roof.

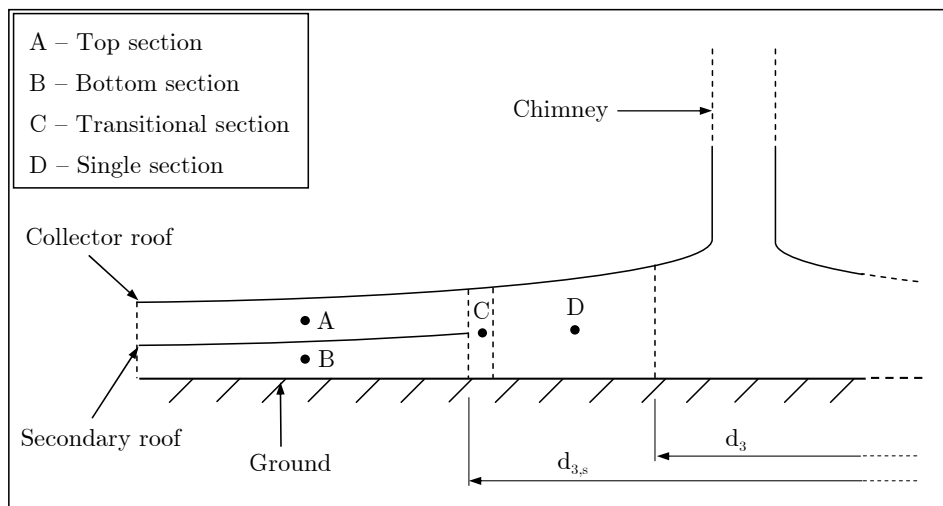


Figure A.1: Definition of sections created in the collector by the inclusion of a secondary collector roof

A.1 Definition of sections in the collector

Top and bottom section

The incorporation of a secondary collector roof divides the collector air-flow region into two sections, namely a top and bottom section (see figure A.1). It is assumed that air flows constantly through the top section (the region between the main and secondary collector roofs), while the air-flow through the bottom section (the region between the secondary roof and the ground surface) can be regulated by an air-flow regulating mechanism at the bottom section outlet (refer to Chapter 6).

Transition section

The transition section is defined as the region under the main collector roof where the secondary roof ends (see figure A.1). At this point the top and bottom sections of the collector merge, forming a single section between the main collector roof and the ground surface. This transition section is assumed to stretch over the length of one radial control volume.

Consequently, as mixing of the top and bottom air streams occur in the transition section, it is necessary to distinguish between the properties of the air in the top and bottom sections. Therefore, when evaluating the transition section, all future references to the air properties in the top and bottom sections employ the subscripts *top* and *bot* respectively.

Single section after transition

After the transitional collector control volume, the air-flow is simply considered as flow between parallel plates in a single section, i.e. between the main collector roof and the ground surface (see figure A.1).

A.2 Collector continuity equation

A.2.1 Top section

The top section of the collector is defined as the region between the main collector roof and the secondary roof, as illustrated by figure A.1. Air flows through this section from the collector perimeter inwards toward the chimney. By assuming purely radial air-flow, consider from figure A.2 the following mass conservation relation applicable to the air stream flowing through a defined top section collector control volume with radial length Δr and subtended angle $\Delta\theta$

$$\rho v r \Delta\theta (H - H_s) = \rho v r \Delta\theta (H - H_s) + \frac{\partial}{\partial r} (\rho v r \Delta\theta (H - H_s)) \Delta r + \frac{\partial}{\partial t} (\rho r \Delta\theta \Delta r (H - H_s)) \quad (\text{A.1})$$

where ρ and v represent the air density and radial velocity respectively, while H and H_s are the respective heights of the main collector roof and secondary roof at a specific radial position. Simplifying and dividing equation (A.1) by $r \Delta\theta \Delta r$ gives

$$\frac{1}{r} \frac{\partial}{\partial r} (\rho v r (H - H_s)) = -(H - H_s) \frac{\partial \rho}{\partial t} \quad (\text{A.2})$$

During steady state conditions or when transient effects are negligible, equation (A.2) becomes

$$\frac{\partial}{\partial r} (\rho v r (H - H_s)) = 0 \quad (\text{A.3})$$

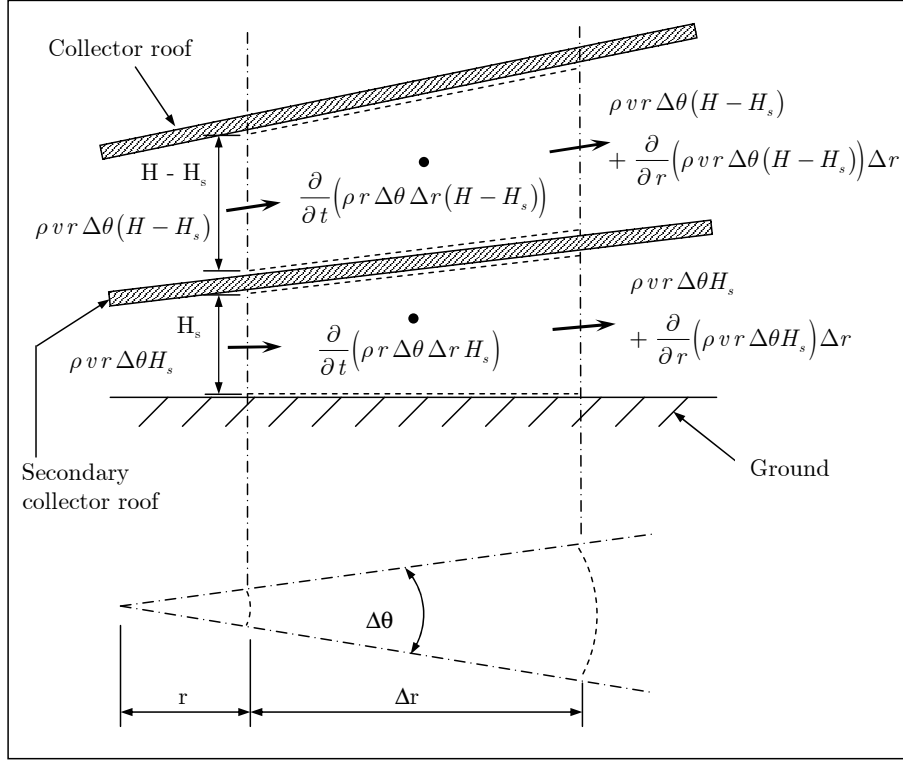


Figure A.2: Conservation of mass applied to the air flowing through a defined top and bottom section collector control volume

A.2.2 Open bottom section

The bottom section of the collector is the section between the secondary roof and the ground surface (see figure A.1). When evaluating figure A.2 and assuming purely radial air-flow, the following mass conservation relation can be developed for the air stream moving through a defined elementary control volume in the bottom section of the collector

$$\rho v r \Delta \theta H_s = \rho v r \Delta \theta H_s + \frac{\partial}{\partial r} (\rho v r \Delta \theta H_s) \Delta r + \frac{\partial}{\partial t} (\rho r \Delta \theta \Delta r H_s) \quad (\text{A.4})$$

where ρ and v refer to the respective air density and radial velocity of the bottom air stream. When simplifying and dividing equation (A.4) by $r \Delta \theta \Delta r$, we find

$$\frac{1}{r} \frac{\partial}{\partial r} (\rho v r H_s) = -H_s \frac{\partial \rho}{\partial t} \quad (\text{A.5})$$

During steady state conditions or when transient effects are negligible, equation (A.5) reduces to

$$\frac{\partial}{\partial r} (\rho v r H_s) = 0 \quad (\text{A.6})$$

A.2.3 Closed bottom section

With the air-flow regulating mechanism at the bottom section outlet fully closed (refer to Chapter 6), no air-flow is possible through this section. This implies an air-flow velocity of zero in the bottom section of the collector.

A.2.4 Transition section

The transition section is defined as the section where the secondary roof ends and the top and bottom air streams are merged into a single stream (see figure A.1). The transition section is assumed to span the length of a single radial collector control volume.

Open bottom section

When assuming purely radial air-flow and considering figure A.3, the following approximated mass conservation relation is derived for the air-flow through a defined transitional collector control volume

$$\begin{aligned}
 &(\rho_{top} v_{top} r (H - H_s))_{i-1} \Delta\theta + (\rho_{bot} v_{bot} r H_s)_{i-1} \Delta\theta \\
 &= (\rho v r H)_i \Delta\theta + \frac{\partial}{\partial t} (\rho r \Delta\theta \Delta r H)
 \end{aligned} \tag{A.7}$$

where the subscripts *top* and *bot* refer to the properties of the air in the top and bottom section control volumes respectively. Dividing equation (A.7) by $\Delta\theta$ and rearranging gives

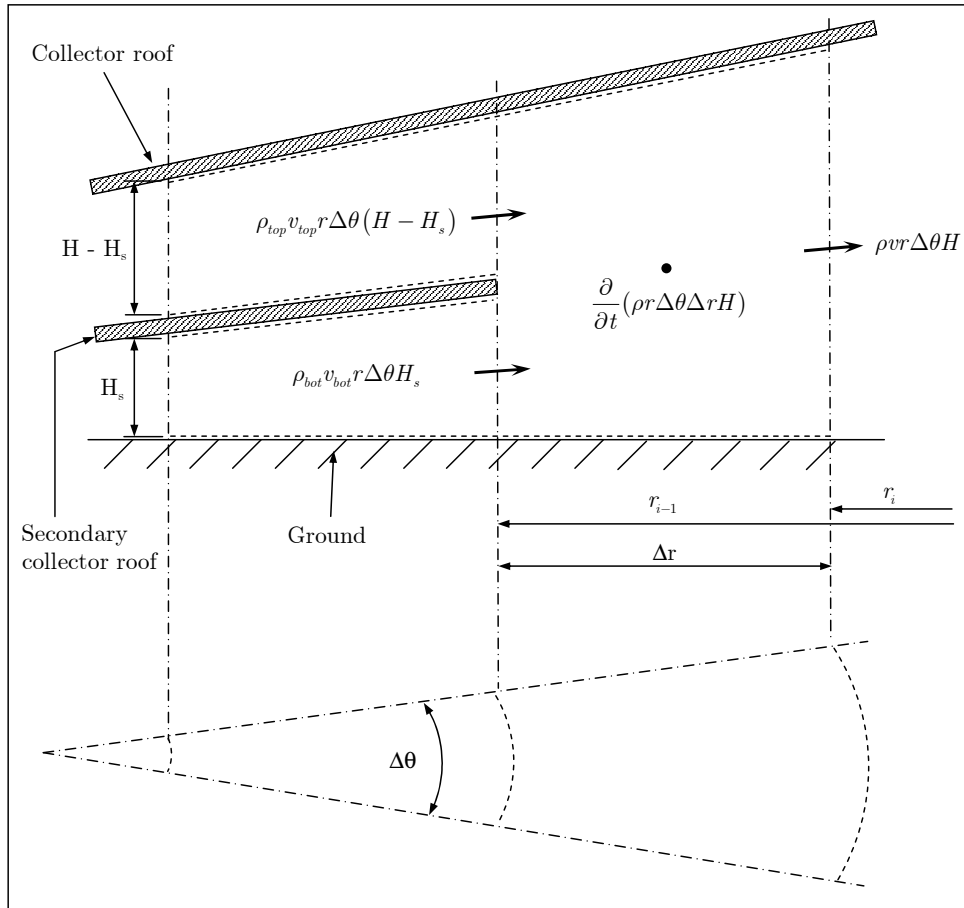


Figure A.3: Conservation of mass applied to the air flowing through a defined transitional collector control volume

$$(\rho_{top}v_{top}r(H - H_s))_{i-1} + (\rho_{bot}v_{bot}rH_s)_{i-1} = (\rho vrH)_i + r\Delta rH \frac{\partial \rho}{\partial t} \quad (\text{A.8})$$

During steady state conditions or when transient effects are negligible, equation (A.8) can be simplified and rearranged to find the velocity at the transitional section outlet (at node i)

$$v_i = \frac{(\rho_{top}v_{top}r(H - H_s))_{i-1} + (\rho_{bot}v_{bot}rH_s)_{i-1}}{(\rho rH)_i} \quad (\text{A.9})$$

Closed bottom section

With the air-flow regulating mechanism at the bottom section outlet fully closed, no air-flow through the bottom section is possible. The approximated mass conservation relation applicable to the air flowing through the transitional control volume during these times will be similar to that of equation (A.7), except for the second term on the left-hand-side. Subsequently, after dividing by $\Delta\theta$ we find

$$(\rho_{top}v_{top}r(H - H_s))_{i-1} = (\rho vrH)_i + r\Delta rH \frac{\partial \rho}{\partial t} \quad (\text{A.10})$$

During steady state conditions or when transient effects are negligible, equation (A.10) can be simplified and rearranged to find the velocity after the transition at node i

$$v_i = \frac{(\rho_{top}v_{top}r(H - H_s))_{i-1}}{(\rho rH)_i} \quad (\text{A.11})$$

A.3 Collector momentum equation

A.3.1 Top section

When regarding figure A.4 and assuming purely radial air-flow, the following momentum equation can be formulated for the air-flow through the defined top section control volume of the collector:

$$\begin{aligned} \sum F = & -\rho v^2 r \Delta\theta (H - H_s) + \rho v^2 r \Delta\theta (H - H_s) \\ & + \frac{\partial}{\partial r} (\rho v^2 r \Delta\theta (H - H_s)) \Delta r + \frac{\partial}{\partial t} (\rho vr \Delta\theta \Delta r (H - H_s)) \end{aligned} \quad (\text{A.12})$$

where $\sum F$ represents the sum of the forces acting on the control volume.

Consider figure A.5 showing schematically the forces exerted on the top and bottom collector control volumes. The sum of the normal forces acting on the sides of the top section control volume is calculated by taking the average pressure and height on each of the sides:

$$\begin{aligned} F_{top,side,normal} &= 2p_{avg}A_{side,top} \\ &= 2 \left[0.5 \left(p + p + \frac{\partial p}{\partial r} \Delta r \right) \right] \times \\ &\quad \left[0.5 \left((H - H_s) + (H - H_s) + \frac{\partial H}{\partial r} \Delta r - \frac{\partial H_s}{\partial r} \Delta r \right) \Delta r \right] \end{aligned} \quad (\text{A.13})$$

The radial component of the full normal force is determined by multiplying by $\sin(\Delta\theta/2)$. It is assumed that both $\Delta\theta$ and Δr are small, therefore $\sin(\Delta\theta/2) \approx (\Delta\theta/2)$ and higher orders of Δr are neglected, giving

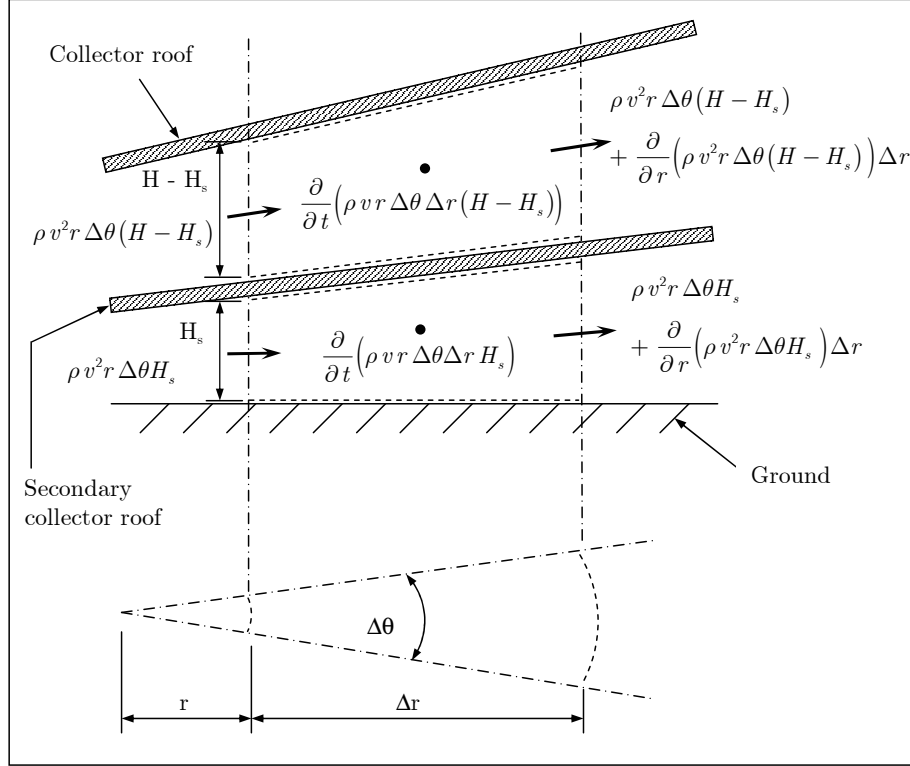


Figure A.4: Conservation of momentum applied to the air flowing through a defined top and bottom section collector control volume

$$\begin{aligned}
 F_{\text{top,side,radial}} &= 0.25\Delta\theta\Delta r \left[\left(2p + \frac{\partial p}{\partial r}\Delta r \right) \left(2(H - H_s) + \Delta r \left(\frac{\partial H}{\partial r} - \frac{\partial H_s}{\partial r} \right) \right) \right] \quad (\text{A.14}) \\
 &= p\Delta\theta\Delta r(H - H_s)
 \end{aligned}$$

The inclined main collector roof exerts a normal force on the top boundary of the top control volume, as shown in figure A.5. This force is calculated using the average pressure on the top of this particular control volume. Due to the assumption of a small collector roof inclination, the control volume roof area is approximated as $r\Delta\theta\Delta r$ and $\sin\phi_r \approx \frac{\partial H}{\partial r}$. Therefore the normal force is

$$F_{\text{top,roof,normal}} = p_{\text{avg}}A_{\text{roof}} = 0.5 \left(p + p + \frac{\partial p}{\partial r}\Delta r \right) r\Delta\theta\Delta r \quad (\text{A.15})$$

The radial component of this normal force is calculated by multiplying with $\sin\phi_r$. Once again, higher order terms may be neglected giving the radial force

$$F_{\text{top,roof,radial}} = \left(pr\Delta\theta\Delta r + 0.5\frac{\partial p}{\partial r}r\Delta\theta\Delta r^2 \right) \frac{\partial H}{\partial r} = pr\Delta\theta\Delta r \frac{\partial H}{\partial r} \quad (\text{A.16})$$

The inclination of the secondary collector roof also causes a normal force acting on the bottom boundary of the top control volume, as illustrated by figure A.5. This force is calculated using the average pressure on the bottom of the top control volume. As with the main collector roof, due to the assumption of a small secondary collector roof inclination, the bottom area of the top control volume is also approximated as $r\Delta\theta\Delta r$ and analogously, $\sin\phi_s \approx \frac{\partial H_s}{\partial r}$. Thus the normal force exerted by the secondary roof is

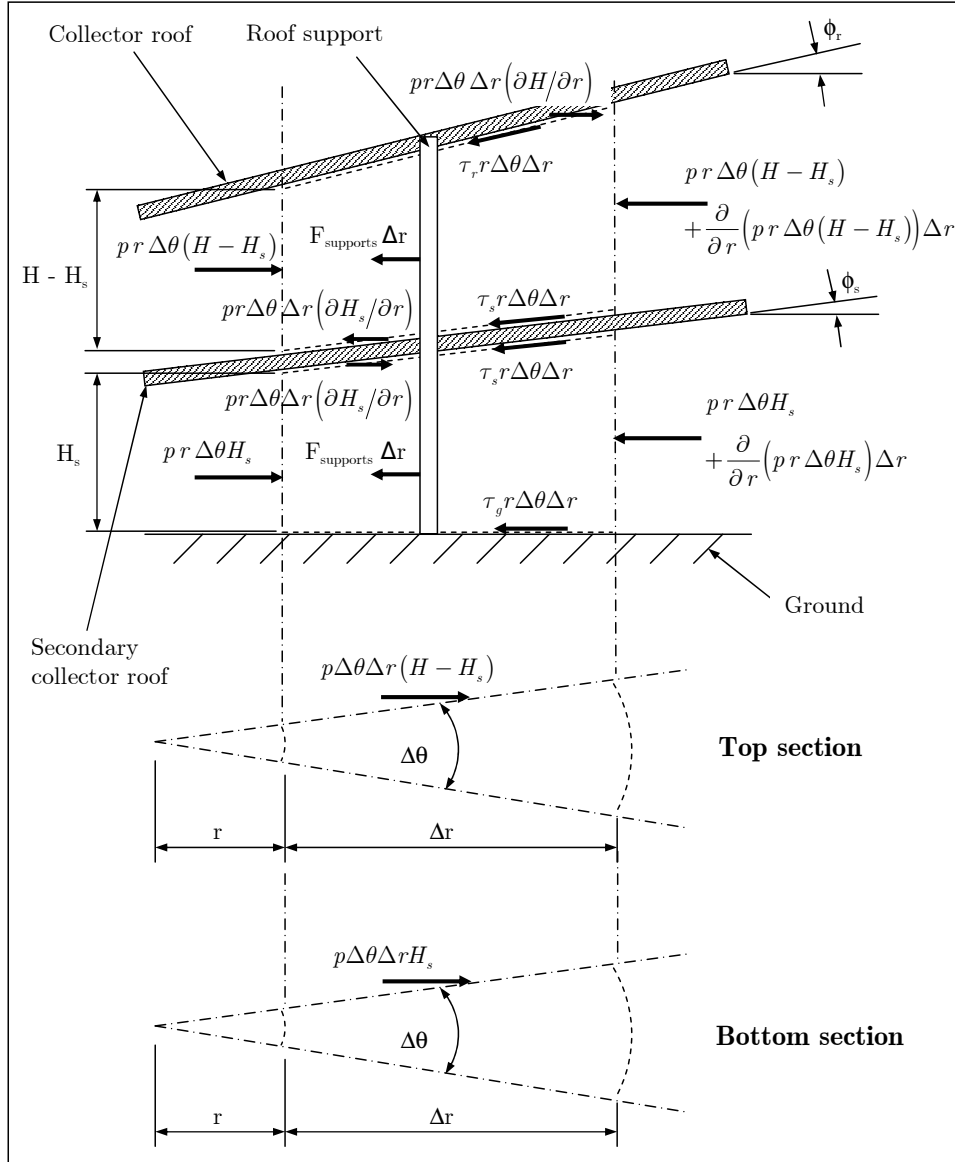


Figure A.5: Forces acting on the defined top and bottom air stream control volumes in the collector

$$F_{\text{top,sec.roof,normal}} = p_{\text{avg}} A_{\text{sec.roof}} = 0.5 \left(p + p + \frac{\partial p}{\partial r} \Delta r \right) r \Delta\theta \Delta r \quad (\text{A.17})$$

Similar to previous calculations, the radial component is obtained by multiplying the normal force with $\sin \phi_s$. Higher order terms are neglected giving the radial force

$$F_{\text{top,sec.roof,radi al}} = \left(pr\Delta\theta\Delta r + 0.5 \frac{\partial p}{\partial r} r \Delta\theta\Delta r^2 \right) \frac{\partial H_s}{\partial r} = pr\Delta\theta\Delta r \frac{\partial H_s}{\partial r} \quad (\text{A.18})$$

When considering figure A.5 and substituting the above-calculated forces into the left side of equation (A.12), we find

$$\begin{aligned}
& -\frac{\partial}{\partial r} (pr\Delta\theta(H - H_s)) \Delta r + pr\Delta\theta\Delta r \frac{\partial H}{\partial r} + p\Delta\theta\Delta r(H - H_s) \\
& \quad - \tau_r r \Delta\theta\Delta r - \tau_s r \Delta\theta\Delta r - F_{\text{supports}} \Delta r - pr\Delta\theta\Delta r \frac{\partial H_s}{\partial r} \\
& \quad = \frac{\partial}{\partial r} (\rho v^2 r \Delta\theta(H - H_s)) \Delta r + \frac{\partial}{\partial t} (\rho v r \Delta\theta\Delta r(H - H_s)) \quad (\text{A.19})
\end{aligned}$$

with p the driving pressure causing the air in the collector to flow, while τ_r and τ_s represent the main collector roof and secondary collector roof shear stresses respectively acting on the air stream in the top control volume. These viscous stresses are assumed to be constant over the radial distance Δr of the control volume. The term F_{supports} is the total drag force per unit radial distance that the roof supports (supporting both the main and secondary collector roofs) enforce on the air stream in the top control volume.

The first term on the left-hand-side of equation (A.19) can be split into the two terms:

$$-\frac{\partial}{\partial r} (pr\Delta\theta(H - H_s)) \Delta r = -\frac{\partial}{\partial r} (pr\Delta\theta H) \Delta r + \frac{\partial}{\partial r} (pr\Delta\theta H_s) \Delta r \quad (\text{A.20})$$

Applying the differential operator to the first term on the right-hand-side of equation (A.20) leads to

$$-\frac{\partial}{\partial r} (pr\Delta\theta H) \Delta r = -pr\Delta\theta\Delta r \frac{\partial H}{\partial r} - p\Delta\theta\Delta r H - r\Delta\theta\Delta r H \frac{\partial p}{\partial r} \quad (\text{A.21})$$

When applying the differential operator to the second term on the right-hand-side of equation (A.20), we find

$$\frac{\partial}{\partial r} (pr\Delta\theta H_s) \Delta r = pr\Delta\theta\Delta r \frac{\partial H_s}{\partial r} + p\Delta\theta\Delta r H_s + r\Delta\theta\Delta r H_s \frac{\partial p}{\partial r} \quad (\text{A.22})$$

Substitute equation (A.21) and (A.22) into equation (A.19), simplify, divide by $r\Delta\theta\Delta r$ and find

$$(H_s - H) \frac{\partial p}{\partial r} - \tau_r - \tau_s - \frac{F_{\text{supports}}}{r\Delta\theta} = \frac{1}{r} \frac{\partial}{\partial r} (\rho v^2 r (H - H_s)) + (H - H_s) \frac{\partial}{\partial t} (\rho v) \quad (\text{A.23})$$

Applying the differential operator to the first term on the right-hand-side of equation (A.23) yields

$$\frac{1}{r} \frac{\partial}{\partial r} (\rho v^2 r (H - H_s)) = \frac{v}{r} \frac{\partial}{\partial r} (\rho v r (H - H_s)) + \rho v (H - H_s) \frac{\partial v}{\partial r} \quad (\text{A.24})$$

When we apply the differential operator to the second term on the right-hand-side of equation (A.23), it follows that

$$(H - H_s) \frac{\partial}{\partial t} (\rho v) = \rho (H - H_s) \frac{\partial v}{\partial t} + v (H - H_s) \frac{\partial \rho}{\partial t} \quad (\text{A.25})$$

Substitute equation (A.2) into equation (A.25) and obtain

$$(H - H_s) \frac{\partial}{\partial t} (\rho v) = \rho (H - H_s) \frac{\partial v}{\partial t} - \frac{v}{r} \frac{\partial}{\partial r} (\rho v r (H - H_s)) \quad (\text{A.26})$$

Substitute equations (A.24) and (A.26) into equation (A.23) and find

$$(H_s - H) \frac{\partial p}{\partial r} - \tau_r - \tau_s - \frac{F_{\text{supports}}}{r\Delta\theta} = \rho (H - H_s) \left(v \frac{\partial v}{\partial r} + \frac{\partial v}{\partial t} \right) \quad (\text{A.27})$$

During steady state conditions or when transient effects are negligible, equation (A.27) becomes

$$(H_s - H) \frac{\partial p}{\partial r} - \tau_r - \tau_s - \frac{F_{\text{supports}}}{r \Delta \theta} = \rho v (H - H_s) \frac{\partial v}{\partial r} \quad (\text{A.28})$$

A.3.2 Open bottom section

As we again consider figure A.4 and assume purely radial air-flow, the following momentum relation follows for the air stream flowing through an elementary bottom section collector control volume:

$$\sum F = -\rho v^2 r \Delta \theta H_s + \rho v^2 r \Delta \theta H_s + \frac{\partial}{\partial r} (\rho v^2 r \Delta \theta H_s) \Delta r + \frac{\partial}{\partial t} (\rho v r \Delta \theta \Delta r H_s) \quad (\text{A.29})$$

Analogous to the top section calculations, the sum of the normal forces acting on the sides of the bottom section control volume is evaluated by taking the average pressure and height on each of the sides:

$$\begin{aligned} F_{\text{bot,side,normal}} &= 2p_{\text{avg}} A_{\text{side,bot}} \\ &= 2 \left[0.5 \left(p + p + \frac{\partial p}{\partial r} \Delta r \right) 0.5 \left(H_s + H_s + \frac{\partial H_s}{\partial r} \Delta r \right) \Delta r \right] \end{aligned} \quad (\text{A.30})$$

When multiplying by $(\Delta \theta / 2)$ in order to find the radial component of the full normal force and neglecting the higher orders of Δr , we find

$$F_{\text{bot,side,radial}} = 0.25 \Delta \theta \Delta r \left[\left(2p + \frac{\partial p}{\partial r} \Delta r \right) \left(2H_s + \frac{\partial H_s}{\partial r} \Delta r \right) \right] = p \Delta \theta \Delta r H_s \quad (\text{A.31})$$

The secondary collector roof exerts a normal force on the top boundary of the bottom control volume, which is calculated using the average pressure at this point of the bottom control volume. This normal force is

$$F_{\text{bot,sec.roof,normal}} = p_{\text{avg}} A_{\text{sec.roof}} = 0.5 \left(p + p + \frac{\partial p}{\partial r} \Delta r \right) r \Delta \theta \Delta r \quad (\text{A.32})$$

Multiplying by $\sin \phi_s \approx \frac{\partial H_s}{\partial r}$ to determine the radial component and neglecting higher orders of Δr gives

$$F_{\text{bot,sec.roof,radial}} = \left(p r \Delta \theta \Delta r + 0.5 \frac{\partial p}{\partial r} r \Delta \theta \Delta r^2 \right) \frac{\partial H_s}{\partial r} = p r \Delta \theta \Delta r \frac{\partial H_s}{\partial r} \quad (\text{A.33})$$

When again regarding figure A.5, the left side of equation (A.29) may now be expanded as follows:

$$\begin{aligned} & - \frac{\partial}{\partial r} (p r \Delta \theta H_s) \Delta r + p r \Delta \theta \Delta r \frac{\partial H_s}{\partial r} + p \Delta \theta \Delta r H_s - \tau_s r \Delta \theta \Delta r - \tau_g r \Delta \theta \Delta r \\ & - F_{\text{supports}} \Delta r = \frac{\partial}{\partial r} (\rho v^2 r \Delta \theta H_s) \Delta r + \frac{\partial}{\partial t} (\rho v r \Delta \theta \Delta r H_s) \end{aligned} \quad (\text{A.34})$$

where τ_s and τ_g are the secondary collector roof and ground surface shear stresses respectively acting on the air stream in the defined bottom control volume. These viscous stresses

are also assumed to be constant over the radial length of the control volume. The term F_{supports} is the total drag force per unit radial distance that the roof supports (supporting both the main and secondary collector roofs) enforce on the air stream in the bottom control volume.

Applying the differential operator to the first term on the left-hand-side of equation (A.34) leads to

$$-\frac{\partial}{\partial r} (p r \Delta \theta H_s) \Delta r = -p r \Delta \theta \Delta r \frac{\partial H_s}{\partial r} - p \Delta \theta \Delta r H_s - r \Delta \theta \Delta r H_s \frac{\partial p}{\partial r} \quad (\text{A.35})$$

When substituting equation (A.35) into equation (A.34), simplifying and dividing by $r \Delta \theta \Delta r$ we obtain

$$-H_s \frac{\partial p}{\partial r} - \tau_s - \tau_g - \frac{F_{\text{supports}}}{r \Delta \theta} = \frac{1}{r} \frac{\partial}{\partial r} (\rho v^2 r H_s) + H_s \frac{\partial}{\partial t} (\rho v) \quad (\text{A.36})$$

Apply the differential operator to the first right-hand-side term of equation (A.36) and find

$$\frac{1}{r} \frac{\partial}{\partial r} (\rho v^2 r H_s) = \frac{v}{r} \frac{\partial}{\partial r} (\rho v r H_s) + \rho v H_s \frac{\partial v}{\partial r} \quad (\text{A.37})$$

Applying the differential operator to the second term on the right-hand-side of equation (A.36) gives

$$H_s \frac{\partial}{\partial t} (\rho v) = \rho H_s \frac{\partial v}{\partial t} + v H_s \frac{\partial \rho}{\partial t} \quad (\text{A.38})$$

Substituting equation (A.5) into equation (A.38) gives the following

$$H_s \frac{\partial}{\partial t} (\rho v) = \rho H_s \frac{\partial v}{\partial t} - \frac{v}{r} \frac{\partial}{\partial r} (\rho v r H_s) \quad (\text{A.39})$$

Substituting equations (A.37) and (A.39) into equation (A.36) yields

$$-\left(H_s \frac{\partial p}{\partial r} + \tau_s + \tau_g + \frac{F_{\text{supports}}}{r \Delta \theta} \right) = \rho H_s \left(v \frac{\partial v}{\partial r} + \frac{\partial v}{\partial t} \right) \quad (\text{A.40})$$

During steady state conditions or when transient effects are negligible, equation (A.40) reduces to

$$-\left(H_s \frac{\partial p}{\partial r} + \tau_s + \tau_g + \frac{F_{\text{supports}}}{r \Delta \theta} \right) = \rho v H_s \frac{\partial v}{\partial r} \quad (\text{A.41})$$

A.3.3 Closed bottom section

As previously mentioned, with the air-flow regulating mechanism at the bottom section outlet fully closed, no air-flow is possible through this section. During such times the pressure in the bottom section is approximated to be equal to the ambient pressure at ground level.

A.3.4 Transition section

Open bottom section

As the air in the collector flows from the perimeter through the top and bottom sections, it should experience different pressure changes due to friction and support drag in the respective sections. However, the flow will regulate itself in order to produce an equal air pressure at the point where the sections meet. Consider figure A.6. This means that, independent of the amount of air-flow regulated through the bottom section, at the end of the secondary roof $p_{\text{top}} \approx p_{\text{bot}}$.

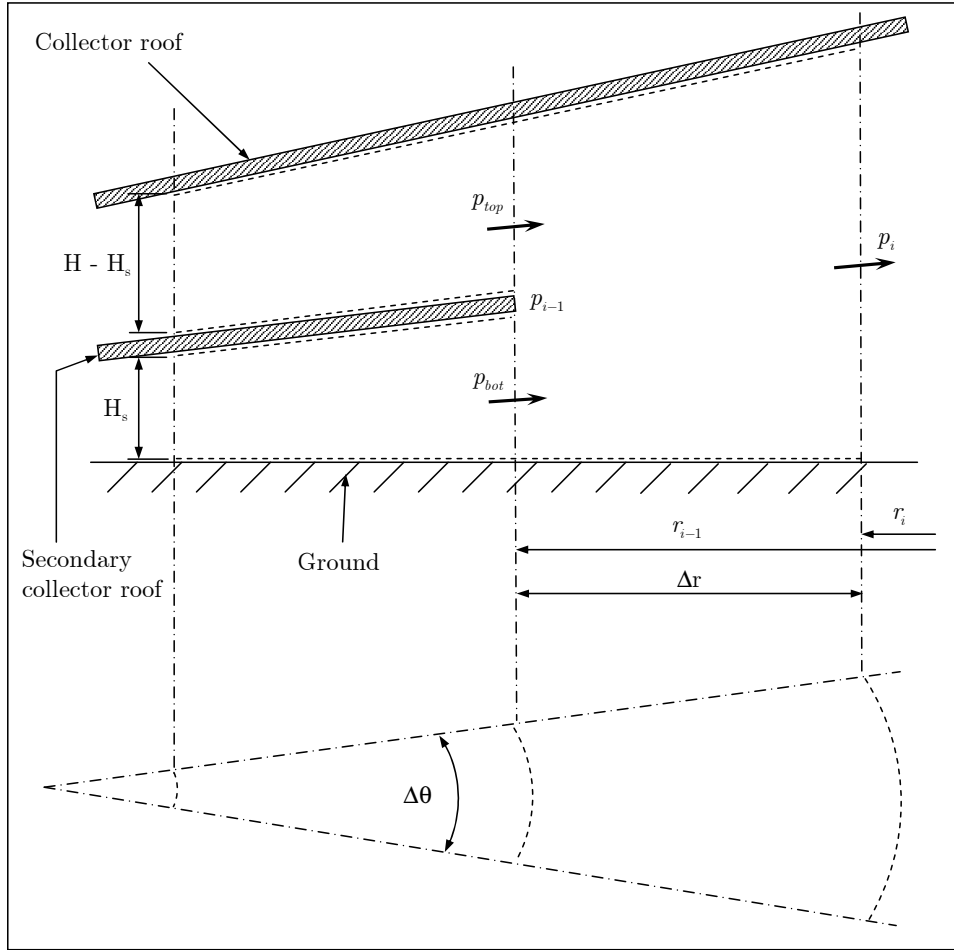


Figure A.6: Conservation of momentum applied to the air stream flowing through the defined transitional collector control volume

Subsequently, in order to simplify the numerical model, the following condition is assumed for the evaluation of the air-flow momentum in the transitional collector control volume (see figure A.6)

$$p_{i-1} = (p_{top})_{i-1} = (p_{bot})_{i-1} \quad (\text{A.42})$$

where p_{i-1} refers to the pressure at the inlet of the transitional control volume (at collector radius r_{i-1}), at the point where the air streams of the top and bottom sections merge.

It is assumed that the flow through the transitional control volume will be normal single channel flow. Therefore, the conservation of momentum applied to the air stream moving through the transitional collector control volume will be evaluated according to the original steady state collector momentum equation (equation (2.2) in Chapter 2). This partial differential equation is repeated here for convenience

$$-\left(H \frac{\partial p}{\partial r} + \tau_r + \tau_g + \frac{F_{\text{supports}}}{r \Delta \theta}\right) = \rho v H \frac{\partial v}{\partial r} \quad (\text{A.43})$$

Closed bottom section

With the air-flow regulating mechanism at the bottom section outlet fully closed, air from the collector perimeter flows only through the top section of the collector. At the inlet of the transitional control volume, the collector through-flow area increases from the area of the top section only to the total collector through-flow area between the main collector roof and the ground surface. The following condition is assumed in this case (see figure A.6)

$$p_{i-1} = (p_{top})_{i-1} \quad (\text{A.44})$$

The effects of friction and support drag on the air-flow momentum over the radial length of a single collector control volume is small. In order to simplify the numerical model it is assumed that these losses are negligible for the evaluation of the momentum equation over the transitional collector control volume. Therefore, in the case of a fully closed bottom section, the flow at the transitional control volume is approximated as flow between parallel plates that experience an abrupt expansion. Applying a relation by Kröger (2004) which pertains to the flow in a duct that experience an abrupt expansion, the static pressure difference over the transitional section can be evaluated by (see figure A.6)

$$\Delta p_e = \frac{1}{2}(\rho_{top} v_{top}^2)_{i-1} \left[K_e - \left(1 - \left(\frac{A_{coll, top}}{A_{coll}} \right)_{i-1}^2 \right) \right] \quad (\text{A.45})$$

where K_e denotes the expansion loss coefficient, while $A_{coll, top}$ and A_{coll} represent the respective total collector through-flow area of the top section and the total collector through-flow area after the expansion at the collector radius r_{i-1} . Kröger (2004) gives this loss coefficient for turbulent flow as

$$K_e = \left[1 - \left(\frac{A_{coll, top}}{A_{coll}} \right)_{i-1} \right]^2 \quad (\text{A.46})$$

The collector air pressure at the transitional control volume outlet is thus simply determined by:

$$p_i = p_{i-1} - \Delta p_e \quad (\text{A.47})$$

After the evaluation of the transitional control volume, the effects of friction and support drag on the air-flow momentum are again considered for the remaining collector control volumes.

A.4 Collector roof energy equation

It is assumed that the rise in the main collector roof height over the length of a radial control volume may be considered to be negligible. Therefore, the area of the roof exposed to heat flows may be approximated as $r\Delta\theta\Delta r$.

From figure A.7 the following energy balance can be derived for the radial control volume of the main collector roof

$$\begin{aligned} I_h r \Delta\theta \Delta r + q_{sr} r \Delta\theta \Delta r = (\rho_{er} + \tau_{er}) I_h r \Delta\theta \Delta r + q_{ra} r \Delta\theta \Delta r + q_{rs} r \Delta\theta \Delta r \\ + q_{rth} r \Delta\theta \Delta r + \frac{\partial}{\partial t} (\rho_r r \Delta\theta \Delta r t_r c_r T_r) \end{aligned} \quad (\text{A.48})$$

where ρ_r , c_r , and t_r are the density, specific heat capacity and thickness of the collector roof respectively while T_r is the temperature of the roof.

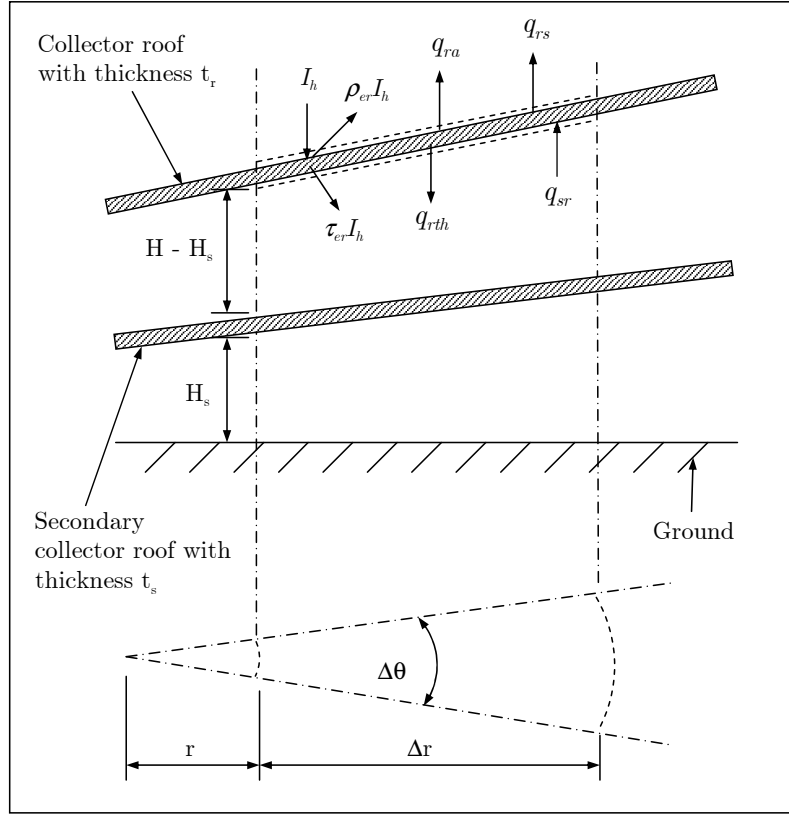


Figure A.7: Conservation of energy applied to a radial control volume for the main collector roof

The effective solar radiation (beam and diffuse) striking the collector roof is represented by I_h , while ρ_{er} and τ_{er} are the effective reflectance and transmittance of the roof respectively. The term q_{rth} is the convection heat flux from the collector roof to the air underneath it (thus to the air in the top section collector control volume), while q_{sr} is the radiation heat flux from the secondary collector roof to the main collector roof. Moreover, q_{ra} and q_{rs} represent the convection heat flux from the collector roof to the ambient air and the radiation heat flux to the sky respectively. Any temperature gradient across the collector roof is assumed to be negligible, while the roof properties are assumed constant over a radial control volume.

When expanding the effective solar radiation, effective reflectance and effective transmittance into their respective beam and diffuse radiative components, substituting them into equation (A.48) and dividing by $r\Delta\theta\Delta r$, we find

$$I_{hb} + I_{hd} + q_{sr} = (\rho_{er} + \tau_{er})_b I_{hb} + (\rho_{er} + \tau_{er})_d I_{hd} + q_{ra} + q_{rs} + q_{rth} + \rho_r t_r c_r \frac{\partial T_r}{\partial t} \quad (\text{A.49})$$

According to Modest (1993), for a transparent medium $\rho_e + \tau_e + \alpha_e = 1$ where α_e represents the effective absorptance of the medium (in this case the collector roof). After rearranging equation (A.49) we now obtain

$$(\alpha_{er} I_h)_b + (\alpha_{er} I_h)_d + q_{sr} = q_{ra} + q_{rs} + q_{rth} + \rho_r t_r c_r \frac{\partial T_r}{\partial t} \quad (\text{A.50})$$

where $\alpha_{er,b}$ and $\alpha_{er,d}$ indicate the effective beam and effective diffuse absorptance components respectively of the overall effective absorptance α_{er} . The determination of all solar

radiative roof properties are explained in Appendix G of this dissertation.

During steady state conditions or when transient effects are negligible, equation (A.50) becomes

$$(\alpha_{er}I_h)_b + (\alpha_{er}I_h)_d + q_{sr} = q_{ra} + q_{rs} + q_{rth} \quad (\text{A.51})$$

A.5 Secondary roof energy equation

Analogous to the main collector roof, the secondary collector roof is assumed to also have a negligible inclination over the length of a radial control volume. Consequently, the area of the secondary roof exposed to heat flows is approximated as $r\Delta\theta\Delta r$.

Consider the following energy balance from figure A.8 for the radial secondary roof control volume

$$\begin{aligned} \tau_{er}I_h r \Delta\theta \Delta r + q_{gs} r \Delta\theta \Delta r = & (\rho_{es} + \tau_{es}) \tau_{er} I_h r \Delta\theta \Delta r + q_{sth} r \Delta\theta \Delta r + q_{sr} r \Delta\theta \Delta r \\ & + q_{sbh} r \Delta\theta \Delta r + \frac{\partial}{\partial t} (\rho_s r \Delta\theta \Delta r t_s c_s T_s) \quad (\text{A.52}) \end{aligned}$$

where ρ_s , c_s , t_s and T_s are the density, specific heat capacity, thickness and temperature of the secondary collector roof respectively. The variable τ_{er} refers to the effective transmittance of the main collector roof.

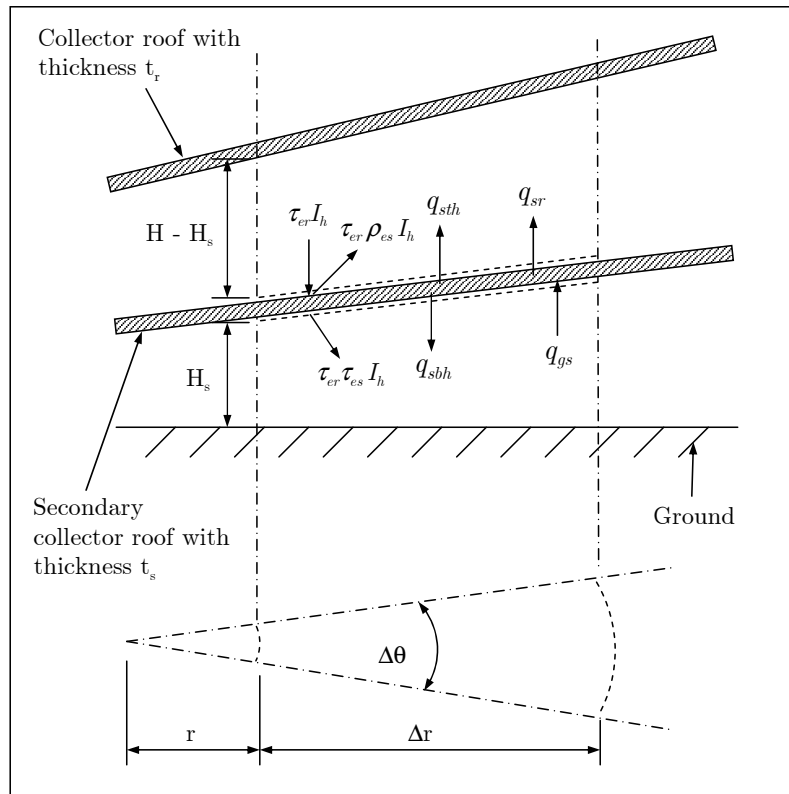


Figure A.8: Conservation of energy applied to a radial control volume for the secondary collector roof

Similar to the main collector roof, ρ_{es} and τ_{es} represent the effective reflectance and transmittance of the secondary roof. The term q_{sth} is the convection heat flux from the secondary roof to the air above it (thus to the air in the top section collector control volume), while q_{sbh} is the convective heat flux from the secondary roof to the air below it (therefore to the air in the bottom section collector control volume). The radiative heat flux from the ground surface to the secondary roof is signified by q_{gs} . Any temperature gradient across the secondary roof is neglected, while the secondary roof properties are assumed constant over a radial control volume.

Once again the effective solar radiation, effective reflectance and effective transmittance can be expanded into their respective beam and diffuse radiative components. After substituting these into equation (A.52) and dividing by $r\Delta\theta\Delta r$, we find

$$\begin{aligned} \tau_{er,b} I_{hb} + \tau_{er,d} I_{hd} + q_{gs} &= (\rho_{es} + \tau_{es})_b \tau_{er,b} I_{hb} + (\rho_{es} + \tau_{es})_d \tau_{er,d} I_{hd} \\ &+ q_{sth} + q_{sr} + q_{sbh} + \rho_s t_s c_s \frac{\partial T_s}{\partial t} \end{aligned} \quad (\text{A.53})$$

Recalling that for a transparent medium (in this case the secondary roof) $\rho_{es} + \tau_{es} + \alpha_{es} = 1$, we can rearrange equation (A.53) and obtain

$$(\alpha_{es} \tau_{er} I_h)_b + (\alpha_{es} \tau_{er} I_h)_d + q_{gs} = q_{sth} + q_{sr} + q_{sbh} + \rho_s t_s c_s \frac{\partial T_s}{\partial t} \quad (\text{A.54})$$

where α_{es} indicates the effective absorptance of the secondary roof, while the subscripts b and d signify the respective beam and diffuse radiative components. The determination of all solar radiative roof properties are explained in Appendix G of this dissertation.

During steady state conditions or when transient effects are negligible, equation (A.54) becomes

$$(\alpha_{es} \tau_{er} I_h)_b + (\alpha_{es} \tau_{er} I_h)_d + q_{gs} = q_{sth} + q_{sr} + q_{sbh} \quad (\text{A.55})$$

A.6 Ground energy equations

This section derives the relevant ground energy equations for the inclusion of a secondary collector roof into the solar chimney power plant. Any radial conduction in the ground is assumed to be negligible.

A.6.1 Open or closed bottom section

At $z = 0$ (Ground surface)

From figure A.9 the energy balance at the ground surface under the secondary collector roof can be evaluated as follows

$$\tau_{tot} I_h r \Delta\theta \Delta r = (1 - \alpha_g) \tau_{tot} I_h r \Delta\theta \Delta r + q_{gbh} r \Delta\theta \Delta r + q_{gs} r \Delta\theta \Delta r + q_g r \Delta\theta \Delta r \quad (\text{A.56})$$

where α_g is the absorptance of the ground surface, while q_g is the conduction heat flux from the surface into the ground. The term q_{gbh} denotes the convection heat flux from the ground to the air in the bottom section of the collector. Furthermore, τ_{tot} is the total transmittance of the solar radiation passing through the main and secondary collector roofs. The determination of τ_{tot} is explained in Appendix G of this dissertation.

When expanding the effective solar radiation I_h and total transmittance τ_{tot} into their respective beam and diffuse components, we find

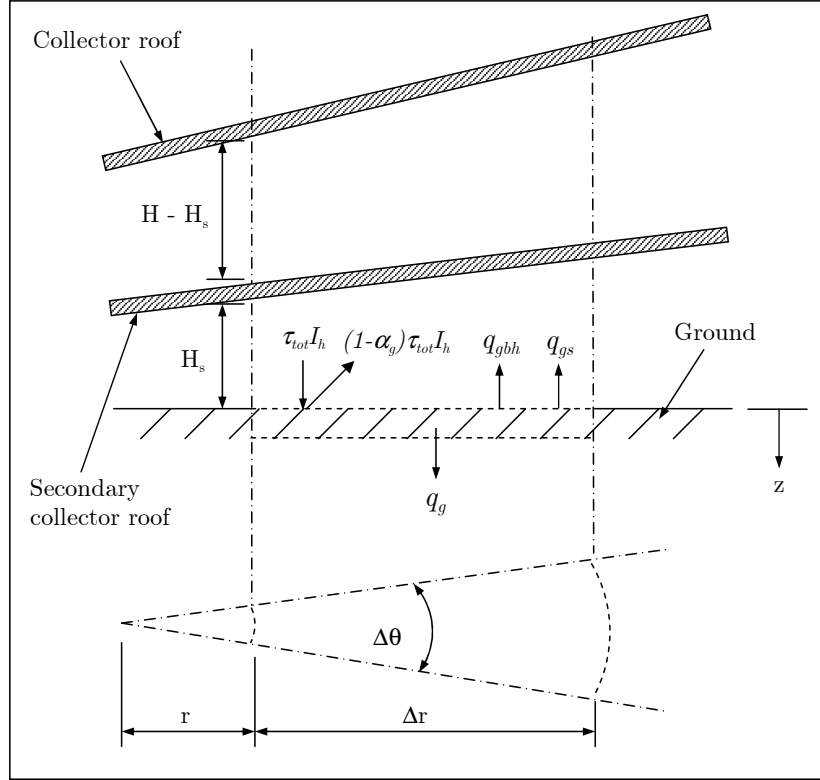


Figure A.9: Conservation of energy applied to a radial control volume for the ground surface under the secondary collector roof

$$\begin{aligned}
 (\tau_{tot} I_h)_b r \Delta\theta \Delta r + (\tau_{tot} I_h)_d r \Delta\theta \Delta r &= (1 - \alpha_g) (\tau_{tot} I_h)_b r \Delta\theta \Delta r + (1 - \alpha_g) (\tau_{tot} I_h)_d r \Delta\theta \Delta r \\
 &+ q_{gbh} r \Delta\theta \Delta r + q_{gs} r \Delta\theta \Delta r \\
 &+ q_g r \Delta\theta \Delta r
 \end{aligned} \tag{A.57}$$

From figure A.9 it is evident that some of the solar radiation that passes through the main and secondary collector roofs and strikes the ground is reflected back to the secondary roof. The reflected radiation is in turn reflected back to the ground. The multiple reflection of diffuse radiation continues, resulting in a slightly higher fraction of energy being absorbed by the ground. This higher fraction of energy is represented by the transmittance-absorptance product ($\tau\alpha$), as discussed in an appendix of the study by Pretorius (2004).

Upon employing the transmittance-absorptance product in equation (A.57), simplifying, expanding the conduction term and dividing by $r\Delta\theta\Delta r$ we find the ground energy relation at $z = 0$:

$$(\tau_{tot}\alpha_g)_b I_{hb} + (\tau_{tot}\alpha_g)_d I_{hd} = q_{gbh} + q_{gs} - k_g \left. \frac{\partial T_g}{\partial z} \right|_{z=0} \tag{A.58}$$

where k_g and T_g are the thermal conductivity and temperature of the ground respectively.

At $z > 0$

The introduction of a secondary collector roof does not change the ground energy equation which expresses the energy fluxes deeper in the ground. Thus the equation remains

unchanged, as from Chapter 2 and is repeated here in its final form for convenience:

$$-k_g \frac{\partial^2 T_g}{\partial z^2} + \rho_g c_g \frac{\partial T_g}{\partial t} = 0 \quad (\text{A.59})$$

where ρ_g and c_g are the density and specific heat capacity of the ground. The ground properties are assumed to be constant.

At $z = \infty$

The introduction of a secondary collector roof also does not change the boundary condition at a certain depth in the ground where the temperature gradient becomes zero. Thus the condition remains unchanged, as from Chapter 2 and is repeated here for convenience:

$$\frac{\partial T_g}{\partial z} = 0 \quad (\text{A.60})$$

A.6.2 Transition section

The numerical model employs the same ground energy equations (at $z = 0$, $z > 0$ and $z = \infty$) for the transition section of the collector as those presented in Chapter 2 of this dissertation.

A.7 Air stream energy equation

A.7.1 Top section

When regarding the defined control volume in the top section of the collector as depicted in figure A.10, an energy balance can be formulated for the air stream between the main and secondary collector roofs. An order of magnitude analysis performed by Hedderwick (2001) on the collector air stream energy equation concludes that the kinetic energy, radial conduction and transient kinetic energy terms are negligible in comparison with the other energy terms. Neglecting these terms, we find

$$\begin{aligned} \rho v r \Delta \theta (H - H_s) c_p T + q_{rth} r \Delta \theta \Delta r + q_{sth} r \Delta \theta \Delta r &= \rho v r \Delta \theta (H - H_s) c_p T \\ + \frac{\partial}{\partial r} (\rho v r \Delta \theta (H - H_s) c_p T) \Delta r + \frac{\partial}{\partial t} (\rho r \Delta \theta \Delta r (H - H_s) c_v T) & \quad (\text{A.61}) \end{aligned}$$

where c_p , c_v and T are the specific heat capacity for a constant pressure, specific heat capacity for a constant volume and temperature of the air stream in the top section collector control volume respectively. Simplifying equation (A.61) and dividing by $r \Delta \theta \Delta r$ gives

$$q_{rth} + q_{sth} = \frac{1}{r} \frac{\partial}{\partial r} (\rho v r (H - H_s) c_p T) + (H - H_s) \frac{\partial}{\partial t} (\rho c_v T) \quad (\text{A.62})$$

When applying the differential operator to the first right-hand-side term of equation (A.62), we find

$$\frac{1}{r} \frac{\partial}{\partial r} (\rho v r (H - H_s) c_p T) = \frac{c_p T}{r} \frac{\partial}{\partial r} (\rho v r (H - H_s)) + \rho v (H - H_s) \frac{\partial}{\partial r} (c_p T) \quad (\text{A.63})$$

Apply the differential operator to the second term on the right-hand-side of equation (A.62) and obtain

$$(H - H_s) \frac{\partial}{\partial t} (\rho c_v T) = \rho (H - H_s) \frac{\partial}{\partial t} (c_v T) + c_v T (H - H_s) \frac{\partial \rho}{\partial t} \quad (\text{A.64})$$

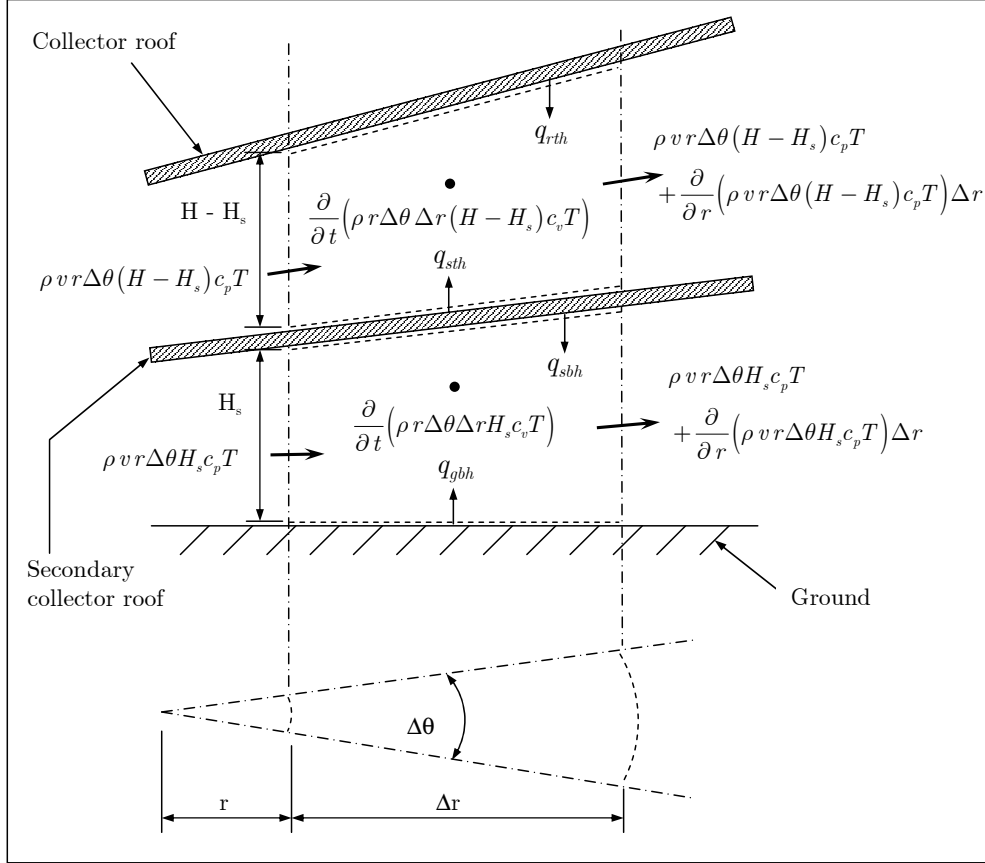


Figure A.10: Conservation of energy applied to the air flowing through a defined top and bottom section collector control volume

When substituting equation (A.2) into equation (A.64), we obtain the following

$$(H - H_s) \frac{\partial}{\partial t} (\rho c_v T) = \rho (H - H_s) \frac{\partial}{\partial t} (c_v T) - \frac{c_v T}{r} \frac{\partial}{\partial r} (\rho v r (H - H_s)) \quad (\text{A.65})$$

If we assume air to be an ideal gas, the relation $(c_p - c_v) = R$ applies, where R is the gas constant. As we now substitute equation (A.63) and (A.65) for the two terms on the right-hand-side of equation (A.62) and simplify, we find the energy equation for the air-flow in the top section of the collector

$$q_{rth} + q_{sth} = \frac{RT}{r} \frac{\partial}{\partial r} (\rho v r (H - H_s)) + \rho (H - H_s) \left[v \frac{\partial}{\partial r} (c_p T) + \frac{\partial}{\partial t} (c_v T) \right] \quad (\text{A.66})$$

An order of magnitude analysis performed by Pretorius (2004) on the chimney air stream energy equation concluded that certain terms may be neglected during steady state conditions or when transient effects are negligible. Similarly, the transient term of equation (A.66) is neglected and gives

$$q_{rth} + q_{sth} = \frac{RT}{r} \frac{\partial}{\partial r} (\rho v r (H - H_s)) + \rho v (H - H_s) \frac{\partial}{\partial r} (c_p T) \quad (\text{A.67})$$

A.7.2 Open bottom section

When considering the defined control volume in the bottom section of the collector, as illustrated in figure A.10, an energy balance for the air stream between the secondary collector roof and ground surface can be derived. Analogous to the air stream energy equation for the top section, after neglecting the terms which do not contribute significantly to the total energy flux, we find

$$q_{sbh}r\Delta\theta\Delta r + q_{gbh}r\Delta\theta\Delta r + \rho vr\Delta\theta H_s c_p T = \rho vr\Delta\theta H_s c_p T + \frac{\partial}{\partial r}(\rho vr\Delta\theta H_s c_p T)\Delta r + \frac{\partial}{\partial t}(\rho r\Delta\theta\Delta r H_s c_v T) \quad (\text{A.68})$$

When simplifying equation (A.68) and dividing by $r\Delta\theta\Delta r$, we find

$$q_{sbh} + q_{gbh} = \frac{1}{r} \frac{\partial}{\partial r}(\rho vr H_s c_p T) + H_s \frac{\partial}{\partial t}(\rho c_v T) \quad (\text{A.69})$$

Apply the differential operator to the first right-hand-side term of equation (A.69) and obtain

$$\frac{1}{r} \frac{\partial}{\partial r}(\rho vr H_s c_p T) = \frac{c_p T}{r} \frac{\partial}{\partial r}(\rho vr H_s) + \rho v H_s \frac{\partial}{\partial r}(c_p T) \quad (\text{A.70})$$

Applying the differential operator to the second right-hand-side term of equation (A.69) yields

$$H_s \frac{\partial}{\partial t}(\rho c_v T) = \rho H_s \frac{\partial}{\partial t}(c_v T) + c_v T H_s \frac{\partial \rho}{\partial t} \quad (\text{A.71})$$

Substitute equation (A.5) into equation (A.71) and obtain the following

$$H_s \frac{\partial}{\partial t}(\rho c_v T) = \rho H_s \frac{\partial}{\partial t}(c_v T) - \frac{c_v T}{r} \frac{\partial}{\partial r}(\rho vr H_s) \quad (\text{A.72})$$

If we assume air to be an ideal gas, the relation $(c_p - c_v) = R$ applies, where R is the gas constant. As we now substitute equation (A.70) and (A.72) for the right-hand-side terms of equation (A.69) and simplify, we find the energy equation for the air-flow in the bottom section of the collector

$$q_{sbh} + q_{gbh} = \frac{RT}{r} \frac{\partial}{\partial r}(\rho vr H_s) + \rho H_s \left[v \frac{\partial}{\partial r}(c_p T) + \frac{\partial}{\partial t}(c_v T) \right] \quad (\text{A.73})$$

During steady state conditions or when transient effects are negligible, equation (A.73) becomes

$$q_{sbh} + q_{gbh} = \frac{RT}{r} \frac{\partial}{\partial r}(\rho vr H_s) + \rho v H_s \frac{\partial}{\partial r}(c_p T) \quad (\text{A.74})$$

A.7.3 Closed bottom section

An energy balance can also be derived for the air in the bottom collector section during times when the air-flow regulating mechanism at the bottom section outlet is fully closed. During such times no air-flow through the bottom section of the collector is possible. The relevant equation is simply equivalent to the air stream energy relation for an open bottom section, with the exception of the air enthalpy energy terms (see figure A.10). Consequently, the resulting air energy equation for a defined control volume in the bottom section of the collector is

$$q_{sbh}r\Delta\theta\Delta r + q_{gbh}r\Delta\theta\Delta r = \frac{\partial}{\partial t}(\rho r\Delta\theta \Delta r H_s c_v T) \quad (\text{A.75})$$

Dividing equation (A.75) by $r\Delta\theta\Delta r$ yields

$$q_{sbh} + q_{gbh} = H_s \frac{\partial}{\partial t}(\rho c_v T) \quad (\text{A.76})$$

During steady state conditions or when transient effects are negligible, equation (A.76) reduces to

$$q_{sbh} + q_{gbh} = 0 \quad (\text{A.77})$$

A.7.4 Transition section

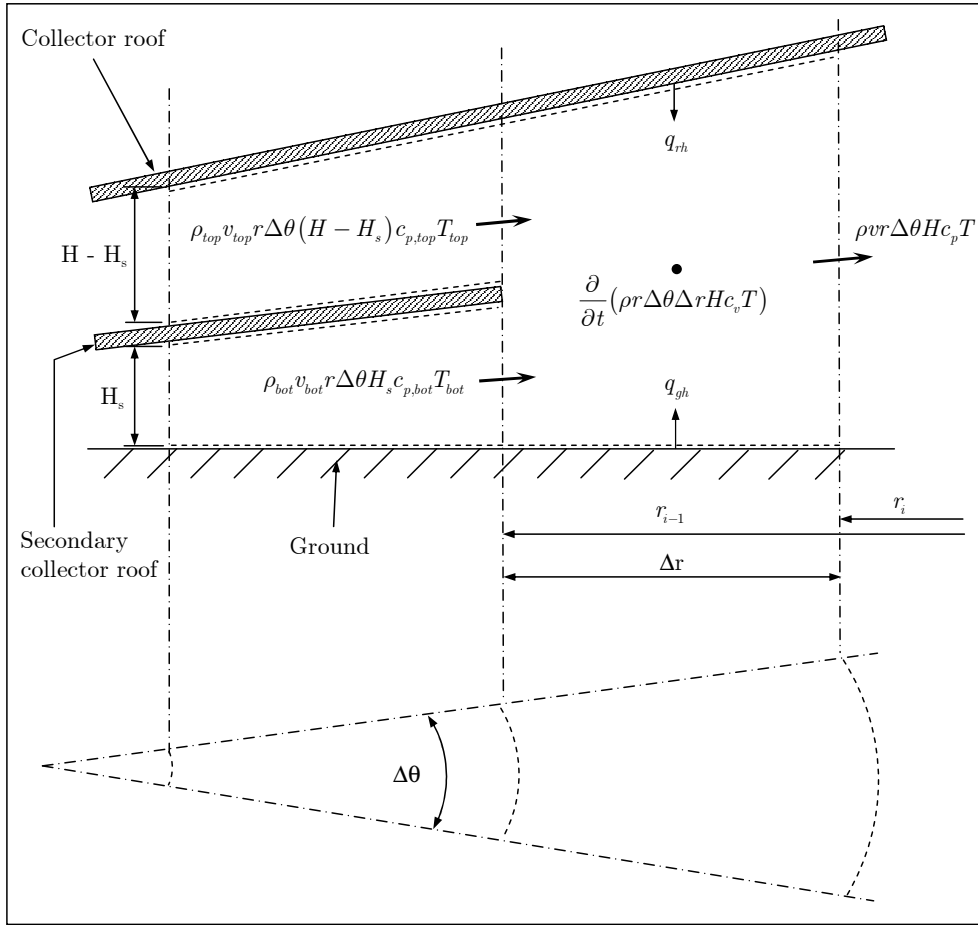


Figure A.11: Conservation of energy applied to the air stream flowing through the transitional control volume of the collector

Open bottom section

By assuming purely radial air-flow, consider from figure A.11 the following air stream energy equation applicable to an elementary transitional control volume in the collector

$$\begin{aligned}
 & (\rho_{top} v_{top} r (H - H_s) c_{p,top} T_{top})_{i-1} \Delta\theta + (\rho_{bot} v_{bot} r H_s c_{p,bot} T_{bot})_{i-1} \Delta\theta \\
 & \quad + q_{rh} r \Delta\theta \Delta r + q_{gh} r \Delta\theta \Delta r \\
 & = (\rho v r H c_p T)_i \Delta\theta + \frac{\partial}{\partial t} (\rho r \Delta\theta \Delta r H c_v T)
 \end{aligned} \tag{A.78}$$

where q_{rh} and q_{gh} are the respective convective heat fluxes from the roof and ground surface to the air in the transitional collector control volume. Dividing equation (A.78) by $\Delta\theta$ and rearranging gives

$$\begin{aligned}
 & (\rho_{top} v_{top} r (H - H_s) c_{p,top} T_{top})_{i-1} + (\rho_{bot} v_{bot} r H_s c_{p,bot} T_{bot})_{i-1} \\
 & \quad + q_{rh} r \Delta r + q_{gh} r \Delta r \\
 & = (\rho v r H c_p T)_i + r \Delta r H \frac{\partial}{\partial t} (\rho c_v T)
 \end{aligned} \tag{A.79}$$

During steady state conditions or when transient effects are negligible, equation (A.79) becomes

$$\begin{aligned}
 & (\rho_{top} v_{top} r (H - H_s) c_{p,top} T_{top})_{i-1} + (\rho_{bot} v_{bot} r H_s c_{p,bot} T_{bot})_{i-1} \\
 & \quad + q_{rh} r \Delta r + q_{gh} r \Delta r \\
 & = (\rho v r H c_p T)_i
 \end{aligned} \tag{A.80}$$

Closed bottom section

With the air-flow regulating mechanism at the bottom section outlet fully closed, no air-flow through the bottom section is possible. The air stream energy relation applicable to the transitional collector control volume during these times will be similar to that of equation (A.78), except for the second term on the left-hand-side. Subsequently, after dividing this equation by $\Delta\theta$ and rearranging we find

$$\begin{aligned}
 & (\rho_{top} v_{top} r (H - H_s) c_{p,top} T_{top})_{i-1} + q_{rh} r \Delta r + q_{gh} r \Delta r \\
 & = (\rho v r H c_p T)_i + r \Delta r H \frac{\partial}{\partial t} (\rho c_v T)
 \end{aligned} \tag{A.81}$$

During steady state conditions or when transient effects are negligible, equation (A.81) becomes

$$(\rho_{top} v_{top} r (H - H_s) c_{p,top} T_{top})_{i-1} + q_{rh} r \Delta r + q_{gh} r \Delta r = (\rho v r H c_p T)_i \tag{A.82}$$

Appendix

B

Conservation Equations: Including a Double Glazed Main or Secondary Roof

Appendix A derives the relevant conservation equations for the inclusion of a secondary collector roof into the collector model of the solar chimney power plant. This appendix conducts an investigation into the inclusion of a double glazed main or secondary roof into the existing collector model, as illustrated respectively by the schematic figures B.1 and B.2.

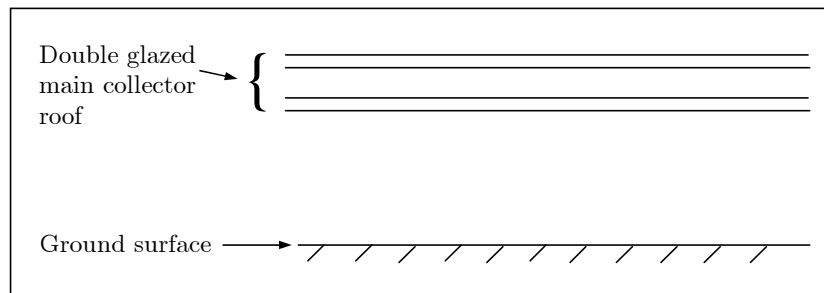


Figure B.1: Collector configuration incorporating double glazed main collector roof

The conservation equations which describe the incorporation of a double glazed main collector roof (with no secondary roof) into the model are similar to those presented in Chapter 2 of this dissertation, except for the collector roof energy equation. Note also that in the case of a double glazed main roof τ_{tot} simply replaces τ_e in the ground surface energy equation. Analogous to the above-mentioned, all conservation equations describing the inclusion of a double glazed secondary roof (with single glazed main roof) into the model are similar to those derived in Appendix A of this dissertation, except for the secondary collector roof energy equation.

Thus the following appendix derives the energy equations for the top and bottom sheet of a double glazed main and double glazed secondary collector roof. The determination of all solar radiative roof properties are explained in Appendix G of this dissertation.

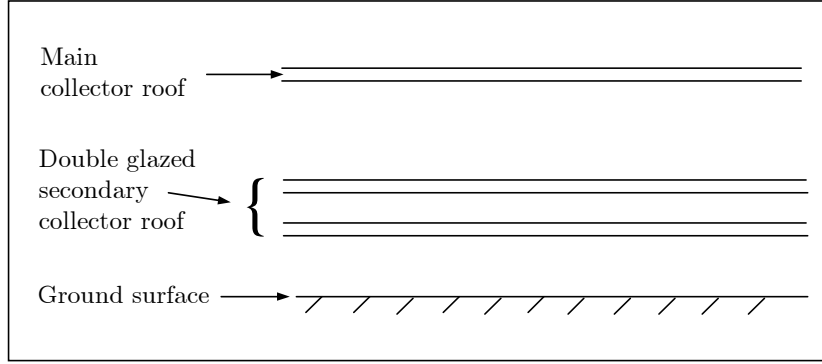


Figure B.2: Collector configuration incorporating a main and double glazed secondary collector roof

B.1 Double glazed main collector roof

B.1.1 Main collector roof energy equation

As with the single glazed main collector roof, it is assumed that the double glazed main collector roof has a negligible inclination over the length of a radial control volume. Subsequently, the area of each sheet of the main roof exposed to the relevant heat fluxes is approximated as $r\Delta\theta\Delta r$.

Top sheet

From figure B.3 (extract from figure B.1) the following energy balance can be derived for the top sheet of the double glazed main collector roof:

$$\alpha_{er1}I_h r\Delta\theta\Delta r + q_c r\Delta\theta\Delta r + q_r r\Delta\theta\Delta r = q_{ra} r\Delta\theta\Delta r + q_{rs} r\Delta\theta\Delta r + \frac{\partial}{\partial t} (\rho_{r1} r\Delta\theta\Delta r t_{r1} c_{r1} T_{r1}) \quad (\text{B.1})$$

where ρ_{r1} , c_{r1} , t_{r1} and T_{r1} are the density, specific heat capacity, thickness and temperature of the top sheet of the main roof respectively.

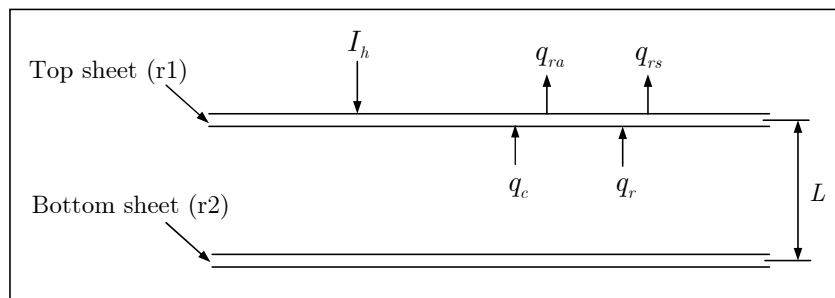


Figure B.3: Conservation of energy applied to the top sheet of the double glazed main collector roof

The variable α_{er1} represents the effective absorptance of the top sheet of the main roof, while q_c and q_r denote the convective and radiative heat fluxes from the bottom to the top sheet of the double glazed main roof. Any temperature gradient across the top sheet of the

main roof is neglected, while the properties of the sheet are assumed constant over a radial control volume.

The effective solar radiation and effective absorptance can be expanded into their respective beam and diffuse radiative components. Substituting these into equation (B.1) and dividing by $r\Delta\theta\Delta r$ gives

$$(\alpha_{er1}I_h)_b + (\alpha_{er1}I_h)_d + q_c + q_r = q_{ra} + q_{rs} + \rho_{r1}t_{r1}c_{r1}\frac{\partial T_{r1}}{\partial t} \quad (\text{B.2})$$

where the subscripts b and d denote the respective beam and diffuse radiative components. During steady state conditions or when transient effects are negligible, equation (B.2) reduces to

$$(\alpha_{er1}I_h)_b + (\alpha_{er1}I_h)_d + q_c + q_r = q_{ra} + q_{rs} \quad (\text{B.3})$$

Bottom sheet

When evaluating figure B.4 (extract from figure B.1), the following energy balance for the bottom sheet of the double glazed main roof can be formulated:

$$\begin{aligned} \alpha_{er2}\tau_{er1}I_h r\Delta\theta\Delta r + q_{gr}r\Delta\theta\Delta r &= q_{rh}r\Delta\theta\Delta r + q_c r\Delta\theta\Delta r + q_r r\Delta\theta\Delta r \\ &+ \frac{\partial}{\partial t}(\rho_{r2}r\Delta\theta\Delta r t_{r2}c_{r2}T_{r2}) \end{aligned} \quad (\text{B.4})$$

where ρ_{r2} , c_{r2} , t_{r2} and T_{r2} are the density, specific heat capacity, thickness and temperature of the bottom sheet of the main collector roof respectively.

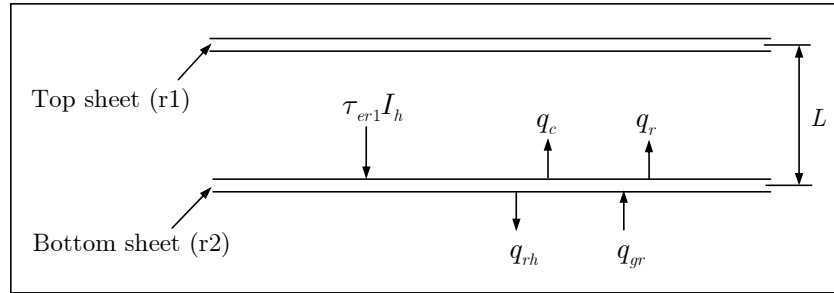


Figure B.4: Conservation of energy applied to the bottom sheet of the double glazed main collector roof

The term τ_{er1} refers to the effective transmittance through the top sheet of the main roof, while α_{er2} denotes the effective absorptance of the bottom sheet. Furthermore, q_{rh} is the convective heat flux from the bottom sheet of the main roof to the air in the collector, whereas q_{gr} is the radiative heat flux from the ground surface to the same bottom sheet. Any temperature gradient across the bottom sheet of the main roof is neglected, while the properties of the sheet are assumed constant over a radial control volume.

When expanding the relevant properties into their respective beam and diffuse components, substituting them into equation (B.4) and dividing by $r\Delta\theta\Delta r$, we find

$$(\alpha_{er2}\tau_{er1}I_h)_b + (\alpha_{er2}\tau_{er1}I_h)_d + q_{gr} = q_{rh} + q_c + q_r + \rho_{r2}t_{r2}c_{pr2}\frac{\partial T_{r2}}{\partial t} \quad (\text{B.5})$$

During steady state conditions or when transient effects are negligible, equation (B.5) becomes

$$(\alpha_{er2}\tau_{er1}I_h)_b + (\alpha_{er2}\tau_{er1}I_h)_d + q_{gr} = q_{rh} + q_c + q_r \quad (\text{B.6})$$

B.2 Double glazed secondary collector roof

B.2.1 Secondary collector roof energy equation

Similar to the main collector roof, it is assumed that the double glazed secondary collector roof has a negligible inclination over the length of a radial control volume. Thus the area of each sheet of the secondary roof exposed to heat flows is approximated as $r\Delta\theta\Delta r$.

Top sheet

When regarding figure B.5 (extract from figure B.2), the following energy equation can be derived for the top sheet of the double glazed secondary collector roof:

$$\begin{aligned} \alpha_{es1}\tau_{er}I_h r\Delta\theta\Delta r + q_c r\Delta\theta\Delta r + q_r r\Delta\theta\Delta r = q_{sth} r\Delta\theta\Delta r + q_{sr} r\Delta\theta\Delta r \\ + \frac{\partial}{\partial t} (\rho_{s1} r\Delta\theta\Delta r t_{s1} c_{s1} T_{s1}) \end{aligned} \quad (\text{B.7})$$

where ρ_{s1} , c_{s1} , t_{s1} and T_{s1} are the density, specific heat capacity, thickness and temperature of the top sheet of the secondary collector roof respectively. The variable τ_{er} refers to the effective transmittance of the (single glazed) main collector roof.

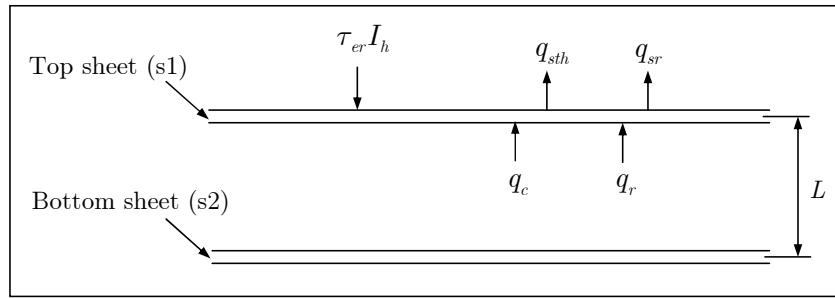


Figure B.5: Conservation of energy applied to the top sheet of the double glazed secondary collector roof

The variable α_{es1} represents the effective absorptance of the top sheet of the secondary roof, while the term q_{sth} is the convection heat flux from the top sheet of the secondary roof to the air above it (thus to the air in the top section collector control volume). Furthermore, the radiative heat flux from the top sheet of the secondary roof to the main collector roof is represented by q_{sr} , while q_c and q_r denote the convective and radiative heat fluxes from the bottom to the top sheet of the double glazed secondary roof. Any temperature gradient across the top sheet of the secondary roof is neglected, while the properties of the sheet are assumed constant over a radial control volume.

Once again, the effective solar radiation and effective absorptance can be expanded into their respective beam and diffuse radiative components. Substituting these into equation (B.7) and dividing by $r\Delta\theta\Delta r$ gives

$$(\alpha_{es1}\tau_{er}I_h)_b + (\alpha_{es1}\tau_{er}I_h)_d + q_c + q_r = q_{sth} + q_{sr} + \rho_{s1}t_{s1}c_{s1}\frac{\partial T_{s1}}{\partial t} \quad (\text{B.8})$$

During steady state conditions or when transient effects are negligible, equation (B.8) becomes

$$(\alpha_{es1}\tau_{er}I_h)_b + (\alpha_{es1}\tau_{er}I_h)_d + q_c + q_r = q_{sth} + q_{sr} \quad (\text{B.9})$$

Bottom sheet

From figure B.6 (extract from figure B.2), the following energy balance can be formulated for the bottom sheet of the double glazed secondary collector roof:

$$\begin{aligned} \alpha_{es2}\tau_{es1}I_h r \Delta\theta \Delta r + q_{gs} r \Delta\theta \Delta r &= q_{sbh} r \Delta\theta \Delta r + q_c r \Delta\theta \Delta r + q_r r \Delta\theta \Delta r \\ &+ \frac{\partial}{\partial t} (\rho_{s2} r \Delta\theta \Delta r t_{s2} c_{s2} T_{s2}) \end{aligned} \quad (\text{B.10})$$

where ρ_{s2} , c_{s2} , t_{s2} and T_{s2} are the density, specific heat capacity, thickness and temperature of the bottom sheet of the secondary collector roof respectively.

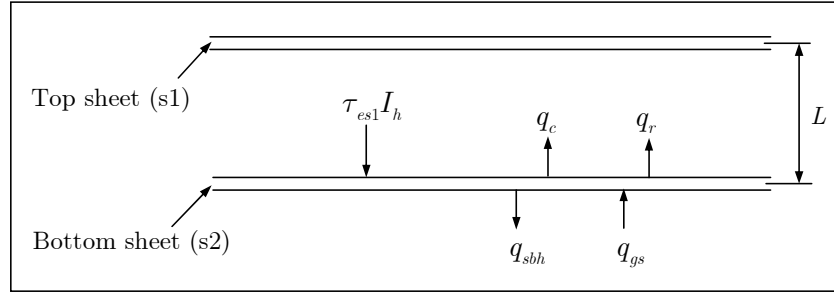


Figure B.6: Conservation of energy applied to the bottom sheet of the double glazed secondary collector roof

For this analysis τ_{es1} refers to the effective transmittance through the (single glazed) main roof and top sheet of the secondary roof, α_{es2} denotes the effective absorptance of the bottom sheet of the secondary roof, while the term q_{sbh} is the convection heat flux from the bottom sheet of the secondary roof to the air below it (thus to the air in the bottom section collector control volume). The variable q_{gs} represents the radiative heat flux from the ground surface to the bottom sheet of the secondary roof. Any temperature gradient across the bottom sheet of the secondary roof is neglected, while the properties of the sheet are assumed constant over a radial control volume.

When expanding the relevant properties into their respective beam and diffuse components, substituting them into equation (B.10) and dividing by $r \Delta\theta \Delta r$, we find

$$(\alpha_{es2}\tau_{es1}I_h)_b + (\alpha_{es2}\tau_{es1}I_h)_d + q_{gs} = q_{sbh} + q_c + q_r + \rho_{s2} t_{s2} c_{s2} \frac{\partial T_{s2}}{\partial t} \quad (\text{B.11})$$

During steady state conditions or when transient effects are negligible, equation (B.11) becomes

$$(\alpha_{es2}\tau_{es1}I_h)_b + (\alpha_{es2}\tau_{es1}I_h)_d + q_{gs} = q_{sbh} + q_c + q_r \quad (\text{B.12})$$

Appendix

C

Conservation Equations: Including a Tertiary Collector Roof

Appendix A derives the relevant conservation equations for the inclusion of a secondary collector roof into the collector model of the solar chimney power plant. Furthermore, Appendix B derives the conservation equations for the inclusion of a double glazed main or secondary collector roof into the existing numerical model. The following appendix evaluates the inclusion of a secondary and tertiary collector roof (illustrated by figure C.1) into the existing collector model.

Relevant conservation equations for the inclusion of a secondary and tertiary roof into the existing solar chimney power plant collector model (Pretorius, 2004) are derived. In light thereof that a complete derivation of the relevant governing equations for a two-section collector (top and bottom section) has been conducted (see Appendix A), the following derivation for a three-section collector, being very similar to that of the two-section collector, only presents the relevant equations in their final form before discretization. These equations are discretized (not presented) according to the schemes discussed by Pretorius (2004) before their inclusion into the existing computer simulation model.

Chapter 6 discusses the modifications to the collector as well as the operation of the solar chimney power plant with the inclusion of a secondary and tertiary collector roof.

C.1 Definition of sections in the collector

Top, middle and bottom section

The incorporation of a secondary and tertiary collector roof divides the collector air-flow region into three sections, namely a top, middle and bottom section (see figure C.1). Air flows constantly through the top section (the region between the main and secondary collector roofs), while the air-flow through the middle (region between the secondary and tertiary roofs) and bottom (the region between the tertiary roof and the ground surface) sections can be regulated by an air-flow regulating mechanism at each respective section outlet (refer to Chapter 6).

Transition section

The transition section is defined as the section under the main collector roof where the secondary and tertiary collector roofs end. At the point where the roofs end the top, middle

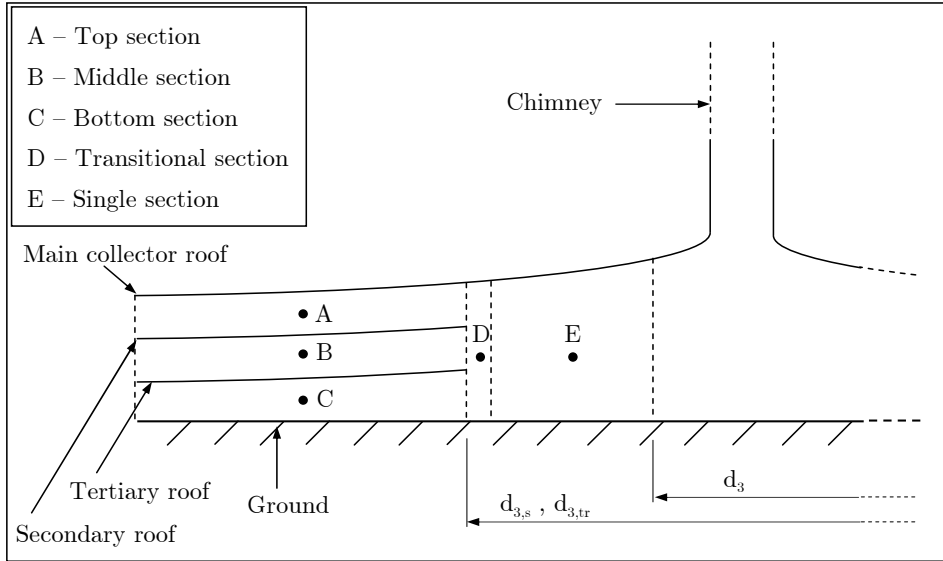


Figure C.1: Definition of sections created in the collector by the inclusion of a secondary and tertiary collector roof

and bottom sections of the collector merge, forming a single section between the main collector roof and the ground surface. The transition section is assumed to stretch over the length of one radial control volume. It is assumed that the secondary and tertiary roofs have equal radii from the collector perimeter up to this point (see figure C.1).

As mixing of the top, middle and bottom air streams occur in the transition section, it is necessary to distinguish between the properties of the various sections. Therefore, when evaluating the transition section, all future references to the air properties in the top, middle and bottom sections employ the subscripts *top*, *mid* and *bot* respectively.

Single section after transition

Similar definition to the one presented in Appendix A (see figure C.1).

C.2 Collector continuity equation

C.2.1 Top section

The steady state continuity equation for the top section of the collector is given by

$$\frac{\partial}{\partial r} (\rho v r (H - H_s)) = 0 \quad (\text{C.1})$$

where H and H_s once again represent the main and secondary collector roof heights at a particular collector radius.

C.2.2 Open middle section

The steady state continuity equation for the middle section of the collector is

$$\frac{\partial}{\partial r} (\rho v r (H_s - H_{tr})) = 0 \quad (\text{C.2})$$

where H_{tr} symbolizes the tertiary collector roof height at a specific collector radius.

C.2.3 Closed middle section

With the air-flow regulating mechanism at the middle section outlet fully closed, no air-flow is possible through this section. This implies an air-flow velocity of zero in the middle section of the collector.

C.2.4 Open bottom section

The steady state continuity equation for the bottom section of the collector is described by

$$\frac{\partial}{\partial r} (\rho v r H_{tr}) = 0 \quad (\text{C.3})$$

C.2.5 Closed bottom section

With the air-flow regulating mechanism at the bottom section outlet fully closed, no air-flow is possible through this section. This implies an air-flow velocity of zero in the bottom section of the collector.

C.2.6 Transition section

All sections open

With air-flow through the top, middle and bottom sections of the collector, the resulting air-flow velocity during steady state conditions at the outlet of the transitional section (node i) is given by

$$v_i = \frac{(\rho_{top} v_{top} r (H - H_s))_{i-1} + (\rho_{mid} v_{mid} r (H_s - H_{tr}))_{i-1} + (\rho_{bot} v_{bot} r H_{tr})_{i-1}}{(\rho r H)_i} \quad (\text{C.4})$$

Closed bottom section

With the air-flow regulating mechanism at the bottom section outlet fully closed, no air-flow is possible through this section. The resulting collector air-flow velocity during steady state conditions at the outlet of the transitional section is (with air-flow only experienced through the top and middle sections of the collector)

$$v_i = \frac{(\rho_{top} v_{top} r (H - H_s))_{i-1} + (\rho_{mid} v_{mid} r (H_s - H_{tr}))_{i-1}}{(\rho r H)_i} \quad (\text{C.5})$$

Closed middle and bottom section

With the air-flow regulating mechanisms at the middle and bottom section outlets fully closed, no air-flow is possible through these sections. The resulting collector air-flow velocity during steady state conditions at the outlet of the transitional section is then described by (with air-flow only experienced through the top section of the collector)

$$v_i = \frac{(\rho_{top} v_{top} r (H - H_s))_{i-1}}{(\rho r H)_i} \quad (\text{C.6})$$

C.3 Collector momentum equation

C.3.1 Top section

The steady state momentum equation for the top section of the collector is given by

$$(H_s - H) \frac{\partial p}{\partial r} - \tau_r - \tau_s - \frac{F_{\text{supports}}}{r\Delta\theta} = \rho v (H - H_s) \frac{\partial v}{\partial r} \quad (\text{C.7})$$

where τ_r and τ_s once again represent the main collector roof and secondary roof shear stresses acting on the air stream in the top section of the collector, while the term F_{supports} is the total drag force per unit radial distance that the roof supports (supporting the main, secondary and tertiary collector roofs) enforce on the air stream in the top section.

C.3.2 Open middle section

The steady state momentum equation for the middle section of the collector is

$$(H_{tr} - H_s) \frac{\partial p}{\partial r} - \tau_s - \tau_{tr} - \frac{F_{\text{supports}}}{r\Delta\theta} = \rho v (H_s - H_{tr}) \frac{\partial v}{\partial r} \quad (\text{C.8})$$

where τ_s and τ_{tr} are the secondary and tertiary roof shear stresses acting on the air stream in the middle section of the collector, while the term F_{supports} is the total drag force per unit radial distance that the roof supports enforce on the air stream in the middle section.

C.3.3 Closed middle section

With the air-flow regulating mechanism at the middle section outlet fully closed, no air-flow is possible through this section. During such times the pressure in the middle section is approximated to be equal to the ambient pressure at ground level.

C.3.4 Open bottom section

The steady state momentum equation for the bottom section of the collector is described by

$$- \left(H_{tr} \frac{\partial p}{\partial r} + \tau_{tr} + \tau_g + \frac{F_{\text{supports}}}{r\Delta\theta} \right) = \rho v H_{tr} \frac{\partial v}{\partial r} \quad (\text{C.9})$$

where τ_{tr} and τ_g are the tertiary roof and ground shear stresses acting on the air stream in the bottom section of the collector, while the term F_{supports} is the total drag force per unit radial distance that the roof supports enforce on the air stream in the bottom section.

C.3.5 Closed bottom section

With the air-flow regulating mechanism at the bottom section outlet fully closed, no air-flow is possible through this section. During such times the pressure in the bottom section is approximated to be equal to the ambient pressure at ground level.

C.3.6 Transition section

All sections open

As the air in the collector flows from the perimeter through the top, middle and bottom sections, it should experience different pressure changes due to friction and support drag in the respective sections. However, the flow will regulate itself in order to produce an equal air pressure at the transitional section inlet. This means that, independent of the amount of air-flow regulated through the middle or bottom sections, at the inlet to the transitional

collector section $p_{top} \approx p_{mid} \approx p_{bot}$. Subsequently, in order to simplify the numerical model, the following condition is assumed for the evaluation of the air-flow momentum in the transitional collector control volume

$$p_{i-1} = (p_{top})_{i-1} = (p_{mid})_{i-1} = (p_{bot})_{i-1} \quad (C.10)$$

where p_{i-1} refers to the pressure at the inlet of the transitional control volume (at collector radius r_{i-1}), at the point where the air streams of the top, middle and bottom sections merge.

It is assumed that the flow through the transitional control volume will be normal single channel flow. Therefore, the conservation of momentum applied to the air stream moving through the transitional collector control volume will be evaluated according to the original steady state collector momentum equation (equation (2.2) in Chapter 2). This partial differential equation is repeated here for convenience

$$- \left(H \frac{\partial p}{\partial r} + \tau_r + \tau_g + \frac{F_{\text{supports}}}{r \Delta \theta} \right) = \rho v H \frac{\partial v}{\partial r} \quad (C.11)$$

Closed bottom section

With the air-flow regulating mechanism at the bottom section outlet fully closed, air from the collector perimeter flows only through the top and middle sections of the collector. At the transitional control volume inlet, the collector through-flow area increases from the area of the top and middle section only to the total collector through-flow area between the main collector roof and the ground surface. The following condition is assumed in this case

$$p_{i-1} = (p_{top})_{i-1} = (p_{mid})_{i-1} \quad (C.12)$$

As mentioned in Appendix A, the effects of friction and support drag on the air-flow momentum over the radial length of a single collector control volume is small. In order to simplify the numerical model it is assumed that these losses are negligible for the evaluation of the momentum equation over the transitional collector control volume. Therefore, in the case of a fully closed bottom section, the flow at the transitional control volume is approximated as flow between parallel plates that experience an abrupt expansion. Applying a relation by Kröger (2004) which pertains to the flow in a duct that experience an abrupt expansion, the static pressure difference over the transitional section can be evaluated by

$$\Delta p_e = \frac{1}{2} (\rho_{avg} v_{avg}^2)_{i-1} \left[K_e - \left(1 - \left(\frac{A_{coll, top} + A_{coll, mid}}{A_{coll}} \right)_{i-1}^2 \right) \right] \quad (C.13)$$

where K_e denotes the expansion loss coefficient, while $A_{coll, top}$, $A_{coll, mid}$ and A_{coll} represent the respective total collector through-flow area of the top section, total collector through-flow area of the middle section and the total collector through-flow area after the expansion at the collector radius r_{i-1} . The subscript *avg* indicates the average properties at the transitional control volume inlet (node $i - 1$), which are calculated by

$$(\rho_{avg})_{i-1} = \frac{1}{2} (\rho_{top} + \rho_{mid})_{i-1} \quad (C.14)$$

and

$$(v_{avg})_{i-1} = \frac{1}{2} (v_{top} + v_{mid})_{i-1} \quad (C.15)$$

Kröger (2004) gives the loss coefficient for turbulent flow as

$$K_e = \left[1 - \left(\frac{A_{coll, top} + A_{coll, mid}}{A_{coll}} \right)_{i-1} \right]^2 \quad (C.16)$$

The collector air pressure at the transitional control volume outlet is thus simply determined by:

$$p_i = p_{i-1} - \Delta p_e \quad (\text{C.17})$$

After the evaluation of the transitional control volume, the effects of friction and support drag on the air-flow momentum are again considered for the remaining collector control volumes.

Closed middle and bottom section

The calculations of the following subsection are performed analogously to the previous subsection. With the air-flow regulating mechanisms at the middle and bottom section outlets fully closed, air from the collector perimeter flows only through the top section of the collector. In this case, at the transitional control volume inlet, the collector through-flow area increases from the area of the top section only to the total collector through-flow area between the main collector roof and the ground surface. We now assume the following condition

$$p_{i-1} = (p_{top})_{i-1} \quad (\text{C.18})$$

The effects of friction and support drag on the air-flow momentum over the length of the transitional collector control volume are once again neglected. The flow at the transitional control volume is also once again approximated as flow between parallel plates that experience an abrupt expansion. When now applying the relation by Kröger (2004), we find

$$\Delta p_e = \frac{1}{2}(\rho_{top} v_{top}^2)_{i-1} \left[K_e - \left(1 - \left(\frac{A_{coll, top}}{A_{coll}} \right)_{i-1}^2 \right) \right] \quad (\text{C.19})$$

where the loss coefficient according to Kröger (2004) now changes to

$$K_e = \left[1 - \left(\frac{A_{coll, top}}{A_{coll}} \right)_{i-1} \right]^2 \quad (\text{C.20})$$

The collector air pressure at the transitional control volume outlet is also simply determined according to equation (C.17). Once again, after the evaluation of the transitional control volume, the effects of friction and support drag on the air-flow momentum are again considered for the remaining collector control volumes.

C.4 Collector roof energy equation

The steady state collector roof energy equation is equivalent to the equation derived in Appendix A and is repeated here for convenience:

$$(\alpha_{er} I_h)_b + (\alpha_{er} I_h)_d + q_{sr} = q_{ra} + q_{rs} + q_{rth} \quad (\text{C.21})$$

C.5 Secondary roof energy equation

Figure C.2 illustrates schematically the various heat fluxes considered when evaluating the secondary collector roof energy equation.

The final form of the steady state secondary roof energy equation is given by

$$(\alpha_{es} \tau_{er} I_h)_b + (\alpha_{es} \tau_{er} I_h)_d + q_{ts} = q_{sth} + q_{sr} + q_{smh} \quad (\text{C.22})$$

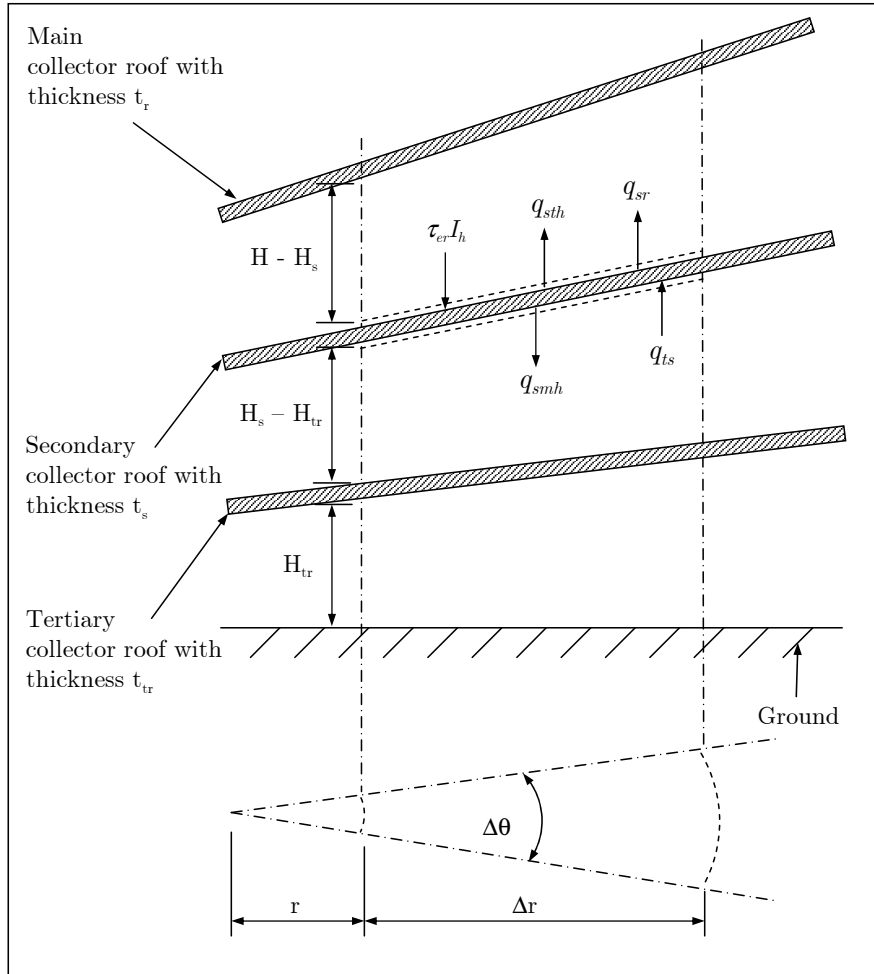


Figure C.2: Conservation of energy applied to a radial control volume for the secondary collector roof

where α_{es} represents the effective absorptance of the secondary roof, while τ_{er} refers to the effective transmittance of the main collector roof. The term q_{sth} is the convection heat flux from the secondary roof to the air above it (thus to the air in the top section collector control volume), while q_{smh} is the convective heat flux from the secondary roof to the air below it (therefore to the air in the middle section collector control volume). The radiative heat flux from the secondary roof to the main roof is represented by q_{sr} , while the radiative heat flux from the tertiary roof to the secondary roof is signified by q_{ts} .

C.6 Tertiary roof energy equation

Figure C.3 illustrates schematically the various heat fluxes considered when evaluating the tertiary collector roof energy equation.

The final form of the steady state tertiary roof energy equation is given by

$$(\alpha_{et}\tau_{es}I_h)_b + (\alpha_{et}\tau_{es}I_h)_d + q_{gt} = q_{tmh} + q_{ts} + q_{tbh} \quad (C.23)$$

where α_{et} represents the effective absorptance of the tertiary roof, while τ_{es} refers to the effective transmittance of the secondary roof (thus the solar transmittance through both the

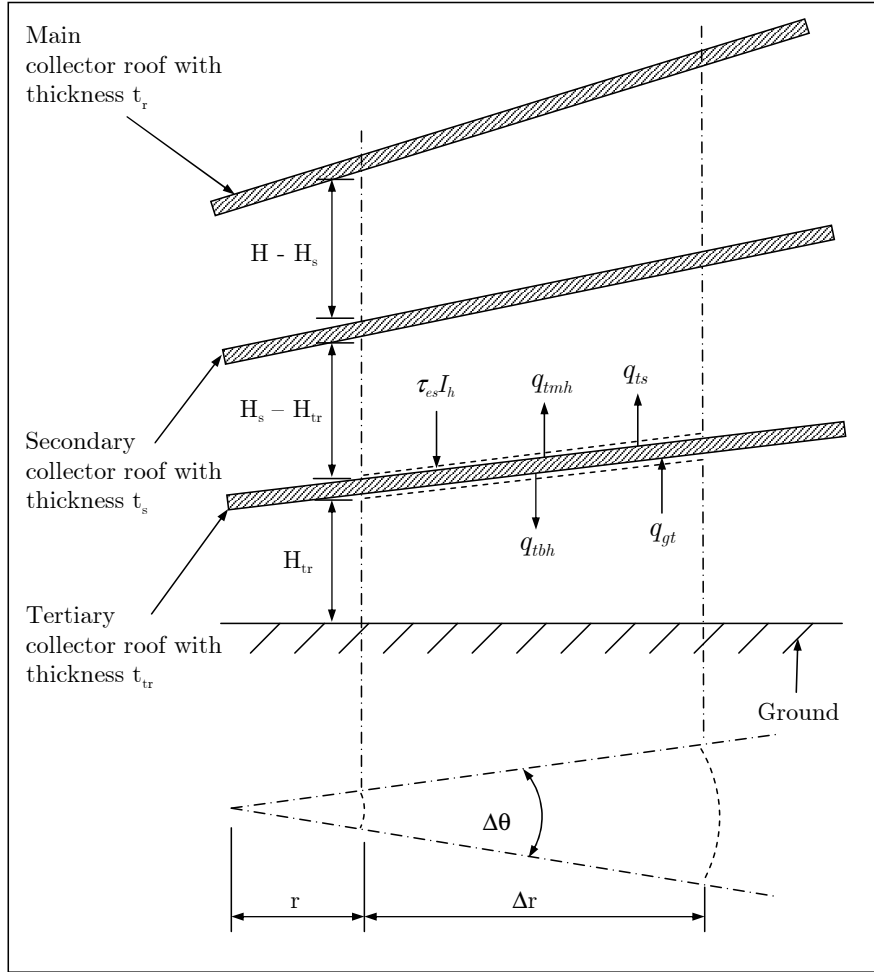


Figure C.3: Conservation of energy applied to a radial control volume for the tertiary collector roof

main and secondary roofs). The term q_{tmh} is the convection heat flux from the tertiary roof to the air above it (thus to the air in the middle section collector control volume), while q_{tbh} is the convective heat flux from the tertiary roof to the air below it (therefore to the air in the bottom section collector control volume). The radiative heat flux from the ground surface to the tertiary roof is represented by q_{gt} .

C.7 Ground energy equations

C.7.1 At $z = 0$ (Ground surface)

The steady state ground surface energy equation is

$$(\tau_{tot}\alpha_g)_b I_{hb} + (\tau_{tot}\alpha_g)_d I_{hd} = q_{gbh} + q_{gt} - k_g \left. \frac{\partial T_g}{\partial z} \right|_{z=0} \quad (C.24)$$

where α_g , k_g and T_g are the absorptance, thermal conductivity and temperature of the ground respectively. The term q_{gbh} denotes the convection heat flux from the ground surface to the air in the bottom section of the collector. Furthermore, τ_{tot} is the total transmittance

of the solar radiation passing through the main, secondary and tertiary collector roofs. The determination of τ_{tot} is explained in Appendix G of this dissertation.

C.7.2 At $z > 0$

The introduction of a secondary and tertiary collector roof does not change the ground energy equation which expresses the energy fluxes deeper in the ground. Thus the equation remains unchanged, as from Chapter 2 and is repeated here in its final form for convenience

$$-k_g \frac{\partial^2 T_g}{\partial z^2} + \rho_g c_g \frac{\partial T_g}{\partial t} = 0 \quad (C.25)$$

where ρ_g and c_g are the density and specific heat capacity of the ground. The ground properties are assumed to be constant.

C.7.3 At $z = \infty$

The introduction of a secondary and tertiary collector roof also does not change the boundary condition at a certain depth in the ground where the temperature gradient becomes zero. Thus the condition remains unchanged, as from Chapter 2 and is repeated here for convenience

$$\frac{\partial T_g}{\partial z} = 0 \quad (C.26)$$

C.8 Air stream energy equation

C.8.1 Top section

The steady state energy equation describing the flow of air through the top section of the collector is identical to equation (A.67) and is repeated here for convenience:

$$q_{rth} + q_{sth} = \frac{RT}{r} \frac{\partial}{\partial r} (\rho v r (H - H_s)) + \rho v (H - H_s) \frac{\partial}{\partial r} (c_p T) \quad (C.27)$$

C.8.2 Open middle section

The steady state air stream energy equation for the middle section of the collector is (derived analogously to the derivation of equation (A.74) in Appendix A)

$$q_{smh} + q_{tmh} = \frac{RT}{r} \frac{\partial}{\partial r} (\rho v r (H_s - H_{tr})) + \rho v (H_s - H_{tr}) \frac{\partial}{\partial r} (c_p T) \quad (C.28)$$

C.8.3 Closed middle section

With the air-flow regulating mechanism at the middle section outlet fully closed, no air-flow is possible through this section. The steady state air energy equation for the middle section during these periods is

$$q_{smh} + q_{tmh} = 0 \quad (C.29)$$

C.8.4 Open bottom section

The steady state air stream energy equation for the bottom section of the collector is (derived analogously to the derivation of equation (A.74) in Appendix A)

$$q_{tbb} + q_{gbb} = \frac{RT}{r} \frac{\partial}{\partial r} (\rho v r H_{tr}) + \rho v H_{tr} \frac{\partial}{\partial r} (c_p T) \quad (C.30)$$

C.8.5 Closed bottom section

With the air-flow regulating mechanism at the bottom section outlet fully closed, no air-flow is possible through this section. The steady state air energy equation for the bottom section during these times is

$$q_{tbb} + q_{gbb} = 0 \quad (C.31)$$

C.8.6 Transition section

All sections open

With air-flow through the top, middle and bottom sections of the collector, the steady state air stream energy balance for the transitional control volume of the collector is as follows:

$$\begin{aligned} & (\rho_{top} v_{top} r (H - H_s) c_{p,top} T_{top})_{i-1} + (\rho_{mid} v_{mid} r (H_s - H_{tr}) c_{p,mid} T_{mid})_{i-1} \\ & + (\rho_{bot} v_{bot} r H_{tr} c_{p,bot} T_{bot})_{i-1} \\ & + q_{rh} r \Delta r + q_{gh} r \Delta r \\ & = (\rho v r H c_p T)_i \end{aligned} \quad (C.32)$$

where q_{rh} and q_{gh} refers to the convective heat fluxes from the main collector roof and ground surface to the air in the transitional control volume respectively.

Closed bottom section

With the air-flow regulating mechanism at the bottom section outlet fully closed, no air-flow is possible through the bottom section. The resulting steady state air stream energy equation for the transitional collector control volume is (with air-flow only experienced through the top and middle sections of the collector)

$$\begin{aligned} & (\rho_{top} v_{top} r (H - H_s) c_{p,top} T_{top})_{i-1} + (\rho_{mid} v_{mid} r (H_s - H_{tr}) c_{p,mid} T_{mid})_{i-1} \\ & + q_{rh} r \Delta r + q_{gh} r \Delta r \\ & = (\rho v r H c_p T)_i \end{aligned} \quad (C.33)$$

Closed middle and bottom section

With the air-flow regulating mechanisms at the middle and bottom section outlets fully closed, no air-flow is possible through the middle and bottom sections. The resulting steady state air stream energy equation for the transitional control volume is (with air-flow only experienced through the top section of the collector)

$$(\rho_{top} v_{top} r (H - H_s) c_{p,top} T_{top})_{i-1} + q_{rh} r \Delta r + q_{gh} r \Delta r = (\rho v r H c_p T)_i \quad (C.34)$$

Appendix

D

Conservation Equations: Including Plastic Covered Water Tanks

In an effort to facilitate a more uniform daily solar chimney power plant output, the following appendix investigates the possibility of energy storage in water by including plastic covered water tanks under the main collector roof of the plant.

Relevant conservation equations are derived for such a plant configuration. These equations are discretized (not presented) according to the schemes discussed by Pretorius (2004) before their inclusion into the existing computer simulation model.

Chapter 6 discusses the modifications to the collector with the inclusion of the water tanks.

D.1 Definition of sections in the collector

Figure D.1 illustrates how the inclusion of water tanks in the collector is modelled by the numerical model.

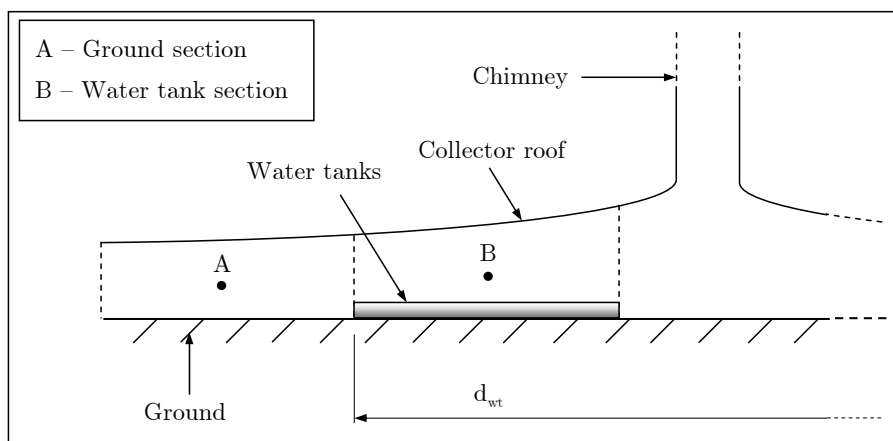


Figure D.1: Definition of sections created in the collector by the inclusion of plastic covered water tanks

D.2 Ground section

All conservation equations for the ground section of the collector (see figure D.1) are identical to the governing equations specified in Chapter 2 of this dissertation (as derived by Pretorius (2004)).

D.3 Water tank section

The continuity equation for the water tank section of the collector (see figure D.1) is identical to the collector continuity equation specified in Chapter 2 of this study (as derived by Pretorius (2004)), while the ground surface and ground energy equations fall away in this section.

D.3.1 Collector momentum equation

The collector momentum equation for the water tank section is similar to the momentum equation for the ground section, except that the ground shear stress term is replaced by a film shear stress term, τ_f . The steady state form of this equation therefore is

$$-\left(H\frac{\partial p}{\partial r} + \tau_r + \tau_f + \frac{F_{\text{supports}}}{r\Delta\theta}\right) = \rho v H \frac{\partial v}{\partial r} \quad (\text{D.1})$$

D.3.2 Collector roof energy equation

The collector roof energy equation for the water tank section of the collector is similar to the collector roof energy equation for the ground section, except that the radiation term q_{gr} (heat transfer from the ground surface to the roof) is replaced by the term q_{fr} , indicating radiation heat transfer from the plastic film to the collector roof. The steady state form of this equation is

$$\alpha_{eb}I_{hb} + \alpha_{ed}I_{hd} + q_{fr} = q_{ra} + q_{rs} + q_{rh} \quad (\text{D.2})$$

D.3.3 Water energy equation

From figure D.2 the energy balance for the water tank in the collector can be evaluated as follows (note that water tank size in the schematic figure is substantially exaggerated for clarity)

$$\tau_e I_h r \Delta\theta \Delta r = \tau_e \rho_{fe} I_h r \Delta\theta \Delta r + q_{fh} r \Delta\theta \Delta r + q_{fr} r \Delta\theta \Delta r + \frac{\partial}{\partial t}(\rho_w r \Delta\theta \Delta r t_w c_w T_w) \quad (\text{D.3})$$

where τ_e , ρ_{fe} , q_{fh} and q_{fr} represent the effective solar radiation transmitted by the collector roof, the effective reflectance of the film, the convection heat transfer from the film to the collector air and the radiation heat transfer from the film to the collector roof respectively. Furthermore, the terms ρ_w , t_w , c_w and T_w refer to the respective water density, depth, specific heat and mean temperature.

By expanding the solar radiation into its respective beam and diffuse components and rearranging, equation (D.3) becomes

$$\begin{aligned} \tau_{eb} I_{hb} (1 - \rho_{feb}) r \Delta\theta \Delta r + \tau_{ed} I_{hd} (1 - \rho_{fed}) r \Delta\theta \Delta r &= q_{fh} r \Delta\theta \Delta r + q_{fr} r \Delta\theta \Delta r \\ &+ \frac{\partial}{\partial t}(\rho_w r \Delta\theta \Delta r t_w c_w T_w) \quad (\text{D.4}) \end{aligned}$$

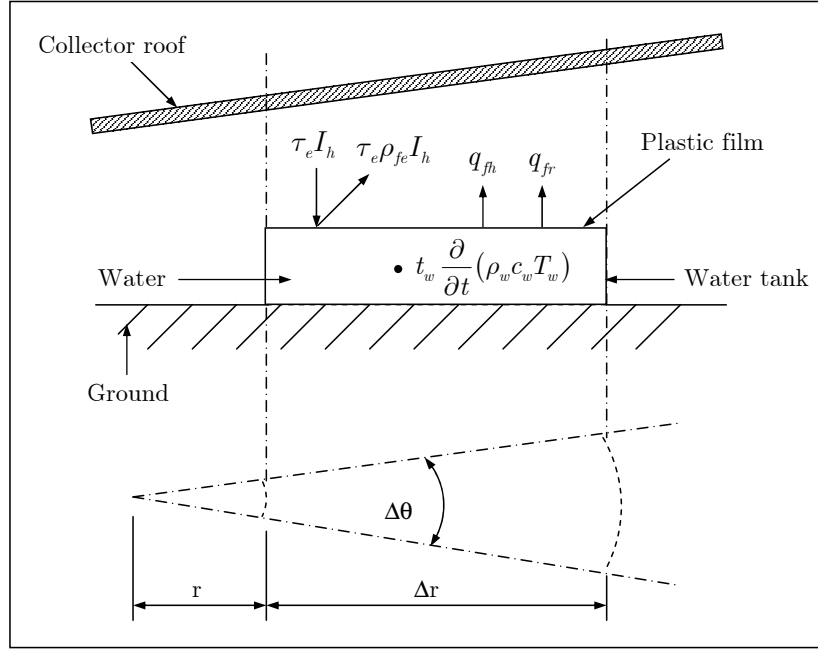


Figure D.2: Conservation of energy applied to a control volume for the water tank in the collector

When dividing equation (D.4) by $r\Delta\theta\Delta r$, we find

$$\tau_{eb} I_{hb}(1 - \rho_{feb}) + \tau_{ed} I_{hd}(1 - \rho_{fed}) = q_{fh} + q_{fr} + t_w \frac{\partial}{\partial t} (\rho_w c_w T_w) \quad (D.5)$$

This is the final form of the water energy equation, as significant transient effects are experienced in the water.

D.3.4 Air stream energy equation

The air stream energy equation for the water tank section of the collector is similar to the air stream energy equation for the ground section, except that the convection heat transfer term q_{gh} (heat transfer from the ground surface to the collector air) is replaced by the term q_{fh} , indicating convection heat transfer from the plastic film to the collector air. The steady state form of this equation is

$$q_{rh} + q_{fh} = \frac{RT}{r} \frac{\partial}{\partial r} (\rho v r H) + \rho v H \frac{\partial}{\partial r} (c_p T) \quad (D.6)$$

Appendix

E

Conservation Equations: Including a Delta Ground Surface Configuration

In an effort to facilitate a more uniform daily solar chimney power plant output, the following appendix investigates the possibility of including a delta ground surface under the collector roof.

Relevant conservation equations for the inclusion of such a ground configuration are presented. These equations are discretized (not presented) according to the schemes discussed by Pretorius (2004) before their inclusion into the existing computer simulation model.

Chapter 6 discusses the implications of including a delta ground surface configuration in the solar chimney power plant.

E.1 Approximating the delta configuration numerically

As mentioned in Chapter 6, the inclusion of a delta ground configuration increases the exposed ground surface area. This delta configuration is included into the existing numerical model by including a ratio F_D into the appropriate equations, which represents the factor by which the exposed ground surface area increases (with reference to a flat surface).

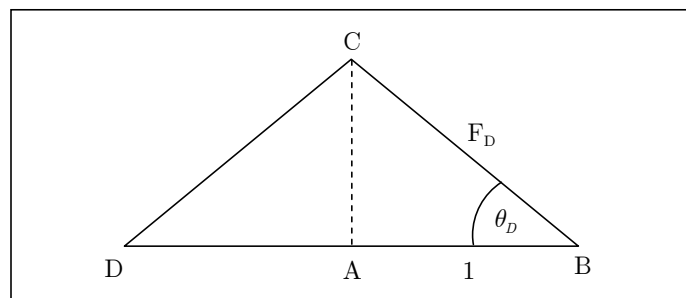


Figure E.1: Calculation of the F_D ratio

Consider the profile of a delta configuration ground surface illustrated in figure E.1. In general, F_D is the ratio of BC/AB . From figure E.1, F_D may also be determined as

$$F_D = \frac{BC}{AB} = \frac{1}{\cos \theta_D} \quad (\text{E.1})$$

This ratio influences the ground convection and conduction terms in the energy equations that are to follow.

The inclusion of a delta ground configuration also decreases the available through-flow area in the collector if the height of the roof at the inlet of the collector remains unchanged. The reduced through-flow area is incorporated (approximated) into the computer simulation model.

E.2 Ground surface energy equation

The study by Pretorius (2004) derived the ground surface energy equation in the collector of the solar chimney power plant (repeated in its final form in this dissertation as equation (2.4)). With the inclusion of a delta ground configuration into the numerical model, the ground surface energy equation is modified as follows:

$$\tau_e I_h r \Delta \theta \Delta r = (1 - \alpha_g) \tau_e I_h r \Delta \theta \Delta r + q_{gr} r \Delta \theta \Delta r + q_g F_D r \Delta \theta \Delta r + q_{gh} F_D r \Delta \theta \Delta r \quad (\text{E.2})$$

where α_g is the absorptivity of the ground surface, while q_g is the conduction heat flux from the surface into the ground. The term q_{gr} denotes the radiative heat flux from the ground surface to the collector roof.

When expanding the relevant terms into their respective beam and diffuse components, expanding the conduction term, dividing by $r \Delta \theta \Delta r$ and employing the transmittance-absorptance product, we find

$$(\tau_e \alpha_g)_b I_{hb} + (\tau_e \alpha_g)_d I_{hd} = q_{gr} - F_D k_g \left. \frac{\partial T_g}{\partial z} \right|_{z=0} + F_D q_{gh} \quad (\text{E.3})$$

E.3 Air stream energy equation

The study by Pretorius (2004) derived the air stream energy equation for the air flowing through the collector of the solar chimney power plant (repeated in this dissertation in a slightly altered final form as equation (2.7)). Thus with the inclusion of a delta ground configuration, the steady state air stream energy equation simply becomes:

$$q_{rh} + F_D q_{gh} = \frac{RT}{r} \frac{\partial}{\partial r} (\rho v r H) + \rho v H \frac{\partial}{\partial r} (c_p T) \quad (\text{E.4})$$

Appendix

F

Conservation Equations: Including Vegetation Under the Collector Roof

As a means of adding value to the solar chimney power plant system, it has been suggested that the collector of the plant should take on a secondary function - acting as a greenhouse for agricultural purposes.

A numerical model of a large-scale solar chimney power plant was created in a previous study (Pretorius, 2004). This study derived conservation (mass, momentum and energy) equations for the collector roof, collector air, ground underneath the collector roof and the air in the chimney.

The following appendix conducts an investigation into the potential of including vegetation under the collector roof. Relevant conservation equations for a collector incorporating vegetation are derived. All equations, except for the vegetation and ground energy equations in the vegetation section (at $z > 0$), are discretized according to the schemes discussed by Pretorius (2004) before their inclusion into the existing computer simulation model.

F.1 Definition of sections in the collector

Figure F.1 illustrates how the inclusion of vegetation in the collector is modelled by the numerical model.

F.2 Vegetation section

F.2.1 Collector continuity equation

Dry air

The steady state collector continuity equation for dry air in the vegetation section is identical to equation (2.1) in Chapter 2 of this dissertation.

Water vapor

Consider from figure F.2 the following water vapor mass conservation relation applicable to purely radial air-flow through a defined elementary control volume in the vegetation section of the collector, with radial length Δr and subtended angle $\Delta\theta$ under the roof of the collector:

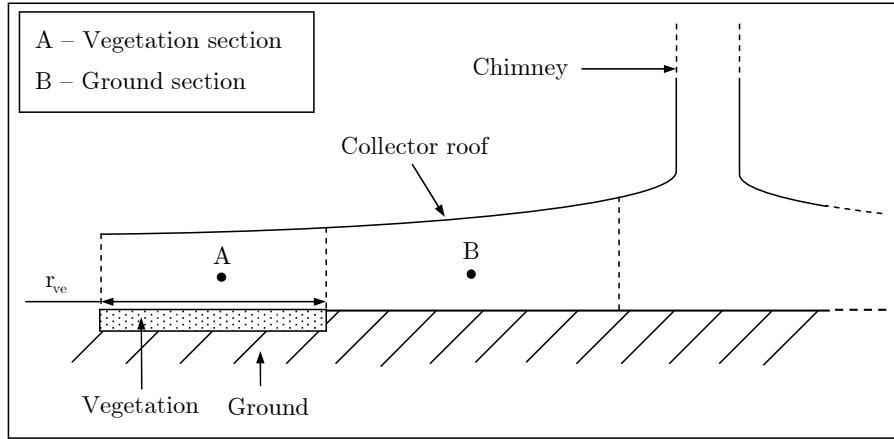


Figure F.1: Definition of sections created in the collector by the inclusion of vegetation

$$\rho v r \Delta \theta H \omega + \left(\frac{\dot{m}_v}{A} \right) r \Delta \theta \Delta r = \rho v r \Delta \theta H \omega + \frac{\partial}{\partial r} (\rho v r \Delta \theta H \omega) \Delta r + \frac{\partial}{\partial t} (\rho r \Delta \theta \Delta r H \omega) \quad (\text{F.1})$$

where ρ and v are the density and radial velocity of the dry air moving through the defined control volume respectively, while H is the height of the collector roof at a specific radial position. The term (\dot{m}_v/A) represents the mass-flow rate of water per unit area from the transpiring (vegetation) surface, while ω is the absolute humidity. Divide equation (F.1) by $r \Delta \theta \Delta r$, simplify and find

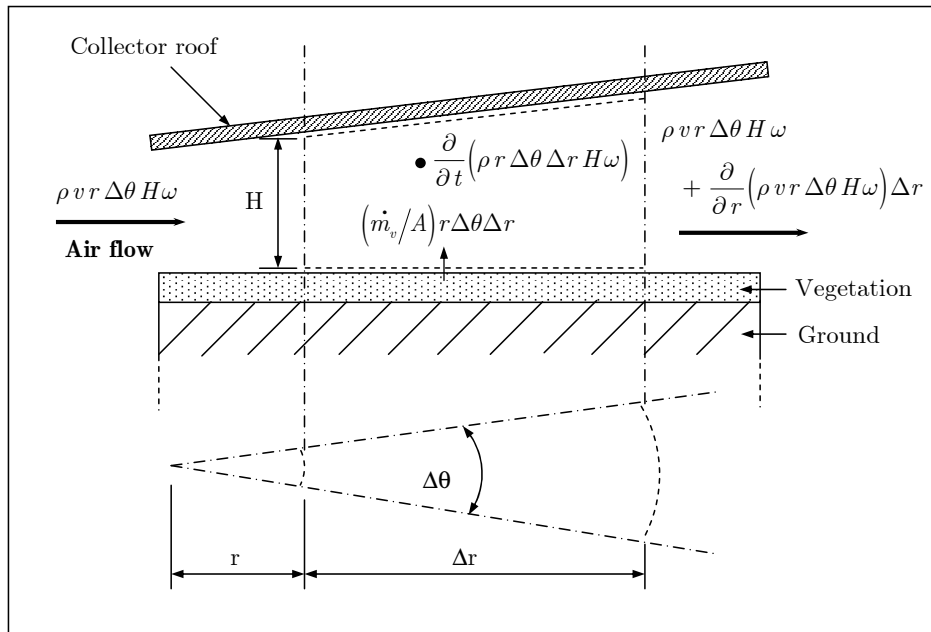


Figure F.2: Conservation of water vapor mass applied to a control volume in the vegetation section of the collector

$$\frac{1}{r} \frac{\partial}{\partial r} (\rho v r H \omega) + H \frac{\partial}{\partial t} (\rho \omega) = \left(\frac{\dot{m}_v}{A} \right) \quad (\text{F.2})$$

During steady state conditions or when transient effects are negligible, equation (F.2) becomes

$$\frac{1}{r} \frac{\partial}{\partial r} (\rho v r H \omega) = \left(\frac{\dot{m}_v}{A} \right) \quad (\text{F.3})$$

F.2.2 Collector momentum equation

It is approximated that the water vapor in the collector air will have a negligible effect on the momentum of the air flowing through the collector. Therefore, the momentum equation is only evaluated for dry air and is subsequently similar to equation (2.2) in Chapter 2, with the exception that the ground shear stress term is replaced by a vegetation shear stress term.

Thus the steady state collector momentum equation for the vegetation section of the collector is

$$- \left(H \frac{\partial p}{\partial r} + \tau_r + \tau_{ve} + \frac{F_{\text{supports}}}{r \Delta \theta} \right) = \rho v H \frac{\partial v}{\partial r} \quad (\text{F.4})$$

where τ_{ve} represents the vegetation shear stress.

F.2.3 Collector roof energy equation

The inclusion of vegetation in the collector of the solar chimney power plant only affects the radiation exchange (between the collector roof and the ground surface) term of the collector roof energy equation (equation (2.3) in Chapter 2).

Thus, the steady state collector roof energy equation for the vegetation section is given by

$$\alpha_{eb} I_{hb} + \alpha_{ed} I_{hd} + q_{ver} = q_{ra} + q_{rs} + q_{rh} \quad (\text{F.5})$$

where q_{ver} denotes the radiation exchange between the vegetation surface and the collector roof.

F.2.4 Vegetation/Ground energy equations

At $z = 0$ (Vegetation surface)

From figure F.3 the energy balance at the surface of the vegetation in the collector can be evaluated as follows

$$\begin{aligned} \tau_e I_h r \Delta \theta \Delta r = (1 - \alpha_{ve}) \tau_e I_h r \Delta \theta \Delta r + \left(\frac{\dot{m}_v}{A} \right) r \Delta \theta \Delta r h_v + q_{ver} r \Delta \theta \Delta r \\ + q_{cond,o} r \Delta \theta \Delta r + q_{veh} r \Delta \theta \Delta r \quad (\text{F.6}) \end{aligned}$$

where α_{ve} is the absorptivity of the vegetation surface, while $q_{cond,o}$ is the conduction heat flux from the surface into the vegetation layer. The term q_{veh} denotes the convection heat flux from the vegetation surface to the air under the collector roof, while h_v is the enthalpy of water vapor.

The effective solar radiation I_h and the effective transmittance τ_e can be expanded into their respective beam and diffuse components to give

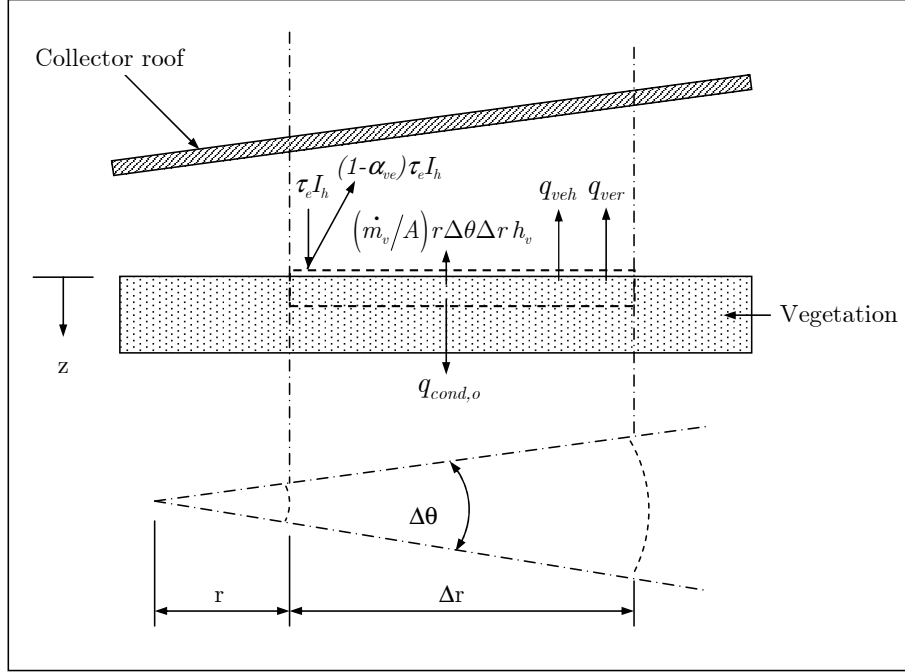


Figure F.3: Conservation of energy applied to a control volume for the vegetation surface in the collector

$$\begin{aligned}
 \tau_{eb} I_{hb} r \Delta \theta \Delta r + \tau_{ed} I_{hd} r \Delta \theta \Delta r &= (1 - \alpha_{ve}) \tau_{eb} I_{hb} r \Delta \theta \Delta r + (1 - \alpha_{ve}) \tau_{ed} I_{hd} r \Delta \theta \Delta r \\
 &+ \left(\frac{\dot{m}_v}{A} \right) r \Delta \theta \Delta r h_v + q_{ver} r \Delta \theta \Delta r + q_{cond,o} r \Delta \theta \Delta r \quad (F.7) \\
 &+ q_{veh} r \Delta \theta \Delta r
 \end{aligned}$$

As seen in figure F.3, some of the radiation that passes through the collector roof and strikes the vegetation is reflected back to the roof. The reflected radiation is in turn reflected back to the vegetation. The multiple reflection of diffuse radiation continues, resulting in a slightly higher fraction of energy being absorbed by the vegetation. This higher fraction of energy is represented by the transmittance-absorptance product ($\tau\alpha$), as discussed in an appendix of the study by Pretorius (2004).

Upon employing the transmittance-absorptance product, simplifying the equation and expanding the conduction term, we find at $z = 0$:

$$(\tau_e \alpha_{ve})_b I_{hb} + (\tau_e \alpha_{ve})_d I_{hd} = \left(\frac{\dot{m}_v}{A} \right) h_v + q_{ver} - k_{ve} \left. \frac{\partial T_g}{\partial z} \right|_{z=0} + q_{veh} \quad (F.8)$$

where k_{ve} is the thermal conductivity of the vegetation. In order to simplify the analysis of a collector which incorporates vegetation and ground, all vegetation and ground temperatures are referred to as T_g .

At $z > 0$ (In vegetation)

Consider from figure F.4 an energy balance in the vegetation

$$q_{cond,i} r \Delta \theta \Delta r = q_{cond,o} r \Delta \theta \Delta r + \frac{\partial}{\partial t} (\rho_{ve} r \Delta \theta \Delta r \Delta z c_{ve} T_g) \quad (F.9)$$

where $q_{cond,i}$ and $q_{cond,o}$ refer to the conduction heat fluxes into and out of the specific control volume. The variables ρ_{ve} and c_{ve} are the density and specific heat capacity of the vegetation respectively, while Δz is the depth of the control volume in the vegetation.

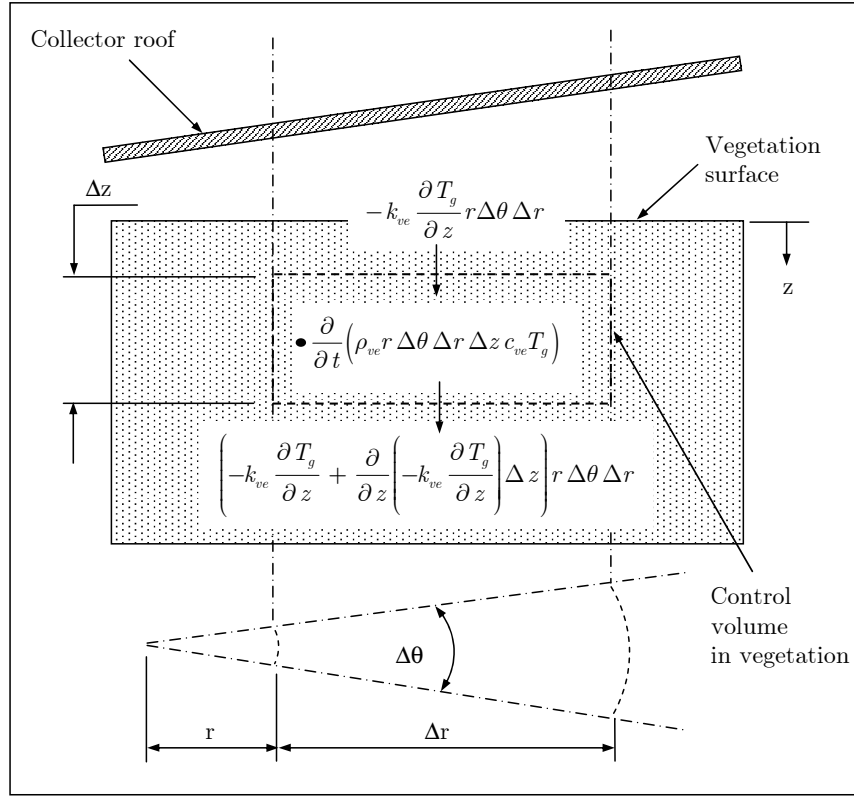


Figure F.4: Conservation of energy applied to a control volume for the vegetation in the collector

When expanding the conduction terms, equation (F.9) becomes

$$-k_{ve} \frac{\partial T_g}{\partial z} r \Delta \theta \Delta r = \left[-k_{ve} \frac{\partial T_g}{\partial z} + \frac{\partial}{\partial z} \left(-k_{ve} \frac{\partial T_g}{\partial z} \right) \Delta z \right] r \Delta \theta \Delta r + \frac{\partial}{\partial t} (\rho_{ve} r \Delta \theta \Delta r \Delta z c_{ve} T_g) \quad (\text{F.10})$$

Dividing equation (F.10) by $r \Delta \theta \Delta r \Delta z$ and assuming that the properties of the vegetation are constant gives

$$-k_{ve} \frac{\partial^2 T_g}{\partial z^2} + \rho_{ve} c_{ve} \frac{\partial T_g}{\partial t} = 0 \quad (\text{F.11})$$

Vegetation/Ground interface boundary conditions

In order to solve the vegetation/ground temperatures, the following boundary conditions must be defined for the interface between the vegetation and ground.

Vegetation side

Consider from figure F.5 the following energy balance regarding a boundary control volume on the vegetation side of the vegetation/ground interface

$$q_{cond,i} = q_{cond,o} + \frac{\partial}{\partial t} (\rho_{ve} r \Delta \theta \Delta r \Delta z_k c_{ve} T_g) \quad (F.12)$$

where Δz_k is equal to the thickness (depth) of the boundary control volume on the vegetation side.

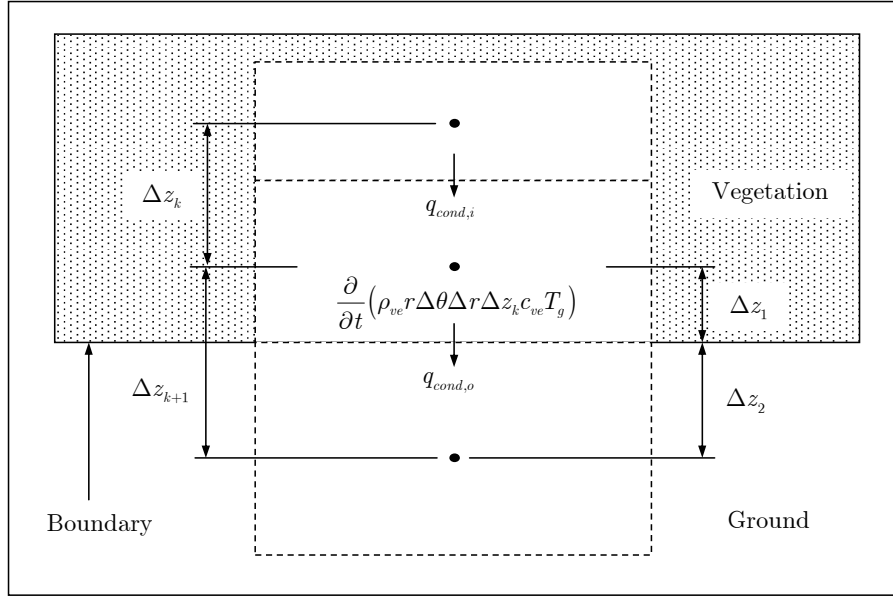


Figure F.5: Conservation of energy applied to a boundary control volume on the vegetation side of the interface between the vegetation and ground

When applying a relation by Mills (1995) which evaluates heat conduction through a composite material (in our case, vegetation and ground), we find that the conduction heat flux across the vegetation/ground boundary is given by

$$q_{cond,o} = \frac{\Delta T_g}{\Delta z_1/k_{ve} + \Delta z_2/k_g} \quad (F.13)$$

where Δz_1 and Δz_2 are the distances depicted in figure F.5, while k_g is the thermal conductivity of the ground. When rearranging, we find

$$q_{cond,o} = \left(\frac{k_{ve} k_g}{\Delta z_1 k_g + \Delta z_2 k_{ve}} \right) \Delta T_g \quad (F.14)$$

Substituting equation (F.14) into equation (F.12) and expanding gives

$$-k_{ve} r \Delta \theta \Delta r \frac{\partial T_g}{\partial z} = - \left(\frac{k_{ve} k_g}{\Delta z_1 k_g + \Delta z_2 k_{ve}} \right) r \Delta \theta \Delta r \Delta T_g + \frac{\partial}{\partial t} (\rho_{ve} r \Delta \theta \Delta r \Delta z_k c_{ve} T_g) \quad (F.15)$$

When dividing equation (F.15) by $r \Delta \theta \Delta r$ and realizing that $\Delta z_1 = \frac{1}{2} \Delta z_k$ and $\Delta z_2 = \frac{1}{2} \Delta z_{k+1}$, it follows that

$$-k_{ve} \frac{\partial T_g}{\partial z} = - \left(\frac{2k_{ve}k_g}{\Delta z_k k_g + \Delta z_{k+1} k_{ve}} \right) \Delta T_g + \rho_{ve} c_{ve} \Delta z_k \frac{\partial T_g}{\partial t} \quad (\text{F.16})$$

Ground side

Consider from figure F.6 the following energy balance regarding a boundary control volume on the ground side of the vegetation/ground interface

$$q_{cond,i} = q_{cond,o} + \frac{\partial}{\partial t} (\rho_g r \Delta \theta \Delta r \Delta z_k c_g T_g) \quad (\text{F.17})$$

where ρ_g and c_g are the density and specific heat capacity of the ground, while Δz_k is now equal to the thickness (depth) of the boundary control volume on the ground side. The ground properties are assumed to be constant.

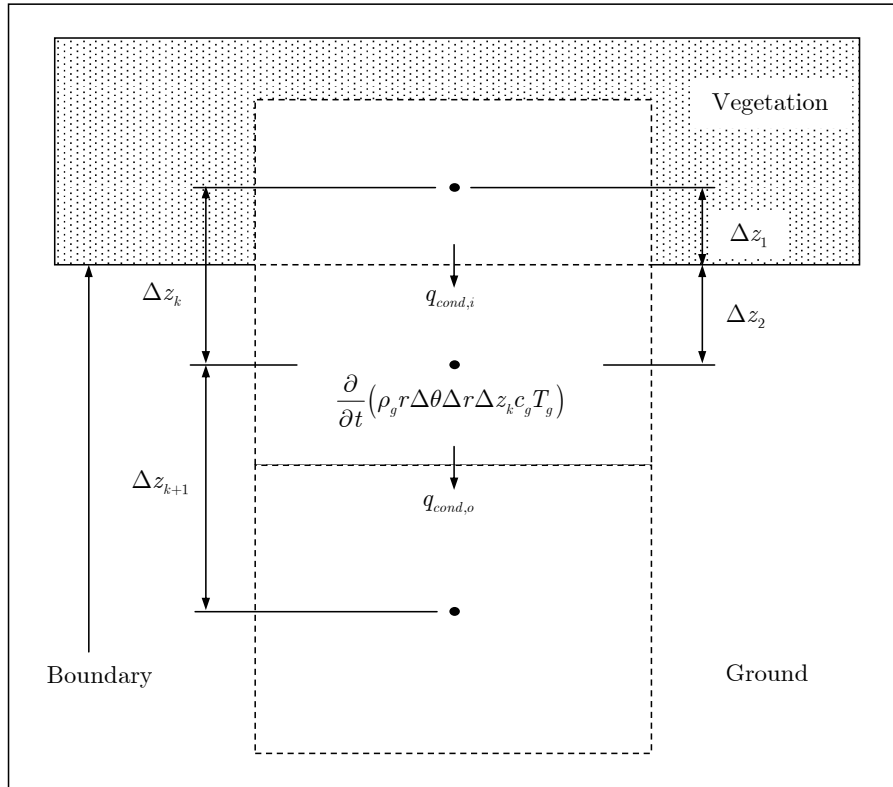


Figure F.6: Conservation of energy applied to a boundary control volume on the ground side of the interface between the vegetation and ground

When once again applying the relation by Mills (1995) (as for the vegetation side), it follows that the conduction heat flux across the vegetation/ground boundary is given by

$$q_{cond,i} = \frac{\Delta T_g}{\Delta z_1/k_{ve} + \Delta z_2/k_g} \quad (\text{F.18})$$

where Δz_1 and Δz_2 are the distances illustrated in figure F.6. Rearranging gives

$$q_{cond,i} = \left(\frac{k_{ve}k_g}{\Delta z_1 k_g + \Delta z_2 k_{ve}} \right) \Delta T_g \quad (\text{F.19})$$

When substituting equation (F.19) into equation (F.17) and expanding, we find

$$-\left(\frac{k_{ve}k_g}{\Delta z_1 k_g + \Delta z_2 k_{ve}}\right) r \Delta \theta \Delta r \Delta T_g = -k_g r \Delta \theta \Delta r \frac{\partial T_g}{\partial z} + \frac{\partial}{\partial t} (\rho_g r \Delta \theta \Delta r \Delta z_k c_g T_g) \quad (\text{F.20})$$

Dividing equation (F.20) by $r \Delta \theta \Delta r$ and realizing that $\Delta z_1 = \frac{1}{2} \Delta z_{k-1}$ and $\Delta z_2 = \frac{1}{2} \Delta z_k$ gives

$$-\left(\frac{2k_{ve}k_g}{\Delta z_{k-1} k_g + \Delta z_k k_{ve}}\right) \Delta T_g = -k_g \frac{\partial T_g}{\partial z} + \rho_g c_g \Delta z_k \frac{\partial T_g}{\partial t} \quad (\text{F.21})$$

At $z > 0$ (In ground)

The ground energy equation expresses the heat fluxes deeper in the ground, below the vegetation layer. This equation is identical to equation (2.5) in Chapter 2 of this dissertation.

At $z = \infty$

At a certain depth in the ground the temperature gradient becomes zero. The boundary condition is identical to equation (2.6) in Chapter 2.

F.2.5 Air stream energy equation

When regarding the defined control volume in figure F.7, an energy balance relation can be formulated for the air stream (air-vapor mixture) flowing between the collector roof and the vegetation in the vegetation section of the collector. An order of magnitude analysis performed by Hedderwick (2001) on the collector air stream energy equation concludes that the kinetic energy, radial conduction and transient kinetic energy terms are negligible in comparison with the other energy terms. Neglecting these terms, we find the energy balance

$$\begin{aligned} q_{rh} r \Delta \theta \Delta r + q_{veh} r \Delta \theta \Delta r + \left(\frac{\dot{m}_v}{A}\right) r \Delta \theta \Delta r h_v + \rho v r \Delta \theta H (c_p T + \omega h_v) \\ = \rho v r \Delta \theta H (c_p T + \omega h_v) + \frac{\partial}{\partial r} (\rho v r \Delta \theta H (c_p T + \omega h_v)) \Delta r \\ + \frac{\partial}{\partial t} (\rho r \Delta \theta \Delta r H (c_v T + \omega h_v)) \end{aligned} \quad (\text{F.22})$$

where c_p , c_v and T are the specific heat capacity at a constant pressure, specific heat capacity at a constant volume and temperature of the air stream in the collector respectively. Simplifying equation (F.22) and dividing by $r \Delta \theta \Delta r$ gives

$$q_{rh} + q_{veh} + \left(\frac{\dot{m}_v}{A}\right) h_v = \frac{1}{r} \frac{\partial}{\partial r} (\rho v r H (c_p T + \omega h_v)) + H \frac{\partial}{\partial t} (\rho (c_v T + \omega h_v)) \quad (\text{F.23})$$

The first term on the right-hand-side of equation (F.23) can be split into the following two terms

$$\frac{1}{r} \frac{\partial}{\partial r} (\rho v r H (c_p T + \omega h_v)) = \frac{1}{r} \frac{\partial}{\partial r} (\rho v r H c_p T) + \frac{1}{r} \frac{\partial}{\partial r} (\rho v r H \omega h_v) \quad (\text{F.24})$$

By applying the differential operator to the first term on the right-hand-side of equation (F.24) and simplifying, we find

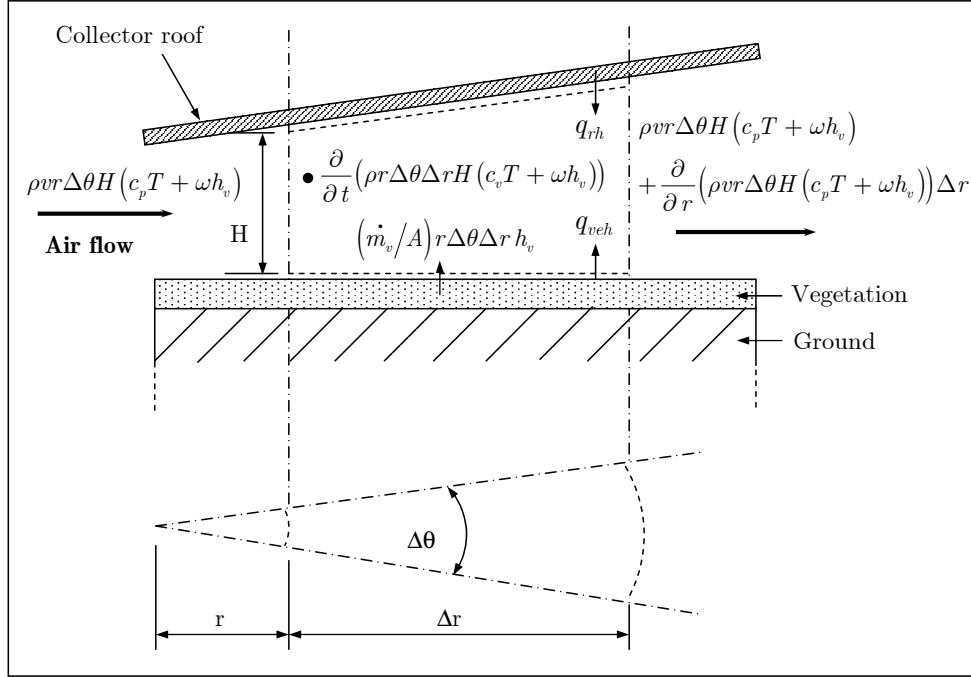


Figure F.7: Conservation of energy applied to a control volume for the air stream in the vegetation section of the collector

$$\frac{1}{r} \frac{\partial}{\partial r} (\rho v r H c_p T) = \frac{c_p T}{r} \frac{\partial}{\partial r} (\rho v r H) + \rho v H \frac{\partial}{\partial r} (c_p T) \quad (\text{F.25})$$

When we apply the differential operator to the second term on the right-hand-side of equation (F.24) and simplify, we find

$$\frac{1}{r} \frac{\partial}{\partial r} (\rho v r H \omega h_v) = \frac{\omega h_v}{r} \frac{\partial}{\partial r} (\rho v r H) + \rho v H \frac{\partial}{\partial r} (\omega h_v) \quad (\text{F.26})$$

The second term on the right-hand-side of equation (F.23) can be split as follows

$$H \frac{\partial}{\partial t} (\rho (c_v T + \omega h_v)) = H \frac{\partial}{\partial t} (\rho c_v T) + H \frac{\partial}{\partial t} (\rho \omega h_v) \quad (\text{F.27})$$

Apply the differential operator to the first term on the right-hand-side of equation (F.27) and obtain

$$H \frac{\partial}{\partial t} (\rho c_v T) = \rho H \frac{\partial}{\partial t} (c_v T) + c_v T H \frac{\partial \rho}{\partial t} \quad (\text{F.28})$$

When substituting the transient form of equation (2.1) (from Pretorius (2004)) into equation (F.28), we obtain the following

$$H \frac{\partial}{\partial t} (\rho c_v T) = \rho H \frac{\partial}{\partial t} (c_v T) - \frac{c_v T}{r} \frac{\partial}{\partial r} (\rho v r H) \quad (\text{F.29})$$

Applying the differential operator to the second term on the right-hand-side of equation (F.27) gives

$$H \frac{\partial}{\partial t} (\rho \omega h_v) = \rho H \frac{\partial}{\partial t} (\omega h_v) + \omega h_v H \frac{\partial \rho}{\partial t} \quad (\text{F.30})$$

Substitute the transient form of equation (2.1) (from Pretorius (2004)) into equation (F.30) and obtain

$$H \frac{\partial}{\partial t} (\rho \omega h_v) = \rho H \frac{\partial}{\partial t} (\omega h_v) - \frac{\omega h_v}{r} \frac{\partial}{\partial r} (\rho v r H) \quad (\text{F.31})$$

If we assume air to be an ideal gas, the relation $(c_p - c_v) = R$ applies, where R is the gas constant. Now, substituting equations (F.25), (F.26), (F.29) and (F.31) for the two terms on the right-hand-side of equation (F.23) and simplifying gives the energy equation for the air-flow in the vegetation section of the collector

$$q_{rh} + q_{veh} + \left(\frac{\dot{m}_v}{A} \right) h_v = \frac{RT}{r} \frac{\partial}{\partial r} (\rho v r H) + \rho H \left[v \frac{\partial}{\partial r} (c_p T + \omega h_v) + \frac{\partial}{\partial t} (c_v T + \omega h_v) \right] \quad (\text{F.32})$$

An order of magnitude analysis performed by Pretorius (2004) on the chimney air stream energy equation concludes that certain terms may be neglected during steady state conditions or when transient effects are negligible. Similarly, equation (F.32) may be reduced to

$$q_{rh} + q_{veh} + \left(\frac{\dot{m}_v}{A} \right) h_v = \frac{RT}{r} \frac{\partial}{\partial r} (\rho v r H) + \rho v H \frac{\partial}{\partial r} (c_p T + \omega h_v) \quad (\text{F.33})$$

F.3 Ground section

The dry air continuity equation, momentum equation, roof energy equation and all ground energy equations for the ground section of the collector (see figure F.1) are identical to those equations presented in Chapter 2 of this dissertation.

F.3.1 Collector continuity equation

Water vapor

In the ground section of the collector (see figure F.1), it is assumed that the air flows over a dry ground surface. This implies that no water is added to the collector air. Therefore, the derivation of the continuity equation for water vapor in the ground section of the collector is similar to that presented in this appendix for the vegetation section, with the exception that the source term (\dot{m}_v/A) is excluded.

Thus the steady state water vapor mass conservation relation for air-flow in the ground section of the collector is given by

$$\frac{\partial}{\partial r} (\rho v r H \omega) = 0 \quad (\text{F.34})$$

F.3.2 Air stream energy equation

As discussed above, it is assumed that the air in the ground section of the collector flows over a dry ground surface. Therefore, the derivation of the air stream energy equation (air-vapor mixture) in the ground section of the collector is similar to that presented in this appendix for the vegetation section, with the exceptions that the source term (\dot{m}_v/A) is excluded and that the convection from the vegetation to the collector air (q_{veh}) term is replaced by the convection from the ground surface to the collector air (q_{gh}) term.

Thus the steady state energy balance for air-flow in the ground section of the collector is given by

$$q_{rh} + q_{gh} = \frac{RT}{r} \frac{\partial}{\partial r} (\rho v r H) + \rho v H \frac{\partial}{\partial r} (c_p T + \omega h_v) \quad (\text{F.35})$$

Appendix

G

Solar Radiative Properties of the Solar Collector

The previous study by Pretorius (2004) determined the radiative properties for a single sheet and absorber configuration, represented by the collector canopy and ground surface of the solar chimney power plant. The calculations incorporated the effects of polarization, regarding both the beam and diffuse solar radiation components. The ground transmittance-absorptance product and the solar radiation incidence angle were also evaluated.

The current study investigates the incorporation of a secondary collector roof, double glazed main roof, double glazed secondary roof, tertiary collector roof and plastic covered water tanks into the model of the solar chimney power plant. This appendix therefore builds on the previous work by determining the relevant radiative properties for a multiple parallel sheet and absorber application.

It is assumed that the inclinations of the roofs under consideration are small enough to consider the canopies as parallel semi-transparent sheets.

G.1 The secondary collector roof

The inclusion of a secondary collector roof into the solar chimney power plant model produces a double parallel sheet and absorber configuration (see figure G.1), represented by the main and secondary roofs and ground surface respectively. The thickness and all properties of the main and secondary collector roofs are assumed to be similar.

Most of the solar radiation striking the main collector roof or canopy is transmitted through the roof while some is reflected and some is absorbed. The radiation transmitted by the main roof strikes the secondary roof where it is again reflected, absorbed and transmitted. Figure G.1 illustrates the path of the incident solar radiation through the collector roofs.

Solar radiation consists of a parallel and perpendicular polarized component. From Fresnel's equation in Modest (1993), for the special case where the same media surrounds a sheet (in this case air), we find

$$r_{\parallel} = \left[\frac{\tan^2(\theta_i - \theta_{re})}{\tan^2(\theta_i + \theta_{re})} \right] \quad (\text{G.1})$$

for the parallel polarization component and

$$r_{\perp} = \left[\frac{\sin^2(\theta_i - \theta_{re})}{\sin^2(\theta_i + \theta_{re})} \right] \quad (\text{G.2})$$

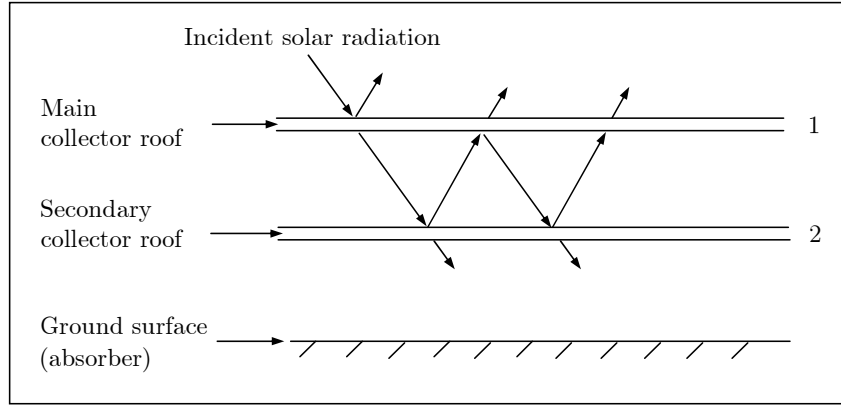


Figure G.1: The path of incident solar radiation as it is reflected and transmitted through a double parallel sheet system, represented by the main and secondary collector roofs

for the perpendicular polarization component of the interface reflection. Snell's law defines the relation between the incident and refractive angles to the refractive indices of the media as follows

$$\theta_{re} = \sin^{-1} \left(\frac{n_a \sin \theta_i}{n_r} \right) \quad (\text{G.3})$$

where θ_i and θ_{re} are the incident and refractive radiation angles, while n_a and n_r represent the refractive indices of the air and the main collector roof material respectively.

Equations (G.1) to (G.3) pertain to the main collector roof specifically. However, as it is assumed that the main and secondary collector roofs have similar refractive indices, the incidence and refractive angles will be equal for both surfaces, implying equal interface reflections for both sheets.

Each semi-transparent sheet absorbs some of the solar radiation that passes through it. This is known as the transmittance due to the absorptance of the sheet τ_α . Modest (1993) gives a relation for the transmittance due to the absorptance of a semi-transparent medium as

$$\tau_\alpha = e^{-C_e t / \cos \theta_{re}} \quad (\text{G.4})$$

where C_e is the extinction coefficient of the medium and t is the sheet (main or secondary collector roof) thickness. Due to the assumption that the main and secondary roofs have similar extinction coefficients, thicknesses and refractive angles, their τ_α values will also be equal.

The respective reflectance, transmittance and absorptance for the parallel polarization component of a single sheet are given by the following equations:

$$\rho_{\parallel} = r_{\parallel} \left[1 + \frac{(1 - r_{\parallel})^2 \tau_\alpha^2}{1 - r_{\parallel}^2 \tau_\alpha^2} \right] \quad (\text{G.5})$$

$$\tau_{\parallel} = \frac{(1 - r_{\parallel})^2 \tau_\alpha}{1 - r_{\parallel}^2 \tau_\alpha^2} \quad (\text{G.6})$$

$$\alpha_{\parallel} = \frac{(1 - r_{\parallel})(1 - \tau_\alpha)}{1 - r_{\parallel} \tau_\alpha} \quad (\text{G.7})$$

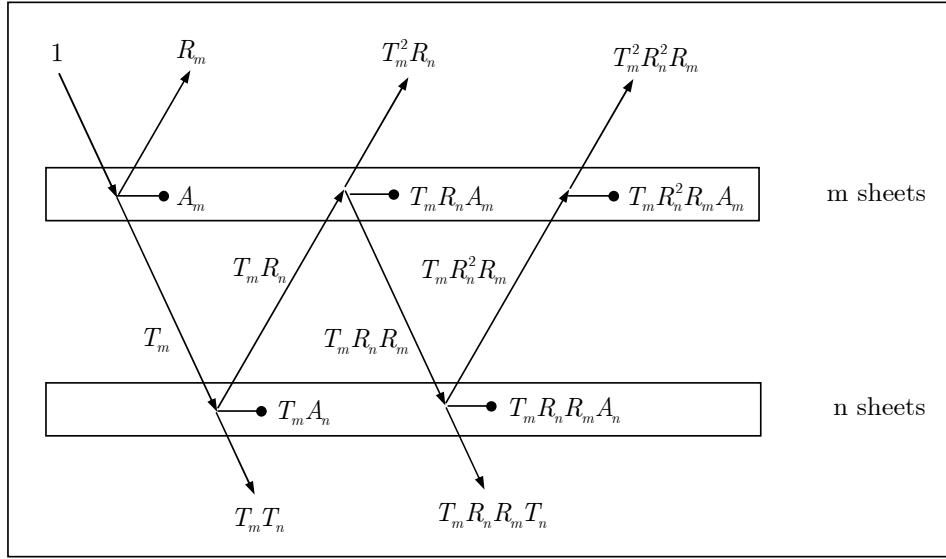


Figure G.2: Ray tracing through a system of multiple parallel semi-transparent sheets

The perpendicular polarization components of these properties can be determined analogously. In the case of a single semi-transparent sheet, the respective total reflectance, total transmittance and total absorptance are given by

$$R_1 = \rho_e = \frac{1}{2}(\rho_{\parallel} + \rho_{\perp}) \quad (\text{G.8})$$

$$T_1 = \tau_e = \frac{1}{2}(\tau_{\parallel} + \tau_{\perp}) \quad (\text{G.9})$$

$$A_1 = \alpha_e = \frac{1}{2}(\alpha_{\parallel} + \alpha_{\perp}) \quad (\text{G.10})$$

where the subscript e denotes the effective (or total) sheet properties. Equations (G.8) to (G.10) are employed when considering a collector configuration that only includes a main collector roof (as presented by Pretorius (2004)).

Siegel and Howell (1992) derive equations for evaluating the radiative properties of multiple parallel sheet systems. Their analysis considers a system of sheets consisting of a group of m identical sheets and a group of n identical sheets, as shown in figure G.2.

When summing all the reflected and transmitted terms of figure G.2, we find the respective total reflectance and total transmittance for a system of $m + n$ sheets

$$R_{m+n} = R_m + \frac{R_n T_m^2}{1 - R_m R_n} \quad (\text{G.11})$$

$$T_{m+n} = \frac{T_m T_n}{1 - R_m R_n} \quad (\text{G.12})$$

The total fraction of radiation absorbed by the system of $m + n$ sheets is found from

$$A_{m+n} = 1 - R_{m+n} - T_{m+n} \quad (\text{G.13})$$

When evaluating the performance of the collector of the solar chimney power plant, it is necessary to determine the respective temperatures of the main and secondary collector roofs. In order to find these temperatures, the effective energy absorbed and transmitted

by each individual sheet has to be determined. It should be noted that the fraction of solar radiation absorbed and transmitted by each sheet changes with the number of sheets or roofs in the system. Siegel and Howell (1992) present the following equation for determining the effective energy absorbed by a group of m sheets in a system of $m + n$ parallel sheets (from figure G.2)

$$A_m^{(m+n)} = A_m \left(1 + \frac{T_m R_n}{1 - R_m R_n} \right) \quad (\text{G.14})$$

while the effective energy absorbed by the group of n sheets is given by

$$A_n^{(m+n)} = \frac{T_m A_n}{1 - R_m R_n} \quad (\text{G.15})$$

The effective energy transmitted by the group of m sheets is found by the following:

$$T_m^{(m+n)} = \frac{T_m}{1 - R_n R_m} \quad (\text{G.16})$$

We now consider specifically the case of a double parallel sheet application (thus with $m = 1$ and $n = 1$), as given by a collector configuration that incorporates a main and secondary collector roof. From equations (G.11) to (G.13), we find

$$R_2 = R_1 + \frac{R_1 T_1^2}{1 - R_1^2} \quad (\text{G.17})$$

for the total reflectance,

$$T_2 = \frac{T_1^2}{1 - R_1^2} \quad (\text{G.18})$$

for the total transmittance and

$$A_2 = 1 - R_2 - T_2 \quad (\text{G.19})$$

for the total absorptance of a collector with a main and secondary roof. Furthermore, from equations (G.14) to (G.16), we find that the effective fraction of energy absorbed by the main collector roof is (with $m = 1$ and $n = 1$)

$$\alpha_{er} = A_1 \left(1 + \frac{T_1 R_1}{1 - R_1^2} \right) \quad (\text{G.20})$$

while the effective energy absorbed by the secondary collector roof is

$$\alpha_{es} = \frac{T_1 A_1}{1 - R_1^2} \quad (\text{G.21})$$

The effective fraction of energy transmitted by the main roof is

$$\tau_{er} = \frac{T_1}{1 - R_1^2} \quad (\text{G.22})$$

The fraction of radiation transmitted by the secondary collector roof is simply equal to the total transmittance through the system and is given by

$$\tau_{tot} = T_2 \quad (\text{G.23})$$

where the subscript *tot* indicates the total transmitted radiation that ultimately strikes the ground surface.

The properties determined by equations (G.20), (G.21) and (G.22) are specifically utilized for the evaluation of the collector roof and secondary collector roof energy equations.

Furthermore, all properties are evaluated separately for the beam and diffuse components of the solar radiation. The subscripts er and es denote the effective roof and effective secondary roof properties respectively.

G.2 The double glazed main collector roof

The inclusion of a double glazed main roof into the solar chimney power plant model also produces a double parallel sheet and absorber configuration (see figure G.3), represented by the top and bottom sheets of the main roof and ground surface respectively.

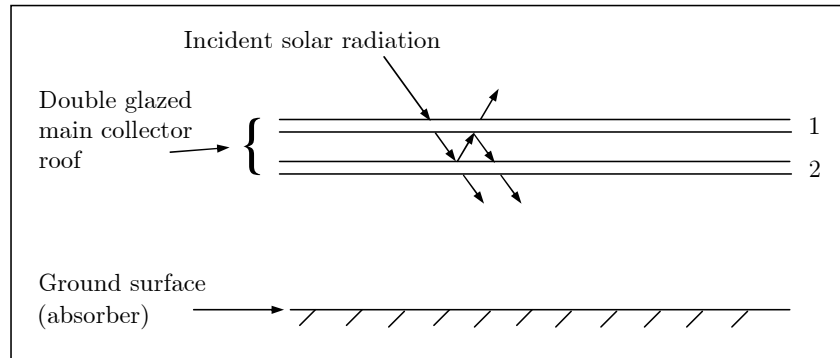


Figure G.3: The path of incident solar radiation as it is reflected and transmitted through a double parallel sheet system, represented by the top and bottom sheets of the double glazed main collector roof

Except for the spacing between the sheets, this configuration is similar to the configuration illustrated by figure G.1. The spacing between the sheets arranged in parallel do not affect their radiative properties. Therefore, the top and bottom sheets of the double glazed collector roof will have equivalent radiative properties to the main and secondary roofs evaluated in the previous section.

Thus by assuming that both sheets of the double glazed main roof have similar thicknesses and properties, all radiative properties are evaluated analogous to the method evaluating the main and secondary roofs, with the only change being that the subscripts $er1$ (effective property for the top sheet of the main collector roof) and $er2$ (effective property for the bottom sheet of the main collector roof) replaces er and es respectively.

G.3 The double glazed secondary collector roof

The inclusion of a double glazed secondary collector roof into the solar chimney power plant collector model produces a triple parallel sheet and absorber configuration, as illustrated by figure G.4. Once again, it is assumed that main collector roof and each sheet of the secondary collector roof have similar thicknesses and properties.

In addition to determining R_1 , T_1 , A_1 , R_2 , T_2 and A_2 as discussed in section G.1, we now calculate the total reflectance, total transmittance and total absorptance for the triple sheet system from the respective equations (G.11), (G.12) and (G.13) (with $m = 1$ and $n = 2$):

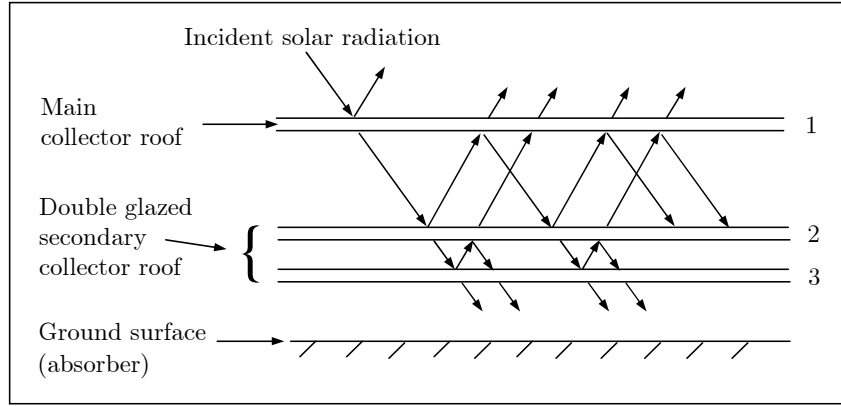


Figure G.4: The path of incident solar radiation as it is reflected and transmitted through a triple parallel sheet system, represented by the main and double glazed secondary collector roofs

$$R_3 = R_1 + \frac{R_2 T_1^2}{1 - R_1 R_2} \quad (\text{G.24})$$

$$T_3 = \frac{T_1 T_2}{1 - R_1 R_2} \quad (\text{G.25})$$

$$A_3 = 1 - R_3 - T_3 \quad (\text{G.26})$$

Equivalent results are obtained if it is assumed that a group of $m = 2$ sheets and a group of $n = 1$ sheets are involved. Once again we have to evaluate the fraction of energy absorbed and transmitted by each individual sheet. For a sheet system with more than two sheets, it should be noted that the n in equation (G.14) now represents the number of sheets after the one under current consideration. Thus, when we evaluate the effective fraction of energy absorbed by the main collector roof (sheet 1), we set $m = 1$ (the sheet considered) and $n = 2$ (the number of sheets after sheet 1), which gives

$$\alpha_{er} = A_1 \left(1 + \frac{T_1 R_2}{1 - R_1 R_2} \right) \quad (\text{G.27})$$

The effective radiation absorbed by the second sheet in a triple sheet system is found by subtracting the effective energy absorbed by the first sheet from the value obtained using equation (G.14). Therefore, when considering the top sheet of the double glazed secondary roof (sheet 2), we set $m = 2$ while the number of remaining sheets are $n = 1$ and find

$$\alpha_{es1} = A_2 \left(1 + \frac{T_2 R_1}{1 - R_2 R_1} \right) - \alpha_{er} \quad (\text{G.28})$$

where the subscript *es1* denotes the effective absorptance of the first (top) sheet of the double glazed secondary collector roof. The effective energy absorbed by the bottom sheet of the double glazed secondary roof is simply calculated by subtracting the effective energies absorbed by the first and second sheets in the system from the total system absorptance:

$$\alpha_{es2} = A_3 - \alpha_{er} - \alpha_{es1} \quad (\text{G.29})$$

where the subscript *es2* refers to the second (bottom) sheet of the secondary collector roof. The effective fraction of radiation transmitted by the main collector roof in the triple parallel sheet system is determined from equation (G.16). As we are considering the first sheet in the system, we set $m = 1$ and $n = 2$, which gives

$$\tau_{er} = \frac{T_1}{1 - R_2 R_1} \tag{G.30}$$

When regarding the second sheet, we substitute $m = 2$ and $n = 1$ into equation (G.16) and find

$$\tau_{es1} = \frac{T_2}{1 - R_1 R_2} \tag{G.31}$$

for the effective fraction of solar radiation transmitted through the first (top) sheet of the secondary collector roof. The effective radiation transmitted through the bottom sheet of the double glazed secondary collector roof is simply equal to the total transmitted radiation of the system:

$$\tau_{tot} = T_3 \tag{G.32}$$

The radiative properties evaluated by equations (G.27) to (G.32) are employed in the main and both secondary collector roof energy equations for the calculation of each sheet temperature. Once again, all properties are evaluated separately for the beam and diffuse components of the solar radiation.

G.4 The secondary and tertiary collector roofs

The inclusion of a secondary and tertiary collector roof into the solar chimney power plant collector model also produces a triple parallel sheet and absorber configuration, as illustrated by figure G.5. Except for the spacing between the sheets, this configuration is similar to the configuration illustrated by figure G.4. The spacing between the sheets arranged in parallel do not affect their radiative properties. Therefore, the secondary and tertiary collector roofs will have equivalent radiative properties to the top and bottom sheet of the double glazed secondary collector roof, evaluated in the previous section.

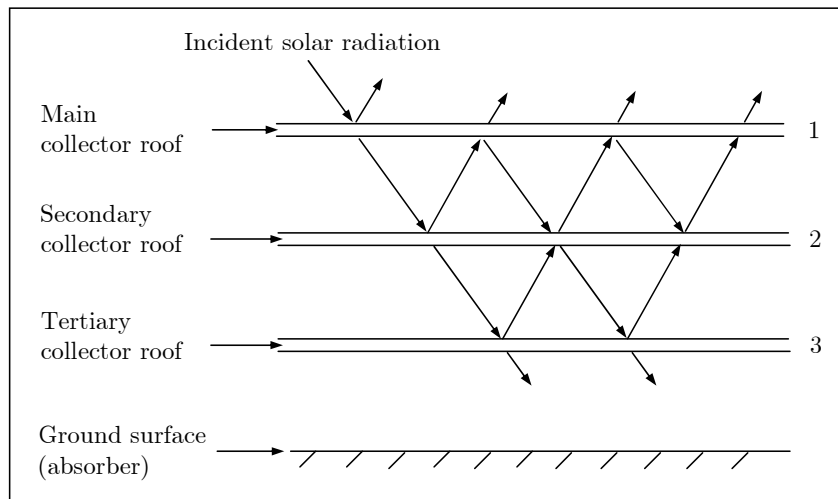


Figure G.5: The path of incident solar radiation as it is reflected and transmitted through a triple parallel sheet system, represented by the main, secondary and tertiary collector roofs

Thus by assuming that the main, secondary and tertiary collector roofs have similar thicknesses and properties, all radiative properties are evaluated analogous to the method for

the double glazed secondary roof, with the only change being that the subscripts *es* (effective property for the secondary collector roof) and *etr* (effective property for the tertiary collector roof) replaces *es1* and *es2* respectively.

G.5 The plastic covered water tanks

The inclusion of plastic covered water tanks into the solar chimney power plant model produces a single sheet and absorber configuration (see figure G.6), represented by the main collector roof and water tanks respectively. The analysis of this configuration differs somewhat from the original single sheet (main collector roof) and absorber (ground) configuration presented by Pretorius (2004).

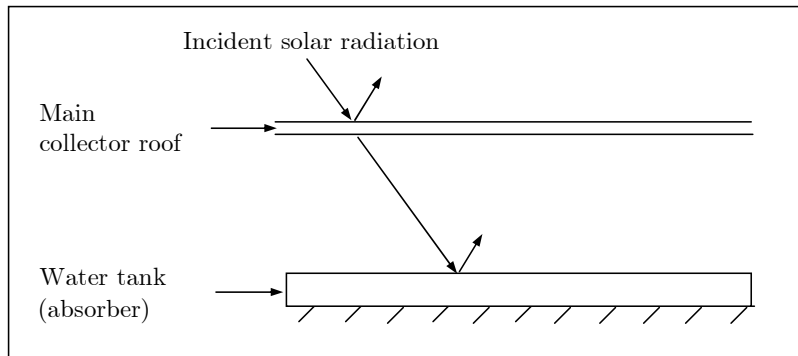


Figure G.6: Single sheet and absorber configuration, represented by the main collector roof and water tank respectively

The total reflectance, transmittance and absorptance of the main collector roof is simply determined from equations (G.1) to (G.10). In order to evaluate the water tank energy equation, the effective reflectance of the plastic film covering the water tank has to be calculated. It is assumed that the plastic film covers the tank in such a manner that there is no air gap between the film and the water surface. Therefore the film is surrounded by different media, that of air and water.

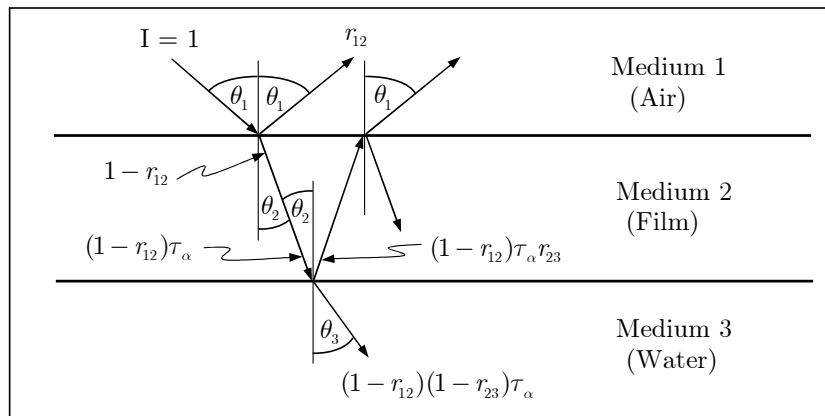


Figure G.7: Reflectance and transmittance of a semi-transparent sheet (plastic film) surrounded by different media (air and water)

Consider the schematic illustration in figure G.7, showing the reflectance and transmittance of a semi-transparent sheet surrounded by different media. In the case of the current solar chimney power plant model, the semi-transparent sheet represents the plastic film covering the water tank, with medium one being the collector air and medium three being the water in the tank. The incident radiation I represents the transmitted solar radiation through the main collector roof. In this case, the air-film interface reflection is determined by

$$r_{12,\parallel} = \left[\frac{\tan^2(\theta_1 - \theta_2)}{\tan^2(\theta_1 + \theta_2)} \right] \quad (\text{G.33})$$

for the parallel polarization component and

$$r_{12,\perp} = \left[\frac{\sin^2(\theta_1 - \theta_2)}{\sin^2(\theta_1 + \theta_2)} \right] \quad (\text{G.34})$$

for the perpendicular polarization component. The angles θ_1 and θ_2 refer to the respective incident and refractive radiation angles at the air-film interface (see figure G.7), with θ_2 determined from equation (G.3). Similarly, the respective parallel and perpendicular film-water interface reflections are given by

$$r_{23,\parallel} = \left[\frac{\tan^2(\theta_2 - \theta_3)}{\tan^2(\theta_2 + \theta_3)} \right] \quad (\text{G.35})$$

$$r_{23,\perp} = \left[\frac{\sin^2(\theta_2 - \theta_3)}{\sin^2(\theta_2 + \theta_3)} \right] \quad (\text{G.36})$$

where the angles θ_2 and θ_3 refer to the respective incident and refractive radiation angles at the film-water interface (see figure G.7), with θ_3 determined from equation (G.3), relative to θ_2 . According to Modest (1993), for the case where a semi-transparent sheet is bordered by different media, the respective reflectance, transmittance and absorptance (for the parallel polarization component) of the sheet are determined by the following equations:

$$\rho_{\parallel} = r_{12,\parallel} + \frac{r_{23,\parallel}(1 - r_{12,\parallel})^2\tau_{\alpha}^2}{1 - r_{12,\parallel}r_{23,\parallel}\tau_{\alpha}^2} \quad (\text{G.37})$$

$$\tau_{\parallel} = \frac{(1 - r_{12,\parallel})(1 - r_{23,\parallel})\tau_{\alpha}}{1 - r_{12,\parallel}r_{23,\parallel}\tau_{\alpha}^2} \quad (\text{G.38})$$

$$\alpha_{\parallel} = \frac{(1 - r_{12,\parallel})(1 + r_{23,\parallel}\tau_{\alpha})(1 - \tau_{\alpha})}{1 - r_{12,\parallel}r_{23,\parallel}\tau_{\alpha}^2} \quad (\text{G.39})$$

where τ_{α} is evaluated for the film according to equation (G.4). The perpendicular polarization components of these properties can be determined analogously. After calculating the corresponding values for the perpendicular polarization component, the effective (or total) reflectance, transmittance and absorptance of the film can be determined according to equations (G.8), (G.9) and (G.10). Thus the effective radiation reflected by the plastic film (ρ_{fe}) is equal to the effective reflectance from equation (G.8). It should be noted that all properties are evaluated separately for the beam and diffuse components of the solar radiation.

Appendix

H

Meteorological Data Tables

A numerical simulation model of a solar chimney power plant was developed in the study by Pretorius (2004) and is further refined in the current study. The model simulates the operation and performance of a large-scale solar chimney power plant for a specific reference location.

This appendix presents the meteorological input data of the reference location (Sishen, South Africa) used by the numerical model. The format and interpretation of these data tables are explained in Chapter 2 of this dissertation.

Table H.1: Total (I_h) and diffuse (I_{hd}) solar radiation on a horizontal surface, W/m^2

Solar Time	6		7		8		9		10		11		12	
	I_h	I_{hd}												
Jan	138	52	357	89	572	108	762	126	909	136	1003	140	1035	135
Feb	68	46	279	86	496	109	691	124	845	144	942	151	976	156
Mar	0	0	190	72	406	102	604	121	763	130	865	138	900	144
Apr	0	0	100	50	299	84	489	112	644	129	745	134	780	148
May	0	0	35	18	220	66	407	85	562	101	664	106	700	105
Jun	0	0	19	10	190	63	368	88	517	109	616	117	650	111
Jul	0	0	35	17	220	66	407	90	562	107	664	113	700	112
Aug	0	0	99	50	295	91	483	106	636	127	735	125	770	123
Sep	0	0	182	78	388	109	578	127	730	139	827	149	861	155
Oct	66	45	272	95	483	121	673	141	822	156	917	165	950	181
Nov	135	62	348	90	558	112	743	126	887	133	979	137	1010	131
Dec	157	58	375	83	587	103	773	108	917	119	1009	121	1040	114

Solar Time	13		14		15		16		17		18	
	I_h	I_{hd}										
Jan	1003	140	909	136	762	130	572	114	357	82	138	40
Feb	942	160	845	161	691	145	496	114	279	75	68	24
Mar	865	138	763	145	604	133	406	102	180	54	0	0
Apr	745	142	644	129	489	108	299	78	110	31	0	0
May	664	100	562	96	407	77	220	48	35	11	0	0
Jun	616	105	517	93	368	70	190	44	19	6	0	0
Jul	664	106	562	96	407	77	220	48	35	12	0	0
Aug	735	125	636	114	483	101	295	71	99	32	0	0
Sep	827	149	730	146	578	121	388	97	182	58	0	0
Oct	917	183	822	173	673	155	483	135	272	90	66	28
Nov	979	137	887	142	743	134	558	117	348	87	135	45
Dec	1009	131	917	128	773	124	587	116	375	86	157	49

Table H.2: Ambient air temperature, °C

Solar Time	1	2	3	4	5	6	7	8	9	10	11	12
Jan	25.52	25.09	24.66	24.33	23.8	23.37	22.94	22.51	24.1	25.9	27.6	29
Feb	24.89	24.46	24.03	23.6	23.17	22.72	22.31	21.88	22.7	24.5	26.2	27.6
Mar	22.59	22.16	21.73	21.3	20.87	20.44	20.01	19.58	20.7	22.8	24.5	25.9
Apr	18.19	17.76	17.33	16.9	16.47	16.04	15.61	15.18	16.5	18.8	20.6	22
May	15.96	15.53	15.1	14.67	14.24	13.81	13.38	12.95	12.52	14.8	16.9	18.4
Jun	13.16	12.73	12.3	11.87	11.44	11.01	10.58	10.15	9.72	11.3	13.6	15.4
Jul	14.06	13.63	13.2	12.77	12.34	11.91	11.48	11.05	10.62	11.4	13.8	15.7
Aug	14.79	14.36	13.93	13.5	13.07	12.64	12.21	11.78	11.35	13.7	15.9	17.7
Sep	19.59	19.16	18.73	18.3	17.87	17.44	17.01	16.58	16.15	18.5	20.6	22.2
Oct	22.09	21.66	21.23	20.8	20.37	19.94	19.51	19.08	19.4	21.5	23.3	24.8
Nov	22.52	22.09	21.66	21.23	20.8	20.37	19.94	20	22.2	24.1	25.7	27
Dec	24.92	24.49	24.06	23.63	23.2	22.77	22.34	21.91	24	25.8	27.4	28.6

Solar Time	13	14	15	16	17	18	19	20	21	22	23	24
Jan	30	30.5	30.7	30.5	30.1	29.3	28.1	27.67	27.24	26.81	26.38	25.95
Feb	28.7	29.4	29.5	29.3	28.7	27.9	27.47	27.04	26.61	26.18	25.75	25.32
Mar	26.8	27.4	27.5	27.3	26.5	25.6	25.17	24.74	24.31	23.88	23.45	23.02
Apr	23	23.6	23.9	23.6	23	21.2	20.77	20.34	19.91	19.48	19.05	18.62
May	19.5	20.2	20.4	20.3	19.4	18.97	18.54	18.11	17.68	17.25	16.82	16.39
Jun	16.5	17.3	17.7	17.5	16.6	16.17	15.74	15.31	14.88	14.45	14.02	13.59
Jul	17	17.9	18.3	18.2	17.5	17.07	16.64	16.21	15.78	15.35	14.92	14.49
Aug	19.1	20	20.5	20.5	19.9	17.8	17.37	16.94	16.51	16.08	15.65	15.22
Sep	23.5	24.3	24.7	24.7	24.1	22.6	22.17	21.74	21.31	20.88	20.45	20.02
Oct	25.9	26.6	26.9	26.9	26.3	25.1	24.67	24.24	23.81	23.38	22.95	22.52
Nov	27.9	28.5	28.6	28.4	27.9	27	25.1	24.67	24.24	23.81	23.38	22.95
Dec	29.7	30.1	30.4	30.3	29.7	28.9	27.5	27.07	26.64	26.21	25.78	25.35

Table H.3: Ambient wind speed, in m/s, at 10 m above ground level

Solar Time	1	2	3	4	5	6	7	8	9	10	11	12
Jan	2.68	2.70	2.66	2.68	2.70	2.61	2.71	3.03	3.64	3.44	3.00	2.97
Feb	2.56	2.46	2.25	2.17	2.09	2.11	2.46	2.77	3.13	3.28	3.35	3.28
Mar	2.26	2.31	2.34	2.40	2.40	2.42	2.38	2.64	3.00	3.20	3.31	3.34
Apr	3.04	2.93	2.84	2.75	2.71	2.65	2.67	2.82	3.22	3.63	3.82	3.89
May	2.93	2.93	2.94	2.99	3.02	2.99	2.89	2.76	2.83	3.16	3.32	3.42
Jun	3.40	3.29	3.24	3.19	3.05	2.91	2.79	2.75	3.00	3.37	3.63	3.81
Jul	3.54	3.62	3.50	3.28	3.12	3.05	3.06	3.01	3.31	3.80	4.01	4.02
Aug	3.47	3.60	3.71	3.75	3.82	3.79	3.48	3.33	3.52	3.72	3.90	4.03
Sep	3.65	3.66	3.62	3.47	3.41	3.38	3.50	3.87	4.38	4.58	4.72	4.79
Oct	3.43	3.52	3.35	3.14	3.15	3.16	3.29	3.70	3.96	4.04	4.19	4.21
Nov	3.45	3.47	3.51	3.31	3.22	3.24	3.54	4.18	4.21	4.30	4.33	4.47
Dec	2.69	2.67	2.59	2.72	2.83	2.82	3.04	3.53	4.01	4.27	4.33	4.39

Solar Time	13	14	15	16	17	18	19	20	21	22	23	24
Jan	3.15	3.23	3.15	3.24	3.40	3.26	2.71	2.60	2.63	2.75	2.93	2.69
Feb	3.21	3.33	3.59	3.69	3.54	3.29	2.94	2.68	2.61	2.53	2.57	2.38
Mar	3.42	3.54	3.61	3.56	3.30	2.88	2.54	2.58	2.67	2.52	2.50	2.36
Apr	3.87	3.85	3.69	3.56	3.33	2.94	2.79	2.90	3.03	3.05	3.03	3.11
May	3.46	3.45	3.46	3.41	2.99	2.49	2.54	2.73	2.73	2.88	3.02	2.99
Jun	3.86	3.84	3.77	3.62	3.12	2.69	2.82	3.00	3.14	3.29	3.44	3.44
Jul	4.01	3.95	3.89	3.75	3.32	2.95	2.93	3.05	3.19	3.33	3.46	3.46
Aug	3.99	3.98	4.01	3.88	3.50	2.96	2.75	2.98	3.11	3.23	3.41	3.45
Sep	4.81	4.77	4.78	4.64	4.38	3.84	3.44	3.43	3.42	3.47	3.71	3.68
Oct	4.41	4.51	4.64	4.50	4.38	4.11	3.36	2.95	3.11	3.18	3.23	3.27
Nov	4.53	4.58	4.53	4.51	4.50	4.38	3.88	3.38	3.26	3.18	3.32	3.30
Dec	4.44	4.38	4.22	4.11	4.06	4.01	3.63	3.19	3.27	3.13	2.92	2.78

Table H.4: Ambient relative humidity, %

Solar Time	1	2	3	4	5	6	7	8	9	10	11	12
Jan	80.38	82.32	85.02	87.12	87.97	84.29	75.13	67.65	62.91	57.35	52.17	47.9
Feb	78.14	80.84	82.83	84.54	85.82	83.87	74.48	65.52	59.49	53.88	48.94	44.64
Mar	82.24	84.06	85.52	86.72	88.06	88.02	81.52	73.06	66.03	59.71	54.71	50.83
Apr	82.9	84.67	86.55	88.56	89.64	90.14	86.15	74.83	63.77	56.21	50.36	45.72
May	69.15	71.62	74.25	75.88	76.73	77.67	75.25	64.43	51.54	43.04	36.88	32.09
Jun	63.99	66.36	67.2	67.97	70.17	72.38	71.51	63.14	51.56	43.14	37.11	32.97
Jul	57.52	60.13	62.84	64.94	66.64	67.91	66.65	58.31	47.79	40.75	35.67	31.12
Aug	46.17	47.78	49.39	51.65	53.7	55.28	51.42	41.15	31.96	26.66	22.78	19.52
Sep	51.33	54.9	57.24	57.78	59.73	61.69	57.36	47.52	39.95	34.49	29.89	26.43
Oct	48.69	52.22	55.68	58.3	60.92	60.53	53.95	44.82	38.72	33.08	29.15	25.94
Nov	49.66	52.43	55.93	59.33	61.96	62.34	55.38	48.38	42.09	35.98	29.99	26.29
Dec	68.7	71.98	75.6	78.21	79.99	76.76	67.31	58.58	51.7	46.03	41.55	37.2

Solar Time	13	14	15	16	17	18	19	20	21	22	23	24
Jan	45.57	44.28	43.27	43.62	46.8	52.3	60.98	66.67	70.39	73.38	76.34	78.79
Feb	41.42	41.2	42.18	43.59	43.97	48.93	56.92	62.79	66.53	70.12	73.46	74.86
Mar	47.73	46.4	46.61	47.27	49.83	56.93	64.6	68.31	72.79	76.7	79.79	80.42
Apr	41.58	39.07	38.28	39.03	44.56	55.77	64.81	68.44	70.27	72.89	76.87	80.57
May	27.98	24.72	23.2	23.95	29.37	39.93	48.39	52.62	55.92	58.87	61.55	66
Jun	29.63	27.07	25.75	26.14	31.04	39.47	45.57	49.04	52.11	55.65	58.86	61.15
Jul	27.46	24.78	23.12	22.81	25.64	32.51	38.28	41.25	44.17	47.25	49.73	54.94
Aug	16.9	14.65	13.37	13.28	15.25	20.51	25.9	29.69	33.12	36.61	39.26	43.55
Sep	23.14	20.43	19.02	18.58	19.55	23.39	29.34	34.63	39.14	42.85	45.75	48.8
Oct	23.47	22.66	21.81	21.96	22.85	24.97	29.88	34.44	37	39.71	42.72	45.7
Nov	23.58	21.63	21.04	22.11	23.05	24.58	28.16	33.03	36.51	40.58	43.73	47.7
Dec	33.7	31.68	31.48	32.06	34.21	38.67	45.37	52.39	55.31	58.84	62.73	66.11